Sensorless Plunger Position Control and Differential Plunger Position Self-Sensing using Constant Air Gap Solenoids

by

Bradley Reinholz

B.A.Sc., The University of British Columbia, 2014
M.A.Sc., The University of British Columbia, 2016

A THESIS SUBMITTED IN PARTIAL FULFILLMENT OF
THE REQUIREMENTS FOR THE DEGREE OF

DOCTOR OF PHILOSOPHY

in

THE COLLEGE OF GRADUATE STUDIES

(Electrical Engineering)

THE UNIVERSITY OF BRITISH COLUMBIA

(Okanagan)

January 2022

© Bradley Reinholz, 2022

The following individuals certify that they have read, and recommend to the College of Graduate Studies for acceptance, a thesis/dissertation entitled:

Sensorless Plunger Position Control and Differential Plunger Position Self-Sensing using Constant Air Gap Solenoids

submitted by Bradley Reinholz in partial fulfillment of the requirements of

the degree of Doctor of Philosophy .

Dr. Rudolf Seethaler, School of Engineering

Supervisor

Dr. Wilson Eberle, School of Engineering

Supervisory Committee Member

Dr. Homayoun Najjaran, School of Engineering

Supervisory Committee Member

Dr. Yang Cao, School of Engineering

University Examiner

Dr. Bob Koch, University of Alberta

External Examiner

Abstract

Industry 4.0 cyber-physical systems will require innovative new technologies including smart sensors that can monitor their own health and smart actuators that can be controlled without a dedicated position sensor. A novel constant air gap solenoid (CAS) is presented that is configurable as a smart actuator or a smart sensor. The novel CAS actuator and CAS sensor have the unique ability to simultaneously produce two distinct self-sensed plunger position measurements unlike other electromagnetic actuators or inductive differential position sensors. These measurements can then be fused to produce a single wide-bandwidth position measurement that performs more robustly than the individual self-sensed measurements.

The CAS actuator is first studied by deriving equations to describe and predict its behavior. Next, finite element analysis is utilized to investigate a basic CAS actuator geometry and predict its force and inductance characteristics. The finite element analysis results are then imported into a lumped-parameter simulation built within Simulink to predict CAS actuator performance characteristics. Afterwards, a physical prototype of the simulated geometry is fabricated and experimentally validated. The experimental results demonstrate that the prototype is capable of 40Hz sensorless plunger control for 1mm ramp and step trajectories.

The CAS sensor is developed by configuring two CASs to pull against each other to allow differential measurements to be obtained. The derived analytical equations prove that the differential measurements are immune to factors, such as resistance changes due to temperature. The CAS sensor, like the CAS actuator is first studied using finite element analysis, then a Simulink simulation and is finally experimentally validated with a physical prototype. The

experimental results show accurate noise-cancelling measurements that can maintain less than 1% nonlinearity. If a current sensor is removed, the CAS sensor can still achieve approximately 3% nonlinearity over its 3mm stroke, proving that it has inherent failure redundancy.

The results of this work demonstrate the CAS actuator and CAS sensor have distinct advantages over comparable actuation and sensing technologies. Furthermore, this work experimentally demonstrates a CAS can be configured to be a smart actuator or a smart sensor and therefore is applicable to cyber-physical systems and other practical applications.

Lay Summary

Sensors and actuators are critical components for any motion control task. This thesis presents a new type of solenoid that can be configured as a sensor or an actuator. As a sensor, it is able to measure low-speed and high-speed position movements with high resolution and accuracy, even when factors like the temperature change. As an actuator, this type of solenoid is able to control its plunger position without the need for an external position sensor. A key feature of the proposed solenoid design is its unique ability to simultaneously produce low and high-speed plunger position measurements. These measurements can then be fused to only extract the accurate features of each measurement, while rejecting the erroneous parts. This allows the proposed actuator and sensor to perform well at both low and high-speeds unlike comparable electromagnetic actuators and inductive sensors that only produce a single plunger measurement.

Preface

The research and development of the constant air gap solenoid technology presented in this thesis was supported both financially and in-kind by Westport Fuel Systems Canada Inc. All research was performed under the supervision of Dr. Rudolf Seethaler. Experiments and prototyping work were completed in the Control and Automation Laboratory within the School of Engineering at UBC Okanagan.

Chapter 2 and Chapter 4 include published works from B. A. Reinholz and R. J. Seethaler, "Design and Validation of a Variable Reluctance Differential Solenoid Transducer," *IEEE Sensors,* vol. 19, no. 23, pp. 11063-11071, 2019. In particular, this publication introduced the concept of a constant air gap solenoid and a sensor configuration. The back electromotive force-based algorithm and inductance-based algorithms were also derived and experimentally validated within this work. For this paper, I worked collaboratively with Dr. Seethaler to develop analytic models. I then developed finite element analysis and Simulink simulations. Afterwards, I fabricated a prototype sensor and experimentally validated the simulated results. Lastly, I produced the first draft of the article.

The flux linkage-based method and complementary filter discussed in Chapter 2 and Chapter 4 were previously disseminated in B. A. Reinholz and R. J. Seethaler, "Flux Linkage Sensor Fusion of a Variable Reluctance Differential Solenoid Transducer," in *International Conference on Manipulation, Automation and Robotics at Small Scales (MARSS)*, 2020. This work relates primarily to the sensor configuration of the constant air gap solenoid. In this paper, I worked with Dr. Seethaler to develop analytic models. I then developed a Simulink simulation and performed experiments with a prototype sensor to validate the simulated results. I also wrote the first draft of the paper.

The entirety of this work is protected by B. Reinholz, R. Seethaler, G. McTaggart-Cowan, A. Singh and D. Reinholz, "Solenoid Apparatus and Methods". International Patent WO2020186358, 20 3 2020. I initially drafted the UBC invention disclosure. I then worked closely with a Westport Fuel Systems Canada Inc. patent specialist to transcribe the invention disclosure into the full patent. I am listed as the inventor with the largest percent contribution.

Table of Contents

List of Tables

List of Figures

List of Symbols

A_ϕ	Cross-sectional area of flux path
A_g	Cross-sectional area of the air gap
A_w	Stator area available for windings
B	Magnetic flux density
B_a	Flux density amplitude
B_{sat}	Saturation flux density
B_m	DC external magnetic flux density in a voice coil
b	Plunger damping
C_e	Eddy current material constant
C_{ff}	Winding fill-factor
C_L	The inductance vs. position slope
D_g	Air gap depth
E_f	Field energy
F_c	CAS force
F_{sat}	Peak force at saturation
F_v	Variable air gap solenoid force
f	Frequency
f_{AC}	Superimposed AC voltage frequency
f_{CF}	Complementary filter center frequency
f_I	Current controller frequency

f_P Position controller frequency

f_{res} Online resistance calculation lowpass filter frequency

$f_{y_L max}$ Maximum frequency the inductance-based measurement can operate

H Magnetizing field

I Current

I_{AC} Superimposed AC current

I_{ACRMS} RMS AC current

I_{min} Minimum CAS actuator current

I_{max} Maximum CAS actuator current

I_{ref} Reference current used as the input for the current controller

I_{sat} Current that causes magnetic saturation

$\dot{I}$ Time derivative of current

J Current density

K_{dI} Current controller derivative gain

K_f CAS force constant

K_{iCF} Complementary filter integral gain

K_{iI} Current controller integral gain

K_{iP} Position controller integral controller gain

K_{pCF} Complementary filter proportional gain

K_{pI} Current controller proportional gain

K_{pP} Position controller proportional gain

k_s Spring constant

L	Inductance
L_c	Corrected inductance
L_{c1}	Inductance of the upper CAS
L_{c2}	Inductance of the lower CAS
L_o	CAS inductance when the plunger is at its zero-position
L_t	Terminal inductance
l_g	Air gap length
l_{ht}	Winding half-turn length
l_w	Length of windings
l_ϕ	Length of flux path
m	Plunger mass
N	Number of windings
n_{BPF}	Bandpass filter order
n_{CF}	Complementary filter input integrator order
n_p	Number of parallel stator gaps
n_s	Number of series stator gaps
P_e	Power loss due to eddy currents
P_{cu}	Power loss due to resistive heating
Q_{BPF}	Bandpass filter quality factor
Q_{res}	Online resistance calculation lowpass filter quality factor
R	Resistance
R_c	CAS resistance

Rc_1	Resistance of the upper CAS
Rc_2	Resistance of the lower CAS
R_o	Initial resistance
R_t	Terminal resistance
s	Laplace variable
T	Temperature change
t	Time
t_{lam}	Lamination thickness
U	Voltage
U_1	Voltage across CAS-1 within a CAS sensor
U_2	Voltage across CAS-2 within a CAS sensor
U_A	Voltage across the upper coil in an LVDT or DVRT
U_B	Voltage across the lower coil in an LVDT or DVRT
U_{AC}	Superimposed AC voltage
U_{ACRMS}	RMS AC voltage
U_{BEMF}	Backwards electromotive force
U_{max}	Maximum supply voltage available
U_{out}	Output voltage of an LVDT or DVRT
U_{ref}	Reference voltage
V	Volume
v	Velocity
w_g	Air gap width

w_{g1}	Air gap width of CAS-1 in a CAS sensor
w_{g2}	Air gap width of CAS-2 in a CAS sensor
w_{gp1}	Air gap width from the prior timestep for CAS-1 within a CAS sensor
w_{gp2}	Air gap width from the prior timestep for CAS-2 within a CAS sensor
w_o	Virtual plunger-stator overlap
w_p	Plunger tooth width
w_s	Stator tooth width
y	Plunger or core position
$\hat{y}$	Measured plunger position
$\dot{y}$	Plunger velocity
$\ddot{y}$	Plunger acceleration
y_B	Plunger position estimate produced by the BEMF-based method
$\dot{y}_B$	Plunger velocity estimate produced by the BEMF-based method
y_{CFB}	BEMF complementary filter position
$\dot{y}_{CFB}$	BEMF complementary filter velocity
$y_{CF\lambda}$	Flux-linkage complementary filter output
y_d	Differential plunger position estimate
y_{dL}	Differential inductance-based plunger position estimate
y_{dBEMF}	Differential BEMF-based plunger position estimate
$y_{d\lambda}$	Differential flux linkage-based plunger position estimate
y_L	Plunger position estimate produced by the inductance-based method
y_{max}	Maximum plunger position

y_{min}	Minimum plunger position
y_p	Plunger position from the prior timestep
y_{ref}	Reference plunger position used as the input for the position controller
y_λ	Plunger position estimate produced by the flux linkage-based method
Z_c	Electrical impedance
γ_H	High-speed complementary filter input
γ_L	Low-speed complementary filter input
γ_O	Complementary filter output
λ	Flux linkage
λ_L	Measured flux linkage from the inductance-based method
$\dot{\lambda}$	Time-derivative of flux linkage
$\dot{\lambda}_\lambda$	Measured time-derivative of flux linkage from the flux linkage-based method
ϕ	Magnetic flux
ϕ_{sat}	Flux at saturation
$\dot{\phi}$	Derivative of magnetic flux with respect to time
ρ_r	Material resistivity constant
μ	Material permeability constant
ω_{CF}	Complementary filter center angular frequency
ω_I	Current controller frequency
ω_P	Position controller frequency
ω_r	Resonant frequency
ζ_{CF}	Complementary filter damping ratio

ζ_I	Current controller damping
ζ_P	Position controller damping

List of Abbreviations

Abbreviation	Definition
BEMF	Back electromotive force
CAS	Constant air gap solenoid
DVRT	Differential variable reluctance transducer
FEA	Finite element analysis
IGBT	Insulated-gate bipolar transistor
LSRM	Linear switched reluctance motor
LVDT	Linear variable differential transformer
MMF	Magnetomotive force
PWM	Pulse width modulation
PI	Proportional-integral
PID	Proportional-integral-derivative
RMS	Root-mean-square
SNR	Signal-to-noise ratio

Acknowledgements

I would like to start by thanking my supervisor, Dr. Rudolf Seethaler, for his immense contributions to both my research and my professional development. I first met Dr. Seethaler through a course he taught me in my first year. By chance, we met again a few months later at a retail job I was working at where he recognized me from his lectures and encouraged me to pursue undergraduate research with him. Over the last 11 years Dr. Seethaler supervised me, I received several awards and honors including USRAs, both the CGS-M and CGS-D and was nominated by NSERC and the Royal Society to represent Canada at the 2017 Commonwealth Science Conference. I certainly attribute these accomplishments to Dr. Seethaler's guidance, knowledge and support. Considering that I only ever intended to get a B.A.Sc after high school, it is obvious how profound of an impact Dr. Seethaler has had on my life.

Next, I would like to express my sincerest appreciation to Westport Fuel Systems Canada Inc. for supporting my research both financially and in-kind through a CRD and Mitacs grant. I am tremendously grateful that they pursued a patent of my CAS invention, which I regard as my greatest research accomplishment. I especially would like to thank Dr. Sandeep Munshi, Ashish Singh, Paul Schranz and Dr. Gordon McTaggart-Cowan for their commitment to this project. I am also very appreciative for their guidance and for providing me with an invaluable opportunity to gain industry experience.

I extend my thanks to my committee members, Dr. Wilson Eberle and Dr. Homayoun Najjaran for both guiding my research and my extracurricular pursuits while in academia. I would also like to thank Dr. Yang Cao, Dr. Richard Klukas and Malcolm Metcalfe for always being available to offer their insights and guidance regarding important decisions I have made during my time in academia.

I would like to thank my friends and colleagues who I have shared so many fond memories with. I am especially appreciative of my friends and colleagues in EME2212 who supported my research and tolerated the hours-upon-hours of loud and high-pitched noises coming from my experimental setups.

I would like to express my sincerest appreciation to Pengxia Wu for her thoughtful encouragement, caring support and for helping me survive working three jobs while finishing my research. Without a doubt, the rate at which I was acquiring grey hairs slowed once I met Pengxia and she quickly became the silver lining of the pandemic. I certainly look forward to our bright future and the next chapter of our lives as we near the completion of our PhD degrees.

Lastly, I would like to express my deepest gratitude to my family who have supported me over my lifetime. It has been a privilege to co-author papers with both of my siblings, Dr. Lindsey Reinholz and Devin Reinholz. I would especially like to thank Devin for spending countless evenings with me on campus working past 4:00am trying to get research done to abide by COVID laboratory personnel limits. Finally, I would like to take the opportunity to thank my parents, George Reinholz and Diane Reinholz. They have been tremendously supportive and enabled me to devote more time to my academic pursuits, which allowed me to excel far beyond my own capabilities. I do not think I will ever be able to express how grateful I am to have them as parents, but perhaps dedicating the next page of my thesis to them would be a good start.

Dedication

This thesis is dedicated to my parents.

George Reinholz

Diane Reinholz

Chapter 1: Introduction

The commencement of the third industrial revolution brought about a paradigm shift toward automation and robotic technologies in manufacturing and consumer goods [1]. Programmable logic controllers were considered to be at the core of the third industrial revolution [1]. However, actuation and sensor technologies were also integral as they formed the interface between the physical world and programmable logic controllers. As society progresses toward the fourth industrial revolution centered about cyber-physical systems, the demand for more robust and versatile motion control technologies will continue to increase [2], [3], [4].

The development of smart actuators and sensors will be required to produce robust cyber-physical systems. In order to be robust, smart sensors need to be self-aware of their own health and capable of detecting internal malfunctions and breakages [5]. A smart actuator is generally regarded as an actuator whose health is monitored by external sensors [6], [7]. However, adding sensors to an actuation system often increases cost, size and complexity while reducing reliability [8], [9]. Therefore, actuators that can simultaneously act as a sensor and actuator are highly desirable for cyber-physical systems.

This thesis presents a unique subset of solenoid called a constant air gap solenoid (CAS). A CAS is a simple reluctance machine that has linear-inductance and constant-force characteristics. A CAS shares similar geometry features with a linear switched reluctance motor (LSRM), making it simple to design and fabricate. When several CASs are stacked and share a common plunger, they can be configured as either a self-sensing actuator or a dedicated differential position sensor. A CAS has a novel ability to simultaneously generate two disjoint estimates of its plunger position based on voltage and current measurements [10]. The bandwidths of the two measurements are complementary and they can be fused to combine the desirable aspects of each estimate, helping to overcome the challenges posed by the individual measurements [10]. In the case of an actuator, the CAS can use its self-sensed plunger position estimates to perform closed-loop position control. A CAS sensor, which is referred to as a variable reluctance differential solenoid transducer in literature, can produce the same estimates as a CAS actuator, but also has the ability to produce differential estimates that reject common-mode noise and provide added immunity to high-order effects [10]. Furthermore, both the CAS actuator and sensor can monitor their own health and detect changes from nominal operating conditions. These highly sought-after features and abilities allow the CAS technology to be versatile and robust for a wide range of modern and future applications.

1.1 Overview of Common Motion Control Nonlinearities and High-Order Effects

Nonlinear and high-order effects limit the performance of actuators and sensors. Depending on the type of actuator or sensor, these effects may have negligible or severe implications on its suitability for a particular application. An overview of common high-order effects faced by motion control technologies are provided below.

1.1.1 Thermal Effects

Ambient and self-generated temperature changes can lead to numerous challenges for both sensors and actuators. Many material properties are directly related to temperature which can result in degraded performance or irreversible damage. Temperature changes are known to affect the resistance, inductance and capacitance of electronic devices [11], [12], [13]. In each of these cases, a dependency on temperature creates modeling challenges which can affect the performance of sensors and actuators alike. However, actuators typically generate much larger energy losses than sensors, which often leads to an increase in temperature [14], [15]. Heating effects, such as an increase in winding resistance, can then lead to even larger losses creating a positive-feedback scenario [15]. Naturally, thermal runaway will result if the rate of cooling is insufficient.

All actuators and sensors have finite temperature limits that will lead to failure if exceeded, such as the winding insulation temperature rating [16]. For actuators that use permanent magnets or piezoelectric ceramics, demagnetization and piezoelectric depoling create significant thermal limitations [14], [17], [18], [19]. Neodymium magnets are commonly used in permanent magnet machines due to their high magnetic energy density [20]. However, common grades of neodymium magnets typically begin to irreversibly demagnetize after 80°C, which is well-below common winding insulation B (130°C) and F (155°C) grades [17], [21]. Common piezoelectric materials typically have an operating temperature limit of 150°C, but are poor at dissipating heat, which makes them prone to irreversible depoling [14], [22]. Reversible demagnetization and depoling occur at even lower temperatures and degrade performance within the allowable thermal operating range [14], [17]. For example, reversible demagnetization can reduce permanent magnet flux density by over 10% [17]. Naturally, temperature dependencies introduce a significant source of error in models as material parameters are often assumed to be independent of temperature [23]. It is important to note that high-heat magnet options are available, but may require trade-offs to be made regarding cost and magnetic field strength [17], [24]. Similar temperature-performance-cost compromises need to be made when selecting piezoelectric materials [25].

1.1.2 Drift

Drift is a form of error that generally occurs when a sensor is improperly calibrated or is operated away from its calibrated conditions [26]. Temperature changes and aging effects frequently contribute to drift [27]. Drift is problematic for measurements requiring mathematical integration, such as an angular position measurement from a gyroscope [28]. For example, if one were to integrate the temperature-induced offset seen in Figure 1.1, the drift shown in in Figure 1.2 would result. Clearly, the integrated output accumulates error at a rate that is dependent on the quantity of the offset. Over short durations, the accumulated error may be small and inconsequential, especially if the accumulated drift can be periodically zeroed as shown in Figure 1.2. However, in general, measurements that suffer from drift are inadequate for long-duration measurements.

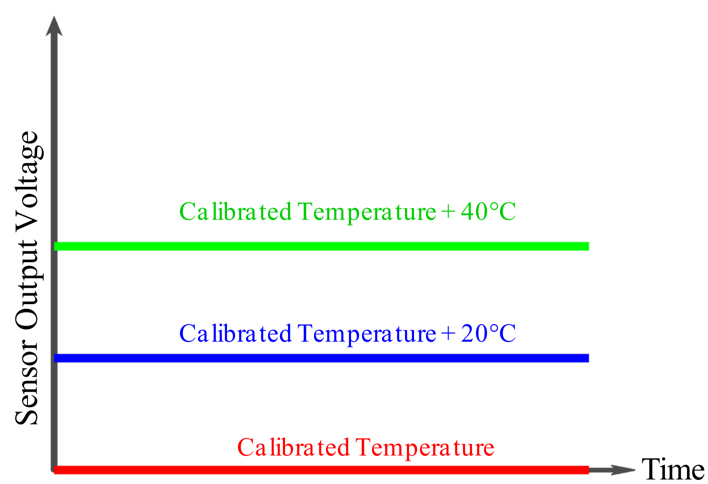

Figure 1.1 A representation of an offset created by an increase in temperature for a sensor at steady state conditions.

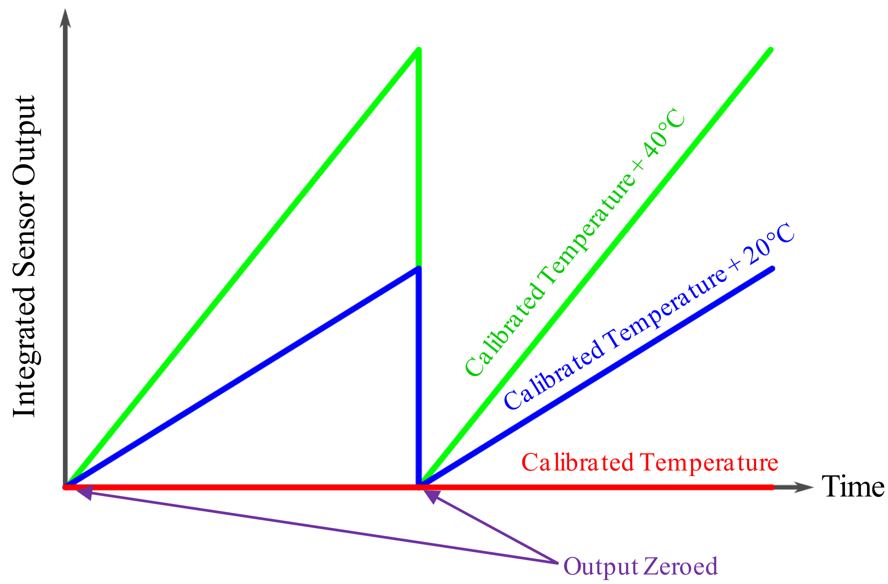

Figure 1.2 Shows how integrating the offset in Figure 1.1 results in drift that accumulates error over time.

1.1.3 Creep

Creep is a nonlinear effect that reduces the positioning precision of some actuators when operating over a range of frequencies [29]. The step response of an actuator affected by creep will continue to settle over time, often taking several minutes [14]. Naturally, creep adds a time dependency to actuator models and can complicate open-loop control. A visualization of creep is provided in Figure 1.3.

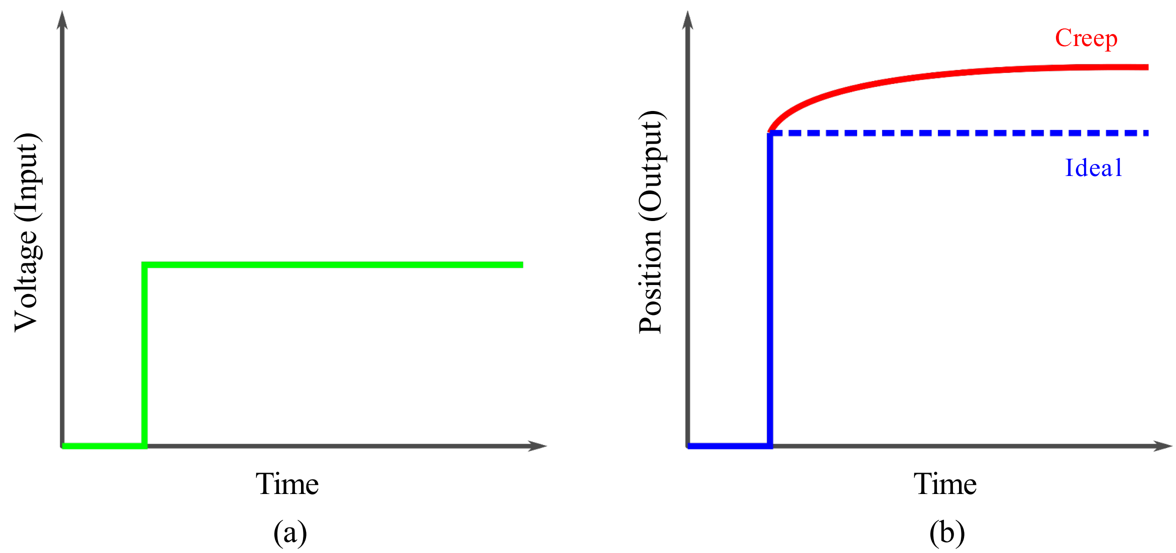

Figure 1.3 A representation of the step response of an actuator affected by creep.

1.1.4 Hysteresis

Hysteresis is a nonlinear effect that can be problematic for both actuators and sensors. Hysteresis can be described as a memory effect that causes the output of a hysteretic device to depend on prior outputs [30]. This is not ideal from an efficiency perspective since a cyclical energy storage process, such as storing potential energy in a mechanical spring, will require a greater quantity of input work than will be subsequently returned [31]. Hysteresis also significantly complicates modeling and control of hysteretic devices as they can produce multiple outputs for a given input as shown in Figure 1.4 [30]. Mechanical hysteresis is caused by friction produced between particles within a material [32]. Magnetic hysteresis is a type of core loss and is caused by the realignment of magnetic dipoles [32]. In each case, hysteresis is heavily dependent upon the properties of the material. When selecting magnetic materials, one often has to compromise between hysteresis and other nonlinear effects such as eddy currents or saturation [33], [34].

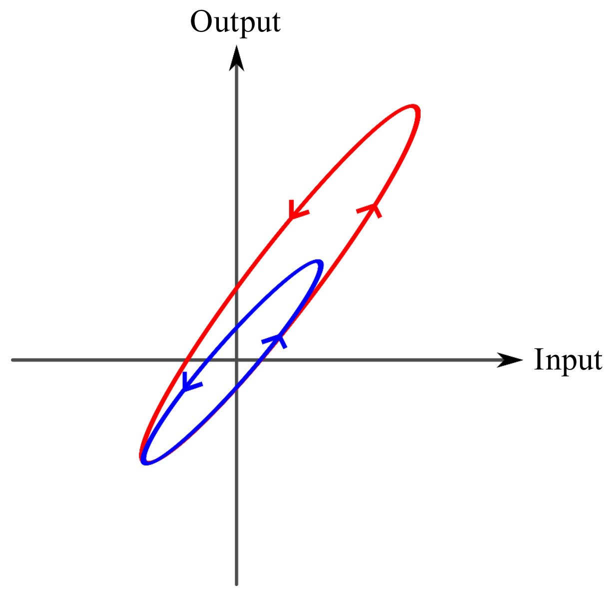

Figure 1.4 A representation of hysteresis loops where the red and blue loops show different cyclical paths.

1.1.5 Magnetic Saturation

Most ferromagnetic materials produce a flux density, B, that varies approximately linearly with magnetic field strength, H. However, if the flux density is pushed beyond a limit defined by material properties, a phenomenon known as magnetic saturation occurs [35]. The onset of saturation produces diminishing returns in regards to the incremental increase in flux density relative to the increase in field strength. The saturation and hysteresis properties of a material are typically displayed in B-H curve plots as seen in Figure 1.5. Actuators that saturate will incur decreased efficiency due to the disproportionately large magnetomotive force (MMF) that needs to be generated [36], [37], [38]. Furthermore, magnetic saturation is a nonlinear effect that leads to unpredictable force output, making saturated actuators difficult to control [18], [39]. Fortunately, saturation can be avoided by choosing an appropriate core size for the magnetic circuit, or by opting for materials that saturate at a higher flux density.

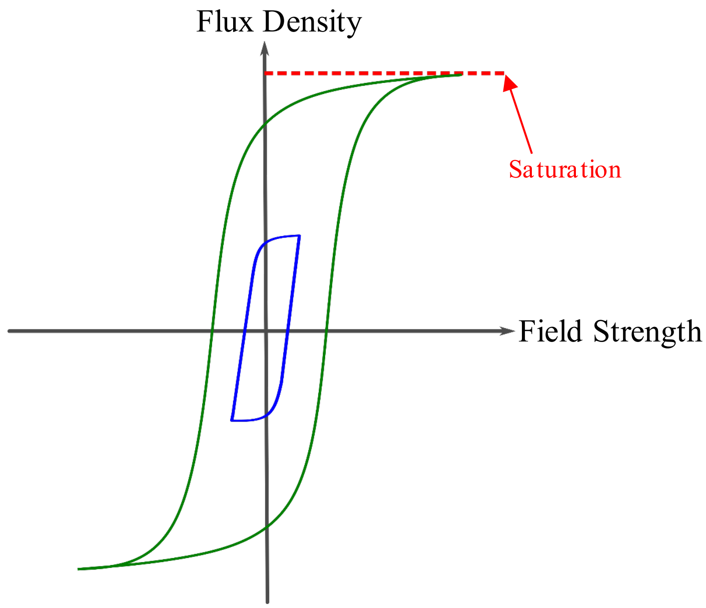

Figure 1.5 Shows an example of saturating (green) and non-saturating (blue) B-H curves.

1.1.6 Eddy Current

Eddy currents are a type of core loss generated when a magnetic field changes within a conductor in accordance with Faraday's Law of Induction [40]. Lenz's Law explains that eddy currents form in the direction that will attempt to counteract the external field as shown in Figure 1.6 [40]. Eddy currents are frequency dependent which make them challenging to model, particularly for magnetic circuits that operate over a wide range of frequencies [41]. Eddy currents are generally considered a nuisance when they appear in the flux pathways of a magnetic circuit as they lead to increased losses and a slower force response [42], [43]. In some situations, eddy current losses generate substantial heating that greatly increases the risk of demagnetization within permanent magnet machines [42]. Furthermore, eddy currents are temperature dependent since the resistance of the eddy current pathways will change with the temperature. This temperature dependency exacerbates the difficulty of producing accurate eddy current models [44].

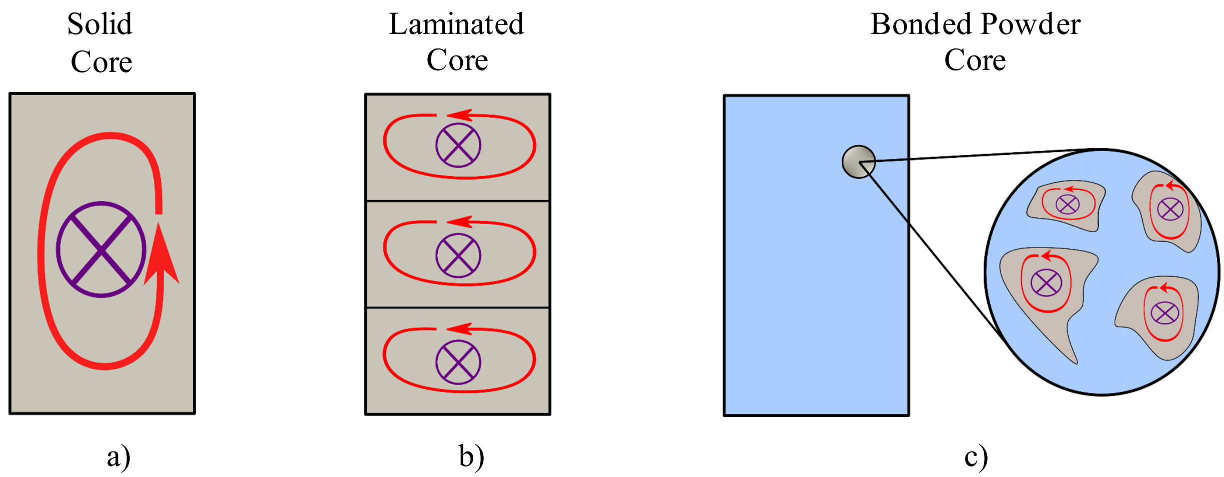

Figure 1.6 Shows the eddy current formation in a solid core (a), a laminated core (b) and the ferromagnetic granules within a bonded powder core (c). The red arrows indicate the direction of the eddy currents created by a transient external field pointing into the page (purple markers).

It is important to note that there are sparse examples in literature that purposefully induce eddy currents in a shorted turn to create a faster force response. Certain voice coil designs can make use of shorted turns to generate eddy currents to lower terminal inductance [45], [46]. The lower terminal inductance allows a faster current transient which creates a faster force response [45]. However, this is only beneficial in limited circumstances where the magnetic fields produced by the actuator and its eddy currents do not oppose the output force. It is important to note that modeling eddy currents within a shorted turn is still regarded in literature as a challenging task, despite the eddy current pathway being well-defined [46].

Due to the complexity of accurately modeling eddy currents and the performance challenges they pose, proactive measures to avoid eddy currents are often taken when designing the magnetic core of an actuator or sensor. One way to suppress eddy currents is to make a core out of electrically insulated laminations. The insulation on the laminations prevents eddy currents from flowing across adjacent laminations [34]. The smaller current pathways make it difficult for eddy current loops to form as shown in Figure 1.6b. AC eddy current power losses can be defined by the equation below where C_e is a material-dependent constant, V is the volume of the material, t_{lam} is the lamination thickness and B_a is the flux density amplitude [34].

$$P_e = C_e V f^2 t_{lam}^2 B_a^2 \tag{1.1}$$

From (1.1) it is evident that the laminations should be as thin as possible. At higher frequencies, eddy currents become large even if thin laminations are used as seen in (1.1). However, (1.1) becomes inaccurate at very high frequencies as eddy currents begin suppressing themselves due to skin effect within the laminations [47]. In [48] it was shown that the core losses of various types of laminations became quasi-constant after an excitation frequency of around 4-5kHz. Furthermore, [49] found that the skin effect caused by eddy currents leads to substantial changes to the permeability of the laminations. This also leads to nonuniform flux patterns within the ferromagnetic pathways [50]. Naturally, this additional frequency dependence caused by skin effect would further complicate efforts to accurately model the eddy currents and magnetic characteristics of an actuator or sensor.

For high-frequency circuits, bonded powder cores typically become a preferable alternative to laminations. Bonded powder cores are a composite structure made of ferromagnetic particles and a bonding agent as seen in Figure 1.6c; the bonding agent is not electrically conductive [51]. The fine particles resist the formation of eddy currents similar to laminations, but are much more effective due to their small size. It is important to note that the bonded powder cores have gaps between particles. These gaps increase the reluctance of the magnetic circuit and lower the saturation flux density since there is less ferromagnetic material for a given core volume compared to a laminated or solid core [51]. However, there are a large amount of material and process options that allow the saturation flux density to be compromised with other properties, such as core loss [51], [52].

1.1.7 Magnetic Fringing and Flux Leakage

Magnetic fringing is a phenomenon that causes magnetic flux to spread out within a given medium. In electromagnetic sensors and actuators, fringing predominantly occurs in the vicinity of an air gap. Fringing will cause magnetic flux lines to bulge around an air gap as shown in Figure 1.7. Fringing can be modeled as an increase in air gap length and/or an increase in air gap cross-sectional area [53], [54]. For magnetic circuits with a fixed air gap length, such as gapped inductors, a fringing flux factor is often defined and subsequently found using iterative calculations or manual tuning until the desired inductance value is achieved [54]. However, fringing effects become position-dependent in actuators or sensors where the air gap length changes.

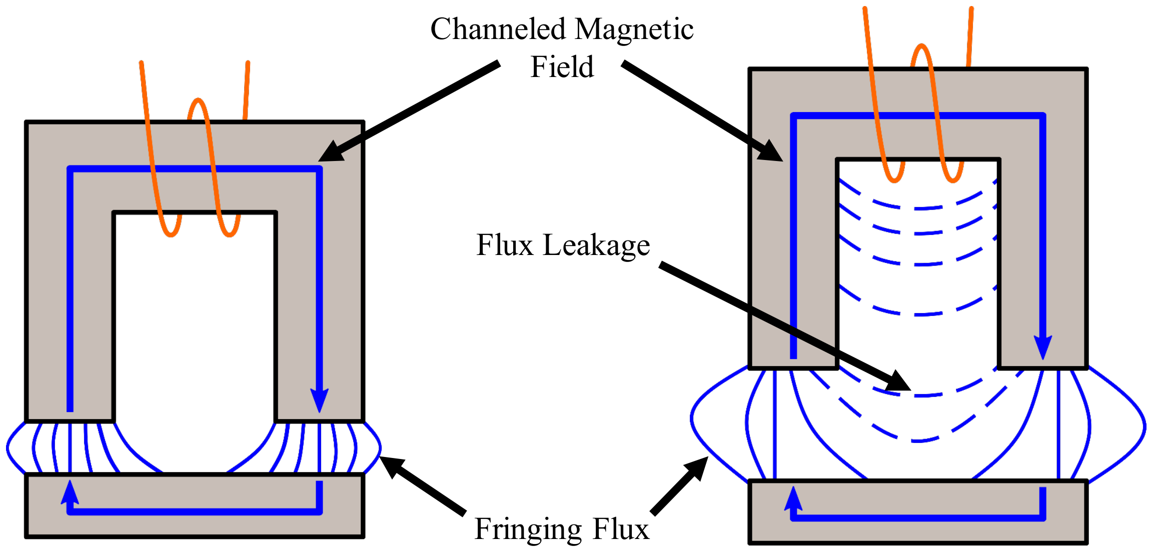

Figure 1.7 Shows how magnetic flux fringes within air gaps. If the air gap is large, a significant amount of flux leakage will result.

If the air gap of a magnetic circuit is large, significant flux leakage can result. Flux leakage causes magnetic flux to bypass large portions of the magnetic circuit as seen in Figure 1.7. Flux leakage becomes significant when the reluctance of the intended magnetic circuit begins to approach the reluctance of leakage pathways [55]. These leakage pathways change the behaviour of the magnetic circuit and lead to increased losses [56]. Literature notes that modeling flux leakage is complex and often requires three-dimensional analysis [56]. Excessive flux leakage is preventable using carefully-designed magnetic circuit geometries that ensure the reluctance of magnetic pathways are small relative to potential leakage pathways.

1.2 Common Translational Actuator Technologies

There are many types of translational actuators with unique performance attributes. The performance attributes of the various types of actuators make them ideal for certain applications and infeasible for others. It is important to understand the performance characteristics of conventional actuator technologies in order to evaluate the improvements offered by the CAS actuator presented in this thesis. The subsections below review common actuator types used to obtain translational motion.

1.2.1 Piezoelectric Stack Actuators

Piezoelectric stack actuators are a common type of electrostatic actuator that are used to generate linear motion. Piezoelectric actuators are energy-efficient actuators that have a very large force density [57]. Piezoelectric stack actuators consist of piezoelectric wafers that are stacked in series and are separated by metallic electrodes that are electrically connected in parallel as shown in Figure 1.8 [58]. These wafers expand or contract depending on the applied voltage polarity. It is important to note that the piezoelectric wafers can only displace a small amount which is why they are stacked in series to achieve greater displacements. Most commercial piezoelectric actuators are designed to operate within the range of 10pm to 100μm [58]. Piezoelectric actuators are typically used in micro-scale applications such as microgrippers, speakers and fuel injectors [59], [60], [61].

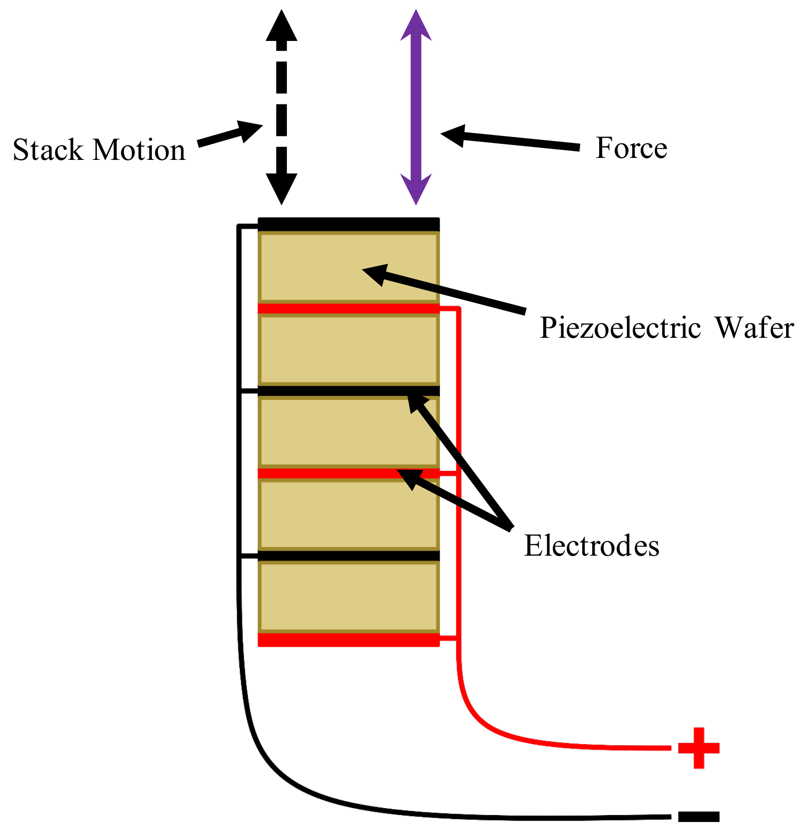

Figure 1.8 A depiction of a piezoelectric stack actuator.

The static mechanical and electrical characteristics of piezoelectric actuators are often approximated to have linear relationships [59]. In reality, piezoelectric actuators are observed to be highly nonlinear [59]. In particular, they are noted to suffer from sizeable hysteresis, creep and drift [29], [58], [62]. Furthermore, piezoelectric actuators are highly susceptible to parameter drift caused by temperature variation and aging [29].

Piezoelectric actuators have the ability to sense their own displacement, allowing them to perform feedback control without a dedicated position sensor. Piezoelectric actuators are known to have a linear relationship between charge and displacement [63]. If current is measured and integrated, then charge can be found and mapped to displacement. Because, this measurement involves an integral, it is susceptible to drift during long-term measurements [63]. Piezoelectric actuators can also perform another displacement measurement simultaneously with the aforementioned charge-method and is referred to as a capacitance or self-strain measurement [63], [64]. This method uses an AC voltage signal to identify capacitance which changes linearly with position [63]. Unlike the charge-method, this method is well-suited for measuring slow displacements over long durations, but is susceptible to noise at high frequencies [63]. The differing frequency range of these measurements can be combined using a complimentary filter to produce a wide-bandwidth measurement that performs well at measuring slow-speed and high-speed displacements [63], [64]. This fused measurement can then be used as feedback for sensorless position control [63]. However, it is important to note that creep, hysteresis and parameter drift still adversely impact the performance of the measurements [63].

1.2.2 Electromagnetic Actuators

Electromagnetic actuators are motion transducers that produce force through the interactions of magnetic fields with ferromagnetic materials or other external magnetic fields. The performance and self-sensing characteristics vary largely among various electromagnetic actuator types. The following subsections provide a review of electromagnetic actuators that have similar stroke capabilities relative to the CAS.

1.2.2.1 Variable Air Gap Solenoids

Variable air gap solenoids are actuators that generate a force which attempts to shrink the air gap between the stator and plunger. It is seen in Figure 1.9 that a generic variable air gap solenoid design attempts to pull the plunger upwards when the coil is energized. It is important to note that a variable air gap solenoid will attempt to pull on the plunger and minimize the air gap regardless of the direction of the winding current. This is reflected in the equation below since the force generated by the variable air gap solenoid, F_v, is proportional to the square of the current, I, where N is the number of windings, A_g is the cross-sectional area of the air gap and l_g is the length of the air gap [65].

$$F_v = \frac{N^2 I^2 \mu A_g}{2{l_g}^2} \tag{1.2}$$

Equation (1.2) is a linear model and does not include nonlinear effects such as saturation. A solenoid is a unidirectional actuator as it is unable to generate a negative force to return its plunger to a prior position since positive and negative currents produce a positive force. However, a second opposing solenoid or external spring mechanism can be used to reset the plunger position [66].

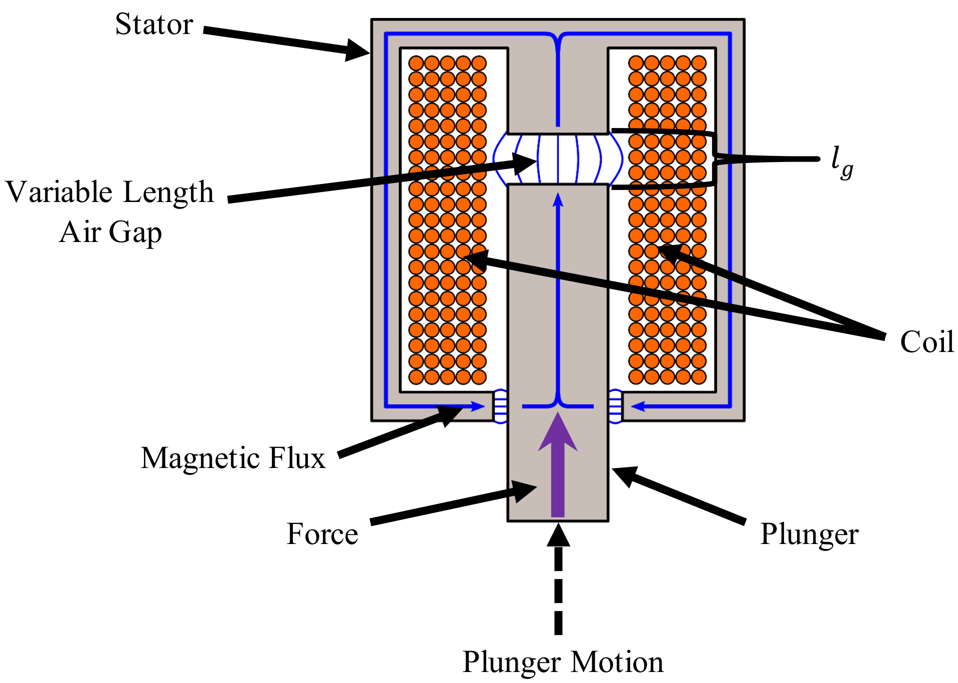

Figure 1.9 A generic geometry for a variable air gap solenoid. The direction the plunger moves is denoted by the dashed arrow.

In literature, variable air gap solenoids are noted to be inherently nonlinear actuators that are challenging to linearize and control [67], [68]. In (1.2) it is seen that the force of the actuator is inversely proportional to the square of the air gap length. This implies the force will drastically change over its stroke as it will be minuscule for a large air gap, but very large for a small air gap. The exponential force characteristic is caused by an exponential inductance characteristic, L as seen in the linear inductance model below which neglects fringing effects [65].

$$L = \frac{N^2 \mu A_g}{l_g} \tag{1.3}$$

From (1.3), it is evident that the inductance becomes very large at small air gaps. When inductance increases, the rate at which current can be adjusted for a given supply voltage, U, is reduced. This is seen in the equation below where $\dot{I}$ is the time derivative of current.

$$U = L\dot{I} \tag{1.4}$$

A sluggish current response will lead to a sluggish force response since $F_v \propto I^2$. If the supply voltage cannot be increased, this will lead to control difficulties. Sluggish performance often results in the plunger slamming into the stator or an end stop despite attempting soft-seating as shown in [66] and [69]. It should also be noted that variable air gap solenoids are highly susceptible to fringing, saturation, eddy currents and hysteresis which degrade or limit their performance [50]. Because of the inherent control challenges faced by variable air gap solenoids, they are generally used in open-loop applications requiring simple on-off control such as fuel injectors and electrical relays [70], [71], [72].

Sensorless position feedback control of a variable air gap solenoid is challenging to robustly implement. In literature, there are methods that attempt to map incremental inductance changes to plunger position. One method utilizes the voltage ripple produced as a biproduct of pulse width modulation (PWM) to find the incremental inductance change within an electrical model of a solenoid [73]. However, this method required the use of a complex three-dimensional lookup table to map the relationship and nonlinearities between current, inductance and position [73]. This method also makes use of model simplifications, such as neglecting back electromotive force (BEMF) from the electrical model of the solenoid, and is accurate for low-speed displacements

[73]. However, [74] shows notable error at higher velocities when neglecting BEMF. There are examples in literature that do not require PWM or lookup tables, but instead require curve fitting with a least-squares regression [75]. Lastly, there are methods that use a dedicated scan current to detect amplitude changes based on a sum-square-difference sliding window [76], or a phase shift across an external capacitor and the solenoid [77]. In both cases, they require lookup tables to map the nonlinear solenoid behavior to position [76], [77]. While these literature examples show that it is possible to self-sense the position of a variable air gap solenoid, in general, it is challenging to obtain low-noise measurements that can sense high-speed plunger movements. Furthermore, variable air gap solenoids have not been shown to have the ability to produce simultaneous plunger position estimates that can be fused together, unlike piezoelectric actuators.

1.2.2.2 Proportional Face Solenoids

Proportional face solenoids often appear structurally similar to variable air gap solenoids. However, proportional face solenoids have carefully-designed plunger faces that make their force characteristics independent of position [78]. The plunger face is often tapered to achieve constant-force characteristics as seen in Figure 1.10. It is important to note that the force characteristics are extremely sensitive to small changes to the shape of the taper [79]. Often, iterative approaches are required to find a geometry that achieves suitable constant-force characteristics [79], [80]. The difficulty and cost associated with producing a specialized plunger geometry is seen as a major disadvantage compared to variable air gap solenoids [78]. In literature, this has been identified as one of the key motivations that leads to the continued development of sophisticated models that attempt to linearize the performance of variable air gap solenoids [73], [78]. Proportional face solenoids are rarely used in comparison to variable air gap solenoids, but when they are, it is typically for fluid flow control valves [78], [81].

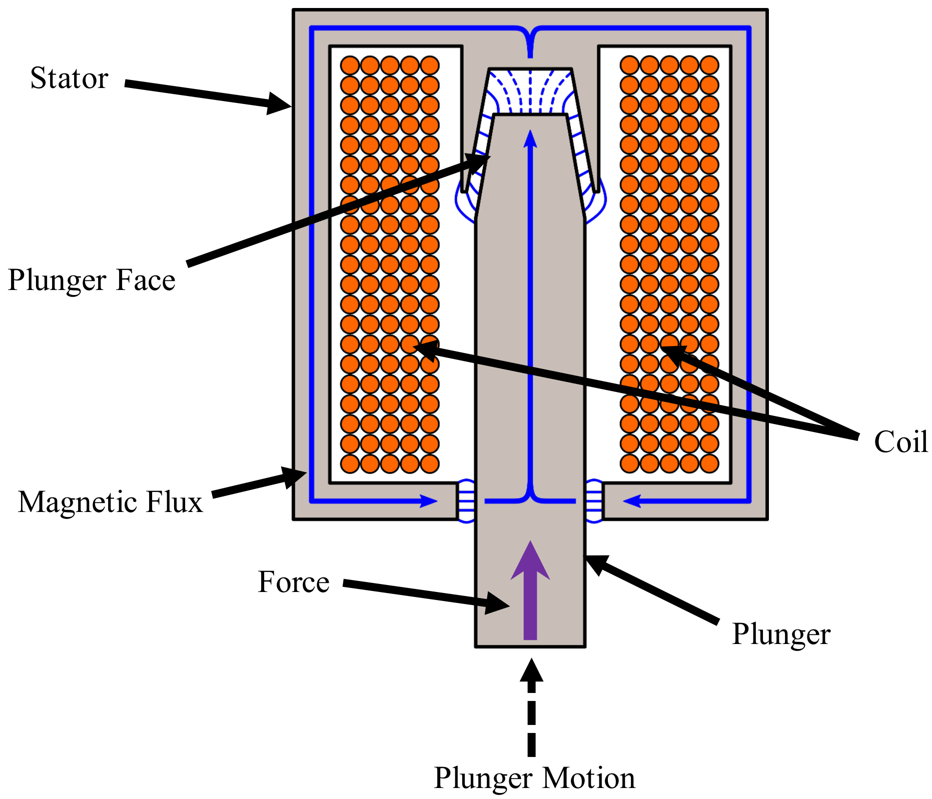

Figure 1.10 A generic proportional face solenoid design. The direction the plunger moves is denoted by the dashed arrow.

Proportional face solenoids require a tapered plunger face that maintains constant-inductance characteristics over its constrained stroke. In [79] it is explained that the region of the plunger where magnetic flux emanates changes throughout the stroke. In particular, when the plunger and stator are substantially overlapped, the flux primarily emanates from the tapered face of the plunger; when the plunger is minimally overlapped, the flux begins to primarily emanate from the bottom of the plunger. The shifting flux location on the plunger varies both the effective air gap length and area in (1.3) to create linear inductance characteristics. This leads to a substantially simpler inductance model compared to a variable air gap solenoid that can be easily characterized with a simple linear regression as opposed to complex lookup tables [82]. Naturally, a proportional face solenoid can perform the same plunger position self-sensing techniques as a variable air gap solenoid, however, much more elegantly [82]. It is important to note that a proportional face solenoid can only operate over a limited stroke range in order to maintain linear inductance and constant-force characteristics. In particular, if the plunger moves too close or too far from the stator, it will begin to behave like a variable air gap solenoid and lose its linear traits [79]. Furthermore, it is important to note that proportional face solenoids, like variable air gap solenoids, are susceptible to nonlinear effects, such as saturation, hysteresis, fringing and eddy currents. Due to these nonlinearities, high-order regressions may still be required to characterize the performance of a proportional face solenoid [83].

1.2.2.3 Linear Switched Reluctance Motors

Reluctance motors are simple, low-cost and rugged actuators that do not require permanent magnets or field windings [84]. Translational versions of reluctance motors are commonly known as linear switched reluctance motors (LSRMs) and are depicted in Figure 1.11 [85]. LSRMs sequentially energize several winding phases to produce bidirectional motion by pulling the nearest translator teeth to align with the stator teeth of the activated phase. LSRMs are noted in literature for being a poor actuator choice for high-speed and high-precision motion control since they are difficult to model and control [86]. Furthermore, the large force ripples they produce while translating multiple teeth create unwanted noise and vibrations [87]. Like variable air gap solenoids, the poor controllability of LSRMs arises from an effective air gap length that changes with position when the stator and translator teeth do not overlap [88]. However, unlike solenoids, LSRMs have regions where the air gap is virtually constant with respect to position when the stator and translator teeth are overlapped [88]. The toggling between a constant and variable air gap when translating creates an inductance profile that looks like trapezoids with rounded peaks and troughs as seen in Figure 1.12 [84], [88], [89]. While the translator and stator teeth are substantially overlapped, LSRMs also exhibit quasi-constant force characteristics [88], [90]. Interestingly, to date there have been no attempts to create an actuator that exploits only the constant air gap region of an LSRM, and this forms the basis of the CAS actuator presented in this thesis. Applications for LSRMs in literature often disregard linear-inductance characteristics and prioritize high-force characteristics [91]. The force produced by LSRMs typically peak near minimum alignment of the stator and translator teeth, and therefore maximizing linear-inductance characteristics and peak force cannot be achieved concurrently [88], [92].

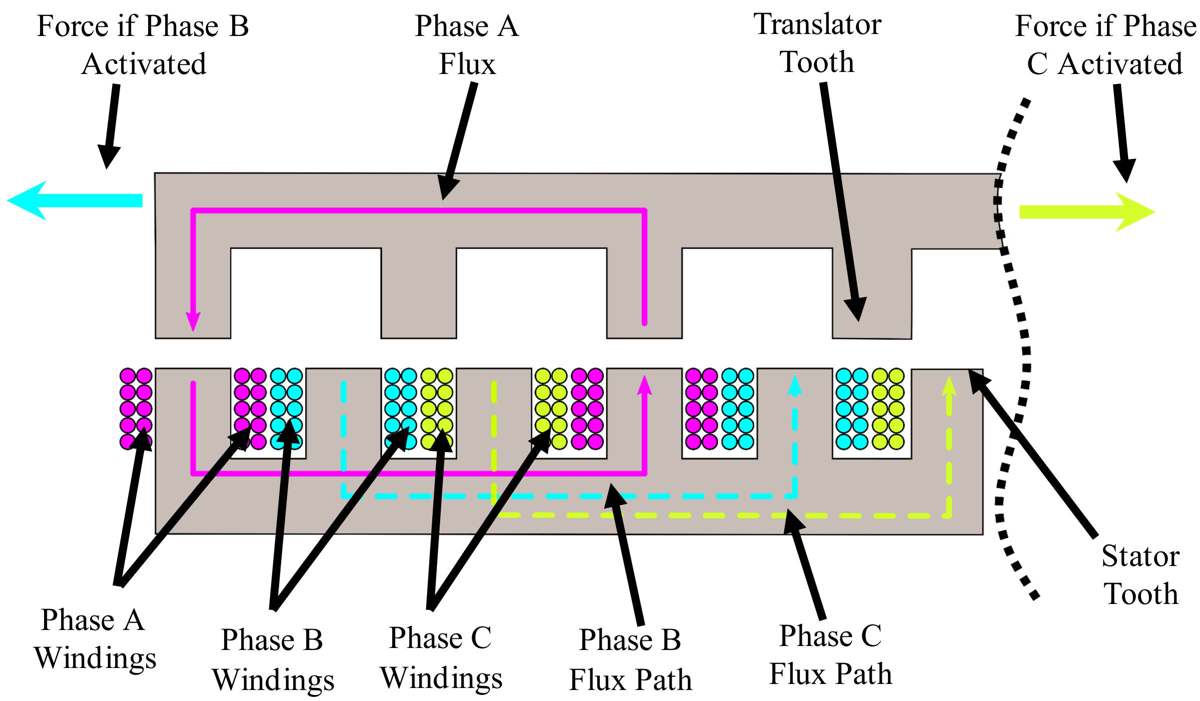

Figure 1.11 A generic LSRM motor design showing the alignment characteristics of the translator and stator teeth when phase A is energized. If phase B or phase C is activated the translator will experience a force that will attempt move the translator to minimize the reluctance of the corresponding phase.

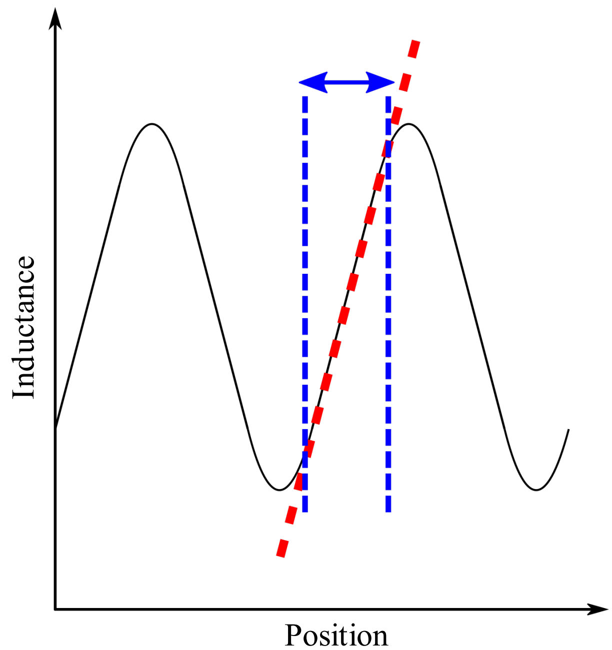

Figure 1.12 Typical inductance characteristics of a single phase of an LSRM. The inductance is highly linear between the two blue lines which occurs when the translator and stator teeth are overlapping.

Several position-self sensing methods for LSRMs can be found in literature, despite the fact that they are considered poor actuators for precision applications. Many of these methods make use of the multi-phase nature of LSRMs as inactive phases can be used to identify translator position. For example, in [93] and [94] the authors excite an unenergized phase and examine the derivative of the current or the integral of current to determine translator position based on inductive changes. This simple method cannot account for high-speed displacements since it neglects BEMF; it also requires curve fitting or lookup tables to account for the nonlinearity of the LSRM [93]. Like solenoids [73], it is also possible to use a superimposed ripple signal to detect an incremental inductance change through phase or amplitude shifts of the measured voltage and current [95]. Another method shown in literature examines the mutual coupling between phases to determine translator position [96]. BEMF-based methods have also been proposed but are difficult to implement since the nonlinear position-inductance characteristics must be modeled [97]. Methods that use flux linkage to determine plunger position have been shown for rotary switched reluctance motors [98]. These methods work well at higher speeds, such as 100-10000RPM, but become problematic at lower speeds [99]. Like variable air gap and proportional face solenoids, LSRMs are susceptible to hysteresis, eddy currents, fringing, and saturation which can degrade sensorless performance [99], [100]. Furthermore, unlike piezoelectric actuators, there are no examples in literature that show LSRMs have the ability to simultaneously produce and fuse two self-sensed position estimates.

1.2.2.4 Voice Coil Actuators (Linear Motors)

Linear motors are electromagnetic actuators that generate a force based on the interaction between two magnetic fields. Permanent magnets or field windings are used to create a DC field. Armature windings are then placed within this field and supplied with current to produce a force governed by Lorentz Force where B_m is the DC field and l_w is the length of the winding [65].

$$F = B_m l_w I N \tag{1.5}$$

Unlike solenoids or reluctance motors, the force of a linear motor is proportional to current rather than the square of the current. Because of this, linear motors can produce a bidirectional force on the armature windings by reversing the direction of the current. Linear motors can also switch the direction of the armature current to allow the armature to step over multiple magnetic poles. Voice coil actuators are a special case of linear motors that do not translate multiple poles. Voice coils have highly linear characteristics which make them excellent candidates for precision actuation applications. For example, as the name suggests, voice coil actuators are used in loudspeakers since their linear characteristics allows them to reproduce sound with low-distortion [101]. It is important to note that the moving component of a voice coil can either be the armature windings or the permanent magnets [102].

A generic voice coil design and the force produced on the armature coil is shown in Figure 1.13. The current-field-force relationship is orthogonal and can be described by the right-hand rule. However, the direction of the force can also be understood by examining the interaction between the magnetic field generated by the permanent magnets and the armature. In Figure 1.13b it is seen that the permanent magnet flux bends in the direction the armature field circulates, creating a concentration of field lines below the armature. The concentrated field lines will create a force that attempts to eject the armature upwards in order to allow permanent magnet field lines to spread out and return to their minimum potential energy state. This principle is synonymous to how the Magnus Effect creates a pressure difference on a spinning table tennis ball which subsequently produces a force [103]. It is important to note that the flux pathway relative to the armature coil negligibly changes as long as it remains withing the confines of the air gap. Because of this, the inductance of the armature coil will remain constant over its stroke. Constant inductance also offers excellent controllability as the transient behaviour of the force and current remain constant over the entire stroke. However, depending on the geometry of a linear motor or voice coil, a nonlinear position-inductance dependency may be introduced by using a design with salient ferromagnetic poles or an overhung armature coil that is longer than the width of the air gap [104], [105].

Therefore, when designing a high-precision voice coil, it is important to carefully select the geometric features.

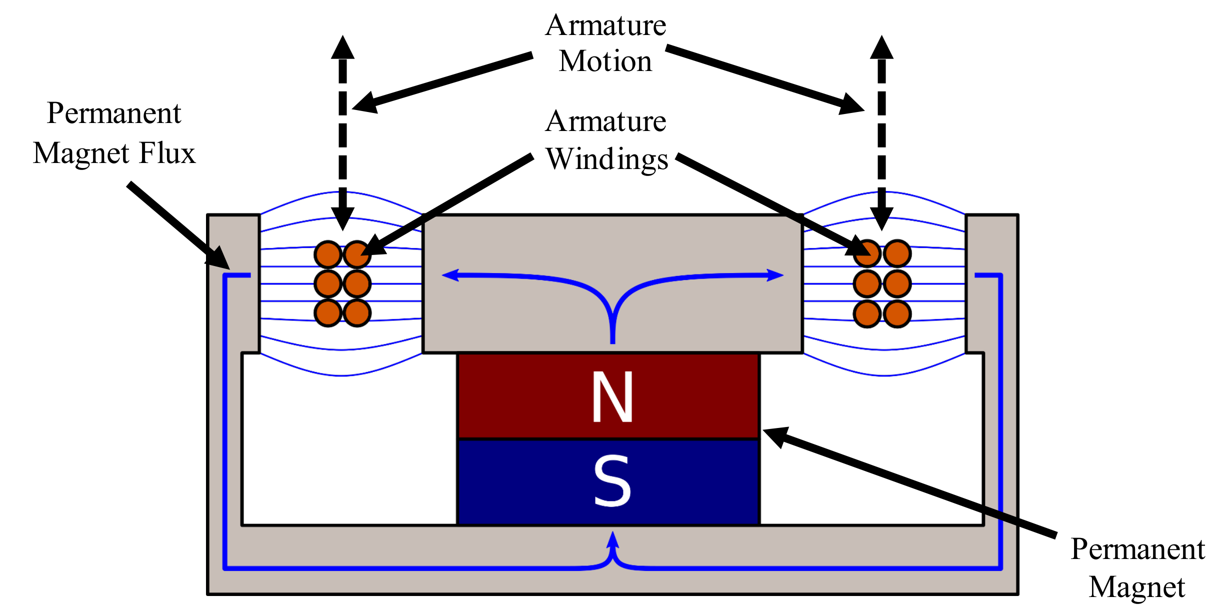

(a)

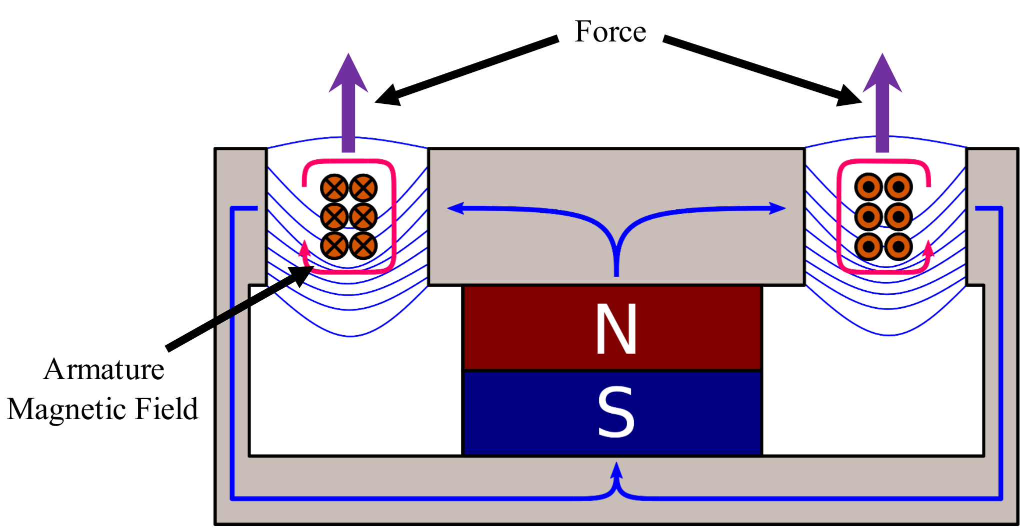

(b)

Figure 1.13 An underhung voice coil design showing the magnetic field behaviour when the armature is unenergized (a) and energized (b).

The design of a voice coil has a large impact on the nonlinearities it is susceptible to. For designs that channel flux through a ferromagnetic path, voice coils can be adversely affected by saturation, hysteresis and eddy currents. However, ironless designs are also possible that negate these issues [106]. In many voice coil designs, permanent magnets are used instead of field windings to increase the efficiency and reduce the size of the actuator [107]. However, permanent magnets introduce additional challenges, such as the risk of demagnetization, which are exacerbated with elevated temperatures as discussed in Subsection 1.1.1. This is a major challenge for high-power voice coil designs since voice coil actuators are inherently inefficient, often converting over 90% of their input energy into heat [108]. Typically, the peak performance of a voice coil is governed by demagnetization and thermal limits as opposed to linear motors, LSRMs and solenoids which are generally governed by magnetic saturation [102].

Since voice coils have a constant inductance, it is not possible to map an inductive change to position unlike solenoids or LSRMs. However, unlike solenoids and LSRMs, the BEMF is only dependent on velocity and does not have an additional dependency on position [109]. If the resistance and inductance can be characterized and assumed constant, the BEMF can be calculated based on terminal voltage and current measurements [109]. If the coil length and magnetic field density are known, then velocity can be solved for where U_{BEMF} is the voltage created due to BEMF.

$$v = \frac{U_{BEMF}}{B_m l N} \tag{1.6}$$

If (1.6) is then integrated, coil position can be found. However, it is important to note this is a relative measurement and not an absolute measurement. It should also be noted that this method becomes more robust at higher velocities as the BEMF becomes more appreciable. However, position estimates produced by this method are prone to drift due to the integration. Since voice coils are highly inefficient, many of the assumed constants, such as the magnetic field density and resistance are likely to change with temperature, creating sizable drift. For these reasons, it is likely that a voice coil that self-senses its position over long durations would be erroneous and ineffective. It is also important to note that BEMF is the only linear self-sensing mechanism voice coils possess, and therefore they are unable to produce multiple position estimates, unlike piezoelectric actuators.

1.3 Inductive Differential Position Sensors

Inductive differential position sensors are robust position sensors that produce measurements with a high degree of linearity and have theoretically-infinite resolution [110]. These types of sensors are used in a wide range of motion control applications, even in harsh environments, such as nuclear reactors [111]. Differential sensors gain many of their robust sensing attributes from their ability to produce an internal subtractive measurement or two measurements that can be externally subtracted to cancel common-mode disturbances. The CAS sensor presented in this thesis can be classified as an inductive differential position sensor and shares many traits with sensors within this category. The subsections below overview two common differential inductive position sensors.

1.3.1 Linear Variable Differential Transformer

Linear variable differential transformers (LVDTs) are one of the most common types of inductive differential position sensors [112]. An LVDT consists of a primary coil and two magnetically coupled secondary coils that encircle a ferromagnetic core as shown in Figure 1.14. It is important to note the secondary coils are wound in opposite directions [113]. When the core of the LVDT moves, the mutual inductive coupling between the primary coil and the upper and lower secondary coils change. In particular, the mutual coupling experienced by the upper secondary coil is inversely proportional to the mutual coupling experienced by the lower secondary coil [114]. When the primary coil is excited with an AC voltage, a voltage will be induced across each secondary coil. Since the secondary coils are wound in opposite directions and series connected, the voltage between the upper and lower terminals will be the subtraction of the individual upper coil voltage, U_A and lower coil voltage U_B. Therefore, when the core is at the middle position, the output voltage, U_{out}, will be zero as seen in Figure 1.15. In order to obtain a linear function that can be mapped to position, the AC signal measured at the terminals of the secondary windings needs to be conditioned through analog or digital post-processing. Conditioning is most commonly performed using a demodulation scheme followed by a lowpass filter, or a rectifier followed by a lowpass filter [115]. Once a conditioned signal is obtained, a linear fit can be applied to the voltage-position mapping as seen in Figure 1.15.

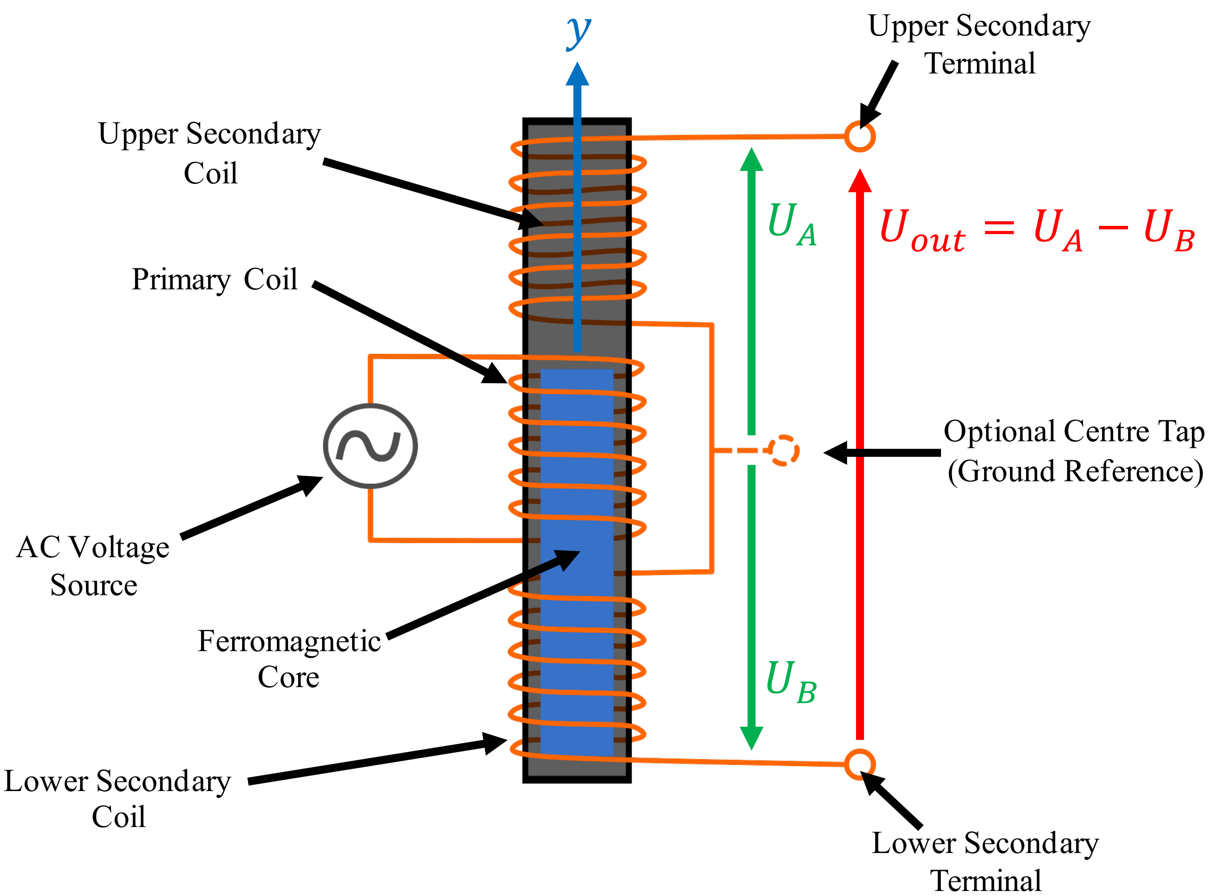

Figure 1.14 A depiction of a linear variable differential transformer. As the blue ferromagnetic core moves, the output voltage will linearly change with position, $\boldsymbol{y}$.

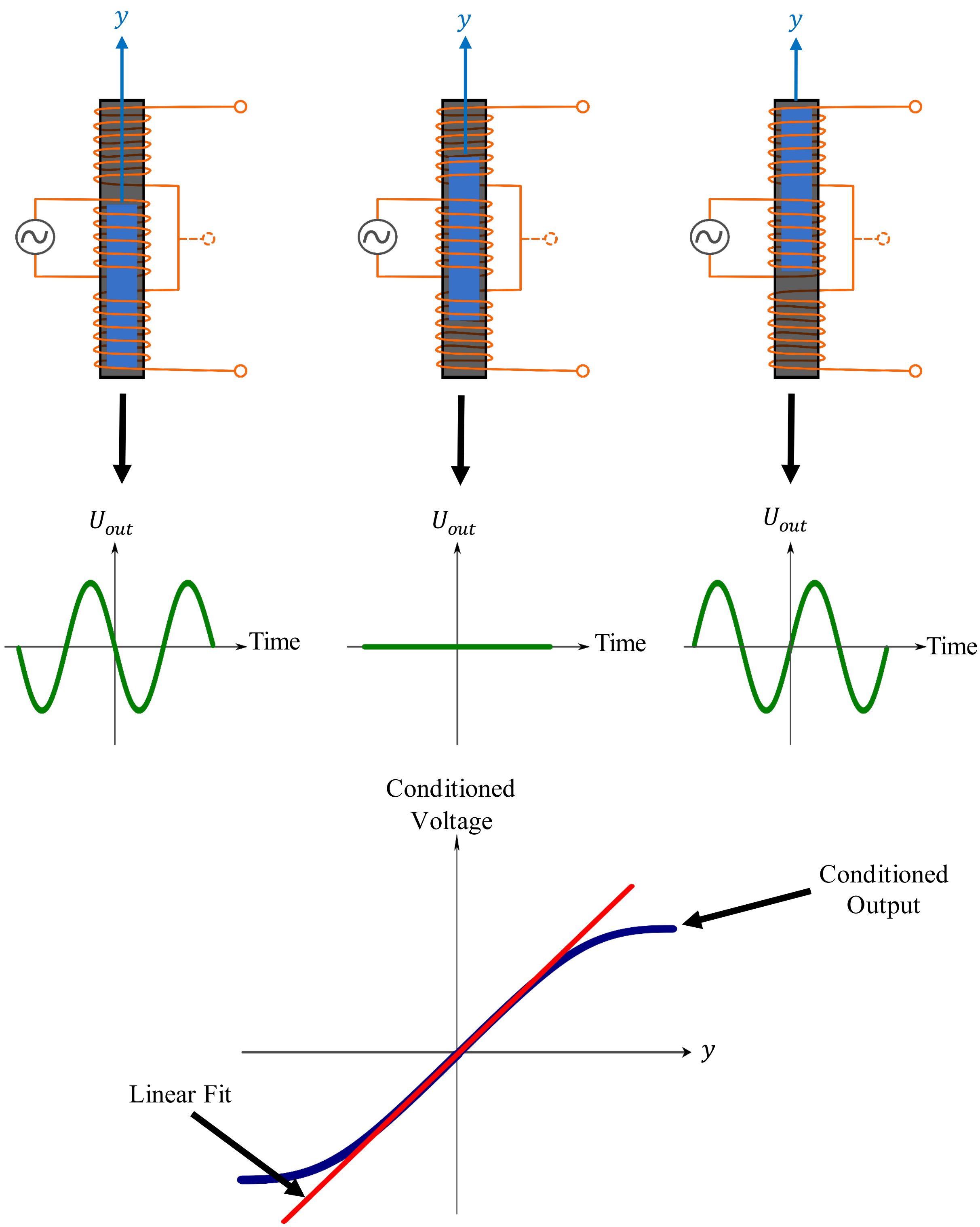

Figure 1.15 Shows the process for how the output voltage produced by and LVDT can be mapped to the position of the ferromagnetic core. It can be noted that near the ends of the stroke, the mapping will become nonlinear.

While LVDTs have many advantageous attributes, they also have numerous challenges and limitations. Inherently, LVDTs are prone to inaccuracies caused by changes to the permeability of the core [111]. However, these permeability changes can be self-compensated if a center tap is added to the LVDT and U_A and U_B voltage measurements (see Figure 1.14) are collected and processed externally [111]. Furthermore, LVDTs are vulnerable to inaccuracies created by external fields and therefore require additional external magnetic shielding to protect the coils from stray magnetic fields [110], [116]. LVDTs are also not well suited for high-speed applications. The theoretical maximum bandwidth of an LVDT is established by the frequency of the AC excitation supplied to the primary coil. The maximum mechanical frequency the core can move must be less than the AC excitation frequency in order to avoid aliasing during demodulation. However, the presence of lowpass filters in the LVDT voltage-conditioning schemes introduce additional poles to the system. As long as the mechanical frequencies are well-within the passband of the lowpass filter, accurate results can be obtained [117]. In [115], the AC excitation is suggested to be an order of magnitude larger than the maximum mechanical core frequency. However, [117] shows that AD598 and AD698 commercial LVDT conditioners attenuated the output voltage by 50% when an LVDT was driven with a primary excitation of 2500Hz while the core was moving at 250Hz. Furthermore, notable attenuation is already visible at 10Hz which is 250 times less than the excitation frequency [117]. This suggests the frequency separation must be significantly larger than an order of magnitude to remain accurate. Unfortunately, increasing the excitation frequency makes digital sampling more challenging and can lead to eddy currents, particularly if the core material is not resistant to eddy currents [118].

1.3.2 Differential Variable Reluctance Transducer

Differential variable reluctance transducers (DVRTs) are similar to LVDTs in many aspects, but have notable physical and functional differences. The most apparent difference between an LVDT and a DVRT is the absence of a primary coil as seen in Figure 1.16. Furthermore, the DVRT must have a center tap and the upper and lower coils are wound in the same direction. The DVRT is excited through its upper and lower terminals with an AC voltage source with the center tap being used to collect the voltage across each coil [119]. It is also possible to connect a DVRT to be half of a Wheatstone bridge and is why DVRTs are sometimes referred to as half-bridge LVDTs [120], [121].

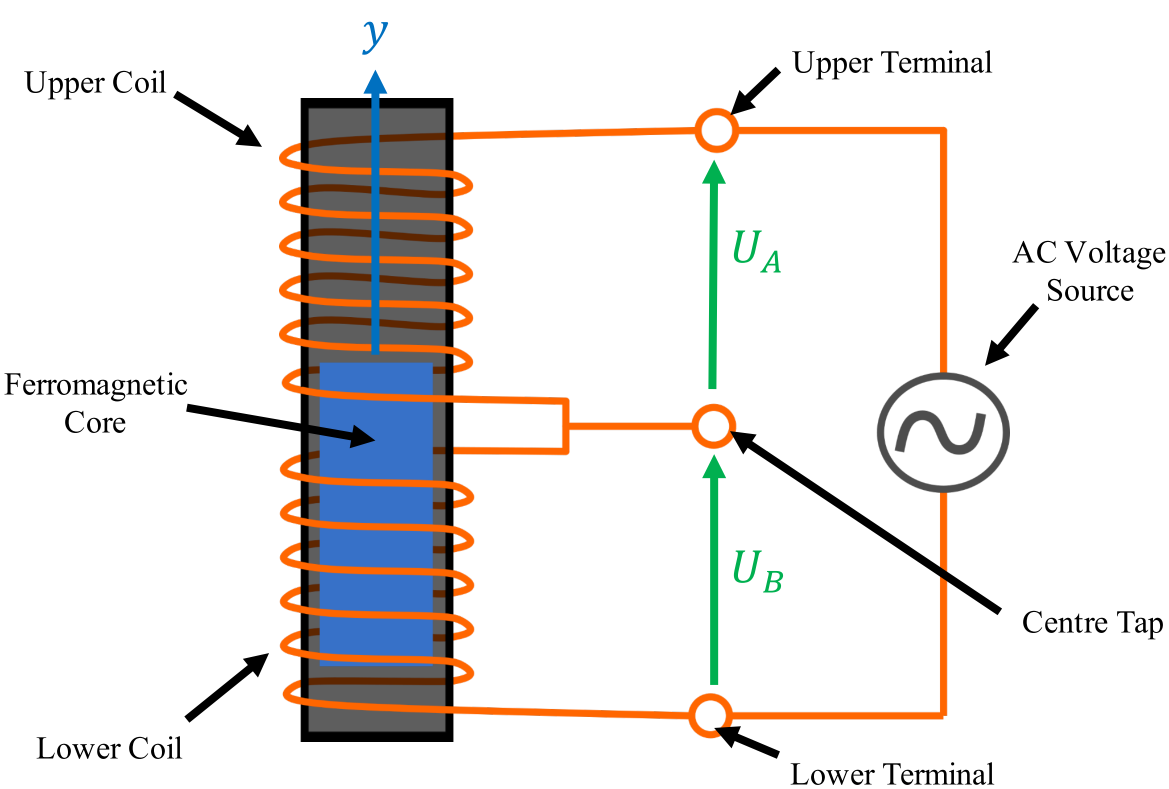

Figure 1.16 A depiction of a differential variable reluctance transducer. As the blue ferromagnetic core moves, the output voltage will linearly change with position, $\boldsymbol{y}$.

As the core of the DVRT moves, the self-inductance of the upper and lower coil change inversely while the mutual inductance remains constant unlike an LVDT [122]. Since the self-inductance of each coil varies proportionally with core position, the voltage that appears across each coil will also be a linear function of position. This allows signal conditioning methods used for LVDTs with a center tap to be applicable for a DVRT [122]. Since the DVRT is center-tapped, differential signal conditioning methods allow it to be inherently immune to temperature effects as was possible with a center-tapped LVDT [111], [119]. Unfortunately, like LVDTs, DVRTs suffer from poor high-speed performance due to the signal conditioning challenges discussed in Section 1.3.1 [122]. Furthermore, DVRTs also require external shielding to protect them from degraded accuracy due to stray magnetic fields or close-proximity metallic objects [121]. The key advantage of the DVRT when compared with an LVDT is its reduced size and improved stroke-to-length ratio due to the absence of the primary coil [121]. However, the reduced size comes at the expense of linearity [122].

1.4 Thesis Scope and Contributions

This thesis introduces a novel CAS actuator and sensor while analyzing and validating their respective capabilities. The unique design of the CAS allows it to exhibit linear-inductance and constant-force characteristics while maintaining a simple and rugged design. The linear-inductance and constant-force characteristics provide the ability to self-sense its plunger position using several methods. Additionally, multiple self-sensed position estimates can be generated simultaneously and subsequently fused to produce a single measurement with higher fidelity and bandwidth. The rare ability to fuse simultaneous self-sensed measurements has never been demonstrated for electromagnetic actuators and has only been demonstrated with limited success in piezoelectric actuators. The CAS is the first electromagnetic actuator demonstrated to have this ability and therefore has the most robust and versatile self-sensing ability among electromagnetic actuators. Furthermore, two CAS actuators can be configured into a novel inductive differential sensor with improved bandwidth and intrinsic redundancy under certain failure conditions. The key contributions are summarized in the list below:

1. The CAS actuator is the first electromagnetic actuator with the proven ability to simultaneously produce two distinct plunger measurements that can be fused to improve performance
2. The CAS sensor is the first differential inductive-based sensor with the proven ability to simultaneously produce two distinct plunger measurements that can be fused to improve performance
3. The novel geometry of the CAS allows it to achieve linear inductance and constant force characteristics similar to a proportional face solenoid without the challenging design/fabrication features of the plunger face
4. The sensorless methods of the CAS actuator/sensor are not encumbered by challenging effects like creep or hysteresis and therefore has more robust sensorless control abilities than piezoelectric actuators
5. The CAS actuator and sensor have significant future potential as they exhibit several of the smart characteristics sought by Industry 4.0 cyber-physical systems
    - Sensorless position control
    - Inherent sensor redundancy and health monitoring capabilities

Chapter 1 introduces the topic of the thesis and provides the required context. Sensor and actuator nonlinearities and challenges are initially discussed. These challenges impose limitations on the application areas and capabilities of common sensor and actuator technologies. Next, common translational actuators are introduced while noting their strengths and weaknesses in regards to their controllability and self-sensing performance. Lastly, inductive differential position sensors are introduced while noting their limitations. The discussed actuators and sensors provide a basis for comparison and allow novel features, improvements and applications for the CAS technology to be identified.

Chapter 2 begins by introducing the premise of the CAS. Next, the electrical, inductive and force characteristics of the CAS are modeled. Important trends and performance attributes are identified from the analytical models. The analytical models are then manipulated to produce high-speed and low-speed position self-sensing methods. Finally, complementary filters are derived to fuse the self-sensed measurements.

Chapter 3 develops and validates a CAS actuator proof-of-concept prototype. The actuator design is first simulated using finite element analysis (FEA) software. A lumped-parameter simulation is developed in Simulink using the analytical models derived in Chapter 2 and the FEA results. A cascaded controller is derived that uses the self-sensed plunger position as feedback. The simulated sensorless control results are then shown and analyzed. Afterwards, a physical prototype is built and details regarding its construction are noted; the surrounding experimental setup is also discussed. Experimental results are then shown and are compared with the simulated results.

Chapter 4 introduces and validates the concept of a CAS differential sensor. The chapter begins by deriving the analytical equations that define the differential measurement. The differential measurement is shown to have immunity to common-mode disturbances. A CAS sensor design is then produced using many of the geometrical features from the CAS actuator design in Chapter 3. The CAS sensor is simulated using FEA software and the output parameters are subsequently used in a lumped-parameter simulation created in Simulink. Simulated results are then provided and analyzed. Next, the construction of a physical CAS sensor prototype and custom driver circuitry are discussed. Finally, experimental results are shown and are used to validate the predicted performance of the Simulink simulations.

Chapter 5 provides a discussion of the results in regards to their practical significance. First the key findings and results from the prior chapters are utilized to provide guidance for designing a CAS for a practical application. Next, possible sources of error and nonlinearity within the self-sensing models are discussed. Finally, the pre-existing actuators and sensors described in Sections 1.2 and 1.3 are contrasted with the CAS actuator and CAS sensor.

Chapter 6 concludes this thesis. First, the key findings and challenges are summarized. In the latter part of the chapter, possible areas of future work are identified.

Chapter 2: Principles of Constant Air Gap Solenoid

This chapter explains the premise and working principles of a CAS. Analytical models are developed to identify performance characteristics and trends of a CAS. From these models, methods are derived to identify plunger position from voltage and current measurements. In the latter part of the chapter, a complementary filter is designed to fuse the self-sensed plunger position estimates.

2.1 Premise of a Constant Air Gap Solenoid

In Section 1.2.2.3, it was noted that LSRMs have highly-linear characteristics when the stator and translator teeth overlap, but are highly nonlinear otherwise. The premise of the CAS is built around the concept of creating an actuator to only operate within the linear region of an LSRM. Therefore, the CAS has a single-phase and only operates over a range where the stator and plunger teeth overlap. The simplest geometry of a CAS is shown in Figure 2.1 where the maximum plunger stroke is determined by the smaller of the stator tooth width, w_s, or the plunger tooth width, w_p. Unlike a proportional face solenoid, the length of the air gap is constant while only the width of the air gap, w_g, varies as follows:

$$0 < w_g < \min(w_s \text{ or } w_p)$$

However, the CAS will have the same objectives as a proportional face solenoid, which include an inductance that varies linearly with position and a constant force over the entire stroke. Essentially, the CAS will behave similarly to a proportional face solenoid over its stroke while having comparable geometric features to a LSRM. This is advantageous since the CAS geometry is simpler than a proportional face solenoid and does not require the challenging task of creating a tapered plunger face that requires a very tight tolerance. Furthermore, the number of CAS teeth can also be easily adapted or stacked into stages to produce greater output force and is discussed in the following section.

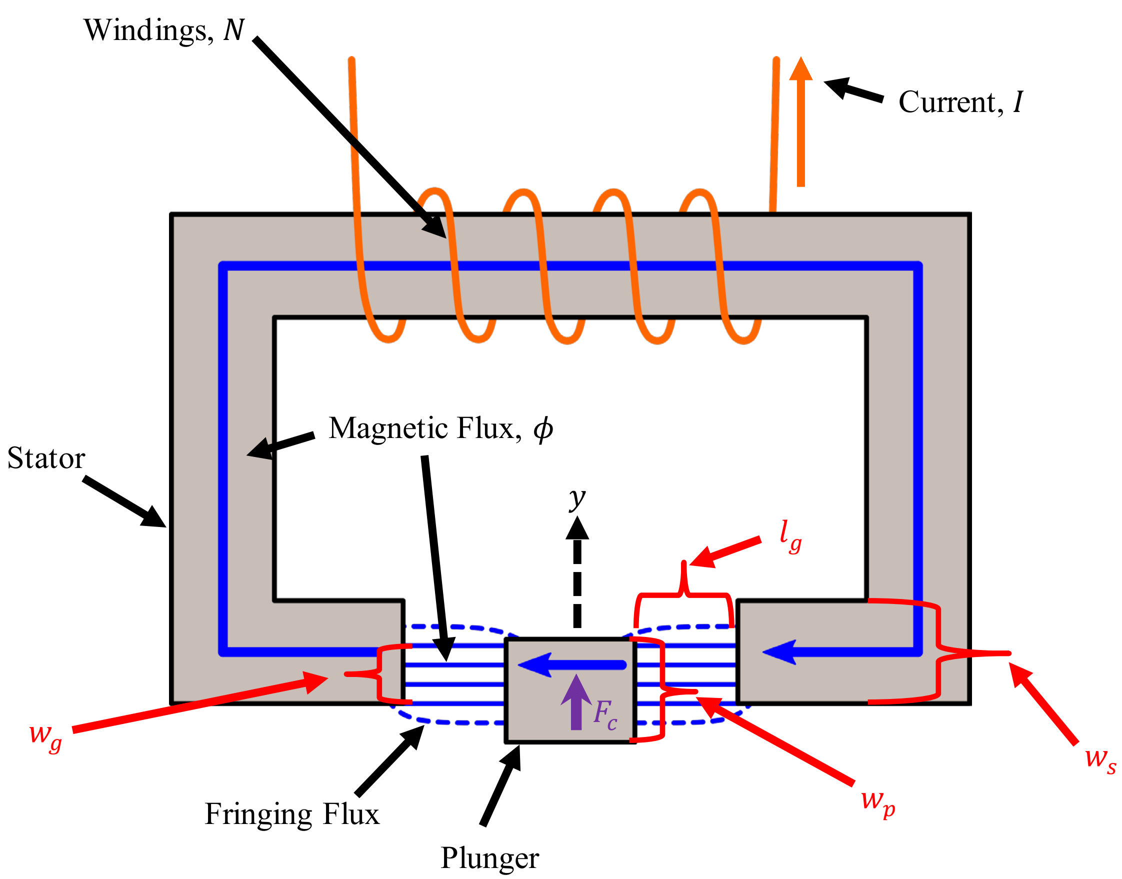

Figure 2.1 A basic CAS geometry. Applying a current to the windings, will produce a plunger for, $\boldsymbol{F_c}$, that will cause the plunger position, $\boldsymbol{y}$, to move vertically. The plunger must be held in unstable equilibrium using guides to prevent horizontal plunger motion. It should be noted that the depth of the actuator, $\boldsymbol{D_g}$, is into the page.

2.2 Constant Air Gap Solenoid Electromagnetic Modeling

A CAS can be modeled using the principles of coenergy and magnetic circuit theory. Magnetic circuit theory allows magnetic circuits to be modeled and analyzed as if they were electrical circuits. As shown in Figure 2.2, voltage is analogous to the MMF (amp-turns), current is analogous to flux, ϕ, and electrical resistance, R, is analogous to reluctance, $\mathcal{R}$.

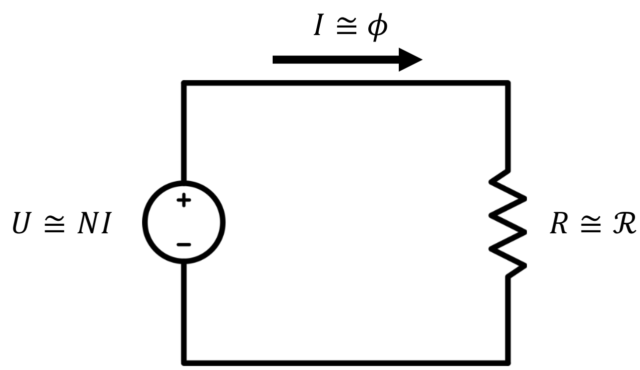

Figure 2.2 Shows the similitude between electrical and magnetic circuits. This allows magnetic circuits to be analyzed with techniques like Ohm's Law.

The reluctance of a magnetic path is dependent on the permeability of the material and geometric parameters, similar to how resistance is affected by resistivity and geometric parameters. This is seen in the equation below where l_ϕ is the length of the flux path and A_ϕ is the area of the flux path [65].

$$\mathcal{R} = \frac{l_\phi}{\mu A_\phi} \tag{2.1}$$

In situations where flux travels through segments of varying size or permeability, multiple reluctances can be defined and modeled in series or parallel. For the basic CAS design in Figure 2.1, the equivalent magnetic circuit can be seen in Figure 2.3a where $\mathcal{R}_s$ is the reluctance of the stator, $\mathcal{R}_g$ is the reluctance of the air gap and $\mathcal{R}_p$ is the reluctance of the plunger. It is important to note that the relative permeability of ferromagnetic steels is often greater than 1000 and are approximately three orders of magnitude larger than air [123]. Because of the large permeability difference, the air gap often dominates the total equivalent reluctance of the circuit. Naturally, this suggest the reluctance contributions of the magnetic material are negligible relative to the air gap. Therefore, we can simplify the circuit in Figure 2.3a into Figure 2.3b by assuming that the flux characteristics of the CAS magnetic circuit are completely dictated by the air gaps.

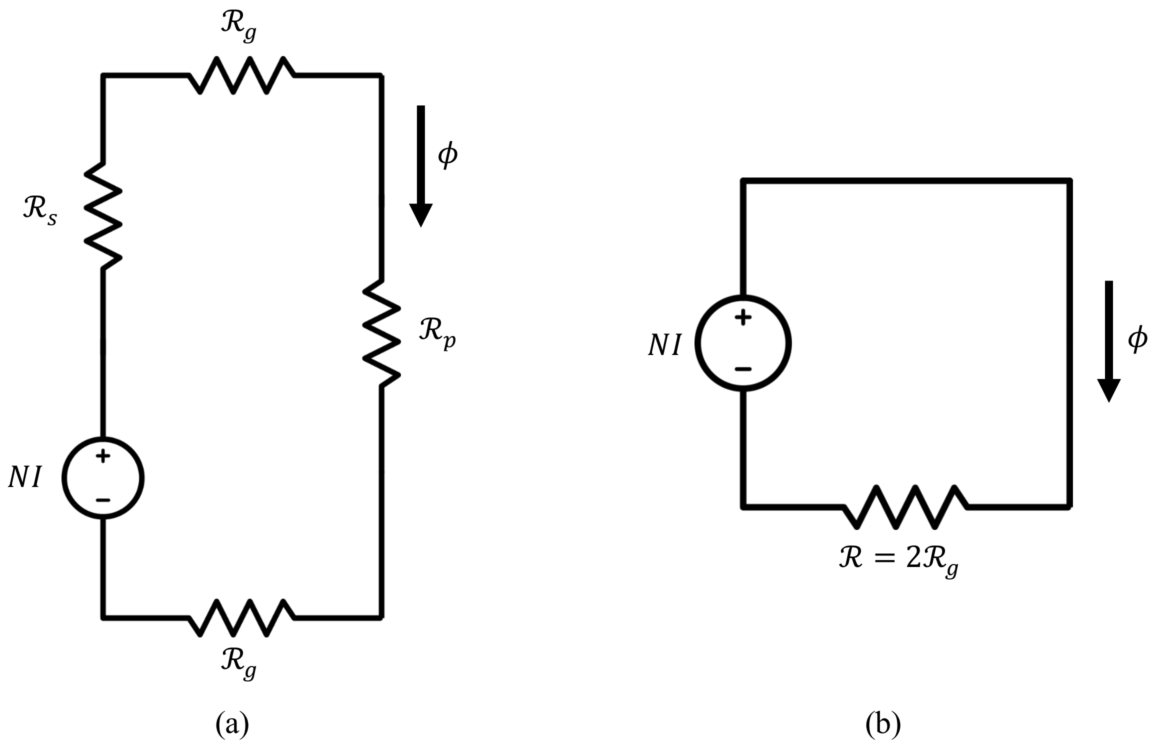

Figure 2.3 Equivalent magnetic circuit (a) and the simplified magnetic circuit (b) for the CAS geometry in Figure 2.1. (b) assumes the air gap reluctance dominates the ferromagnetic plunger and stator pathways.

It is important to note that a CAS can use different stator gap configurations to achieve dissimilar magnetic characteristics. Figure 2.4a shows a parallel stator gap configuration that splits flux between parallel stator and plunger teeth and leads to half the reluctance of the basic CAS in Figure 2.3b. Figure 2.4b shows a series stator gap configuration where the flux must jump consecutive stator gaps and leads to twice the reluctance. Based on these observations, constants can be defined to account for the number of parallel stator gaps, n_p, and number of series stator gaps n_s.

$$\mathcal{R} = \frac{2n_s\mathcal{R}_g}{n_p} \tag{2.2}$$

Equation (2.1) can be adapted define the air gap reluctance of a cuboid-shaped CAS where D_g is the depth of the air gap.

$$A_g = w_g D_g \tag{2.3}$$

$$\mathcal{R}_g = \frac{l_g}{\mu w_g D_g} \tag{2.4}$$

Furthermore, (2.2) and (2.4) can be combined and rewritten in terms of the plunger position, y, which is equivalent to the air gap width as long as the stator and plunger teeth remain overlapped.

$$\mathcal{R} = \frac{2n_s l_g}{n_p \mu y D_g} \tag{2.5}$$

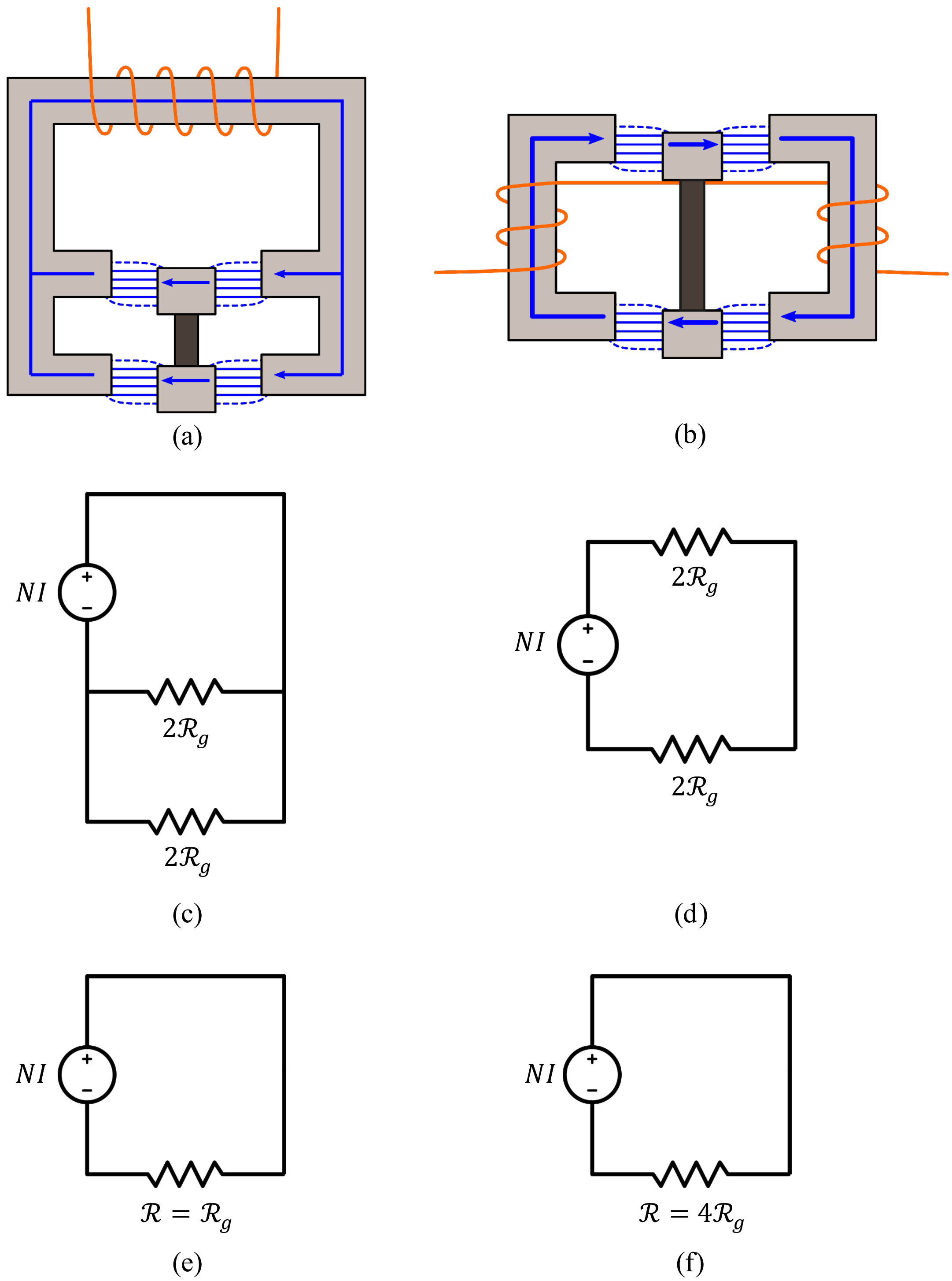

Figure 2.4 (a) and (b) show CASs with a parallel and series stator gap configuration. (c) and (e) show the equivalent magnetic circuit representation of (a). (d) and (f) show the equivalent magnetic circuit representation of (b). From (e) and (f) the constants $\boldsymbol{n_p}$ and $\boldsymbol{n_s}$ can be defined for (2.2).

Applying Ohm's law to any of the magnetic circuits in Figure 2.3 or Figure 2.4 allows the flux to be calculated for a given MMF.

$$\phi = \frac{NI}{\mathcal{R}} \tag{2.6}$$

Flux linkage, λ, is defined by the equations below [65].

$$\lambda = N\phi \tag{2.7}$$

$$\lambda = LI \tag{2.8}$$

Combining (2.5) with (2.8) allows the inductance to be derived.

$$L = \frac{N^2 n_p \mu D_g y}{2 n_s l_g} \tag{2.9}$$

Unfortunately, (2.9) does not accurately model the CAS since it suggests that the CAS would have no inductance at $y = 0$. It can be appreciated that if the plunger ceases to overlap with the stator, fringing and leakage pathways will be established that produce a non-zero inductance. Equation (2.9) can be modified to include an inductance correction that accounts for the initial inductance, L_o.

$$L_c = \frac{N^2 n_p \mu D_g y}{2 n_s l_g} + L_o \tag{2.10}$$

It is important to note that (2.10) can be written in the form of an equation of a line, but is not a linear system due to the offset.

$$\frac{dL}{dy} = \frac{N^2 n_p \mu D_g}{2 n_s l_g} \tag{2.11}$$

$$L_C = \frac{dL}{dy} y + L_o \tag{2.12}$$

Fortunately, a linearization can be performed that has no impact on the accuracy or operational abilities of the CAS. To linearize (2.10), the initial inductance can be modeled as additional virtual (non-physical) overlap, w_o.

$$L_o = \frac{dL}{dy} w_o \tag{2.13}$$

$$L_C = \frac{dL}{dy} y + \frac{dL}{dy} w_o \tag{2.14}$$

$$L_c = \frac{N^2 n_p \mu D_g (y + w_o)}{2 n_s l_g} \tag{2.15}$$

This linearization allows (2.15) to be of the same form as the linear inductance model in (2.9). A depiction of the inductance linearization is provided in Figure 2.5. From the figure, it is seen that the linearization only affects the variable air gap region which the CAS must never be operated within by definition. Therefore, this linearization has no adverse effects. To the contrary, this linearization allows the inductance-position mapping to be a multiplication of a single constant, C_L, which is simply the slope.

$$C_L = \frac{L_c}{y + w_o} = \frac{dL_c}{dy} \tag{2.16}$$

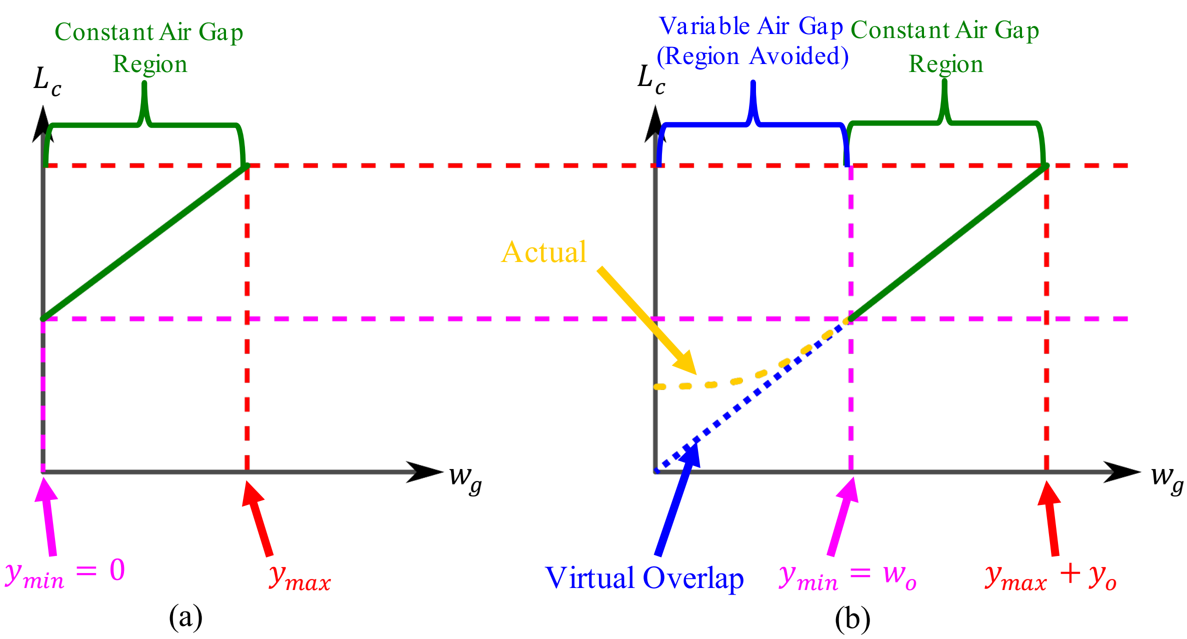

Figure 2.5 Depiction of the CAS corrected inductance (a) and linearized corrected inductance (b).

In order to render the inductance model in (2.15) valid, the following assumptions need to be made:

- A1 – Proper geometric design and material selection make the effects of eddy currents and hysteresis negligible over the operational bandwidth.
- A2 – Fringing and leakage effects remain constant with respect to plunger position as long as the plunger and stator teeth remain substantially overlapped. Any inductance produced by leakage or fringing can therefore be lumped into L_o.

The validity of these assumptions will be investigated in Chapters 3 and 4.

Coenergy analysis can be used to derive the force of a CAS. The field energy within an air gap can be defined using the following equation [65]:

$$E_f = \int_0^I \lambda dI \tag{2.17}$$

Equation (2.17) can be combined with (2.8) and (2.15) and integrated.

$$E_f = \int_0^I \frac{N^2 n_p \mu (y + w_o) D_g}{2 n_s l_g} I dI \tag{2.18}$$

$$E_f = \frac{N^2 I^2 n_p \mu (y + w_o) D_g}{4 n_s l_g} \tag{2.19}$$

As the plunger moves, the field energy changes due to mechanical work being done. By the definition of work, a force will be produced as the plunger translates. If saturation is neglected, the force of the CAS can be derived by looking at the change in energy with respect to plunger position.

$$F_c = \frac{dE_f}{dy} \tag{2.20}$$

$$F_c = \frac{N^2 I^2 n_p \mu D_g}{4 n_s l_g} \tag{2.21}$$

From (2.21) it is seen that the force produced by the CAS is independent of plunger position and behaves similarly to a proportional face solenoid. Force characteristics of a variable air gap solenoid and a CAS are compared in Figure 2.6. In the denominators of (1.2) and (2.21), it is seen that the length of the air gap is squared for a variable air gap solenoid unlike the CAS. For similar cuboid designs, $F_c = \frac{F_v}{2}$ when $w_g = l_g$. However, typically $l_g < w_g$ for a variable air gap solenoid over its entire stroke, and therefore a variable air gap solenoid will produce a much greater force over its stroke.

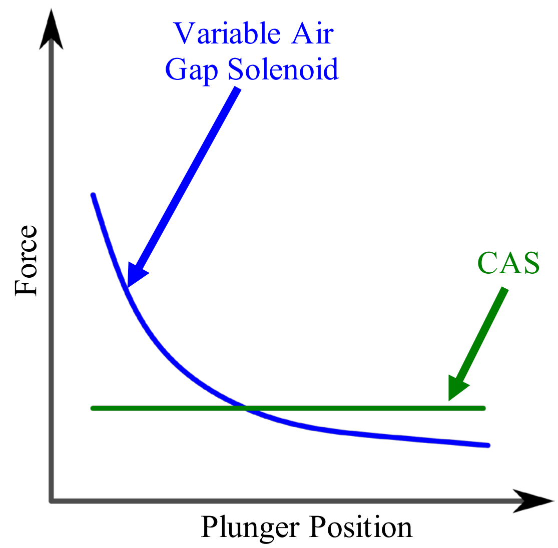

Figure 2.6 Compares the force characteristics of a CAS with a variable air gap solenoid assuming similar designs.

The force constant of a CAS, K_f, can be defined after simplifying (2.21) using (2.15) and (2.16).

$$F_c = \frac{C_L}{2} I^2 \qquad \textbf{(2.22)}$$

$$K_f = \frac{C_L}{2} = \frac{F_c}{I^2} \qquad \textbf{(2.23)}$$

From (2.22), it is evident that a CAS can only generate a positive force, since both negative and positive currents will lead to a positive force.

From (2.21), it is evident that parallel stator gaps will increase the force whereas series stator gaps will reduce the force for a given amp-turn excitation. Exerting a constant force will produce ohmic power losses due to resistive heating. The resistance of a CAS, R_c, and ohmic power loss, P_{cu}, are defined below where l_{ht} is the half-turn length of the windings, A_w is the available stator slot area for windings and C_{ff} is the winding fill-factor.

$$R_c = \frac{N^2 \rho_r (2D_g + 2l_{ht})}{A_w C_{ff}} \tag{2.24}$$

$$P_{cu} = I^2 R_c \tag{2.25}$$

From (2.24) and (2.25) it is seen that $P_c \propto I^2$ and $P_c \propto N^2$. Therefore, if a force is applied to the plunger, a CAS with parallel stator gaps will produce this force with fewer losses. However, despite n_p being in the numerator of (2.21), a CAS with series gaps can produce a larger peak force, F_{sat}. To show this, the saturation flux density of the ferromagnetic core must first be defined where ϕ_{sat} is the flux at saturation:

$$B_{sat} = \frac{\phi_{sat}}{yD_g} \tag{2.26}$$

Next, (2.5), (2.6) and (2.26) can be combined to produce the equation below where I_{sat} is the current required to produce saturation.

$$B_{sat} = \frac{NI_{sat} n_p \mu}{2n_s l_g} \tag{2.27}$$

Finally, the force at saturation can be calculated by combining (2.21) and (2.27).

$$F_{sat} = \frac{B_{sat}^2 n_s l_g D_g}{n_p \mu} \tag{2.28}$$

From (2.28) it is evident that series stator gaps increase the peak force while parallel stator gaps decrease the peak force. It can also be noted that large air gap lengths increase the peak force, however, this will adversely increase fringing and flux leakage. Furthermore, increasing the air gap length will require more amp-turns to maintain a given force as seen in (2.21). Lastly, increasing any parameter within the numerator of (2.28) will lead to an increase in ohmic power loss, while increasing any parameter in the denominator will decrease the ohmic power loss. Clearly, there is a trade-off between efficiency and peak force since it can be concluded that $F_{sat} \propto P_{cu}$.

2.3 Plunger Position Self-Sensing

The linear inductance and constant-force characteristics enable the CAS to have robust plunger position self-sensing abilities. The following subsections derive and discuss three self-sensing methods which have differing performance characteristics.

2.3.1 Inductance-Based Plunger Position Self-Sensing

The inductance of the CAS was analytically shown to vary linearly with position in (2.15). Furthermore, (2.16) demonstrated that inductance and position could be related through a constant, C_L. If C_L is characterized, then plunger position can be identified by using the inductance-position mapping in (2.16). It would be possible to use literature methods, such as the method proposed in [73], to measure inductance. However, an improved method is suggested that requires the same superimposed AC voltage excitation, but does not require the plunger to be moving slowly in order to allow BEMF to be neglected. The required voltage superimposing scheme is shown in Figure 2.7. The proposed inductive-based method is inspired by impedance measurement methods in AC power systems. In AC power systems, the root-mean-square (RMS) of the superimposed AC voltage, U_{ACRMS}, and AC current, I_{ACRMS}, allows the magnitude of the impedance, Z_c, to be calculated by simply using Ohm's Law [124].

$$Z_c = \frac{U_{ACRMS}}{I_{ACRMS}} \tag{2.29}$$

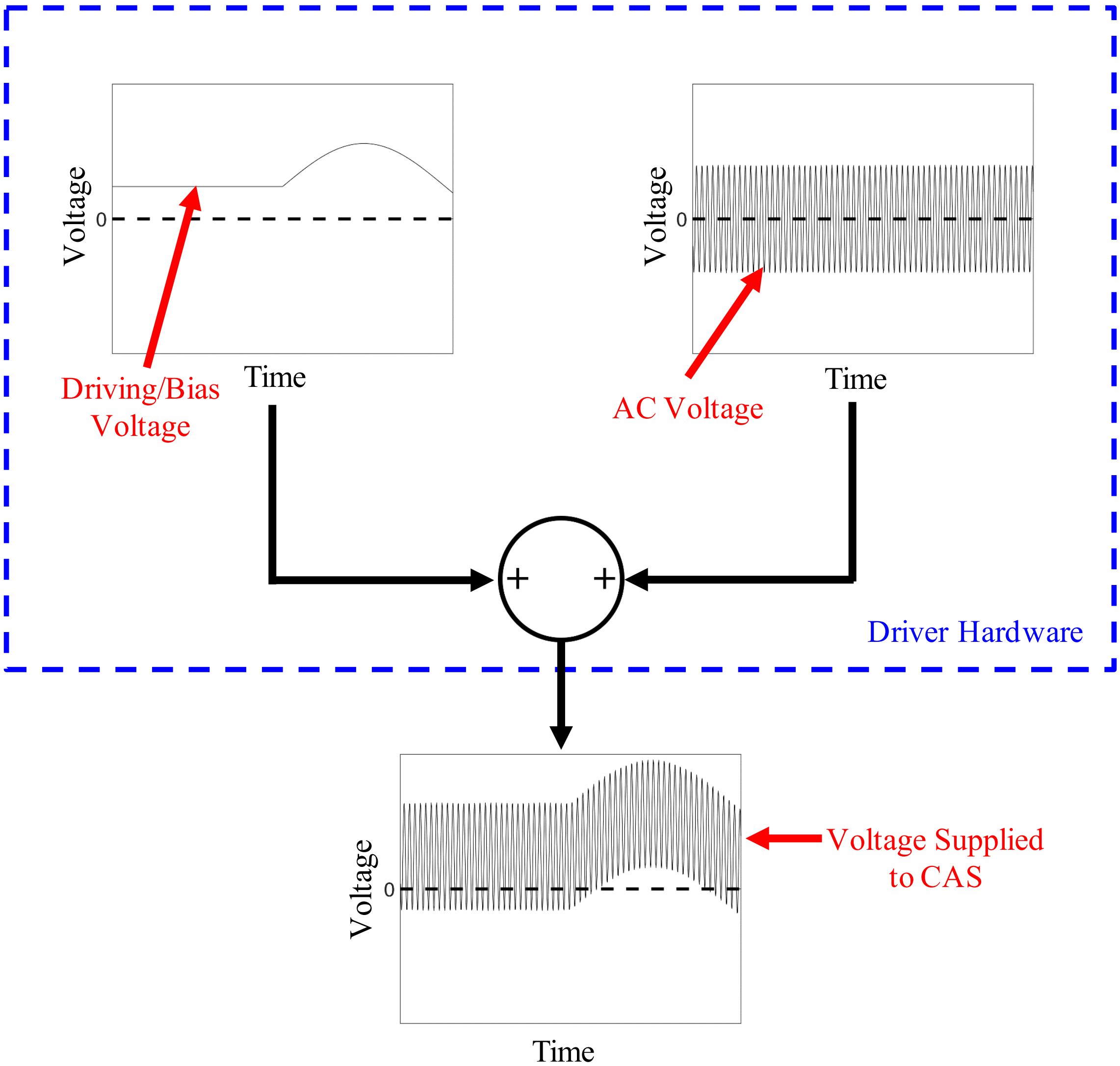

Figure 2.7 Voltage superimposing scheme required for the inductive-based plunger position estimation method. The driver hardware must be capable of producing this superimposing scheme.

The complex nature of the impedance can be observed in Figure 2.8 where X_c is reactance and θ_{UI} is the phase angle difference between the AC voltage and current. It can be noted that impedance is directly related to inductance through the equation below where f_{AC} is the frequency of the AC voltage.

$$L_c = \frac{X_c}{2\pi f_{AC}} \tag{2.30}$$

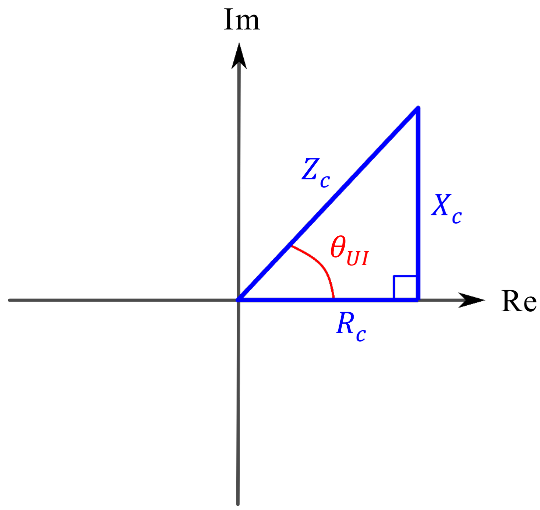

Figure 2.8 Complex nature of impedance and its components.

Given the orthogonal nature of impedance, as long as any two parameters in Figure 2.8 are known, the remaining parameters can be calculated with trigonometry. However, before AC analysis can be performed, the superimposed AC voltage and current needs to be isolated from the voltage and current supplied to the CAS. A sharp bandpass filter centered around the AC frequency can be used to remove BEMF, the driving voltage and high-frequency noise leaving only the AC voltage, U_{AC}, and current, I_{AC}, as shown in the equations below where Q_{BPF} is the quality factor, n_{BPF} is the bandpass filter order and s is the Laplace variable.

$$U_{AC}(s) = \left(\frac{\frac{2\pi f_{AC}}{Q_{BPF}} s}{s^2 + \frac{2\pi f_{AC}}{Q_{BPF}} + (2\pi f_{AC})^2} \right)^{n_{BPF}} U(s) \tag{2.31}$$

$$I_{AC}(s) = \left(\frac{\frac{2\pi f_{AC}}{Q_{BPF}} s}{s^2 + \frac{2\pi f_{AC}}{Q_{BPF}} + (2\pi f_{AC})^2} \right)^{n_{BPF}} I(s) \tag{2.32}$$

The AC voltage and current can then be passed through the sliding window RMS filters shown below to allow the impedance in (2.29) to be calculated.

$$U_{ACRMS}(t) = \sqrt{f_{AC} \int_{t-\frac{1}{f_{AC}}}^{t} \mathcal{L}^{-1}[U_{AC}(s)]^2 \, dt} \tag{2.33}$$

$$I_{ACRMS}(t) = \sqrt{f_{AC} \int_{t-\frac{1}{f_{AC}}}^{t} \mathcal{L}^{-1}[I_{AC}(s)]^2 \, dt} \tag{2.34}$$

Once the impedance is known, either the phase difference between the voltage and current or the resistance of the CAS must be known to find the reactance as seen in Figure 2.8. However, the resistance can be obtained easily, especially if one of three methods listed in Table 2.1 can be applied without adverse effects from the limitations. Often, it is possible to completely neglect the CAS resistance due to the reactance being typically over an order of magnitude larger. In the situation where the resistance cannot be neglected, it can be characterized and assumed constant as long as the operating temperature range is small. It is also possible to account for a variable resistance by performing an online measurement. For example, periodic resistance measurements can be taken during instances where the voltage and current are constant by applying Ohm's Law [125].

Table 2.1 Methods to Establish CAS Resistance

Method	Description	Limitation
1.	Assume $R_c \ll X_c$ and therefore is negligible ($R_C \approx 0 \therefore X_c \approx Z_c$)	f_{AC} and L_C must be large enough to allow $X_c \gg R_C$.
2.	Characterize R_C	R_c needs to remain constant. Winding temperature changes would lead to drift.
3.	Online resistance/temperature measurement	High-power CAS designs may self-heat faster than an online measurement can account for.

The reactance of the CAS can be calculated by applying the Pythagorean Theorem to Figure 2.8.

$$X_c = \sqrt{Z_c^2 - R_c^2} \tag{2.35}$$

Finally, the inductance-based plunger position estimate, y_L, can be established by combining (2.16), (2.29), (2.30) and (2.35) to produce the equation below.

$$y_L = \frac{\sqrt{\left(\frac{U_{ACRMS}}{I_{ACRMS}}\right)^2 - R_c^2}}{2\pi f_{AC} C_L} - w_o \tag{2.36}$$

Equation (2.36) can be analyzed to determine its performance characteristics. If Method 1 or Method 3 from Table 2.1 are applicable, then (2.36) has a large immunity to resistive changes and temperature. The AC RMS voltage and current are naturally susceptible to instrumentation and ambient noise and therefore increasing the AC excitation improves the signal-to-noise ratio (SNR) and will reduce the noise of the position estimate at the expense of increased ohmic loss. It is also important to note that the filtering performed in (2.31)-(2.34) creates an appreciable delay that results in the position estimate lagging the actual plunger position. However, the lag is only appreciable when the plunger is moving quickly relative to the AC frequency. Therefore, the upper bandwidth of the inductance-based measurement, $f_{y_L max}$, is theoretically limited by the AC frequency as aliasing would result at higher frequencies.

$$f_{y_L max} = \frac{f_{AC}}{2} \tag{2.37}$$

Increasing the AC frequency makes driver and sampling hardware requirements more challenging and also increases the risk and magnitude of nonlinear effects, such as eddy currents. Furthermore, increasing the AC frequency increases reactance which subsequently lowers the AC RMS current and degrades the SNR unless the AC RMS voltage is increased to compensate. Overall, the inductance-based plunger position estimate is suitable for measuring a stationary plunger position or low-speed displacements, but is not well suited for high-speed displacements.

2.3.2 BEMF-Based Plunger Position Self-Sensing

The BEMF-based plunger position estimate can be derived from the general electrical model of an electromagnetic machine which is shown in the equation below where $\dot{\phi}$ is the derivative of flux with respect to time [65].

$$U = R_c I + N\dot{\phi} \quad \textbf{(2.38)}$$

Substituting (2.5) and (2.6) into (2.38) and solving the derivative produces the equation below where $\dot{y}$ is the velocity of the plunger.

$$U = R_c I + \frac{N^2 n_p \mu D_g}{2 n_s l_g} (\dot{I}(y + w_o) - \dot{y} I) \quad \textbf{(2.39)}$$

Next, (2.15) can be substituted into (2.39).

$$U = R_c I + L_c \dot{I} + \dot{y} I \frac{L_c}{y + w_o} \quad \textbf{(2.40)}$$

The linearization in (2.16) can then be applied to (2.40) and rearranged to produce the BEMF-based plunger velocity, $\dot{y}_B$, and position, y_B, estimates where y_p is the position from the prior timestep.

$$\dot{y}_B = \frac{U - R_c I - C_L(y_p - w_o)\dot{I}}{I C_L} \tag{2.41}$$

$$y_B = \int \frac{U - R_c I - C_L(y_p - w_o)\dot{I}}{I C_L} dt \tag{2.42}$$

The performance attributes of the BEMF-based plunger position detection algorithm are revealed by analyzing (2.42). It should be noted that the BEMF-based position estimate is a relative measurement unlike the inductance-based position estimate which produces an absolute measurement. This means that (2.42) can only detect a plunger displacement from an initialized starting position unlike the inductance-based method which determines its position based on plunger-stator overlap. It is also important to note that the current must never cross zero in order for (2.42) to remain stable since a division by zero would occur. The magnitude of the current is also directly related to the SNR of the estimated position which is evident by examining the equation below.

$$U_B = \dot{y} I C_L \tag{2.43}$$

From (2.43) it is seen that the larger the current, the more BEMF will be produced. Naturally, the SNR will improve as the BEMF increases relative to the noise floor. Another challenge with (2.42) is characterizing the resistance. Unlike the inductance-based position estimate, the BEMF-based position estimate cannot make use of Method 1 in Table 2.1 as it is not applicable to a DC situation. Furthermore, using Method 2 in Table 2.1 is error-prone since temperature changes will lead to drift. Due to the integral in (2.42), even a subtle temperature rise could lead to a substantial accumulation of error over a long duration. Therefore, Method 3 in Table 2.1 is recommended, but may not be feasible in high-power situations. However, despite the challenges with implementing the BEMF-based position estimate, it has a distinct advantage over the inductance-based position estimate since it does not require bandpass or RMS filters. The absence of these filters allows the output of (2.42) to be in-phase with the actual plunger movement, even at high-speeds, albeit a single timestep delay. The upper limit on the bandwidth of (2.42) would be determined by the onset of nonlinear effects such as eddy currents. Therefore, the BEMF-based position estimate is well-suited for measuring high-speed displacements, but is prone to drift, making it ineffective at measuring low-speed displacements or over long durations.

2.3.3 Flux Linkage-Based Plunger Position Self-Sensing

The flux linkage-based position detection algorithm is also derived from (2.38). If (2.7) is combined with (2.38), then flux linkage of the CAS can be calculated.

$$U = R_C I + \dot{\lambda} \tag{2.44}$$

$$\lambda = \int (U - R_c I)\, dt \tag{2.45}$$

Next, (2.8) can be substituted into (2.45).

$$L_c I = \int (U - R_c I)\, dt \tag{2.46}$$

Finally, the linearization in (2.16) can be applied to produce the flux linkage plunger position estimate [126].

$$y_\lambda = \frac{\int (U - R_c I)\, dt}{C_L I} - w_o \tag{2.47}$$

It is important to note that the BEMF-based and flux linkage-based position detection methods are algebraically equivalent, but behave differently when physically implemented. For example, (2.47) has the advantage that it does not require knowledge of the prior position unlike (2.42) and therefore avoids a timestep delay in a discrete implementation. Furthermore, (2.47) does not require the discrete derivative of the current to be calculated. However, (2.47) is more challenging to initialize than (2.42) since the integral requires present knowledge of the inductance and current instead of just plunger position. It can also be noted that the division by current in the denominator occurs outside of the integral in (2.47) unlike (2.42). Therefore, the flux linkage-based method would be more susceptible to high-frequency current sensor noise since the noise will not be smoothed by an integral. Other than these differences, (2.42) and (2.47) behave similarly as listed below:

- Both methods require resistance to be accurately obtained to avoid excessive drift
- Both methods are best suited for measuring high-speed displacements as they become inaccurate while measuring low-speed displacements or over long durations due to drift
- Both methods become unstable if the current crosses zero

- The SNR of both methods improves as the voltage and current are increased

2.4 Complementary Filter Design

In Section 2.3, it was discussed that the inductance-based position detection method is well-suited for measuring stationary plunger position or low-speed displacements, but is prone to phase-lag error when measuring high-speed displacements. Conversely, the BEMF-based and flux linkage-based methods are well-suited for measuring high-speed displacements, but are prone to drift and therefore would perform poorly when measuring low-speed displacements. Intuitively, the differing bandwidth ranges of the inductance-based and the BEMF-based or flux linkage-based methods are complementary in nature and are prime candidates for a sensor fusion technique [126].

Complimentary filters and Kalman filters are two common sensor fusion techniques. Complementary filters are much simpler and less computationally intensive than Kalman filters [127], [128]. Furthermore, complementary filters are easier to implement since they do not require the noise of the system to be modeled unlike Kalman filters [129]. The accuracy of the complimentary and Kalman filters are typically very similar with some examples in literature showing the complementary filter to be slightly less accurate [129], while others show the complimentary filter to be slightly more accurate [130]. In [63], it was shown that two self-sensed complementary measurements produced by a piezoelectric actuator could be combined using a complementary filter. The complementary measurements of the CAS are similar in nature which implies that a similar-topology complementary filter could be designed for the CAS. Due to the similar performance and greater simplicity of the complementary filter relative to the Kalman filter, the complementary filter will be used to prove the concept of sensor fusion for the complementary measurements produced by the CAS actuator and sensor.

Figure 2.9 shows how a complementary filter can be realized with a lowpass and a highpass filter whose corner frequencies are identical [127]. The lowpass filter attenuates the low-speed input, γ_L, when its frequency is outside of the passband. However, this attenuation occurs at the same rate the high-speed input, γ_H, appreciates. Therefore, the complementary filter output, γ_O, produces unity gain for all frequencies. Furthermore, the lowpass filter also removes high-frequency noise from the low-speed input, while the highpass filter removes low-frequency noise and drift from the high-speed input. It is also important to note that complementary filters can fuse high and low-order signals together by affixing an appropriate-order integrator to the high-speed input where n_{CF} is the order of the integrator. For example, quadcopters often use a complementary filter to fuse angular position provided by an accelerometer with angular velocity provided by a gyroscope [130].

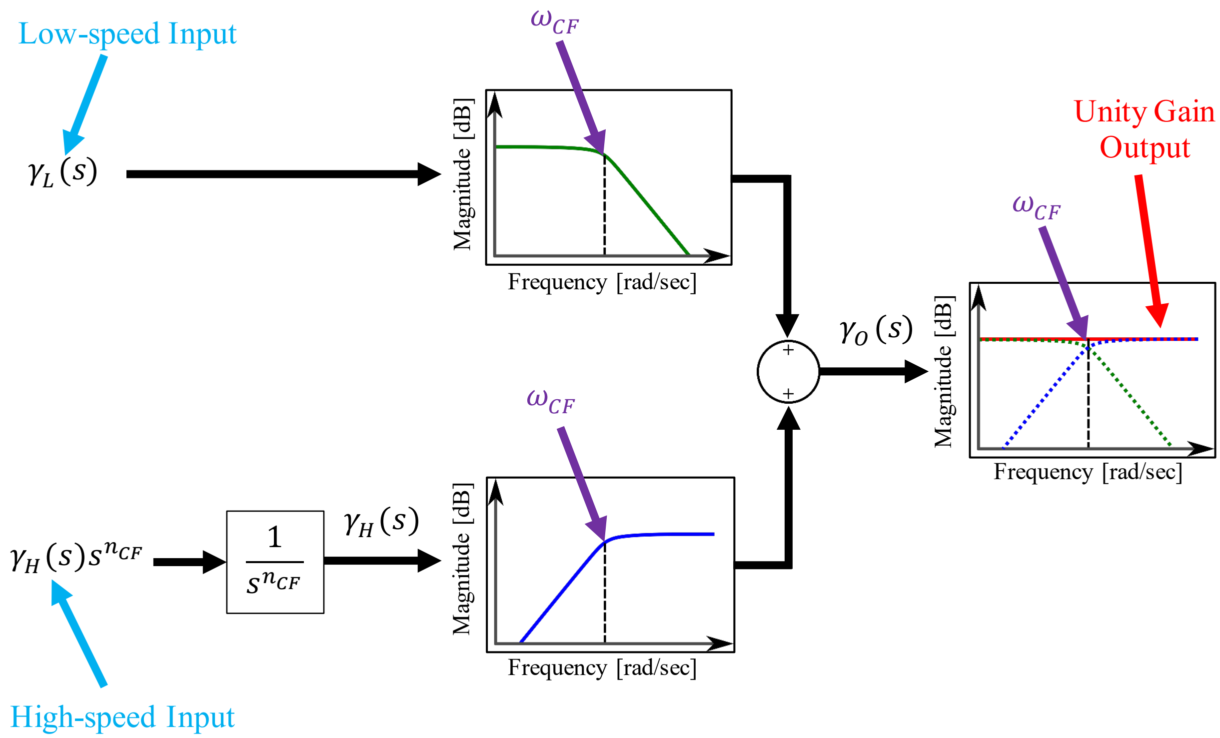

Figure 2.9 A complementary filter schematic.

2.4.1 Complementary Filter for the BEMF-Based Position Detection Method

A second-order complementary filter can be defined for the BEMF-based and inductance-based plunger position estimates. The output of the complementary filter is the summation of the lowpass and highpass filter outputs and is shown below where ω_{CF} is the center frequency of the complementary filter and ζ_{CF} is the damping ratio of the complementary filter.

$$\gamma_O(s) = \frac{\omega_{CF}^2}{s^2 + 2\zeta_{CF}\omega_{CF}s + \omega_{CF}^2}\gamma_L(s) + \frac{s^2}{s^2 + 2\zeta_{CF}\omega_{CF}s + \omega_{CF}^2}\gamma_H(s) \tag{2.48}$$

Since complementary filters require lowpass and highpass filters to have the same corner frequency and sum to unity-gain, we can define a lowpass filter as a unity-output minus a highpass filter.

$$1 - \frac{s^2}{s^2 + 2\zeta_{CF}\omega_{CF}s + \omega_{CF}^2} = \frac{2\zeta_{CF}\omega_{CF}s + \omega_{CF}^2}{s^2 + 2\zeta_{CF}\omega_{CF}s + \omega_{CF}^2} \tag{2.49}$$

$$\gamma_O(s) = \frac{2\zeta_{CF}\omega_{CF}s + \omega_{CF}^2}{s^2 + 2\zeta_{CF}\omega_{CF}s + \omega_{CF}^2}\gamma_L(s) + \frac{s^2}{s^2 + 2\zeta_{CF}\omega_{CF}s + \omega_{CF}^2}\gamma_H(s) \tag{2.50}$$

The position from (2.36) and the velocity from (2.41) can be applied to (2.50) to produce the BEMF-based complementary filter output.

$$y_{CFB}(s) = \frac{2\zeta_{CF}\omega_{CF}s + \omega_{CF}^2}{s^2 + 2\zeta_{CF}\omega_{CF}s + \omega_{CF}^2}y_L(s) + \frac{s^2}{s^2 + 2\zeta_{CF}\omega_{CF}s + \omega_{CF}^2}\frac{\dot{y}_B(s)}{s} \tag{2.51}$$

The complementary filter topology shown in [63] displays how proportional-integral (PI) controller action can be used to describe the behavior of the filter. Equation (2.51) can be algebraically manipulated to obtain the modified complementary filter topology. First, the proportional, K_{pCF}, and integral, K_{iCF} controller gains can be defined and substituted into (2.51).

$$K_{pCF} = 2\zeta_{CF}\omega_{CF} \tag{2.52}$$

$$K_{iCF} = \omega_{CF}^2 \tag{2.53}$$

$$y_{CFB}(s) = \frac{K_{pCF}s + K_{iCF}}{s^2 + K_{pCF}s + K_{iCF}} y_L(s) + \frac{s^2}{s^2 + K_{pCF}s + K_{iCF}} \frac{\dot{y}_B(s)}{s} \tag{2.54}$$

Next, (2.54) can be algebraically manipulated into the form shown below.

$$y_{CFB}(s) = \frac{\frac{1}{s}\left(K_{pCF} + \frac{K_{iCF}}{s}\right)}{1 + \frac{1}{s}\left(K_{pCF} + \frac{K_{iCF}}{s}\right)} y_L(s) + \frac{1}{1 + \frac{1}{s}\left(K_{pCF} + \frac{K_{iCF}}{s}\right)} \frac{\dot{y}_B(s)}{s} \tag{2.55}$$

The PI control loops can be visualized in the block diagram shown in Figure 2.10. It can be appreciated that the PI control action attempts to reduce the steady-state error of the filter output to zero. Therefore, the complementary filter output will converge to the steady-state position estimate provided by the inductance-based method and will not be affected by the drift produced by the BEMF-based position estimate. It should be noted that the output of the complementary filter will be inaccurate at $t = 0$ if the integral within the complementary filter is not initialized. However, the PI control action of the complementary filter will remove any error created by improper initial conditions over time. Therefore, initializing the integral within the complementary filter becomes a trivial task if time can be afforded for the PI controller to suppress the error caused by inaccurate initial conditions.

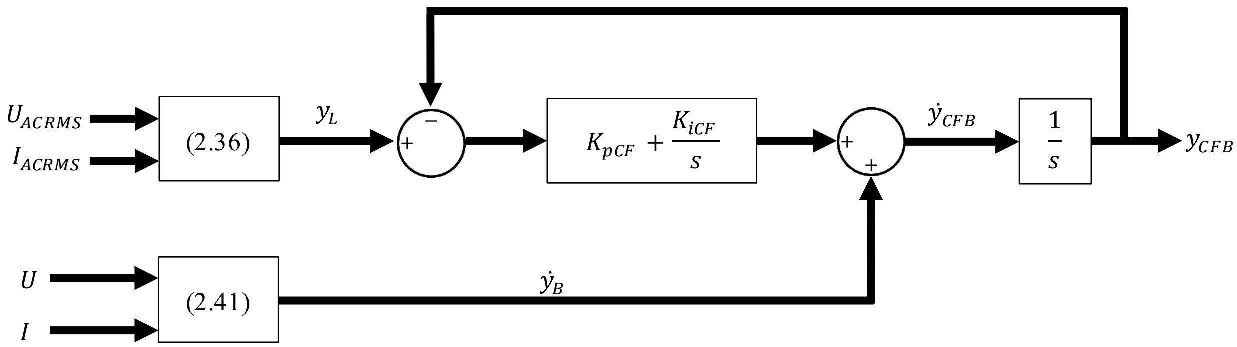

Figure 2.10 Complementary filter design that combines the BEMF-based and inductance-based plunger position detection methods.

2.4.2 Complementary Filter for the Flux Linkage-Based Position Detection Method

A second-order complementary filter can be designed to combine the flux linkage-based and inductance-based plunger position estimates. However, instead of designing a complementary filter to fuse position and velocity measurements as shown in Figure 2.10, flux linkage can be fused instead. It will be shown that the flux linkage complementary filter will allow the challenging integral initialization required for (2.47) to be circumvented.

The inductance-based position estimate in (2.36) can be converted to measure flux linkage instead of position by adapting it with (2.8) and (2.16).

$$\lambda_L = I \frac{\sqrt{\left(\frac{U_{ACRMS}}{I_{ACRMS}}\right)^2 - R_c^2}}{2\pi f_{AC}} \tag{2.56}$$

Equation (2.56) forms the low-speed input for the complementary filter. Next, the high-speed complementary filter input can be resolved by rearranging (2.44).

$$\dot{\lambda}_{\lambda} = U - R_c I \tag{2.57}$$

The output of the complementary filter, $\lambda_{CF\lambda}$, does not immediately provide an estimate of plunger position unlike the complementary filter in Figure 2.10. However, the estimated plunger position can be readily obtained by combining and rearranging (2.8) and (2.16) as shown below.

$$y_{CF\lambda} = \frac{\lambda_{CF\lambda}}{I C_L} - w_o \tag{2.58}$$

A block diagram is provided in Figure 2.11 that summarizes the process required to generate a plunger position estimate with a flux linkage complementary filter. As aforementioned, initializing the integral within the complementary filter is inconsequential if ample time is afforded to the PI controller to suppress the error caused by inaccurate initial conditions. Therefore, the initial flux linkage conditions do not need to be determined, and this circumvents the major initialization challenge identified for the flux linkage-based plunger position estimate in Section 2.3.3. However, unlike Figure 2.10, the complementary filter in Figure 2.11 requires a division by current after the integral and therefore high-frequency noise in the current sensor measurement will not be smoothed by the integral.

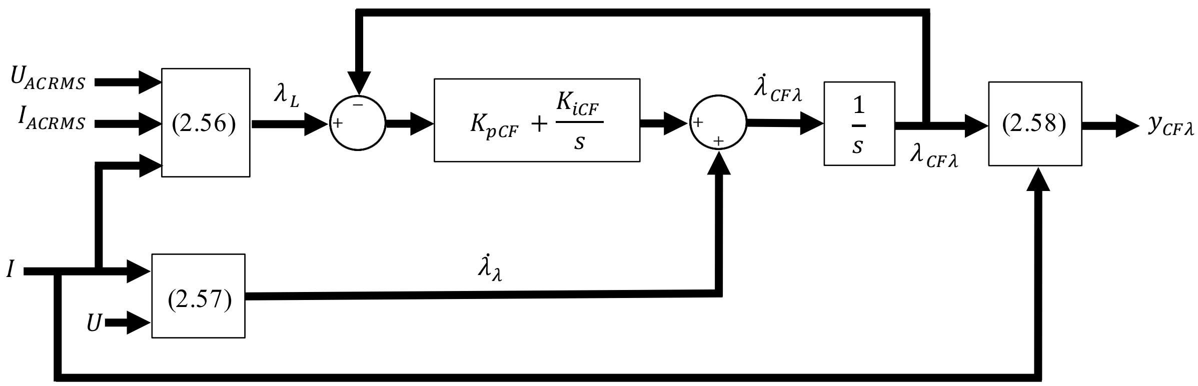

Figure 2.11 A flux linkage complementary filter that can be used to generate a plunger position estimate.

2.5 Summary

In Chapter 2, the premise of a CAS was proposed and developed. The principles of coenergy and magnetic circuits were utilized to develop models that describe CAS geometries with various stator and plunger tooth configurations. The models reveal the CAS possesses linear inductance and constant force characteristics. These characteristics allow the CAS to self-sense its plunger position based on voltage and current measurements. In particular, the CAS can produce multiple distinct plunger position estimates simultaneously based on inductance, BEMF and flux linkage measurements. It was noted that the inductance-based method is complementary with the BEMF-based and flux linkage-based methods since the inductance-based method is best suited for measuring low-speed plunger displacements, while the BEMF-based and flux linkage-based methods are best suited for measuring high-speed plunger displacements. The complementary nature of these self-sensing methods makes them ideal candidates for a sensor fusion technique. The latter part of this chapter derived complementary filters to fuse the inductance-based measurements with the BEMF-based and flux linkage-based measurements. The robust wide-bandwidth characteristics of the complementary filter outputs, suggest they should perform well when used as position feedback to sensorlessly control a CAS actuator, which is investigated in the next chapter.

Chapter 3: Design and Validation of a Constant Air Gap Solenoid Actuator

In this chapter, a CAS actuator prototype is developed and validated. Initially, an easy-to-build design is conceived that allows all anticipated features of a CAS actuator to be evaluated. The investigated design is first analyzed in a simulation study and then is validated experimentally.

3.1 Proposed CAS Actuator Stator Geometry

A proof-of-concept CAS actuator was designed to allow its novel features to be demonstrated. To accomplish this, the following objectives were prioritized:

1. Demonstrate the inductance-based, BEMF-based, and flux linkage-based plunger position estimates
2. Demonstrate that a complementary filter can be used to combine the self-sensed plunger position estimates
3. Demonstrate that the complementary filter plunger position estimate can be used as feedback for a position controller
4. Use a laminated design that can be easily adapted into a CAS sensor to reduce the cost of the prototypes
5. Produce a design that minimizes nonlinear effects where possible

Minimizing nonlinear effects needs to be carefully considered when choosing the geometry and materials for a CAS actuator. Silicon steel laminations are a common type of electrical steel that offer high flux saturation and low core losses [34], [47]. However, laminations can only be effectively employed when the flux does not travel parallel to the stacking direction. Cylindrical solenoid designs, unlike cuboidal designs, have axial flux pathways and laminations will not effectively suppress eddy currents. Therefore, a cuboid CAS shape is required to benefit from a laminated structure.

Possible stator gap configurations are shown in Figure 2.1 and Figure 2.4. In Section 2.3, it was explained that a stator design with parallel air gaps was more energy-efficient, but produced a lower peak force than a stator design with series air gaps. Substantial forces will be required to accelerate the plunger quickly in order to evaluate the high-speed BEMF-based and flux linkage-based position estimates. For this reason, a stator with series air gaps was chosen for the proposed CAS actuator design. The proposed design also stacks two CAS actuators on top of each other to produce a larger plunger force. The stator geometry to be investigated is shown in Figure 3.1.

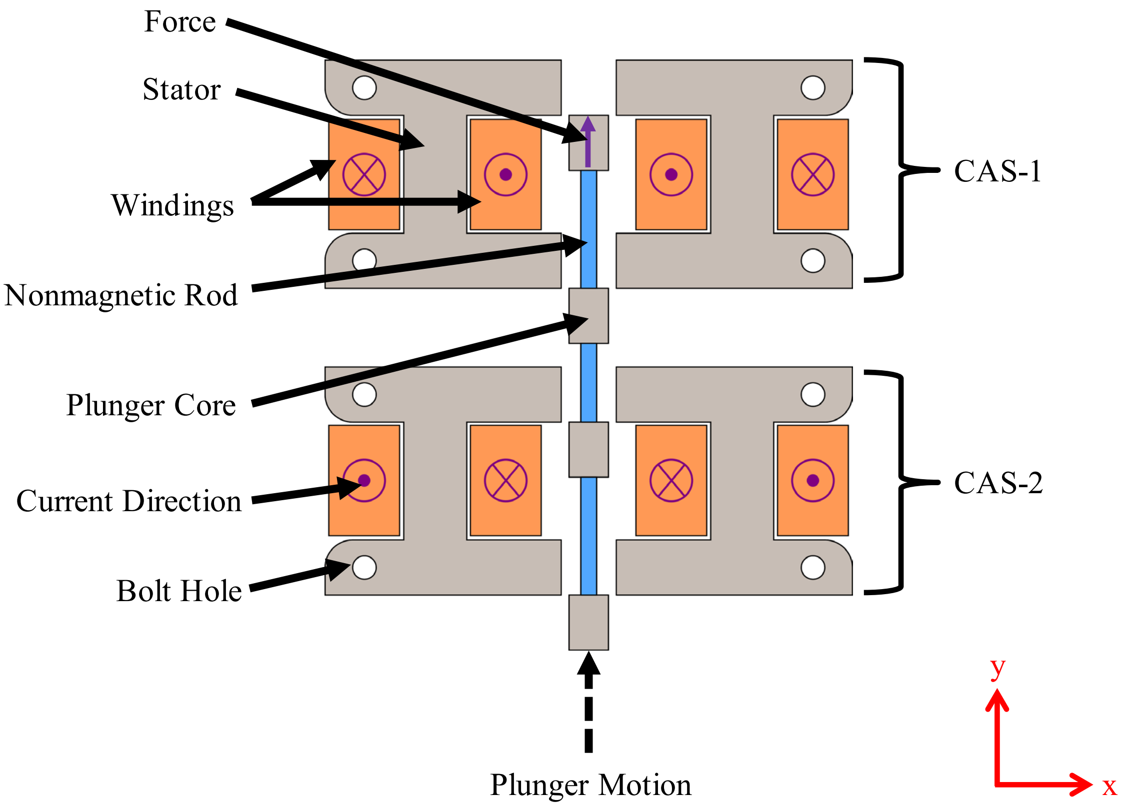

Figure 3.1 The CAS actuator geometry studied with FEA.

The prototype CAS actuator to be designed is a proof-of-concept and therefore is not spatially constrained by an application. Therefore, the CAS actuator was designed in a way that could be easily built with a minimal amount of machining and custom hardware. For example, after investigating plunger spring-return options, it was determined that procuring non-ferromagnetic coil springs with a linear range of more than 5mm would be challenging. Therefore, a maximum stroke of the proposed CAS design was selected to be less than 5mm. The proposed stator lamination design is shown in Figure 3.2a. It was anticipated that nonlinearity would accrue near the minimum and maximum plunger-stator overlap positions as the effective air gap length would begin to change due to fringing; a 7mm stator tooth width was selected in order to allow a highly-linear sub-5mm stroke to be obtained. The stator is proposed to have a laminated design in order to suppress eddy currents. For cost reasons, the stator depth was limited to 30mm which could be obtained by stacking laminations. A relatively large 12mm x 15mm stator slot was chosen as it would allow larger-gauge windings to be used to lower resistance. The large stator slot also suppresses leakage flux due to the large distance between stator teeth. The holes in the stator laminations are designed to accept M3 bolts.

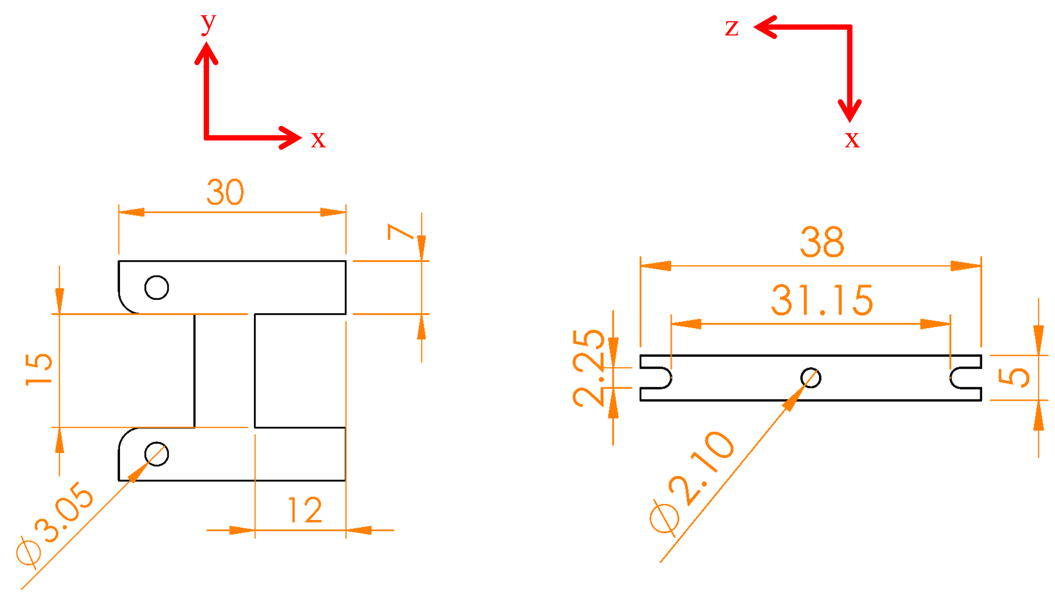

(a) (b)

Figure 3.2 Shows important dimensions for the proposed stator (a) and plunger (b) lamination designs. The dimensions provided are in millimetres. The red coordinate axes show the orientation relative to Figure 3.1.

The proposed plunger lamination design is shown in Figure 3.2b. The plunger laminations would be stacked into plunger cores that are 7mm tall and therefore equivalent to the width of the stator teeth. In order to keep the plunger evenly spaced between the stator sides, 2mm non-ferromagnetic guide rods would align the 2.25mm slots on each end of the laminations. The hole in the center of the lamination is designed to accept a threaded M2 rod which rigidly connects all of the plunger cores.

3.2 Simulation Study

The following subsections investigate the proposed CAS actuator design using FEA and lumped-parameter simulations. The force and inductance characteristics of the proposed design are first found using a 2D magnetostatic FEA simulation. The results of the FEA simulation are then applied to a lumped-parameter Simulink simulation to predict and investigate the closed-loop sensorless position control abilities of the proposed CAS actuator design.

3.2.1 Magnetic Simulation

In Chapter 2, force and inductance models of a CAS were derived. While these equations are useful for identifying performance trends and compromises, they require knowledge of key parameters like C_L and L_o. In order to accurately model these parameters, nonlinear effects, such as fringing, would need to be considered. FEA simulations allow for a much simpler way to account for nonlinear effects, and therefore can lead to more accurate models. Furthermore, FEA simulations also allow the trends and CAS characteristics identified using the analytical equations derived in Chapter 2 to be validated.

ANSYS Maxwell was selected to perform the FEA simulation. The key objectives of the FEA simulation are to obtain C_L, L_o and to investigate the limits and linearity of the current-force relationship under steady-state conditions. A 2D magnetostatic solver was selected since we have previously made the assumptions that eddy currents are negligible and flux fringing is constant;

this removes the need for a transient or 3D solver. The equations that the 2D magnetostatic solver uses are listed below, where B is the magnetic flux density, H is the magnetizing field and J is the current density.

$$\nabla \cdot B = 0 \tag{3.1}$$

$$\nabla \times H = J \tag{3.2}$$

The CAS actuator design was drafted in SolidWorks and subsequently imported into Maxwell. The plunger and stator were assigned the built-in M15 29G silicon steel material, as this was determined to be the best non-oriented grade that lamination companies commonly carried. It should be noted that in ANSYS Maxwell, this material is defined with a nonlinear B-H curve. The windings were assigned the built-in copper material. The joining members between the plunger cores were assigned the built-in HDPE plastic material. A balloon magnetic boundary was selected. The edges of the boundary were selected to be at least 12mm from the CAS actuator geometry to ensure the boundary has a negligible impact on the simulation results. The copper windings were assigned a current excitation to produce a clockwise flux direction for CAS-1 and counter-clockwise flux direction for CAS-2. It was found that the opposing flux directions were preferable since it resisted flux leakage between CAS-1 and CAS-2.

A parametric mesh study was performed before choosing the adaptive triangular mesh shown in Figure 3.3. First, a parametric study was performed to investigate the effect changing the maximum surface deviation has on the simulated results. The maximum element length was varied from the default to the minimum allowed by ANSYS Maxwell as shown in Figure 3.4. It can be noted that over the range of the plot, the inductance negligibly varies. Therefore, the default maximum surface deviation was selected.

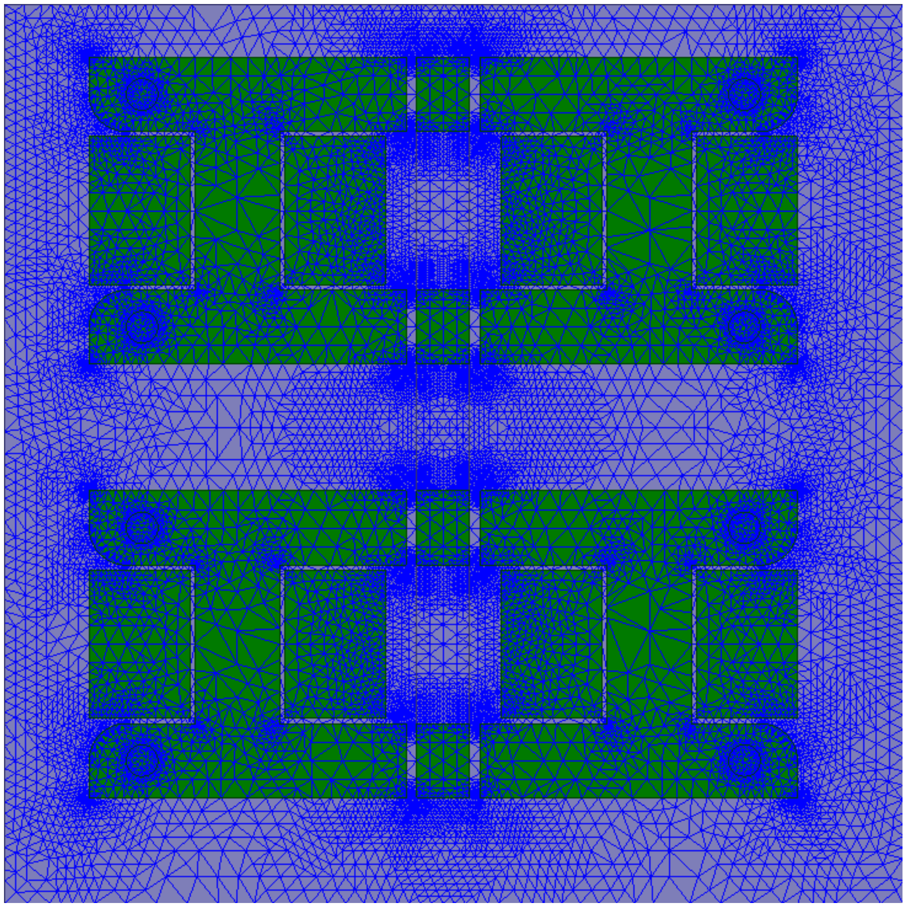

Figure 3.3 Shows the adaptive mesh used for the FEA simulation when the plunger teeth are fully overlapped with the stator teeth.

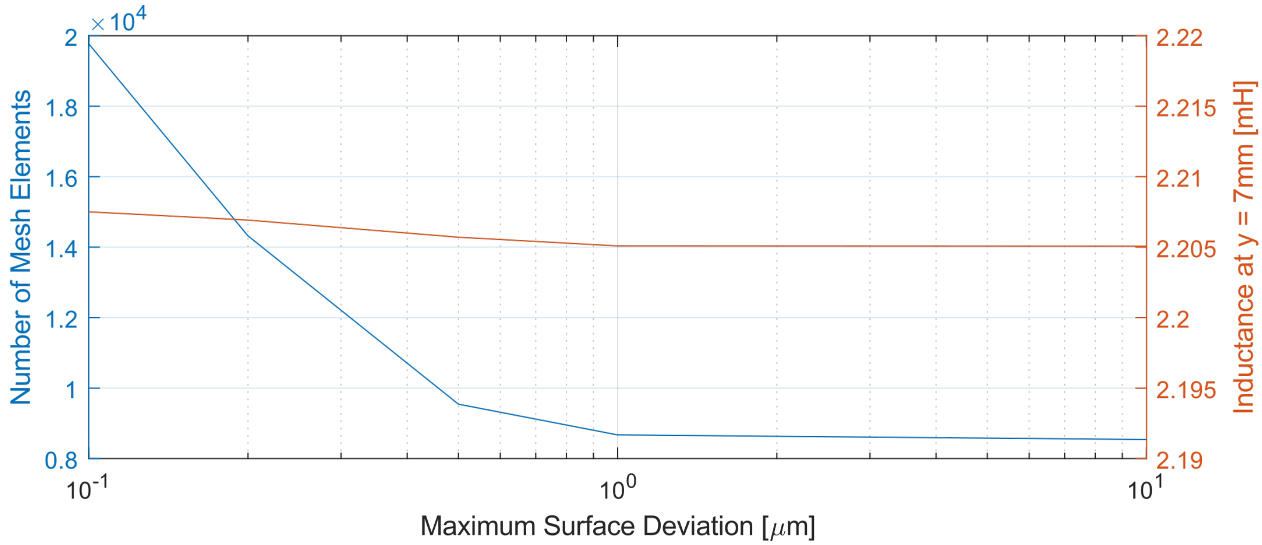

Figure 3.4 Shows the effect increasing the maximum surface deviation of the triangular mesh elements has on the number of mesh elements and the inductance when the plunger and stator teeth are fully overlapped. In this study 20A were applied to the windings.

Next, a parametric solver study was performed to find suitable percent error for the solver. The solver percent error was varied from 5% to 0.01% to see the effect it had on the inductance results and the number of passes required to converge to a solution. The results of this study are shown in Figure 3.5. From the results it is seen that the inductance values negligibly change as the percent error is reduced below 0.1%. However, it can be seen that the number of passes required to converge increases as the solver percent error gets smaller; this leads to significantly longer simulation times. In order to produce accurate results while minimizing the simulation time, a percent error of 0.1% was chosen instead of the ANSYS Maxwell default of 1%.

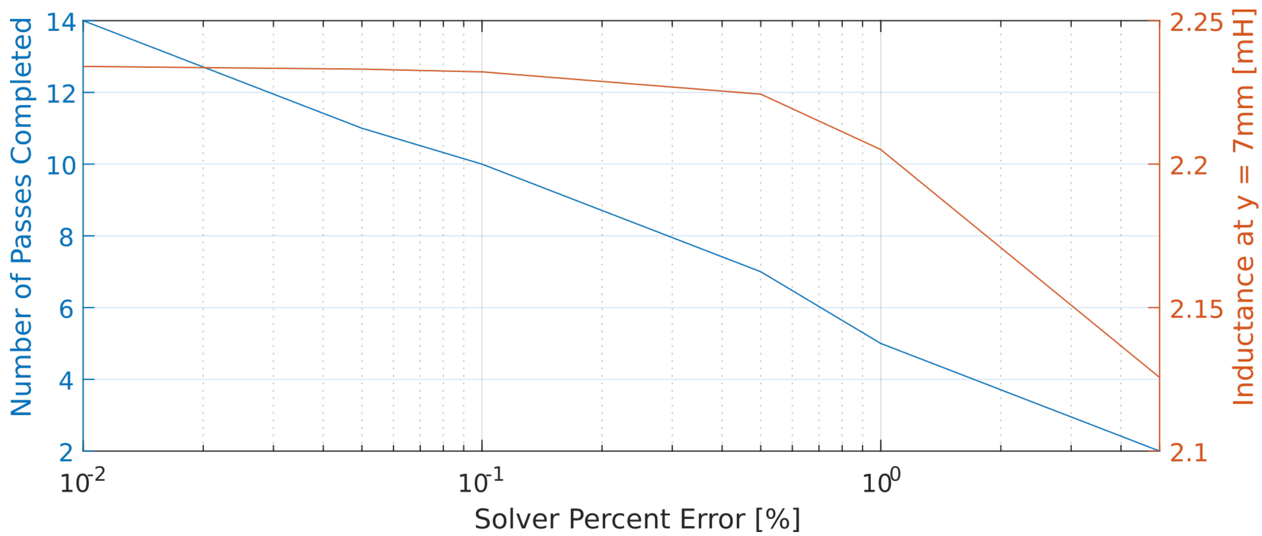

Figure 3.5 Shows the effect reducing the solver percent error has on the number of passes required to converge and the inductance when the plunger and stator teeth are fully overlapped. In this study 20A were applied to the windings.

The plunger position and excitation current were implemented in a parametric sweep. The plunger was varied from 0mm to 7mm in 0.25mm steps, while the current was simultaneously varied from 250A to 1000A in 250A increments. It is important to note that the coils are implemented as a single turn and therefore the current is equal to the MMF. After the simulation, the single turns are then post-processed and subdivided into 50 windings to determine the inductance. For the case of 50 windings, the equivalent parametric sweep of the current is 5A to 20A in 5A increments. The flux characteristics at 20A are shown in Figure 3.6 and it can be noted that the peak flux is generally below 1T and therefore is conservatively within the saturation limit of silicon steel. It should also be noted that the flux density is largest when the plunger is at maximum overlap with the stator. The flux characteristics at the midpoint of the plunger stroke for various current excitations are shown in Figure 3.7.

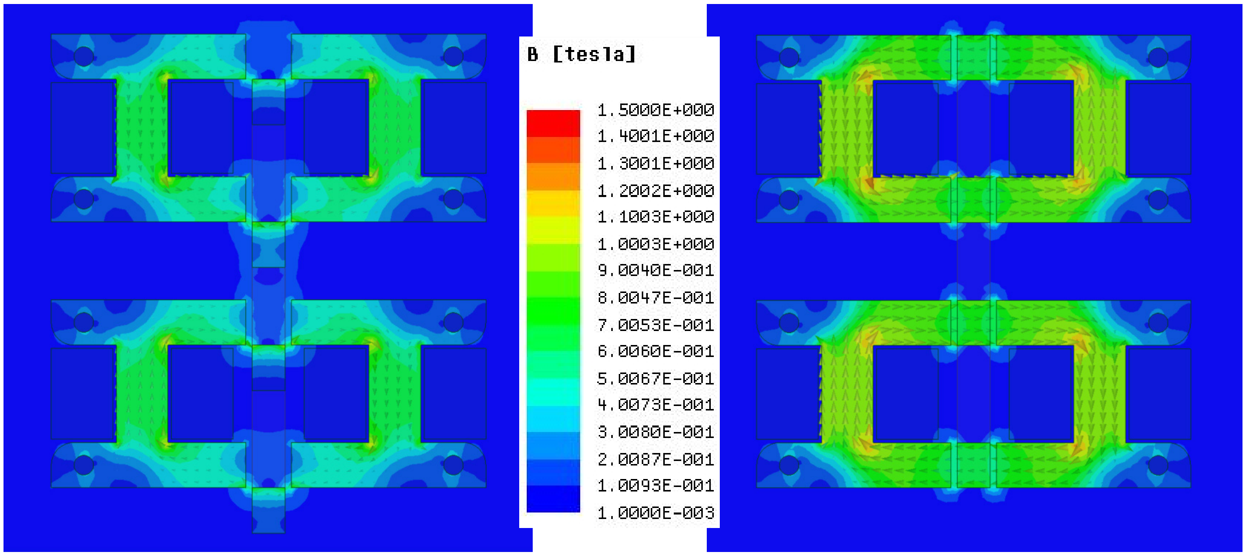

(a) (b)

Figure 3.6 The simulated magnetic flux density when the plunger of the CAS actuator is at its minimum position (a) and maximum position (b).

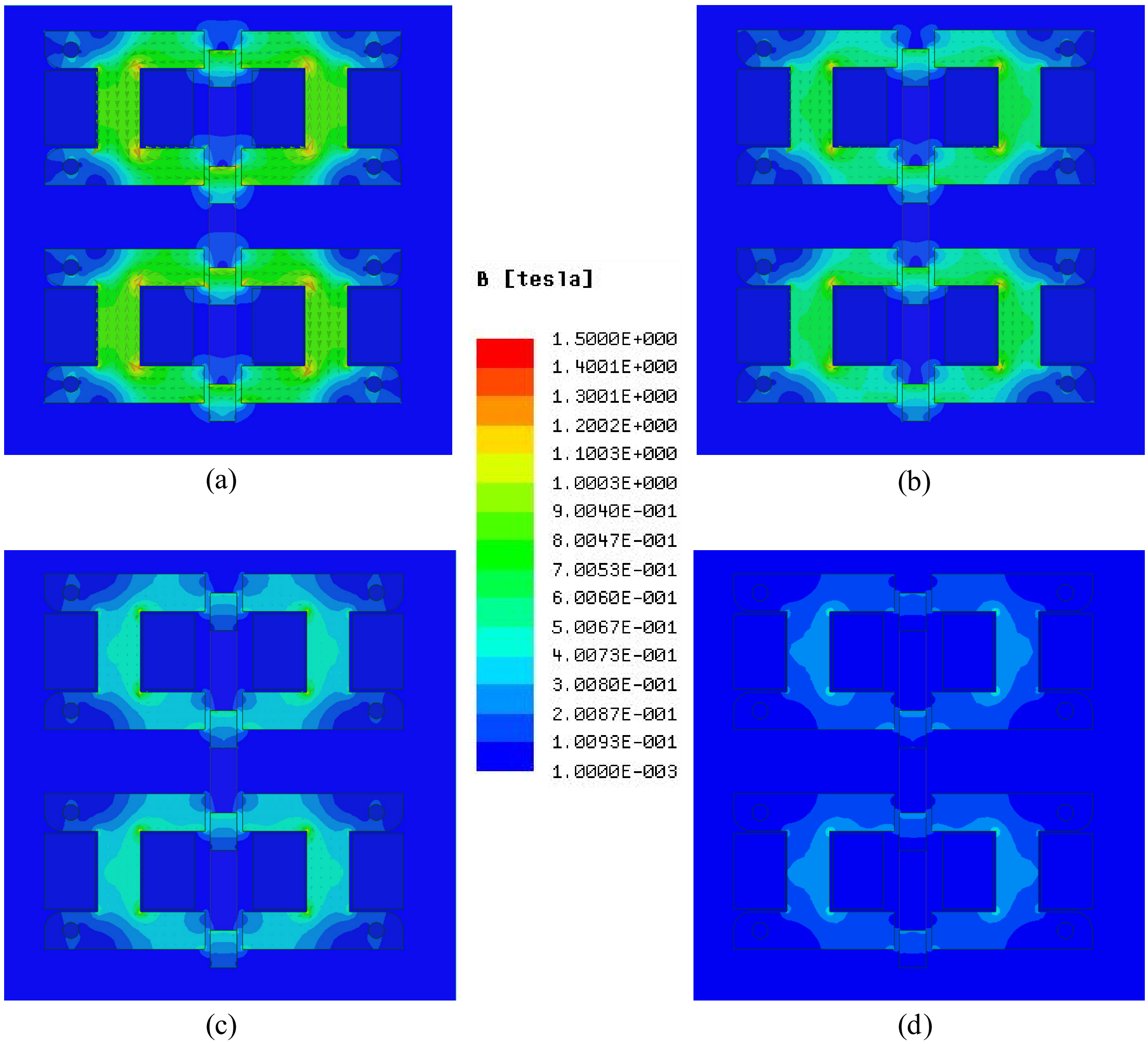

Figure 3.7 Shows the simulated magnetic flux density characteristics at 20A (a), 15A (b), 10A (c), 5A (d) when the plunger is at $\boldsymbol{y} = 3.5$mm.

The simulated force characteristics of the proposed CAS actuator geometry are shown in Figure 3.8. As the current increases, the plunger force approximately increases with the square of the current as predicted in (2.22). Ideally, the force should be independent of plunger displacement in a CAS, but magnetic nonlinearities produce the discrepancy. However, it is seen in Figure 3.8a that the force varies only a small amount if the plunger displaces between 1mm to 4mm, particularly if the current excitation is small. Therefore, a constant force approximation can be made as long as the CAS actuator is restricted to operate within a limited stroke range. It should also be observed that the transverse stator force in Figure 3.8b is approximately an order of magnitude larger than the plunger force when the plunger is fully overlapped. Therefore, it is important to design the surrounding CAS actuator packaging to be rigid or else the transverse force will pull the stator sides together and reduce the air gap. If the air gap becomes a function of current or plunger displacement due to the transverse stator force, then the accuracy of the self-sensing methods will degrade.

The simulated inductance characteristics of the proposed CAS geometry are shown in Figure 3.9. It can be noted that the inductance characteristics of CAS-1 and CAS-2 are very similar as expected, due to the large separation between CAS-1 and CAS-2. When the CAS-1 and CAS-2 inductances are summed the slope and offset double. A simple first-order regression is applied to the summed inductance between 1mm to 4mm to determine the slope and offset required for the self-sensing methods. This finding aligns with the linear inductance characteristics that were predicted with (2.15).

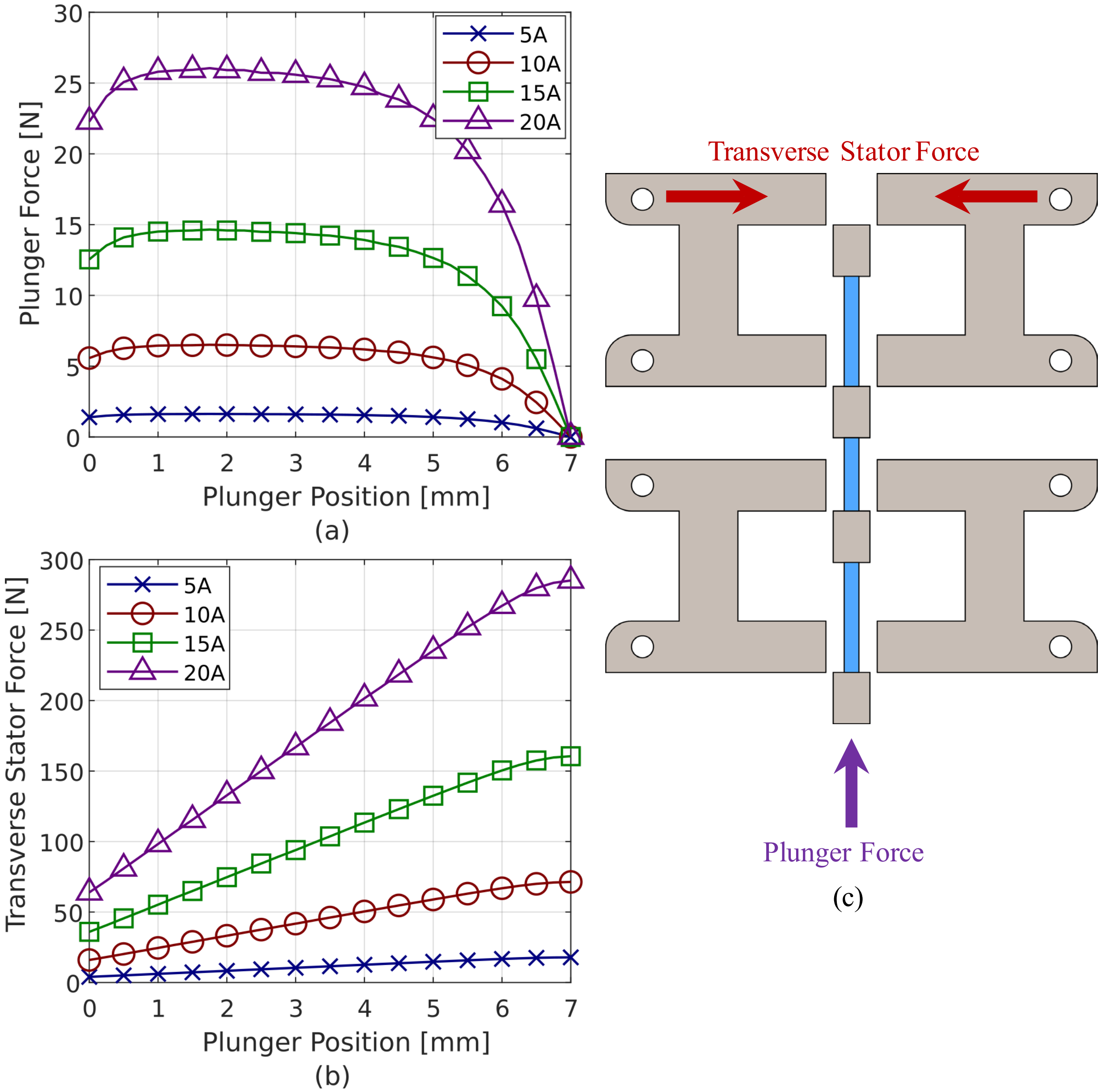

Figure 3.8 The simulated plunger (a) and transverse stator (b) force characteristics of the CAS actuator with varying level of current excitation. The directions of these forces are depicted in (c).

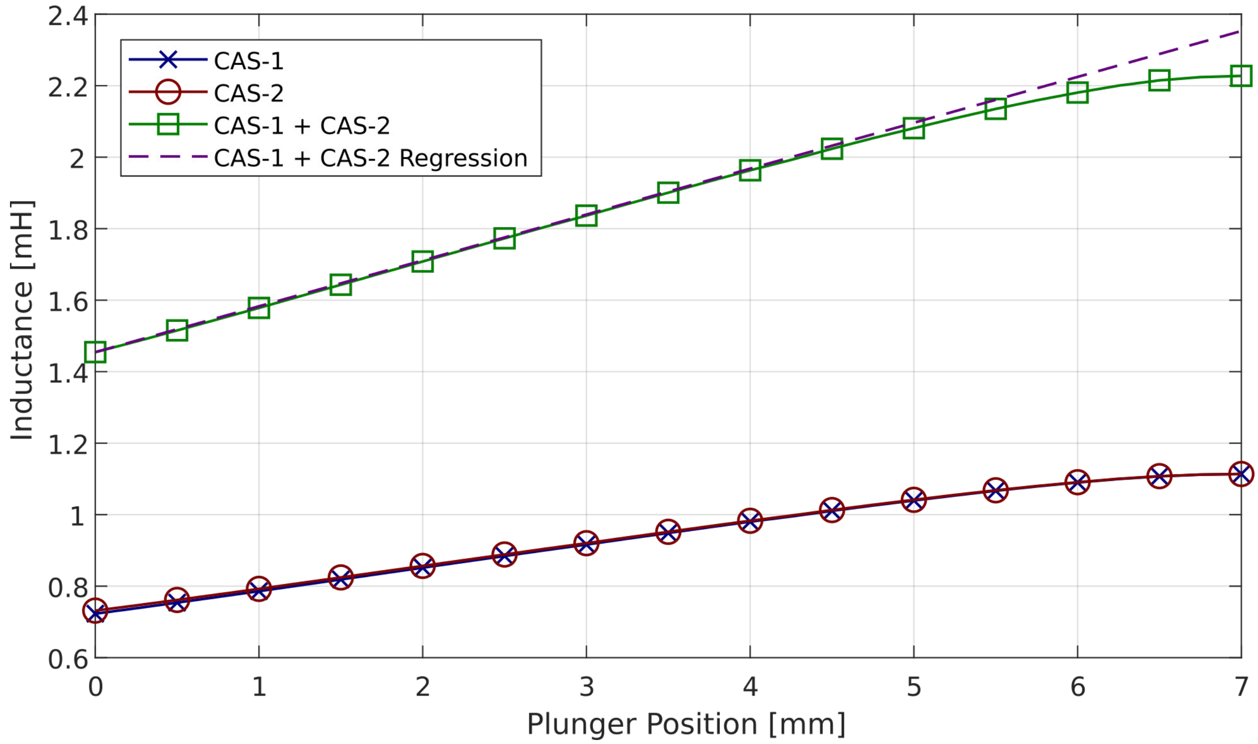

Figure 3.9 The simulated inductance characteristics of the CAS actuator and a first-order regression of the total inductance. The linear regression has a correlation coefficient of 0.99998.

3.2.2 Lumped-Parameter Simulation

The analytical equations derived in Chapter 2 can be implemented in a Simulink simulation to predict the performance characteristics of the proposed CAS actuator geometry. A control system can then be added to allow the sensorless control abilities of the CAS actuator to be investigated. A high-level overview of the Simulink simulation is depicted in Figure 3.10.

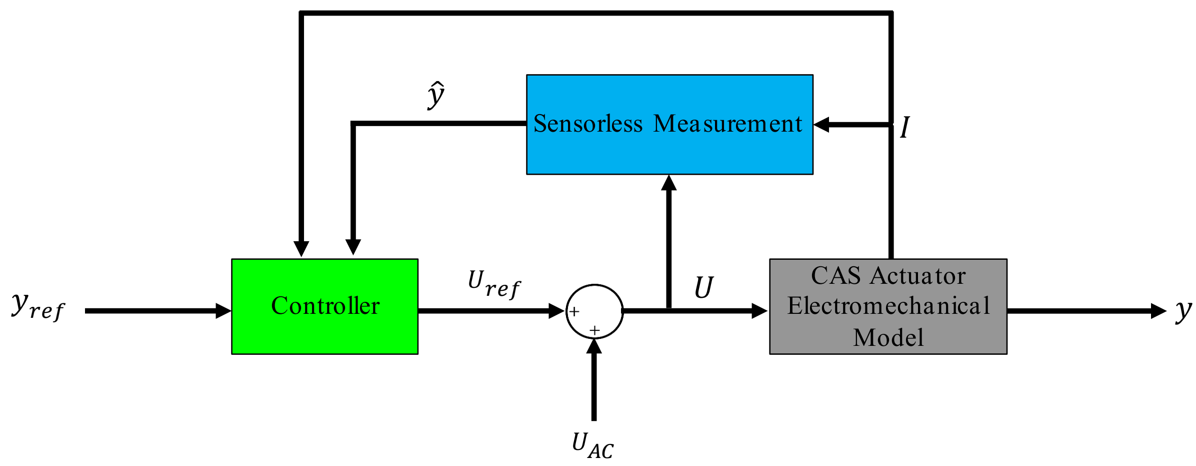

Figure 3.10 A high-level block diagram of the CAS actuator Simulink simulation.

The electromechanical model of the CAS actuator is shown in Figure 3.11. If CAS-1 and CAS-2 are wired in series, then the terminal inductance of the overall CAS actuator will be the sum of the CAS-1 inductance, L_{c1} and the CAS-2 inductance, L_{c2}.

$$L_t = L_{c1} + L_{c2} \tag{3.3}$$

The terminal inductance can be defined using a lookup table that imports the data from Figure 3.9. Similarly, the terminal resistance of the CAS actuator is the sum of the CAS-1 resistance, R_{c1} and the CAS-2 resistance, R_{c2}.

$$R_t = R_{c1} + R_{c2} \tag{3.4}$$

The resistances of CAS-1 and CAS-2 were calculated using (2.24) where N=100, $\rho_r = 16.8$ nΩ·m, D_g=30mm, l_{ht}=15mm, A_w=266mm^2 and C_{ff}=30%. Equation (2.40) can be modified using (3.3) and (3.4) to produce a model that describes the electrical characteristics of the CAS actuator.

$$U = R_t I + L_t \dot{I} + \dot{y} I \frac{L_t}{y + w_o} \tag{3.5}$$

Next, a mechanical model for the CAS actuator can be defined using the equation below where m is the moving mass of the plunger, $\ddot{y}$ is the acceleration of the plunger and k_s is the spring constant.

$$F_c = m\ddot{y} + k_s y \tag{3.6}$$

It should be noted that (3.6) does not account for damping as it is difficult to accurately predict. The spring constant was estimated to be 4800N/m based on two WW-53 springs from Century Spring Corp. The net spring force on the plunger was defined to be zero when the plunger is at the zero-overlap position. The plunger mass was estimated to be 40g using a simplistic mass calculation based on volume and density. Finally, the mechanical and electrical models can be coupled with (2.23). It is important to note that the force constant in (2.23) is defined as a lookup table based on the 20A FEA results displayed in Figure 3.8a. The electromechanical model seen in Figure 3.10 is essentially the combination of (2.23), (3.5) and (3.6). The important electromechanical simulation parameters are summarized in Table 3.1.

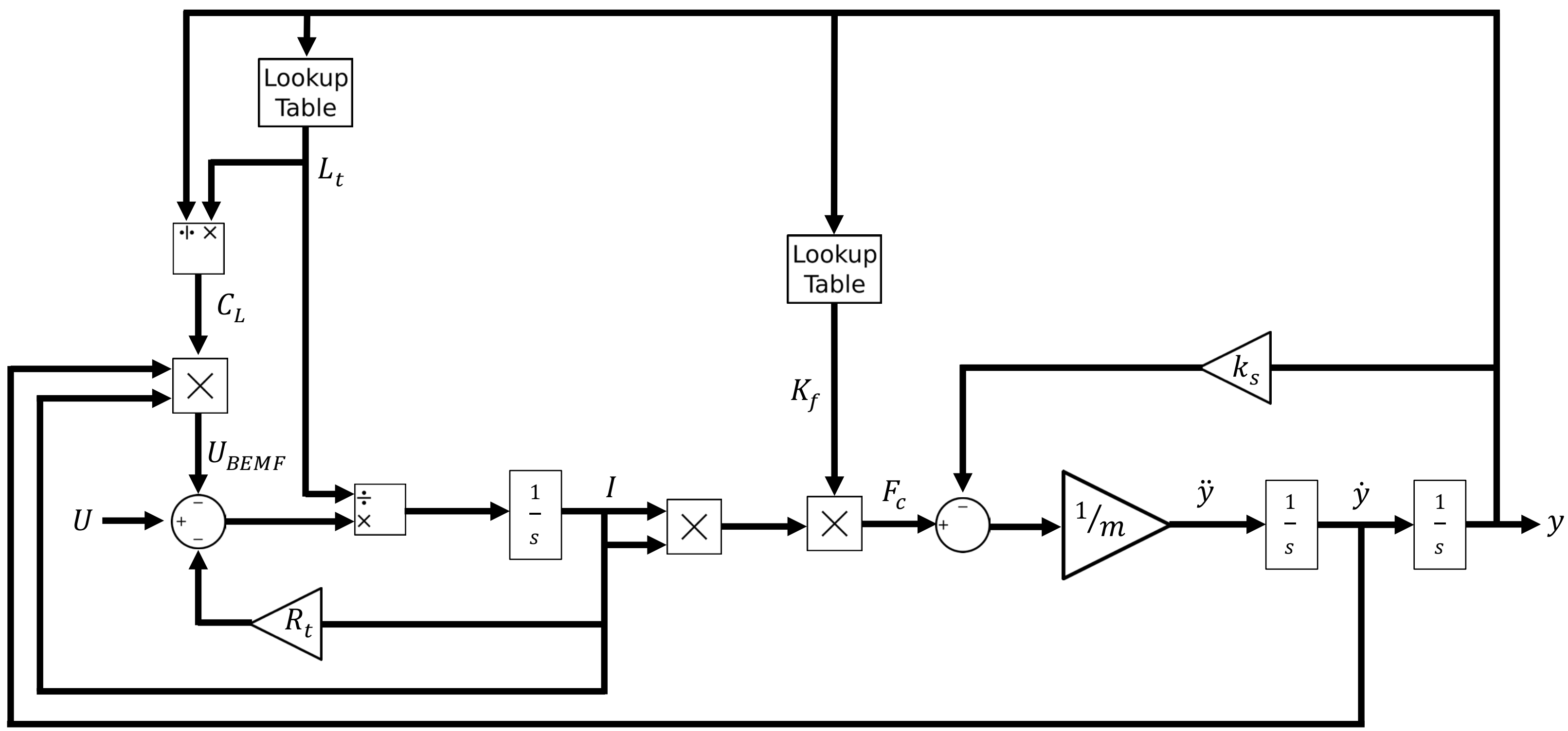

Figure 3.11 A block diagram of the CAS actuator electromechanical model used in the lumped-parameter simulation. The lookup tables are imported from the FEA simulation in Section 3.2.1.

Table 3.1 CAS Actuator Simulation Input Parameters

Symbol	Parameter	Value
C_L	Inductance-position slope [mH/mm]	0.128
w_o	Virtual plunger-stator overlap [mm]	11.3
K_f	Characterized force constant [N·m/A^2]	0.0642
R_t	CAS terminal resistance [Ω]	0.38
n_{BPF}	Bandpass filter order	4
Q_{BPF}	Bandpass filter qualify factor	1
f_{res}	Resistance calculation lowpass filter [Hz]	0.1
Q_{res}	Resistance calculation quality factor	1
f_{AC}	Superimposed AC voltage frequency [Hz]	1000
f_{CF}	Complementary filter center frequency [Hz]	10
ζ_{CF}	Complementary filter damping ratio	1
w_s	Maximum stroke [mm]	7
I_{min}	Minimum current [A]	3
I_{max}	Maximum current [A]	20
U_{max}	Supply voltage [V]	50
f_I	Current controller frequency [Hz]	200
ζ_I	Current controller damping	1
f_P	Position controller frequency [Hz]	40
ζ_P	Position controller damping	1
m	Plunger mass [g]	40
k_s	Spring constant [N/m]	4800

A simple control system is all that is required to demonstrate the working principles of a CAS actuator. A control system built on the principles of classical control theory was selected to demonstrate the sensorless control abilities of the proposed CAS actuator geometry. The nonlinear force-current characteristics and other nonlinear conditions, such as a maximum supply voltage or minimum current can be simply and elegantly accounted for using classical control. A cascaded PID position controller and PI current controller were selected for the controller topology as seen in Figure 3.12. A PID position controller was selected to ensure the CAS actuator would be able to track a step response with zero steady-state error. A PI current controller was selected to shape the error dynamics of the current with a second-order response.

The transfer function of the outer PID position control loop, which encompasses (3.6), is specified by the following transfer function where K_{iP} is the integral gain, K_{pP} is the proportional gain, K_{dP} is the derivative gain, $\hat{y}$ is the measured plunger position and y_{ref} is the reference position the controller tries to follow.

$$\frac{\hat{y}}{y_{ref}} = \frac{\frac{K_{iP}}{m}}{s^3 + \frac{K_{dP}}{m}s^2 + \frac{(K_{pP} + k_s)}{m}s + \frac{K_{iP}}{m}} \tag{3.7}$$

The controller gains can be defined based on the frequency, ω_P, and damping characteristics, ζ_P, of a third-order system.

$$\frac{\frac{K_{iP}}{m}}{s^3 + \frac{K_{dP}}{m}s^2 + \frac{(K_{pP} + k_s)}{m}s + \frac{K_{iP}}{m}} \leftrightarrow \frac{\omega_P^3}{s^3 + (2\zeta_P\omega_P + \omega_p)s^2 + (2\zeta_P\omega_P^2 + \omega_P^2)s + \omega_P^3}$$

$$K_{iP} = \omega_P^3\, m \tag{3.8}$$

$$K_{pP} = 2\zeta_P \omega_P^2 m + \omega_P^2 m - k_s \tag{3.9}$$

$$K_{dP} = 2\zeta_P \omega_P m + \omega_p m \tag{3.10}$$

For the lumped-parameter simulation, the position controller frequency was set to 40Hz which is below the mechanical resonant frequency and was estimated to be obtainable with the hardware available for subsequent experimental validation. Furthermore, the damping constant was set to one to obtain a critically damped response.

The transfer function of the inner PI current control loop requires the velocity-dependent BEMF term to be neglected in (3.5) and is specified by the following transfer function where K_{iI} is the integral gain, K_{pI} is the proportional gain and I_{ref} is the reference current the controller tries to follow.

$$\frac{I}{I_{ref}} = \frac{\frac{K_{iI}}{L_t}}{s^2 + \frac{(R_t + K_{pI})}{L_t} s + \frac{K_{iI}}{L_t}} \tag{3.11}$$

The controller gains can be defined based on the frequency, ω_I, and damping characteristics, ζ_I, of a second-order system.

$$\frac{\frac{K_{iI}}{L_T}}{s^2 + \frac{(R_t + K_{pI})}{L_t}s + \frac{K_{iI}}{L_t}} \leftrightarrow \frac{\omega_I^2}{s^2 + 2\zeta_I\omega_I s + \omega_I^2}$$

$$K_{iI} = \omega_I^2 L_t \tag{3.12}$$

$$K_{pI} = 2\zeta_I\omega_I L_t - R_t \tag{3.13}$$

For the lumped-parameter simulation, the current controller frequency was set to 200Hz as this was estimated to be attainable with the available hardware to subsequently validate the simulated results with a prototype CAS actuator. The damping constant was set to one to obtain a critically damped response. It is important to note that L_T varies with position and must be approximated with a constant value in order to obtain constant controller gains in (3.12) and (3.13). Therefore, L_T was assumed to be a constant value and was set to equal the inductance at the midpoint of the plunger stroke.

It is seen in Figure 3.12 that saturation blocks are added to restrict the limits of the reference voltage and current. The reference voltage limit was restricted to +/-40V since the hardware available for subsequently testing the physical CAS actuator can only supply 50V and 10V is reserved for the superimposed voltage ripple. The maximum reference current was limited to 20A to align with the limits in the FEA simulation. The minimum reference current was limited to 3A to avoid divide-by-zero errors and ensure adequate SNR within the high-speed self-sensing algorithms as discussed in Section 2.3.

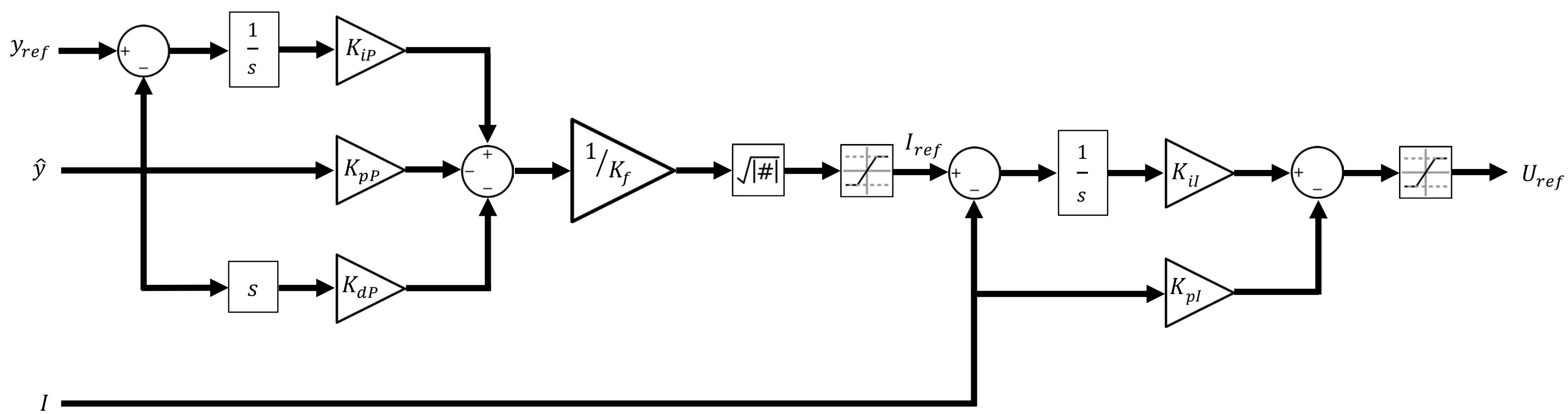

Figure 3.12 CAS actuator control system schematic.

The sensorless measurement block in Figure 3.10 is a conglomerate of the self-sensing methods derived in Chapter 2. The equations that compose the self-sensing methods are structured as shown in Figure 3.13. From the figure, it can be noted that the complementary filter outputs and the inductance-based, BEMF-based and flux linkage-based plunger position estimates can all be produced simultaneously. Naturally, a user would be able to select any of these measurements to use as position feedback for the controller. However, all five of these measurements only require forward calculations and therefore can be simultaneously observed and compared regardless of which method is chosen for feedback. The complementary and bandpass filter parameters used in the lumped-parameter simulation are listed in Table 3.1. Selecting these parameters can require making performance compromises. Appendix A discusses methods to select these parameters. Depending on the intended application or hardware limitations, one may have to select these parameters carefully. However, the scope of this thesis only requires a suitable set of parameters to demonstrate the various attributes and abilities of a CAS actuator. Therefore, these parameters were obtained through iterative tuning until suitable performance was attained.

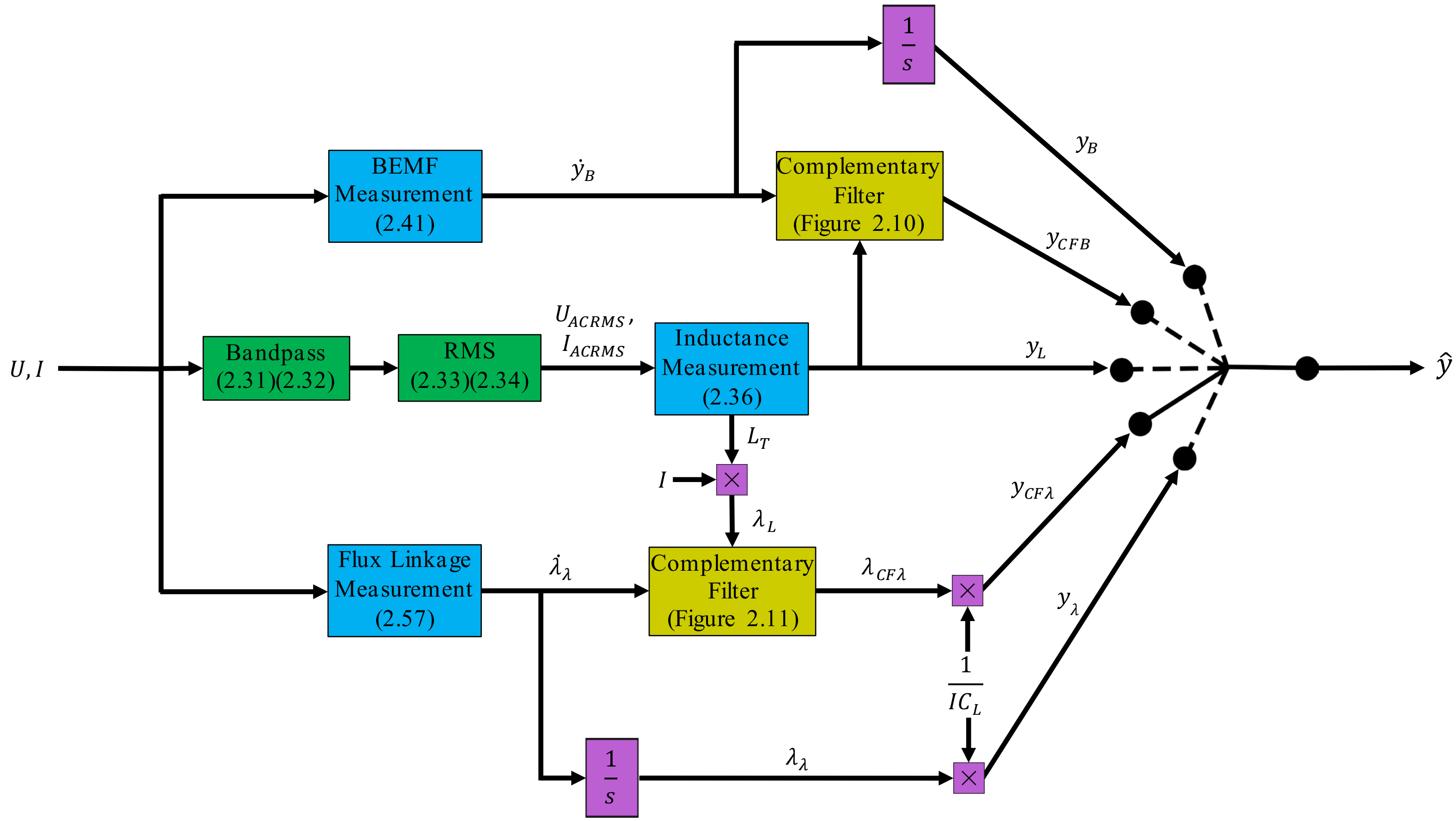

Figure 3.13 Shows a block diagram of the plunger position self-sensing measurements.

Before sensorless feedback control can be investigated, it is first important to analyze the plunger position estimates produced by the self-sensing methods and complementary filter outputs. To analyze the open-loop performance of the self-sensing methods and complementary filter outputs, y can be used as feedback to emulate an ideal position sensor. The position tracking performance and the corresponding voltage and current profiles for an ideal position sensor are seen in Figure 3.10. For the 3mm step pattern, it is seen that the plunger tracks the reference without overshoot or steady-state error as expected due to the PID controller configuration. It should be noted that the current is near the 20A limit at the 4mm position and therefore this CAS design would be unable to achieve larger plunger lifts without changing the spring configuration. However, the 1mm to 4mm range corresponds with the prescribed linear region seen in Figure 3.9. A zoomed-in view of the superimposed voltage and current ripple when the plunger is held at 2.5mm is shown in Figure 3.15. From the figure, it is seen that the specified 10V 1000Hz AC ripple produces approximately 1.7A of current ripple. The position, voltage and current characteristics seen in Figure 3.14 and Figure 3.15 will be used as nominal conditions to evaluate the simulated performance of the self-sensing methods and complementary filters.

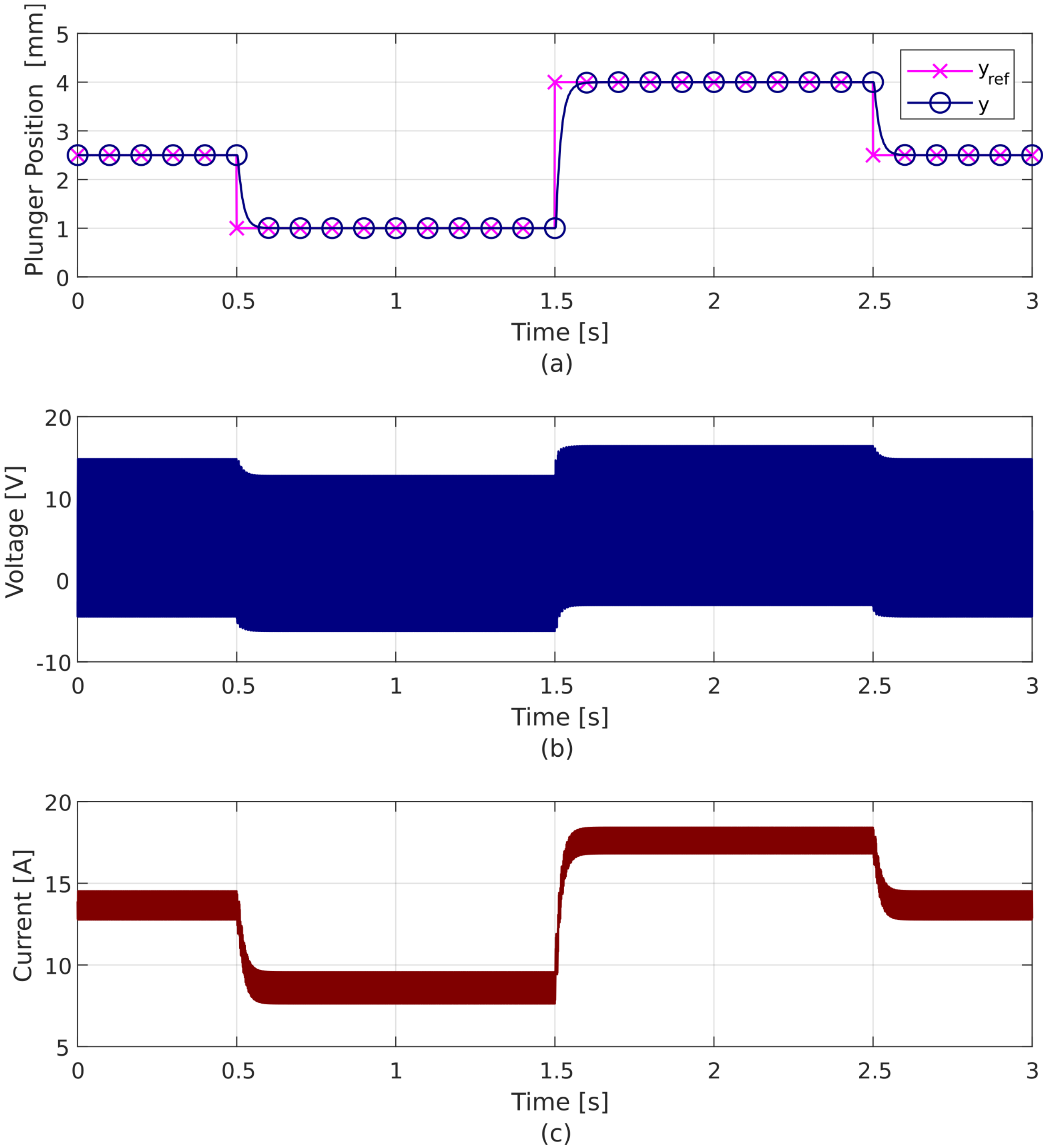

Figure 3.14 Shows the simulated results of the CAS actuator tracking a predefined trajectory using an ideal position sensor for position feedback (a) and the required voltage (b) and current (c).

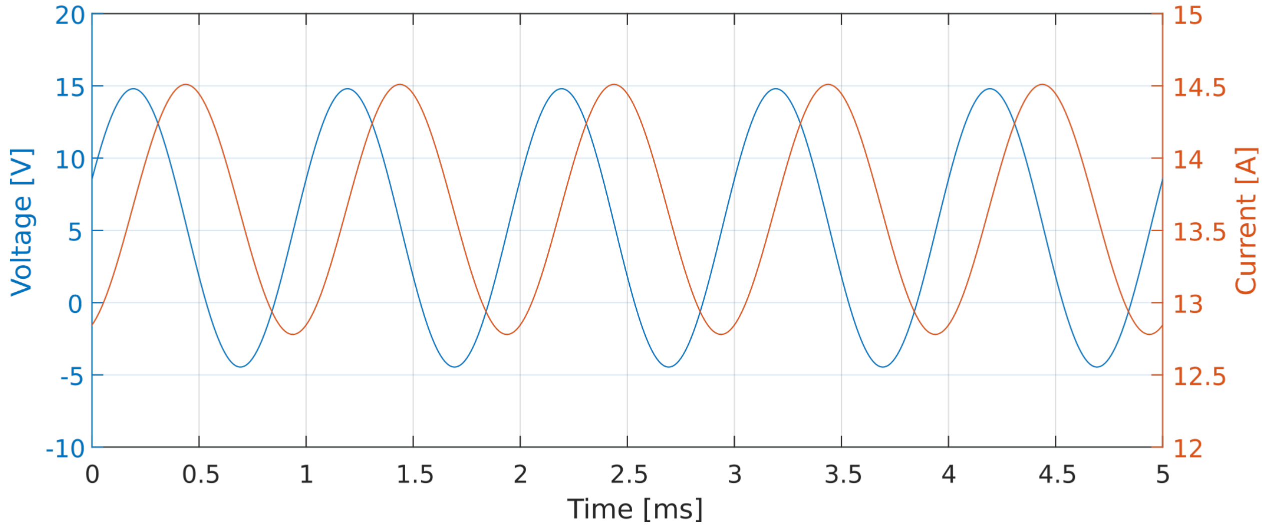

Figure 3.15 Shows the simulated characteristics of the superimposed voltage and current ripple used to calculate the plunger position of the CAS actuator based on inductance.

The open-loop performance of the self-sensing methods and complementary filter outputs are shown in Figure 3.16. From the figure, it is seen that the inductance-based, BEMF-based and flux linkage-based methods all produce accurate measurements of the actual plunger position. However, it is important to note that the zoomed-in region of Figure 3.16a shows the inductance-based measurement slightly lags the actual plunger position as expected due to the inherent lag introduced by the bandpass and RMS filters within the self-sensing method. It can also be noted that there is a slight amount of error at 4mm due to the nonlinear characteristics of the inductance profile in Figure 3.9. In Figure 3.16d, it is seen that the performance of the BEMF-based and flux linkage complementary filters are similar although the BEMF-based output shows a slight amount of sinusoidal error due to the delay introduced by requiring position information from the prior timestep as seen in (2.42). Naturally, this suggest the flux linkage complementary filter output is superior under noiseless conditions. When comparing Figure 3.16c and Figure 3.16d it is seen that the complementary filter outputs offer a slight improvement over the inductance-based measurement, but appear to offer no benefit over the BEMF-based or flux linkage-based methods. However, it is important to note that the complementary filter performance could be improved by decreasing the center frequency to favour the high-speed standalone measurements, but it will be shown in subsequent figures that the opposite is true when sources of error are introduced.

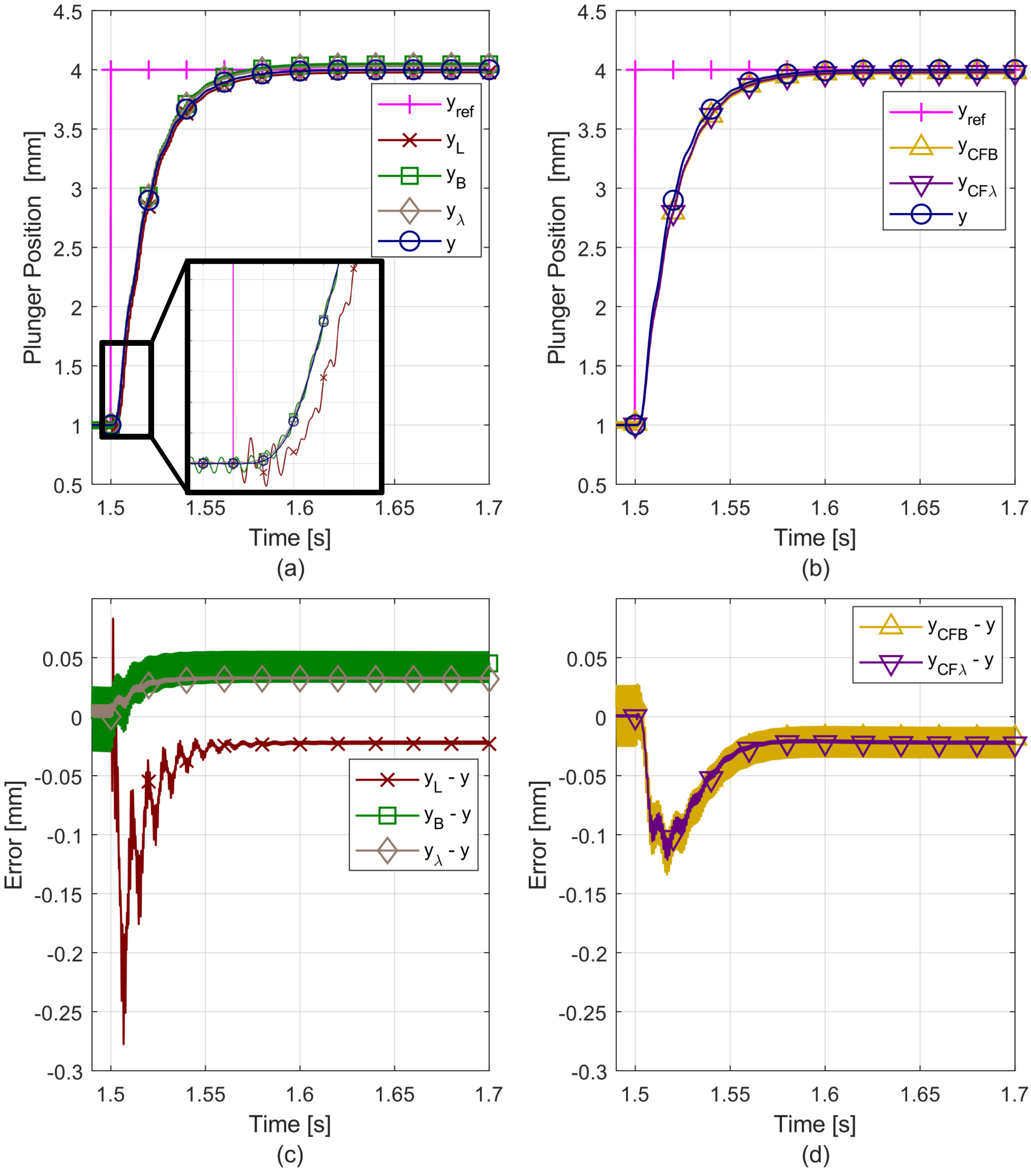

Figure 3.16 Compares the performance of the self-sensing methods (a) and the outputs of the complementary filters that fuse the self-sensed measurements (b) when the simulated CAS actuator is controlled using an ideal position sensor for feedback. The error relative to the actual plunger position is shown in (c) and (d).

The effects of random noise on the self-sensing methods and complementary filter outputs can be explored using the Simulink simulation. The impact of Gaussian noise with zero-mean and a standard deviation of 100mA is seen in Figure 3.17. When comparing Figure 3.16 and Figure 3.17, it is evident that the added noise severely degrades all of the self-sensing methods. For the inductance-based method, the noise contains frequency components that pass through the bandpass filters and create significant high-frequency noise in the plunger position estimate. Both the BEMF-based and flux linkage-based self-sensing methods do not track the reference trajectory well. Interestingly, in Figure 3.17 it is seen that the BEMF-based complementary filter outperforms the flux linkage complementary filter, unlike Figure 3.16. This reversal is a result of the high-frequency current noise being reintroduced after the integral in Figure 2.11 due to the division-by-current in (2.58). However, it can be noted that both complementary filter outputs improve upon the standalone self-sensing methods. In particular, the complementary filter suppresses the high-frequency noise on the inductance-based method while utilizing the low-speed average; the high-speed information from the BEMF-based and flux linkage-based self-sensing methods are used to more accurately capture the fast plunger motion during the trajectory step.

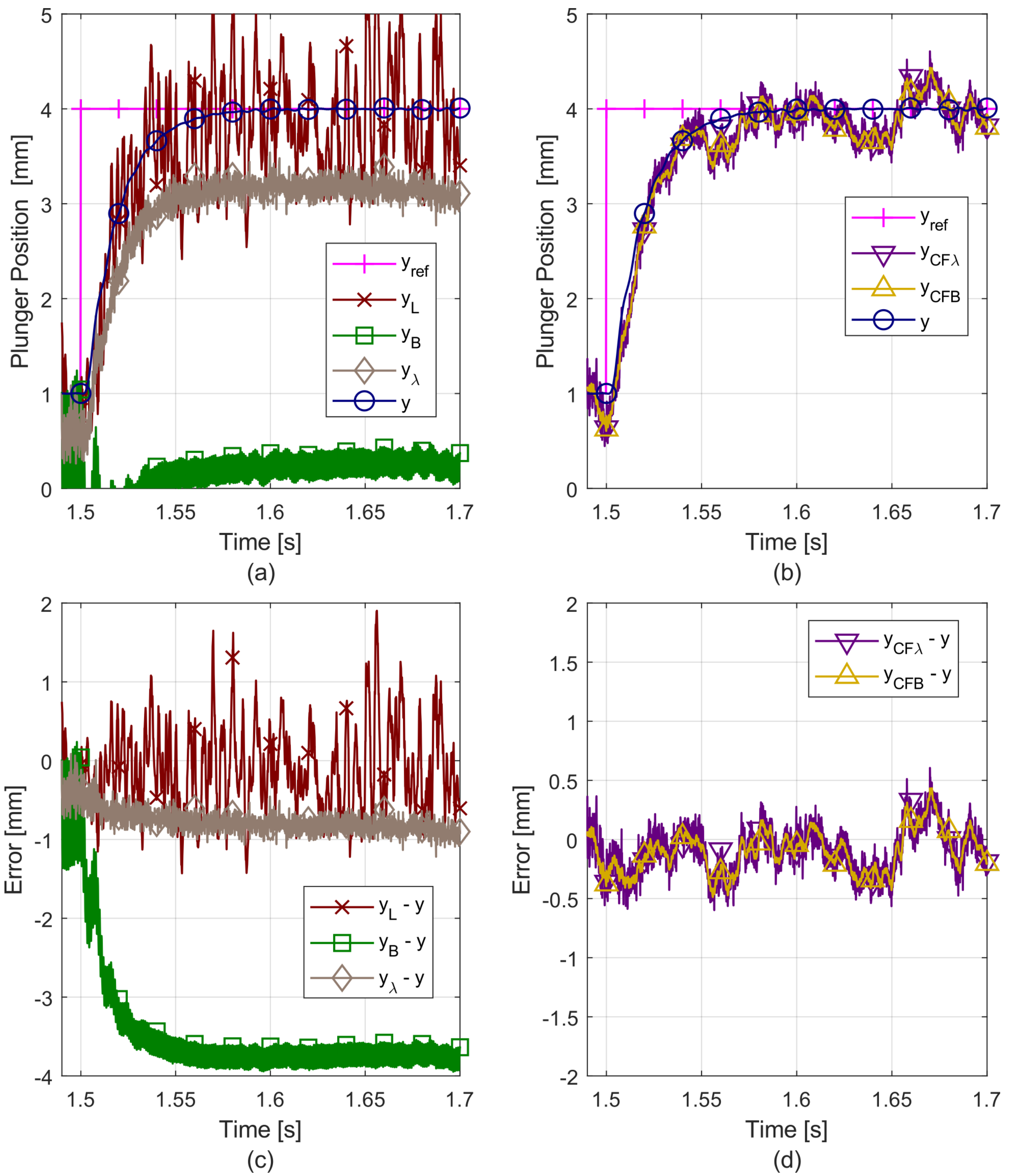

Figure 3.17 Compares the performance of the self-sensing methods (a) and the outputs of the complementary filters that fuse the self-sensed measurements (b) after 100mA of Gaussian noise is added while attempting to perform position control with an ideal position sensor. The error relative to the actual plunger position is shown in (c) and (d).

As was noted in Section 1.1.1 and Section 1.1.2, temperature changes can create significant drift in the measurements of some sensors. The resistivity of copper has a well-defined relationship with temperature as revealed in the equation below where R_o is the initial resistance and T is the change in temperature [131].

$$R = R_o(1 + 0.00393T) \tag{3.14}$$

It is important to recall that the self-sensing methods derived in Section 2.3 require winding resistance to be specified. Naturally, the Simulink simulation enables the impact temperature variation has on the self-sensing methods to be explored. Based on (3.14), a 5°C change in temperature would lead to approximately a 2% increase in the winding resistance of the CAS actuator. If a constant resistance value is supplied to the self-sensing methods as proposed in Method 2 of Table 2.1, then the plots seen in Figure 3.18 will result if the temperature increases by 5°C. From the figure, it can be appreciated that even a slight change in resistance leads to significant error in the BEMF-based and flux linkage-based measurements. In a practical setting, this significant drift would likely make these measurements infeasible to use as a standalone measurement for position control. However, the inductance-based estimate is negligibly affected as predicted in Section 2.3.1 since the reactance of the simulated CAS actuator is over an order of magnitude larger than the resistance. While the inductance-based measurement could continue to be feasibly used as a standalone measurement, it is important to note that the complementary filter outputs are also free from drift, while still improving upon the phase-lag error of the inductance-based measurement. Evidently, a complementary filter is advantageous to use as it allows the high-speed position information contained within the BEMF-based and flux linkage-based measurements to be salvaged. When comparing Figure 3.16d and Figure 3.18d, it is seen that the flux linkage complementary filter output is more prone to the effects of a mischaracterized resistance. Naturally, increasing the center frequency of the complementary filter and biasing it to use the inductance measurement for a wider bandwidth would reduce the effects of resistance changes in the complementary filter output. However, increasing the center frequency would then pass more phase-lag error through the filter which was viewed as being detrimental in the discussion prior to Figure 3.16. Clearly, selecting the center frequency of the complementary filter requires compromising on various types of error sources.

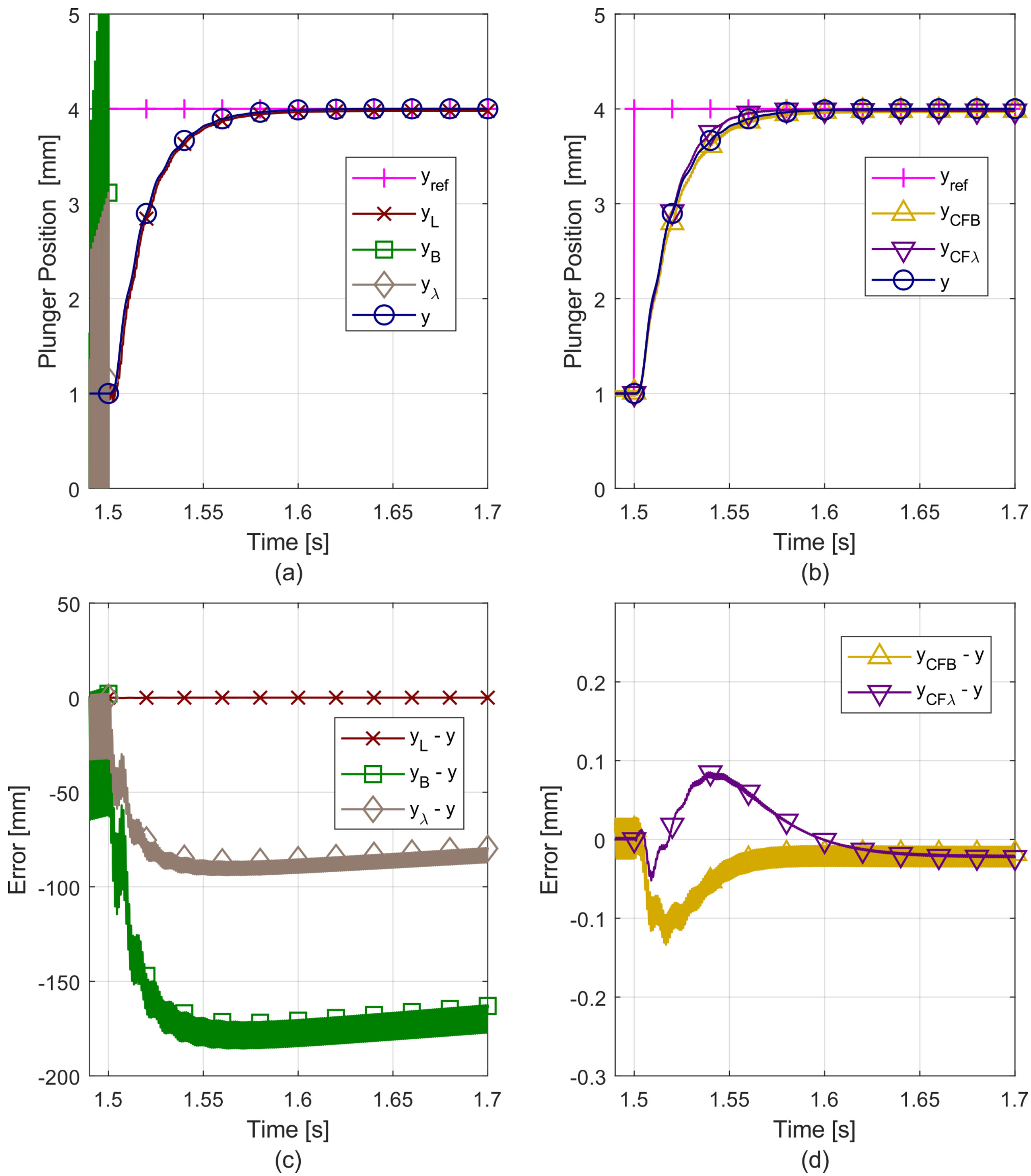

Figure 3.18 Compares the performance of the self-sensing methods (a) and the outputs of the complementary filters that fuse the self-sensed measurements (b) where the CAS actuator is controlled using an ideal position sensor for feedback and its resistance is mischaracterized by 2%. The error relative to the actual plunger position is shown in (c) and (d).

Since the CAS actuator requires a non-zero current for the self-sensing methods to remain finite, it is possible to continuously update the resistance using Ohm's Law which also requires a non-zero current where U_{DC} is the applied DC voltage and I_{DC} is the applied DC current.

$$R_{online} = \frac{U_{DC}}{I_{DC}} \quad \textbf{(3.15)}$$

However, it is important to note that (3.15) is only valid for purely-DC signals and that the superimposed ripple, driving voltage and BEMF produced by the CAS actuator have AC components. Fortunately, the DC voltage and current components can be isolated using lowpass filters as shown in Figure 3.17. The cut-off frequency of the lowpass filters must be carefully selected based on the CAS actuator design. Setting the cut-off frequency too low or too high will lead to the online resistance measurement performing poorly. The Simulink simulation can be used to demonstrate the effects the cut-off filter has on the online resistance measurement. Figure 3.20 shows the performance of two online resistance measurements during plunger position control with critically damped second-order lowpass filters with different cut-off frequencies. Figure 3.20b and Figure 3.20c show a 0.1°C/s and 10°C/s rate of temperature change respectively. From the plots, it is seen that a cut-off frequency of 1Hz, can relatively quickly track a changing temperature, but passes AC components creating significant error. The 0.1Hz lowpass filter does not pass the AC components but is much slower at tracking a temperature change. Ideally, the cut-off frequency of the lowpass filters should be set as high as possible to allow resistance changes to be rapidly corrected, but without passing the AC voltage and current components. However, if the temperature change is too fast, the online resistance measurement will be ineffective as it will not be possible to track the resistance change quick enough without introducing error from the AC components. Nevertheless, even if the temperature change is too fast to track, such as a high-power CAS that self-heats very quickly during intermittent actuations, an online resistance measurement could still improve accuracy by accounting for changing ambient temperature conditions, or tracking the average of the temperature increase.

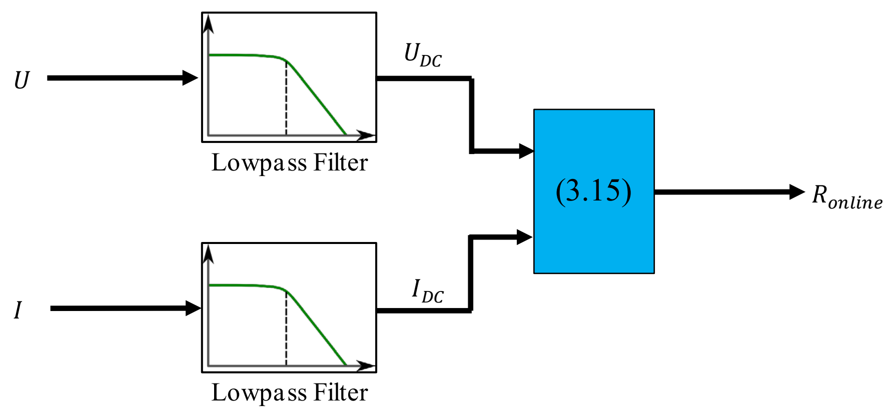

Figure 3.19 Shows the implementation of the online resistance measurement.

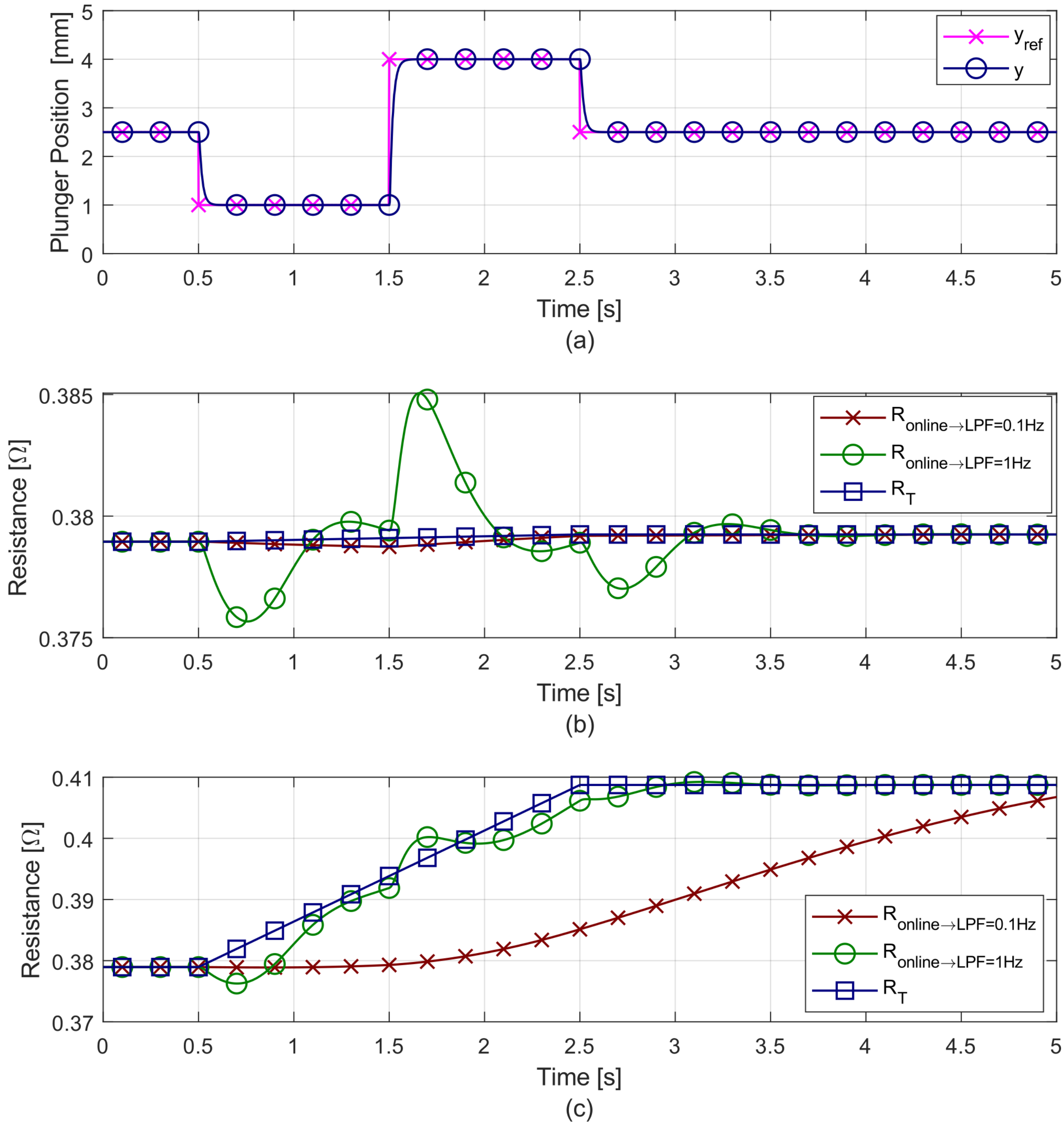

Figure 3.20 Shows two online resistance measurements with different lowpass cut-off frequencies tracking a 0.1°C/s increase in temperature (b) and a 10°C/s (c) when the plunger is controlled to track the trajectory seen in (a).

The impact an online resistance measurement with a 0.1Hz cut-off frequency has on the self-sensing methods and complementary filter outputs is seen in Figure 3.21. For the 0.1°C/s temperature rate of change in Figure 3.21a, it is seen that the BEMF-based and flux linkage-based methods still drift, but the rate of drift of the flux linkage-based method decreases as the resistance is corrected over time. Similarly, in Figure 3.21c it is seen that a 10°C/s temperature rate of change shows a significantly faster drift, but the rate of drift for the flux linkage-based measurement is reduced over time. When examining Figure 3.21b and Figure 3.21d, which correspond to temperature changes of 0.1°C/s and 10°C/s respectively, it is seen that the online resistance measurement is unable to resolve error in the flux linkage complementary filter output when the temperature change is rapid. This is expected since the online resistance measurement is too slow to correct the resistance change and the complementary filter center frequency is set too low and passes the large drift as was seen in Figure 3.18d. Overall, it is seen that the online resistance measurement is relatively inconsequential to the complementary filter outputs which already correct the resistance-based drift with the inductance-based measurement. However, it is important to recall that this is only true if the inductance-based self-sensing method is negligibly affected by resistance changes as is the case with the simulated CAS actuator design. Conversely, it should also be noted that the addition of the online resistance measurement did not adversely affect the self-sensing methods or complementary filter outputs. Therefore, ideally one should use Method 3 instead of Method 2 or Method 1 in Table 2.1, since at worst, an online resistance measurement may offer negligible improvement, but it also has the potential to correct for a significant source of error depending on the design of the CAS actuator.

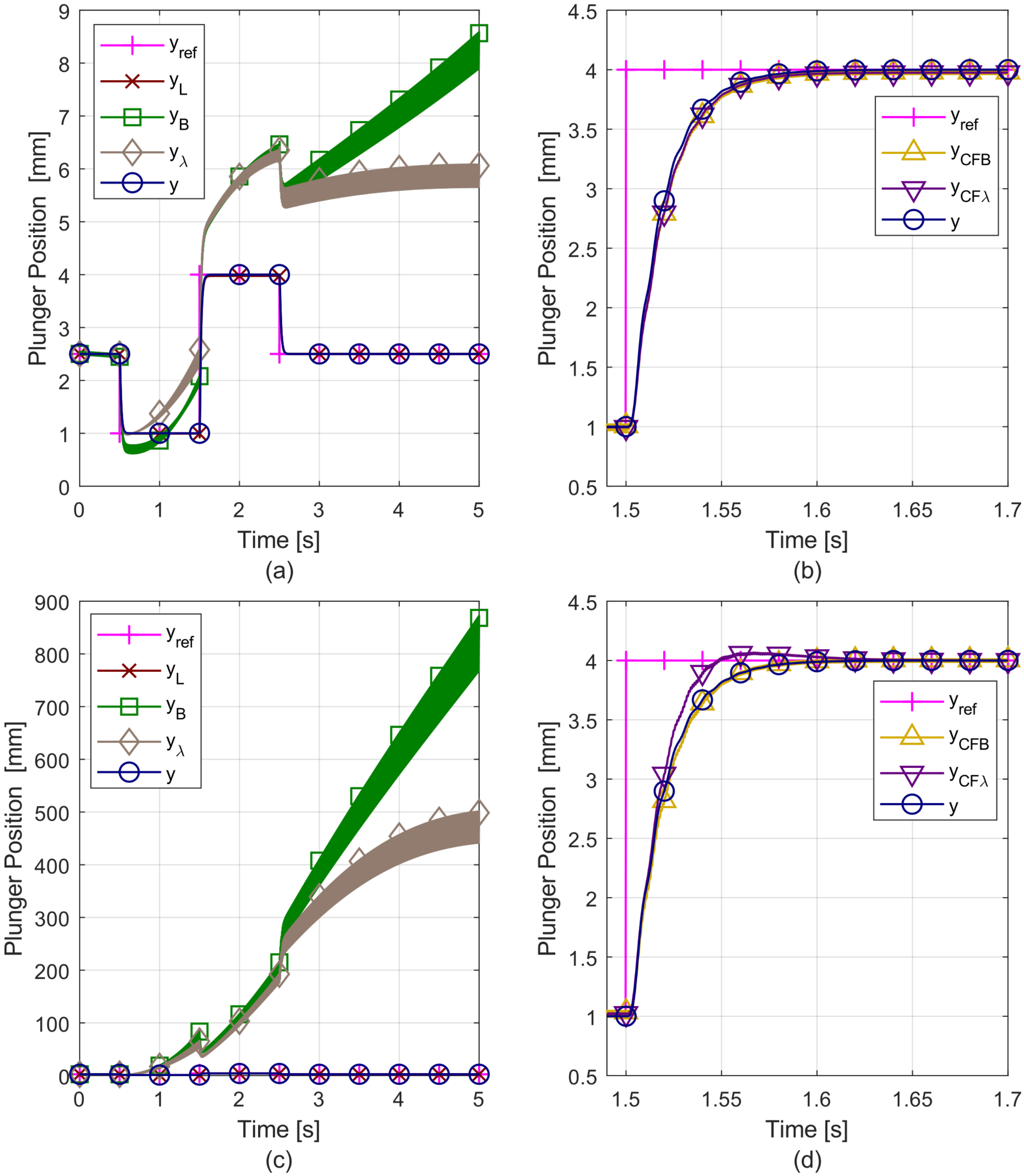

Figure 3.21 The top graphs show the performance of the self-sensing methods (a) and complementary filter outputs (b) for the resistance change shown in Figure 3.20b. The bottom graphs show the performance of the self-sensing methods (c) and complementary filters (d) respectively for the resistance change shown in Figure 3.20c.

Figure 3.22 shows sensorless control of the plunger position under the nominal conditions using the complementary filter outputs as feedback and compares it with an ideal position sensor. When comparing Figure 3.22a with Figure 3.16b, it is seen that the step-tracking performance does not change appreciably when switching from an open-loop measurement to closed-loop position control. From the prior open-loop simulated results, it can be appreciated that the sensorless control abilities of the complementary filter outputs will be limited based on the noise and disturbances present in a physical system. While the magnitude of the noise and disturbances are difficult to predict in a physical system, the prior simulated results suggest that the complementary filter outputs can continue performing well even if various types of noise are present, unlike the individual self-sensing methods. These observations imply that sensorless control using the complementary filter outputs is viable for a physical system with disturbances and this will be experimentally validated in the following section.

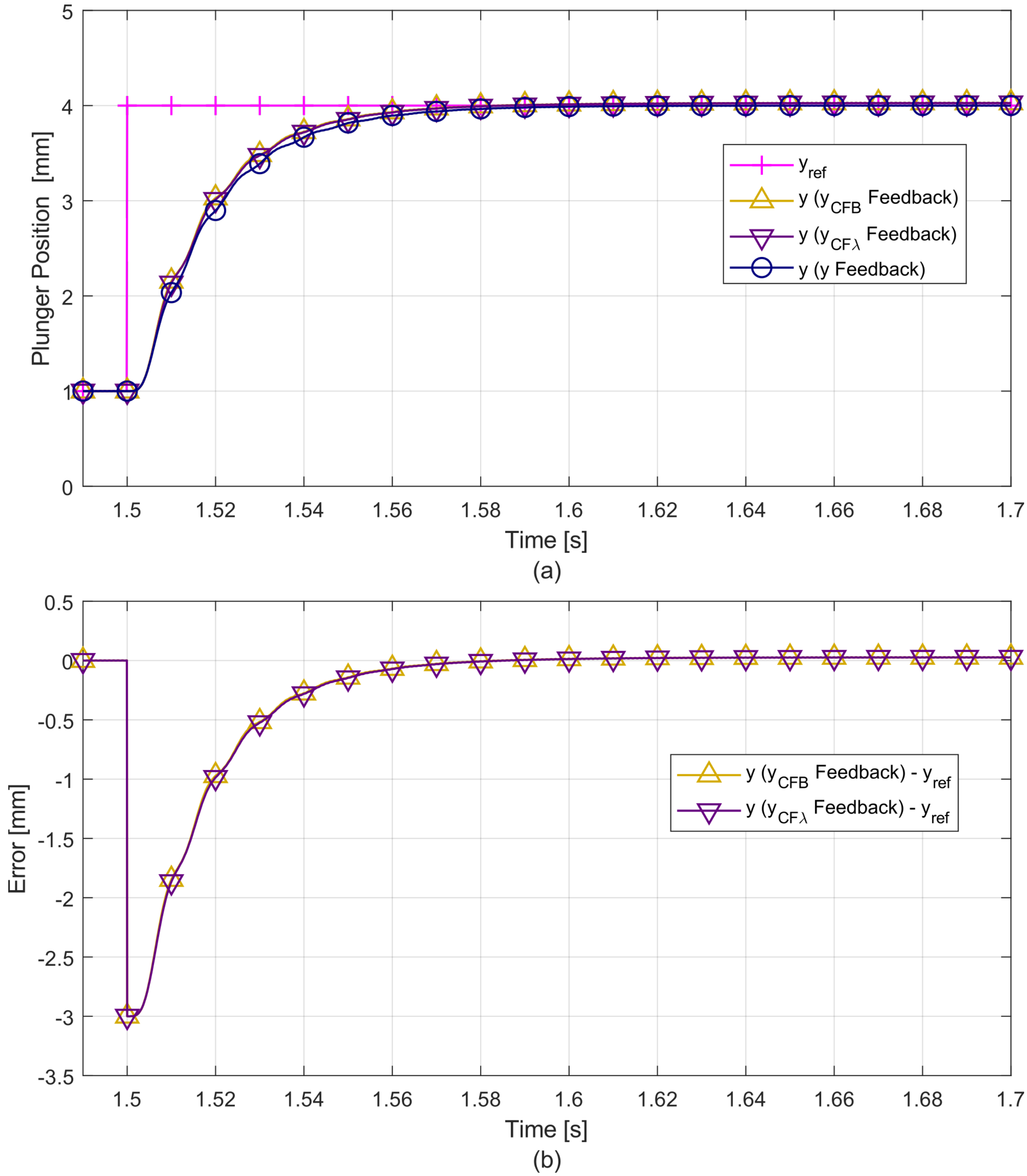

Figure 3.22 Compares the closed-loop plunger position control performance when using the complementary filter outputs as feedback against an ideal position sensor (a). The error relative to the reference trajectory is seen in (b).

3.3 Experimental Validation

This section investigates the real-world performance of a prototype CAS actuator. First, the design and construction of a prototype CAS actuator and the surrounding experimental setup are discussed. Afterwards, the prototype CAS actuator is used to validate the performance characteristics predicted by the analytical models and prior simulated findings.

3.3.1 CAS Actuator Prototype

A prototype CAS actuator was fabricated based on the stator and plunger discussed in Section 3.1. The drawings in Figure 3.2 were used to cut laminations made of M15 29Ga silicon steel with a C5 coating. The laminations were then stacked and bonded with cyanoacrylate glue to achieve approximately a 30mm stator depth and 7mm plunger core height as was used in the simulations. Each of the four stacked stator pieces were then wound with 50 windings each using six parallel strands of 24AWG copper magnet wire. The 200 windings were then soldered together in series so that they would produce the flux directions shown in Figure 3.6 when a positive current is applied.

In order to allow the CAS actuator to be prototyped quickly and inexpensively, a simple bolt-together design was conceived that primarily consisted of 3D printed parts, and readily-available fasteners as seen in Figure 3.23. The components colored in green and blue were 3D printed using a Prusa Mk3 printer with PLA filament. Grade 5 titanium was chosen for the 2mm guide rods and plunger rod due to its nonmagnetic and mechanical properties [132]. The preload screws and end plates were fabricated out of 6061-T6 aluminum due to the nonmagnetic and mechanical properties of aluminum and its low cost [133]. The return springs are WW-53 springs which were procured from Century Spring Corp. These springs are made of 300-series stainless steel with a spring constant of 2.4 N/mm and a 10% tolerance [134]. All of the screws and nuts that fasten the components together are made of 304 stainless steel which is considered a nonmagnetic grade [132]. Overall, the design of the CAS actuator packaging uses nonmagnetic materials to avoid influencing the flux pathways. Furthermore, a substantial amount of distance between the metallic packaging components and the flux pathways was incorporated into the design where possible to reduce the likelihood of eddy currents forming in the packaging components, such as the fasteners. The constructed CAS actuator prototype is show in Figure 3.24. The final outer dimensions are 86mm x 89mm x 165mm with an effective moving plunger mass of 43.5g

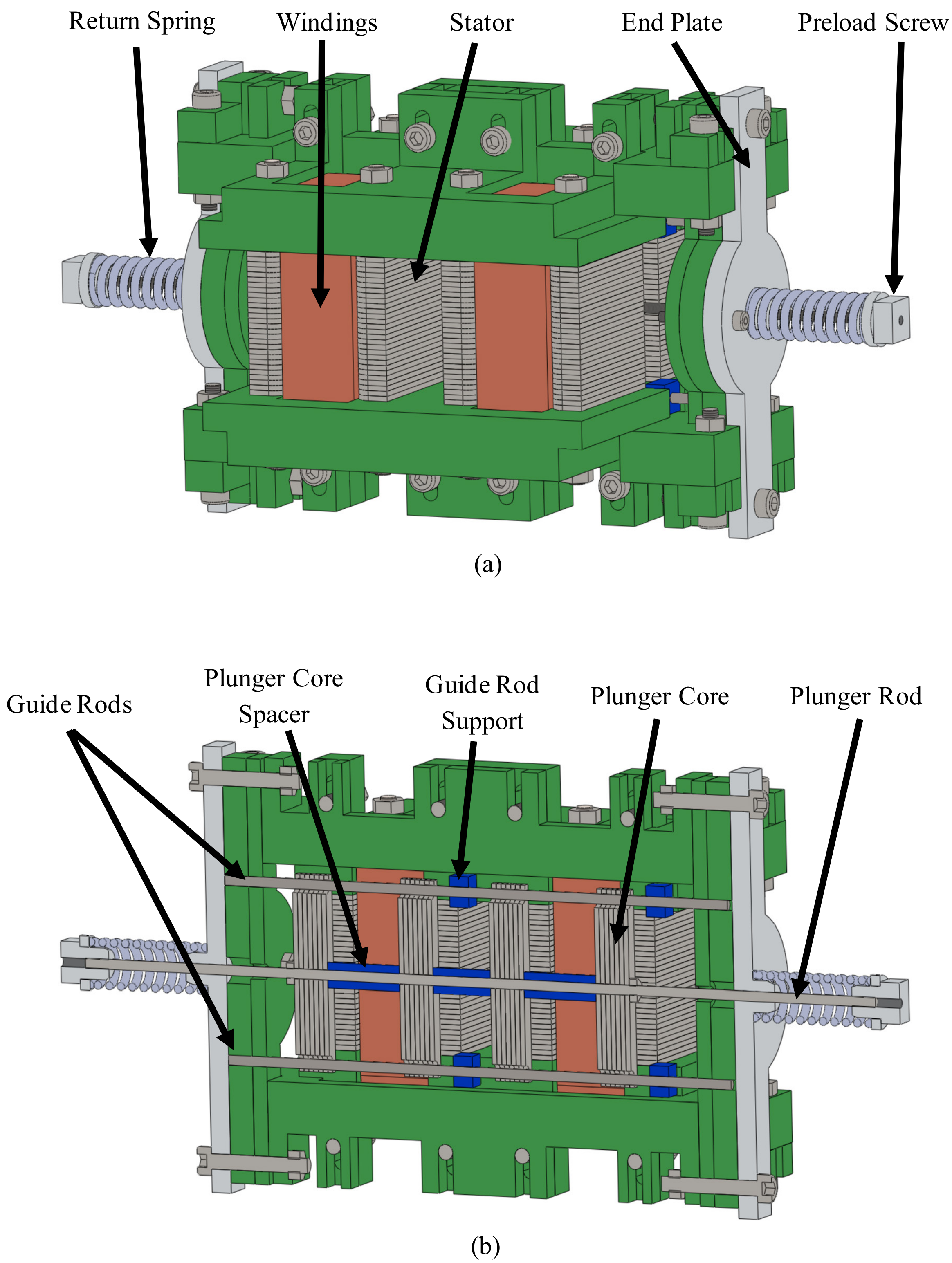

Figure 3.23 A CAD model diagram of the CAS actuator prototype (a), and a cross-section view (b).

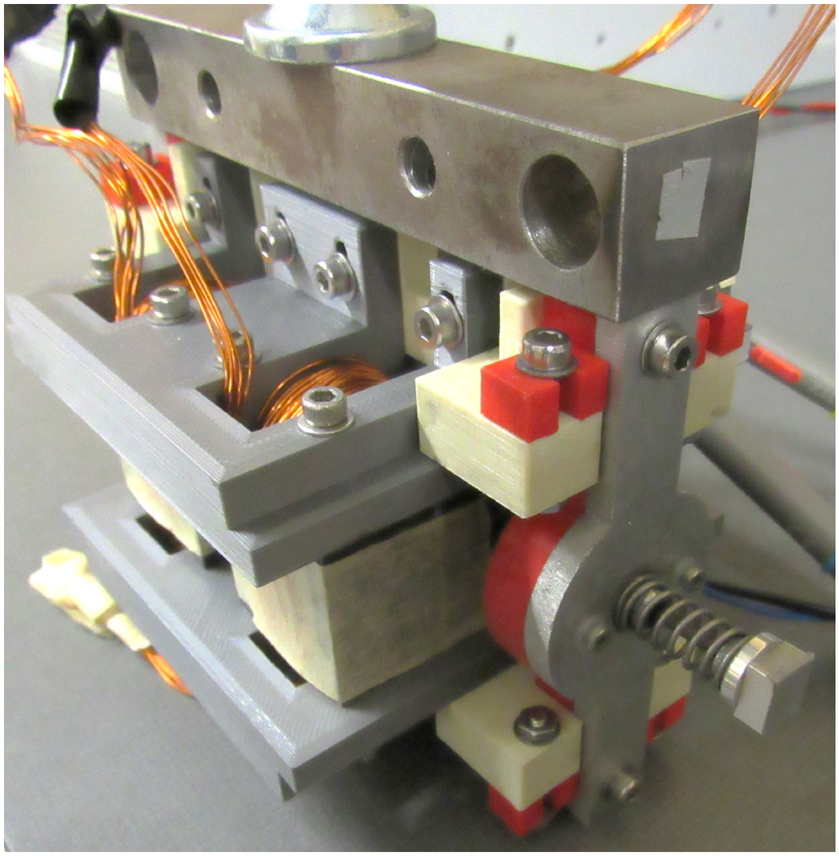

Figure 3.24 Finished CAS actuator prototype.

3.3.2 Hardware Implementation

In order to test the CAS actuator prototype shown in Figure 3.24, several pieces of hardware are required to be connected and configured. A diagram of the hardware and connections are shown in Figure 3.25. A photograph of the physical implementation is provided in Figure 3.26.

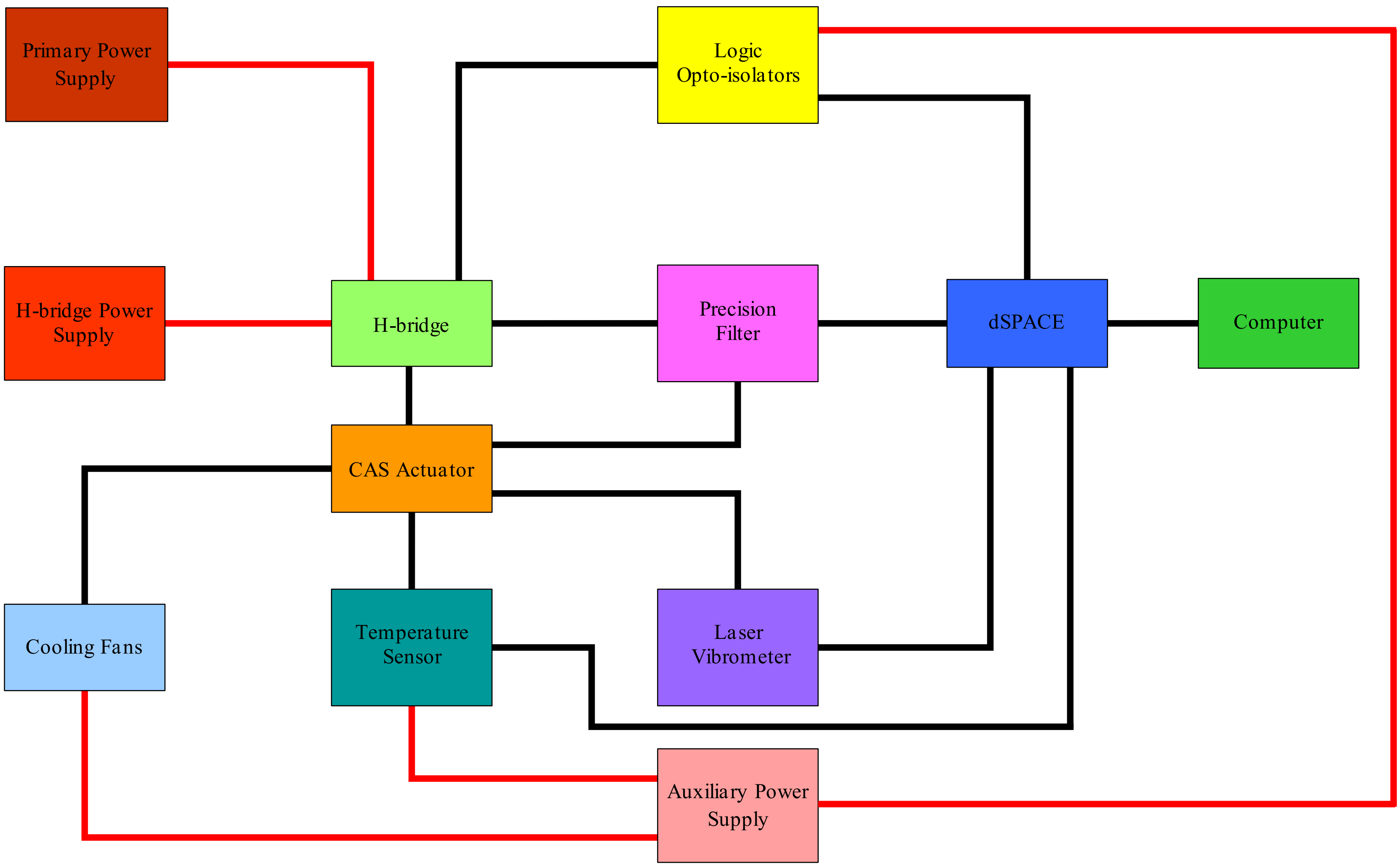

Figure 3.25 A diagram of the CAS actuator experimental setup. The red lines show power supply connections and the black lines show other signal and physical connections.

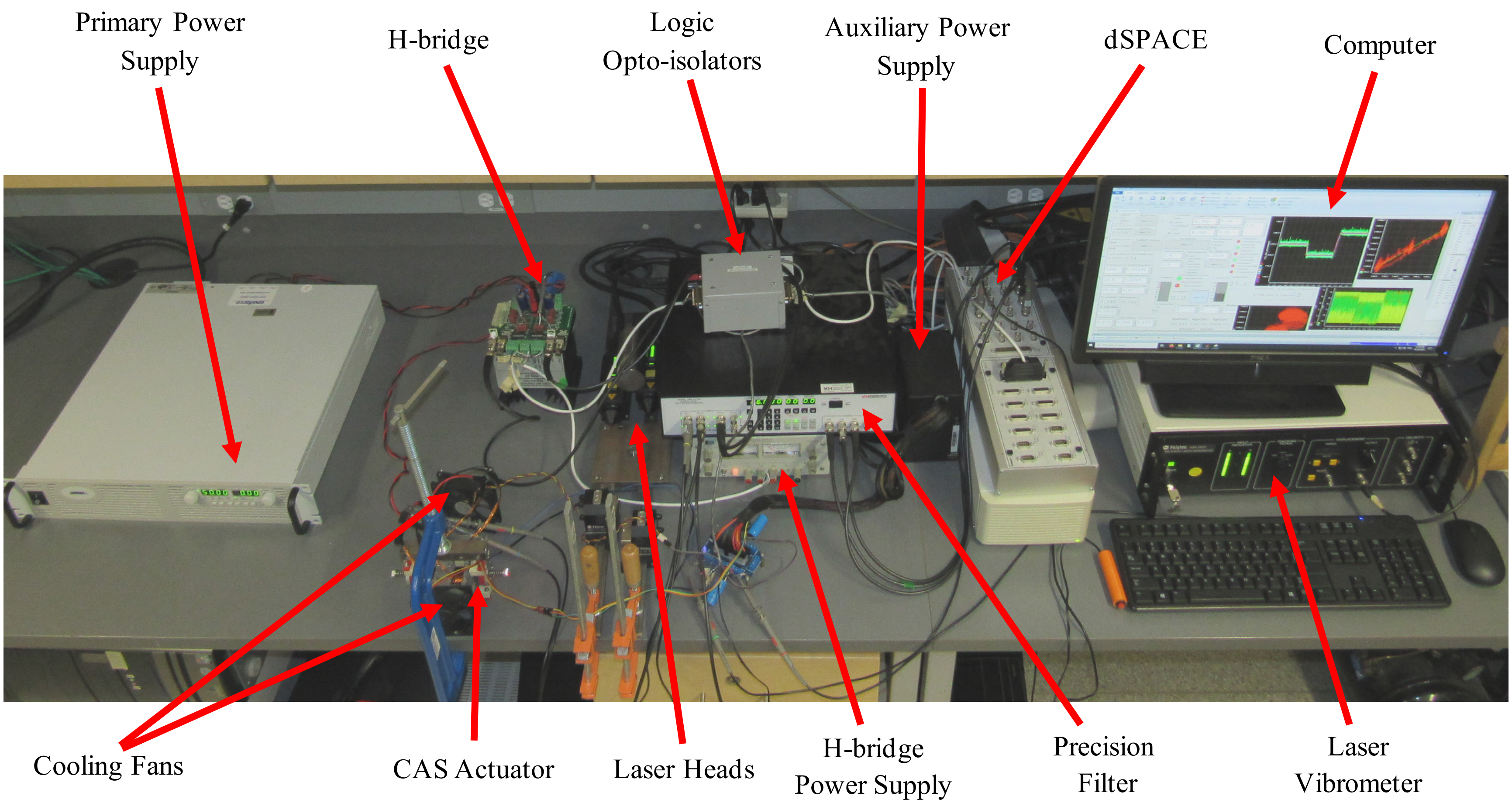

Figure 3.26 A photograph of the CAS actuator experimental setup.

The overall experimental setup is powered by three separate power supplies as seen in Figure 3.25. The primary power supply is a Lambda GEN 60-85-3P208 and is used to power the CAS actuator after being regulated by the H-bridge. The H-bridge power supply is an HP 6236B and is used to provide +5V and +/-15V to operate the IGBT gate drivers. The auxiliary power supply is a Thermaltake TR2-430NL2NC computer power supply. The +12V rail of the auxiliary power supply is used to power the cooling fans and the temperature sensor. The +5V rail of the auxiliary power supply is used to power the logic opto-isolators.

The logic opto-isolators and H-bridge are custom-built circuits that were repurposed from a solenoid-based variable valve actuator thesis project [135]. The opto-isolators are used to protect the dSPACE in the event the H-bridge malfunctions. The H-bridge uses a half-bridge topology with two active insulated-gate bipolar transistor (IGBT) switches and two passive diodes as seen in Figure 3.27. This topology of H-bridge can only supply positive current to the load and is well-suited for a CAS actuator. The maximum supply voltage the H-bridge could handle was never specified in [135]. However, based on a visual inspection, it was noticed that the electrolytic capacitors across the input terminals were only rated to 63V. Therefore, a conservative voltage of 50V was selected. In [135], it is noted that IGBT-1 is bootstrapped as depicted in Figure 3.27. The bootstrapped design requires that the H-bridge be operated below 100% duty cycle to allow the bootstrap capacitor to be recharged. However, [135] did not specify the maximum duty cycle the H-bridge could safely handle and therefore a conservative maximum duty cycle of 95% was chosen. It should be noted that the limited duty cycle and an approximate 4V drop across the IGBTs reduces the effective supply voltage to drive the CAS actuator to approximately 41V [136].

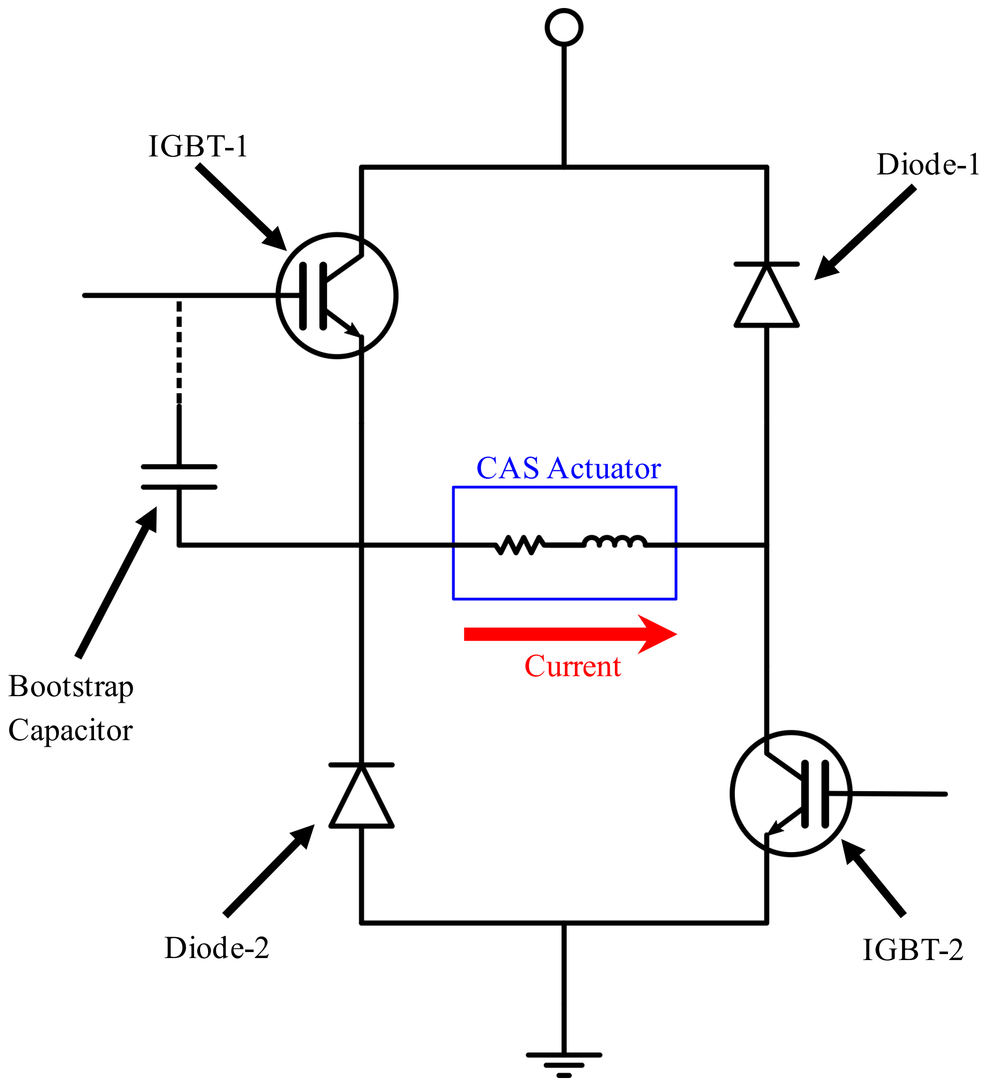

Figure 3.27 Simplified schematic of the H-bridge driver used to operate the CAS actuator.

A dSPACE 1103 is used to command the H-bridge and record data from various sensors. The Simulink simulation discussed in Section 3.2.2 was transcribed into a Simulink program for the dSPACE. The same parameters used in Table 3.1 were used again for the dSPACE program, with the exception of the parameters requiring characterization experiments and the complementary filter center frequency, which was doubled based on the tuning results shown in Appendix A. The H-bridge was specified to be operated with a frequency of 40kHz. The dSPACE sampling frequency was tuned to 32kHz after uploading the Simulink program and monitoring the task turnaround time until it was sufficiently within the capabilities of the dSPACE.

The CAS actuator prototype is monitored with several sensors as depicted in Figure 3.25. A Polytec HSV 2002 laser vibrometer with HSV 800 laser units is used to record the position of the plunger. The laser vibrometer is used as a benchmark to compare the plunger self-sensing methods against. A TMP36 temperature sensor was taped to the surface of one of the copper windings and the voltage produced by the temperature sensor was measured with a P6100 probe on the 1x setting. The voltage at the terminals of the CAS actuator were measured differentially with two P6100 probes on the 10x setting. The current through the CAS actuator was differentially measured using two LEM LA55-P sensors. The method for the differential measurement is shown in Figure 3.28. During the initial CAS actuator tests, it was noted that the H-bridge produced significant ground-plane noise and the differential measurement removed the noise as it was common to both sensors.

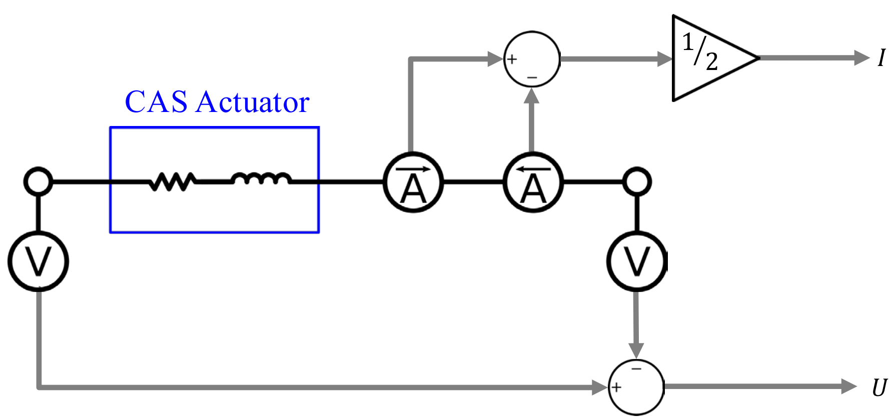

Figure 3.28 A schematic showing how the differential voltage and current measurements were performed.

The average voltage of the PWM waveform outputted by the H-bridge will be equivalent to the reference voltage produced by the current controller. However, the instantaneous PWM waveform has a fundamental frequency of 40kHz and many high-order harmonics due to its rectangular shape. Ideally, the sampling frequency would be as large as possible and greater than the PWM frequency, but this is not achievable with the hardware available to test the CAS actuator. Since the dSPACE sampling frequency is only 32kHz, the 40kHz PWM fundamental frequency and all of its harmonics will alias with the signals required for sensorless control, due to undersampling. Therefore, it is critical that the PWM fundamental frequency and all of its harmonics be removed before being sampled by the dSPACE. A Krohn-Hite 3384 filter was selected to attenuate the PWM frequency components as the cut-off frequencies of the channels can be set very accurately. It is important that the differential voltage and current measurements be passed through filters with identical characteristics to ensure the signals do not acquire an unequal phase-shift. The Krohn-Hite filter channels were configured to operate as eighth-order lowpass Butterworth filters. The cut-off frequencies of the Krohn-Hite filter channels were iteratively tuned and found to perform well at 6kHz. It should be noted that the Krohn-Hite filter must be carefully tuned as setting a low cut-off frequency helps maximize the PWM attenuation, but if the cut-off frequency is set too low then important signals, such as the AC ripple, begin to be attenuated. Ideally, the distance between the lowpass cut-off frequency and the neighboring frequencies shown in Figure 3.29 should be as large as possible to maximize the PWM attenuation, while minimizing the impact on the signals required for sensorless control.

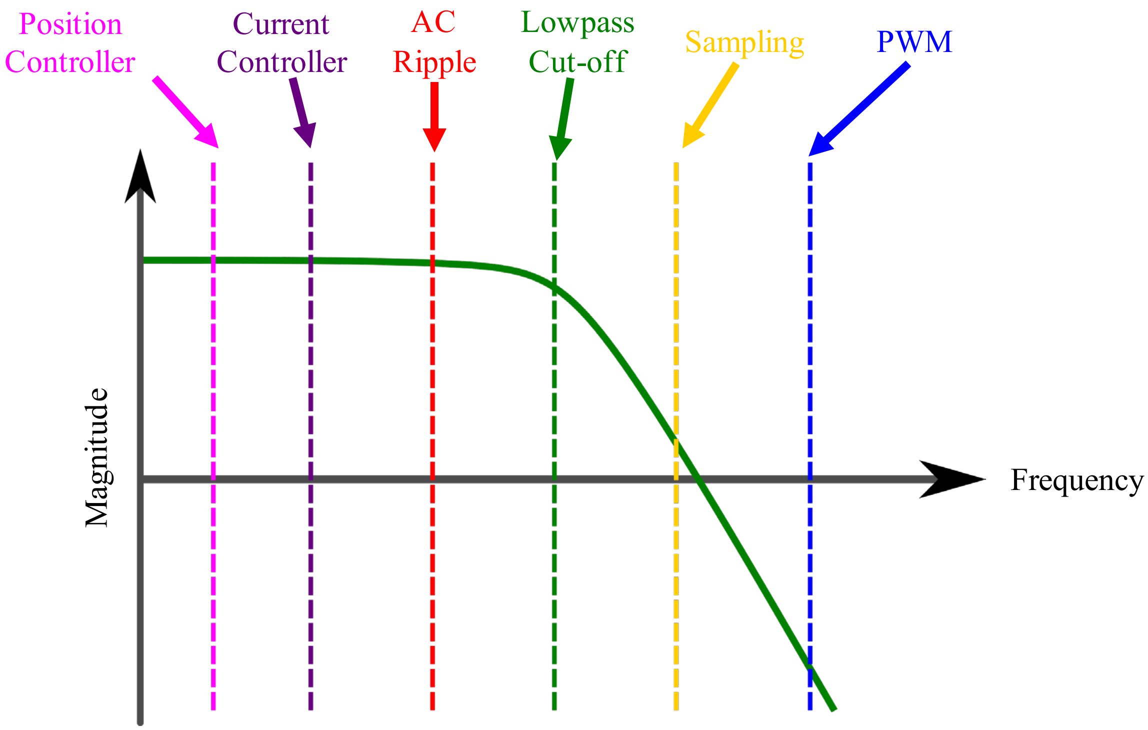

Figure 3.29 Shows the relative location of importance frequencies and if they are passed or attenuated by the Krohn-Hite lowpass filter.

3.3.3 Experimental Results

The following subsections display and discuss experimental results produced by the CAS actuator prototype. First the CAS actuator is characterized to determine its characteristic parameters. Afterwards, the established characterized parameters are used to self-sense plunger position against a laser vibrometer. Finally, the self-sensed measurements are used as feedback for closed-loop position control.

3.3.3.1 CAS Actuator Prototype Characterization

Before sensorless plunger position control can be demonstrated, CAS actuator parameters, such as the inductance-position slope, must first be characterized. In Section 2.3.1 it was explained that an intermediate step within the inductance-based self-sensing method requires inductance to be first calculated. The calculated inductance can be plotted against the plunger position measured with the laser vibrometer to produce an inductance-position mapping. Figure 3.30 shows the AC voltage and current ripple characteristics used to calculate the inductance. The voltage amplitude was chosen based on the tuning observations shown in Appendix A. However, it is important to note that the voltage and current have a sinusoidal shape which indicates the Krohn-Hite filter was effective at attenuating the PWM frequencies.

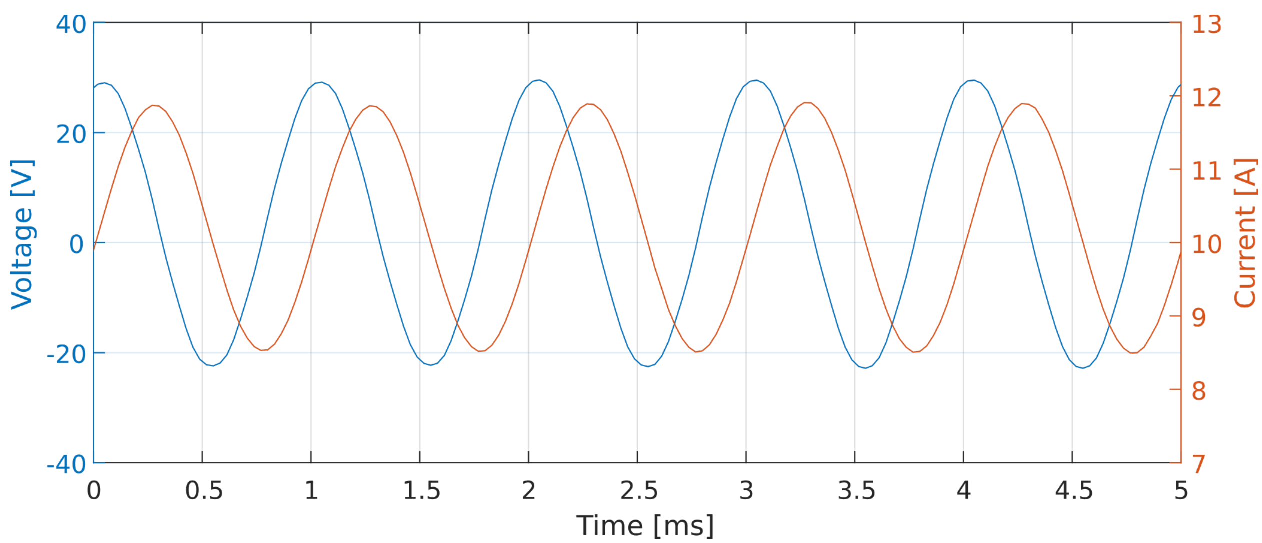

Figure 3.30 Shows the experimentally obtained characteristics of the superimposed voltage and current ripple used to calculate the plunger position of the CAS actuator based on inductance.

In an initial attempt to characterize the inductance, a 10A average current was supplied to the CAS actuator and the plunger was pushed by hand between the end stops as shown in Figure

3.31. The inductance-position map displayed in Figure 3.31d was found to be highly-linear below 5mm of plunger displacement as was predicted based on the simulated inductance-position map seen in Figure 3.9. It should also be noted in Figure 3.31b that the temperature of the windings increased by a fraction of a degree over 8 seconds. Based on the simulated results shown in Figure 3.21, this small temperature change may still have a significant effect on the individual BEMF-based and flux linkage-based methods, but it is expected to have a negligible effect on the inductance-based and complementary filter outputs.

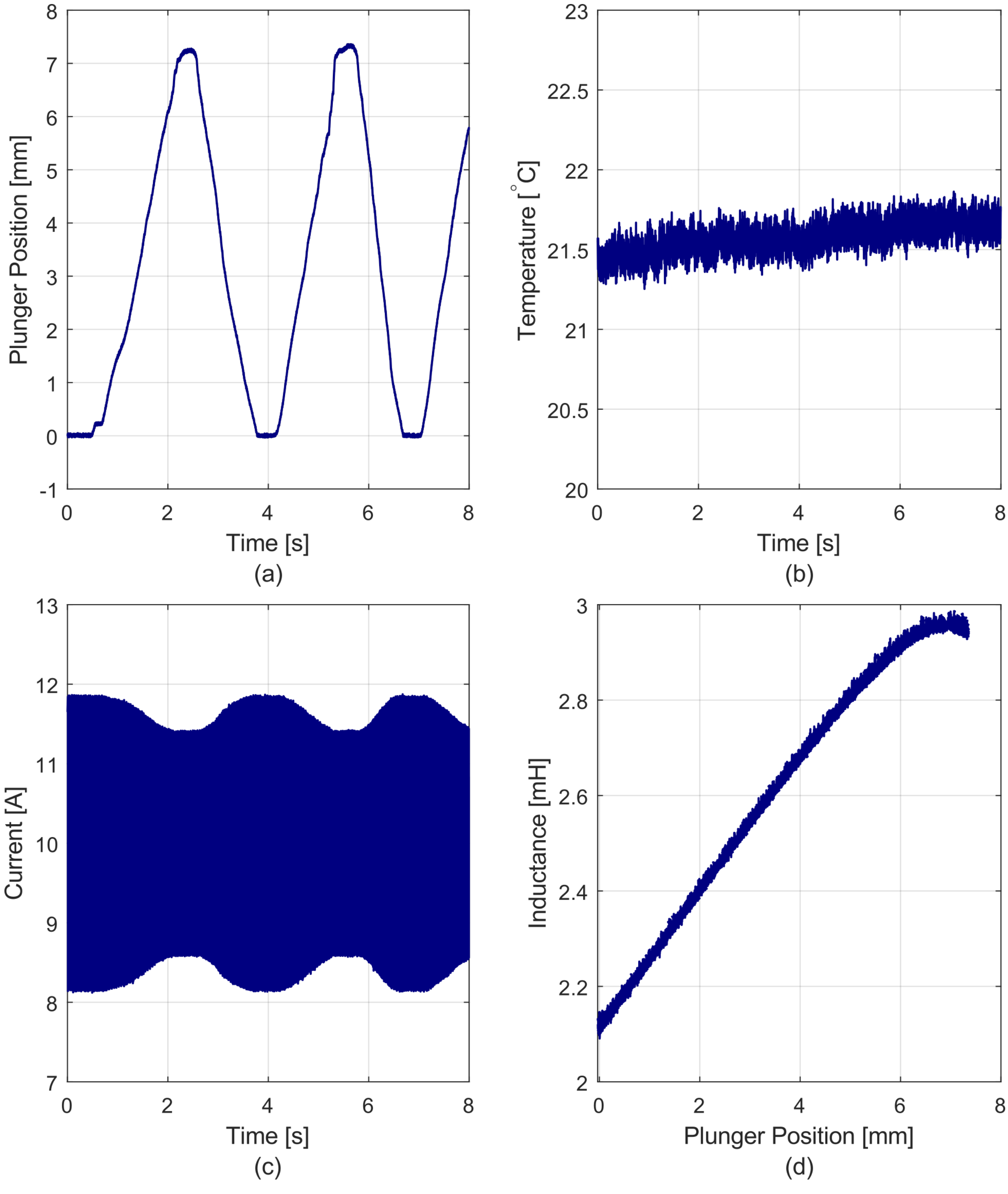

Figure 3.31 Shows the inductance-position characteristics (d) when the plunger is moved by hand (a) with a 10A average current being supplied (c). The temperature increase due to ohmic loss self-heating is displayed in (b).

When performing the characterization experiment in Figure 3.31, it was noticed that the plunger friction increased substantially when 10A was applied. This indicates that the friction is heavily dependent on the current applied. While this is not ideal, it is not surprising considering that a small misalignment of the plunger can lead to substantial transverse forces that cause the plunger to scrape on the guide rods. However, this makes it impractical to characterize the damping with a constant. Therefore, the damping was left to be treated as a disturbance by the controller as was assumed in the lumped-parameter simulation.

When attempting to perform the first self-sensing measurements, it was quickly noted that the inductance-position mapping had a significant dependence on current. When driving the CAS actuator with a sinusoidal current, it was observed that the inductance-position mapping was linear with small currents and displacements, but quickly became nonlinear when large currents were applied. Figure 3.32 shows four different cases when different current profiles were used to drive the CAS actuator. In Figure 3.32i, it is seen that the inductance-current mapping becomes nonlinear when the displacement exceeds approximately 3mm. The loop characteristic of Case 3 and Case 4 are due to the cumulative effects of the inductance-current and friction-current dependencies. The inductance-current nonlinearity was isolated by holding the plunger stationary and applying a sinusoidal driving current as seen in Figure 3.33. It can be noted in Figure 3.33c that the nonlinear behavior significantly increases after approximately 14A and is likely attributable to the B-H curve of silicon steel being nonlinear. While this nonlinearity could be characterized with a lookup table and added to the self-sensing method models to allow for more robust operation at higher currents, it is not required to achieve the goal of demonstrating sensorless control. Instead, the operating conditions of the prototype CAS actuator can be simply restricted to avoid the nonlinear behaviour.

In particular, the maximum reference current in Figure 3.12 was limited to 14A. This allows both the inductance-current and friction-current nonlinearities to be mitigated as both are less significant at lower currents.

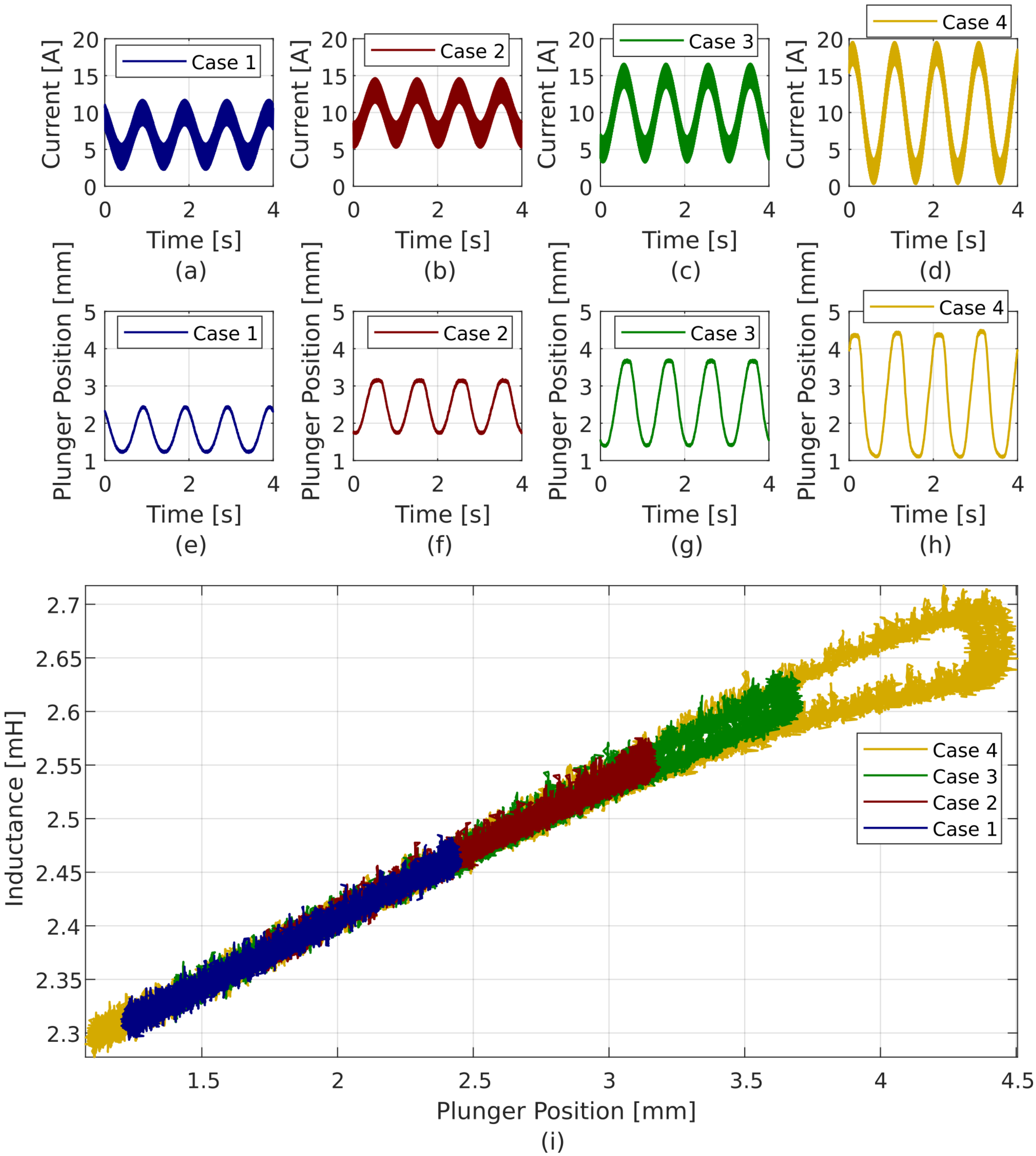

Figure 3.32 (a-d) show different currents being applied the to CAS actuator causing the displacements seen in (e-h) to result. It is seen that the inductance-position profile (i) becomes nonlinear in the large-current cases.

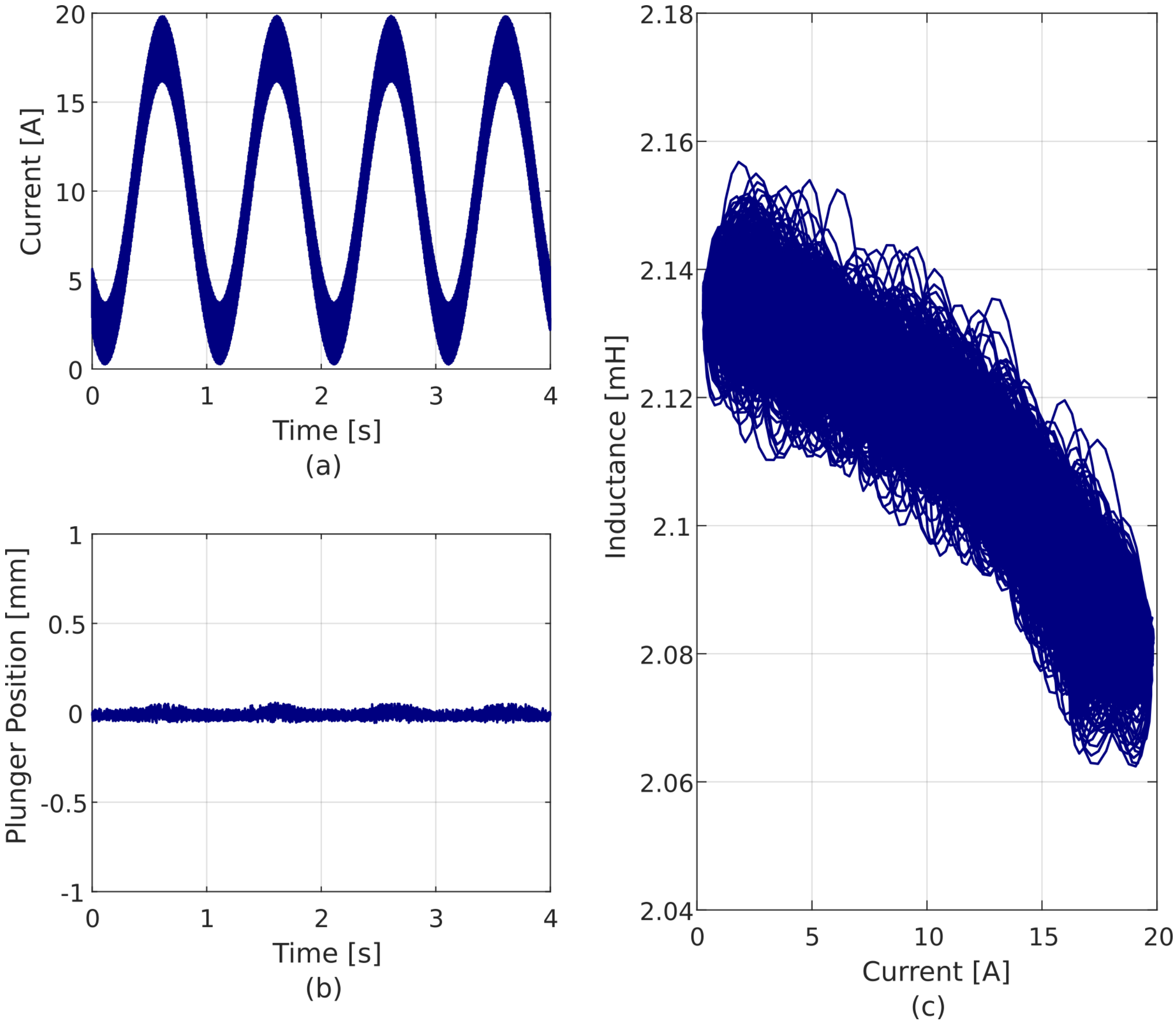

Figure 3.33 Displays the inductance-current nonlinearity (c) when the current is varied (a) and the plunger is held stationary (b).

In Figure 3.32i it was observed that the inductance-position mapping only remained highly-linear up to a plunger position of slightly more than 3mm; consequently, the maximum position must be restricted. Furthermore, it can be noted that the plunger barely returns past 1.5mm even when the current applied is very small. Since the current must never cross zero for the self-sensing methods to remain stable, the minimum position must also be restricted. Therefore, the intended range to demonstrate closed-loop position control was restricted between 2mm and 3mm. The inductance-position mapping over this range was characterized with a linear regression as shown in Figure 3.34. The characterized inductance parameters are summarized in Table 3.2. When compared with the simulated parameters, it is seen that the inductance slope is very similar to the value predicted by the FEA simulation. However, the virtual plunger-stator overlap is quite different from the simulated value. This is likely due to the large tolerances of the bolt-together design since a small change in geometric parameters, such as the air gap length, would have a large effect on the virtual overlap. The online resistance measurement was performed during the inductance characterization experiment and the nominal resistance value is noted in Table 3.2. It is important to recall that the online resistance measurement updates the resistance value on a continuous basis; therefore, the characterized resistance will change with winding temperature. When comparing the nominal simulated and experimental resistances, it is seen that they are relatively similar although the simulated value is larger due to the conservative estimate of the winding half-turns.

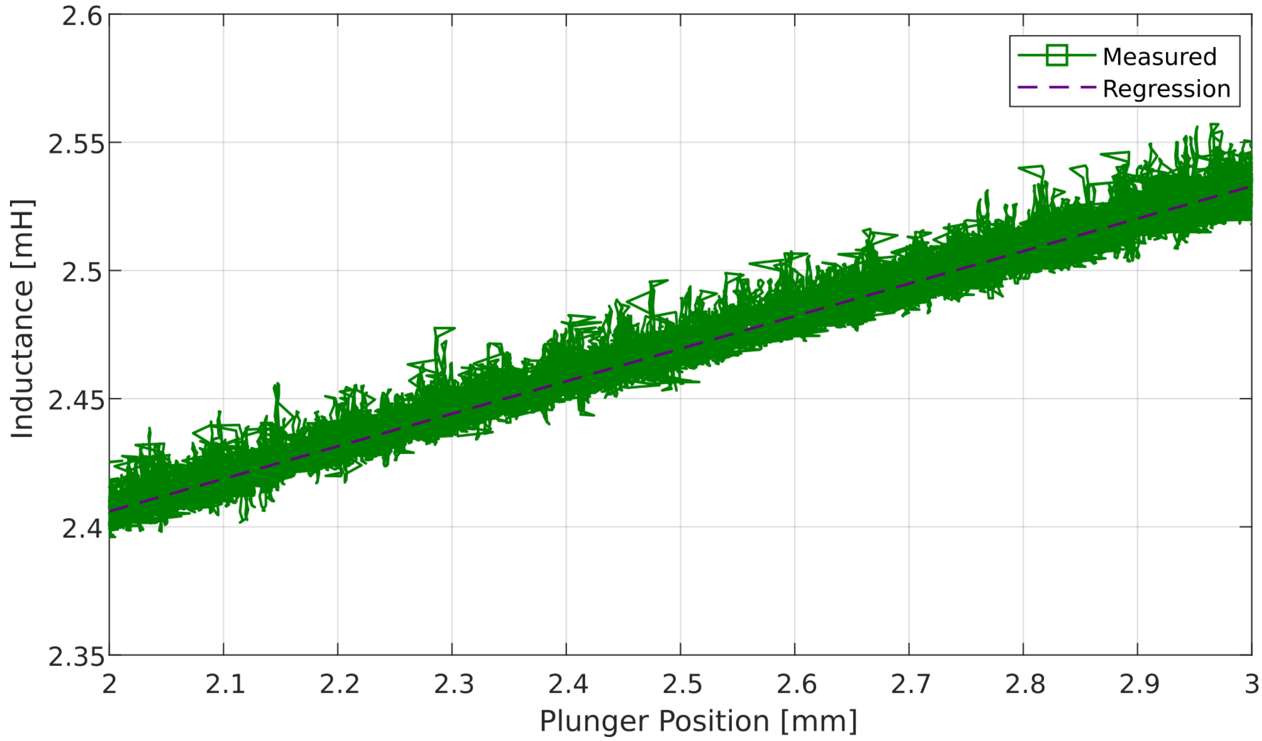

Figure 3.34 Shows the inductance-position profile and regression used to characterize the inductance slope and virtual plunger offset. The correlation coefficient of the linear regression is 0.9926.

Table 3.2 Comparison of Simulated and Characterized Experimental CAS Actuator Parameters

Symbol(s)	Parameter	Simulated	Experimental
C_L	Inductance-position slope [mH/mm]	0.128	0.127
w_o	Virtual plunger-stator overlap [mm]	11.3	17.0
R_T	CAS terminal resistance (nominal) [Ω]	0.38	0.34

3.3.3.2 Plunger Position Self-Sensing

After characterizing the prototype CAS actuator, experiments were conducted to allow the performance of the individual self-sensing methods and complementary filter outputs to be viewed. It is useful to observe the self-sensed measurements open loop to allow the inherent characteristics of the measurements to be understood without introducing additional closed-loop effects.

Furthermore, it is also important to ensure the self-sensed measurements are low-noise and accurate before using them in closed-loop sensorless control where they may lead to instability and damage hardware. Essentially, this section investigates how the self-sensed measurements produced by the CAS actuator compare to the measurement outputted by the Polytec laser vibrometer, which is denoted as y in the subsequent figures.

The results in Figure 3.35 show the individual self-sensing measurement performance when current controlled with a 1Hz and 40Hz driving signal. At 1Hz, it is seen that the flux linkage-based and BEMF-based methods drift and have large amplitude error as they are not well-suited for measuring low-speed plunger movements. Even at 40Hz, which is the intended closed-loop position controller frequency, the BEMF-based and flux linkage-based methods still have significant error and are not suitable to be used by themselves for position control. The inductance-based measurement tracks the laser vibrometer quite well at 1Hz, but is notably noisier than the measurement from the laser vibrometer. Furthermore, the inductance-based measurement shows significant phase lag at 40Hz and therefore performs poorly when measuring high-speed plunger movements as was predicted from the analytical models.

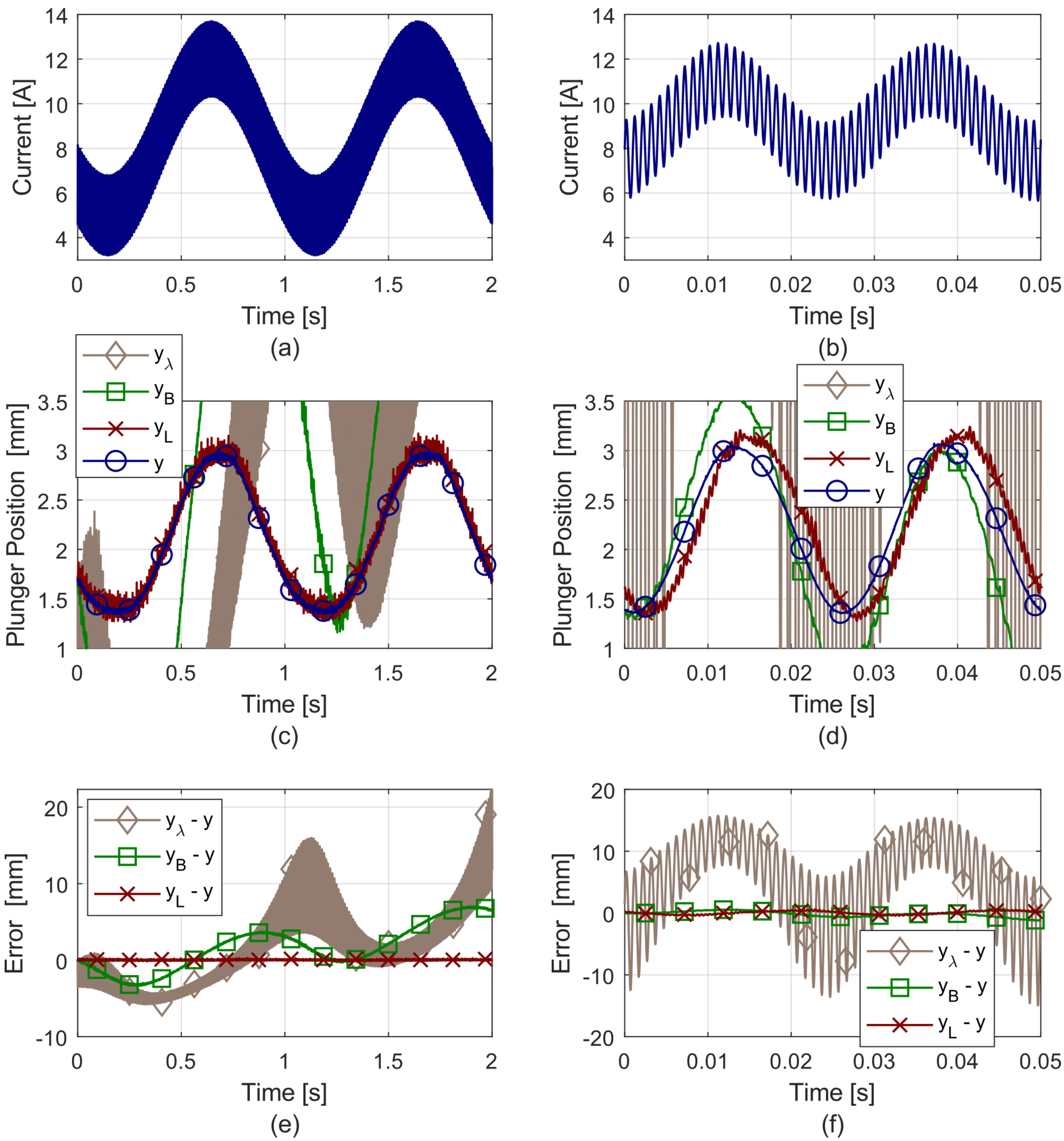

Figure 3.35 Shows how the individual self-sensing methods perform relative to the laser vibrometer when being current controlled at 1Hz and 40Hz. The CAS actuator is driven with the current profiles in (a) and (b) to produce the plunger displacements and measurements in (c) and (d) which results in the errors (e) and (f) that are relative to the measurement produced by the laser vibrometer. The actual plunger position, $\boldsymbol{y}$, is assumed to be the measurement produced by the laser vibrometer.

If the plunger is position controlled using the laser vibrometer for feedback, then the results in Figure 3.36 are produced. The position control results show similar error characteristics in the open-loop self-sensing measurements seen in Figure 3.35. From the lumped-parameter simulation results, such as Figure 3.17 and Figure 3.18, it can be appreciated that the simulation predicted similar error characteristics when high-frequency Gaussian noise was added and when parameters were mischaracterized. Fortunately, the simulation also predicted that the use of a complementary filter would mitigate the effects of the drift, noise and phase lag that are present in the individual self-sensed measurements.

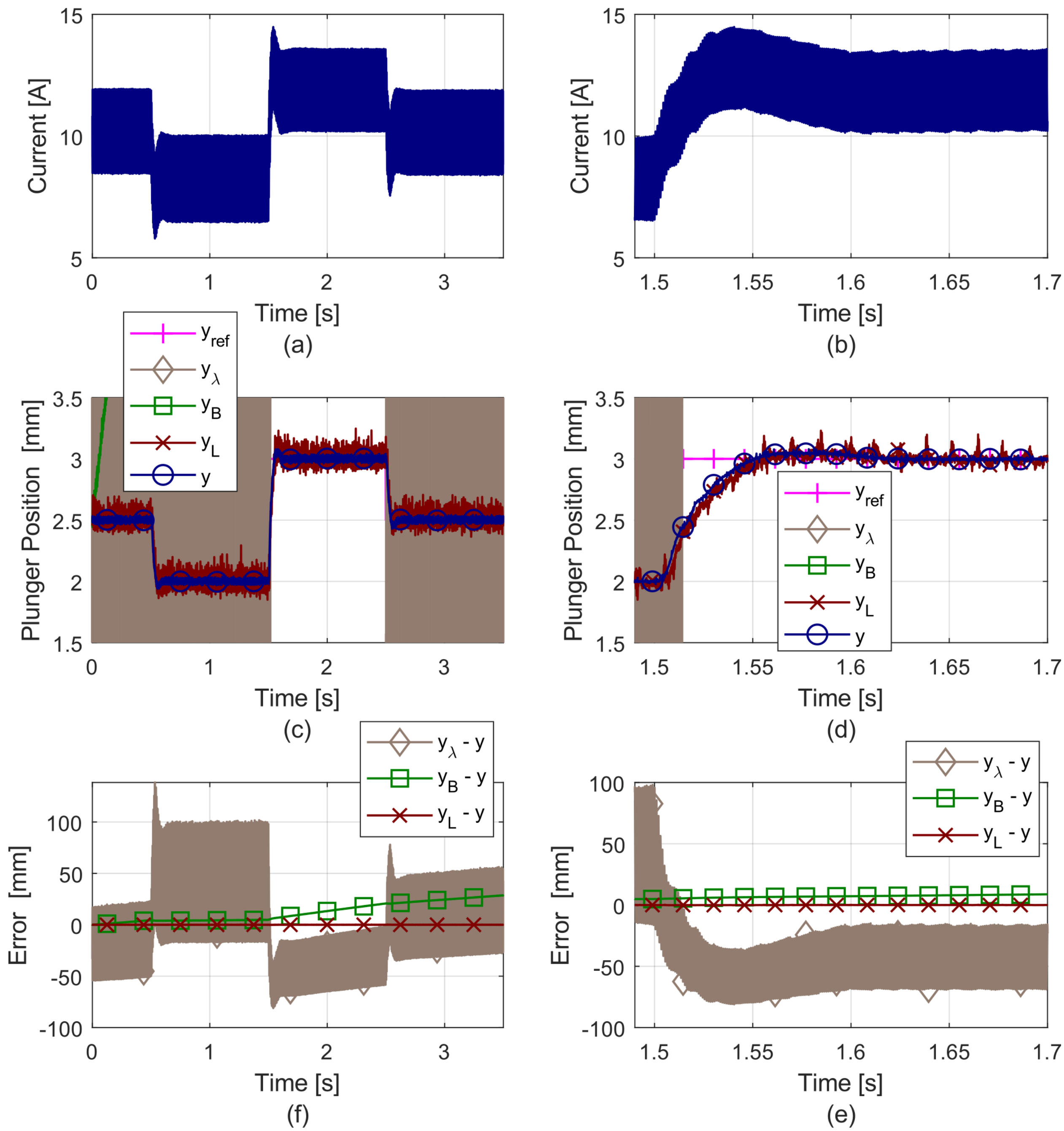

Figure 3.36 Shows how the individual self-sensing methods perform relative to the measurement produced by the laser vibrometer when being position controlled using the laser vibrometer for feedback. The CAS actuator is driven with the current profiles in (a) and (b) to produce the plunger displacements and measurements in (c) and (d) which results in the errors (e) and (f) that are relative to the measurement produced by the laser vibrometer. The actual plunger position, $\boldsymbol{y}$, is assumed to be the measurement produced by the laser vibrometer.

The results in Figure 3.37, show the performance of the complementary filter outputs when current controlled with a 1Hz and 40Hz driving signal. When compared with Figure 3.35, it is seen that the complementary filter outputs significantly improve upon the individual measurements. In particular, the complementary filter outputs do not show the large drift and sinusoidal error seen in the BEMF-based or flux linkage-based measurements or the significant phase lag the inductance-based measurement suffered from at 40Hz. It should be recalled that these significant improvements were also seen in the lumped-parameter simulation results. However, a notable amount of 1000Hz noise remains on the complementary filter outputs as the inductance changes with the AC current ripple due to the inductance-current nonlinearity. Fortunately, a second-order 500Hz lowpass filter on the output of the complementary filter can remove much of this error as seen in Figure 3.38. It is important to note that the lowpass filters have a negligible impact on the underlying position measurement since the cut-off frequency is over an order of magnitude larger.

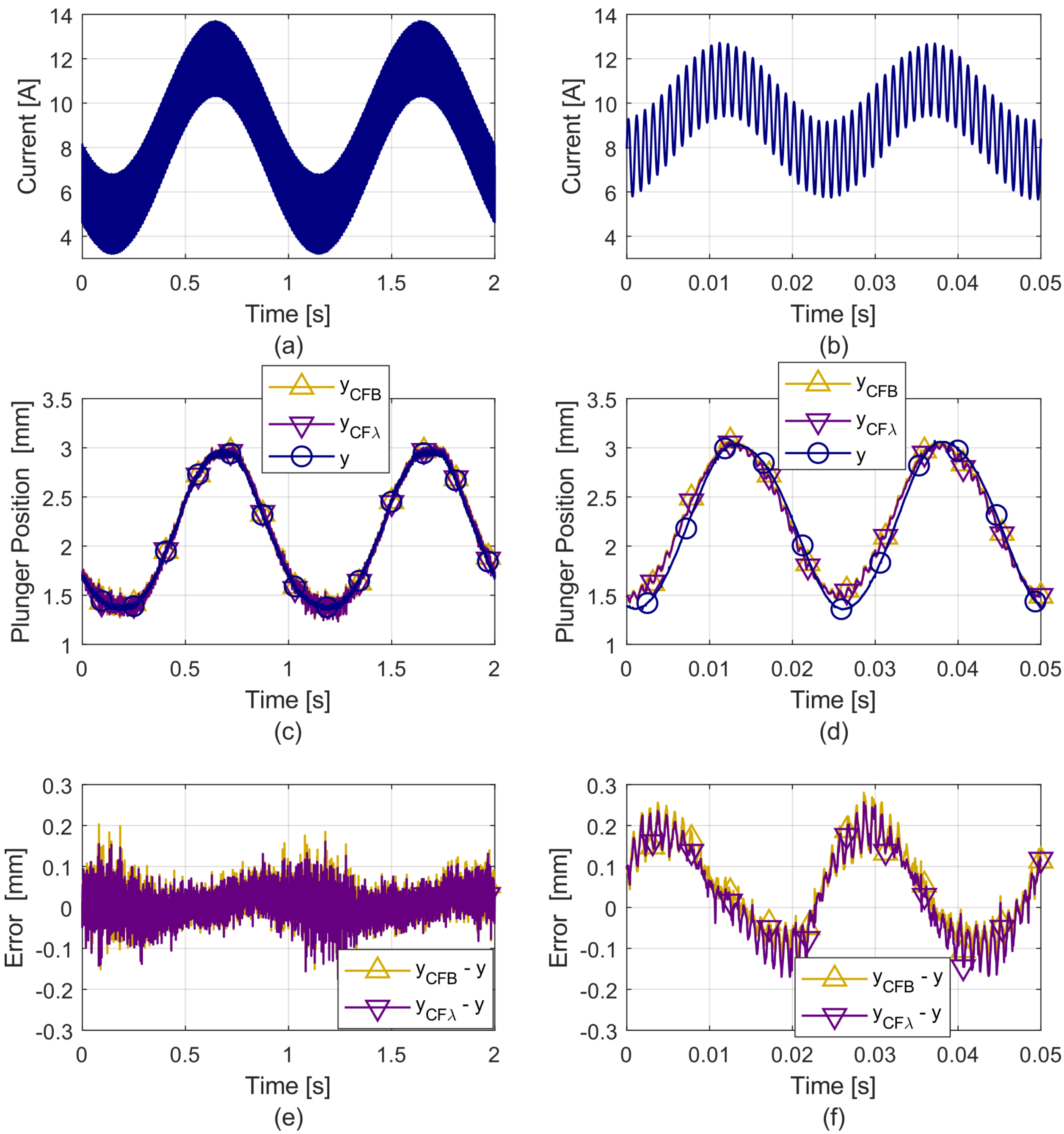

Figure 3.37 Shows how the complementary filter outputs perform relative to the laser vibrometer when being current controlled at 1Hz and 40Hz. The CAS actuator is driven with the current profiles in (a) and (b) to produce the plunger displacements and measurements in (c) and (d) which results in the errors (e) and (f) that are relative to the measurement produced by the laser vibrometer. The actual plunger position, $\boldsymbol{y}$, is assumed to be the measurement produced by the laser vibrometer.

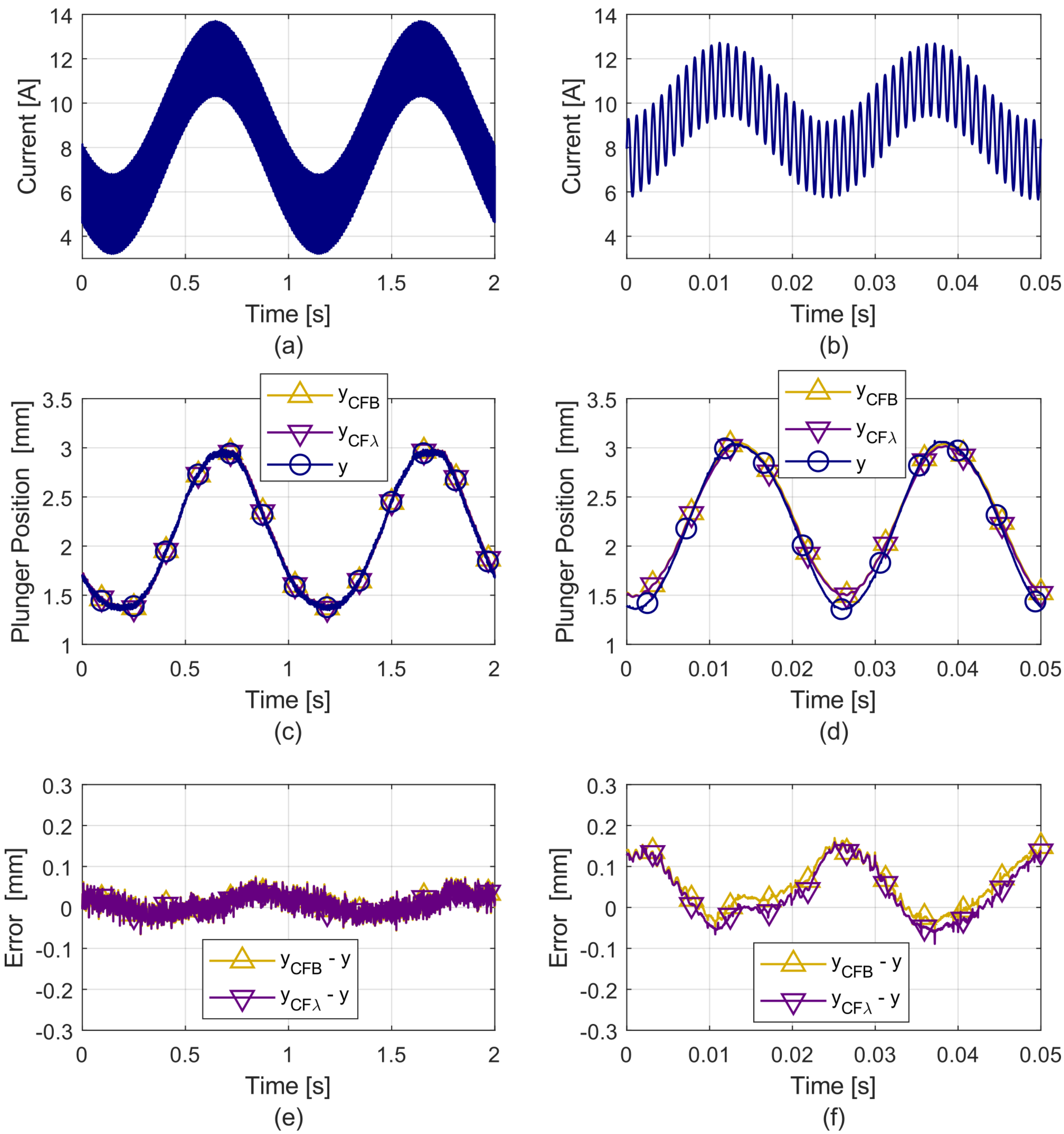

Figure 3.38 Shows how the complementary filter outputs perform after being passed through additional lowpass filters when being current controlled at 1Hz and 40Hz. The CAS actuator is driven with the current profiles in (a) and (b) to produce the plunger displacements and measurements in (c) and (d) which results in the errors (e) and (f) that are relative to the measurement produced by the laser vibrometer. The actual plunger position, $\boldsymbol{y}$, is assumed to be the measurement produced by the laser vibrometer.

Figure 3.39 shows the lowpass-filtered complementary filter outputs for an experiment where the plunger is position controlled using the laser vibrometer for feedback. The complementary filter outputs are shown to accurately track the laser vibrometer measurement with some undershoot as was predicted in the lumped-parameter simulation. The larger undershoot in Figure 3.39 compared to Figure 3.16 is attributable to the higher complementary filter frequency used in the physical experiments. However, these results imply the complementary filter outputs should be suitable for sensorless position control as they have similar accuracy and noise when compared with the laser vibrometer measurement.

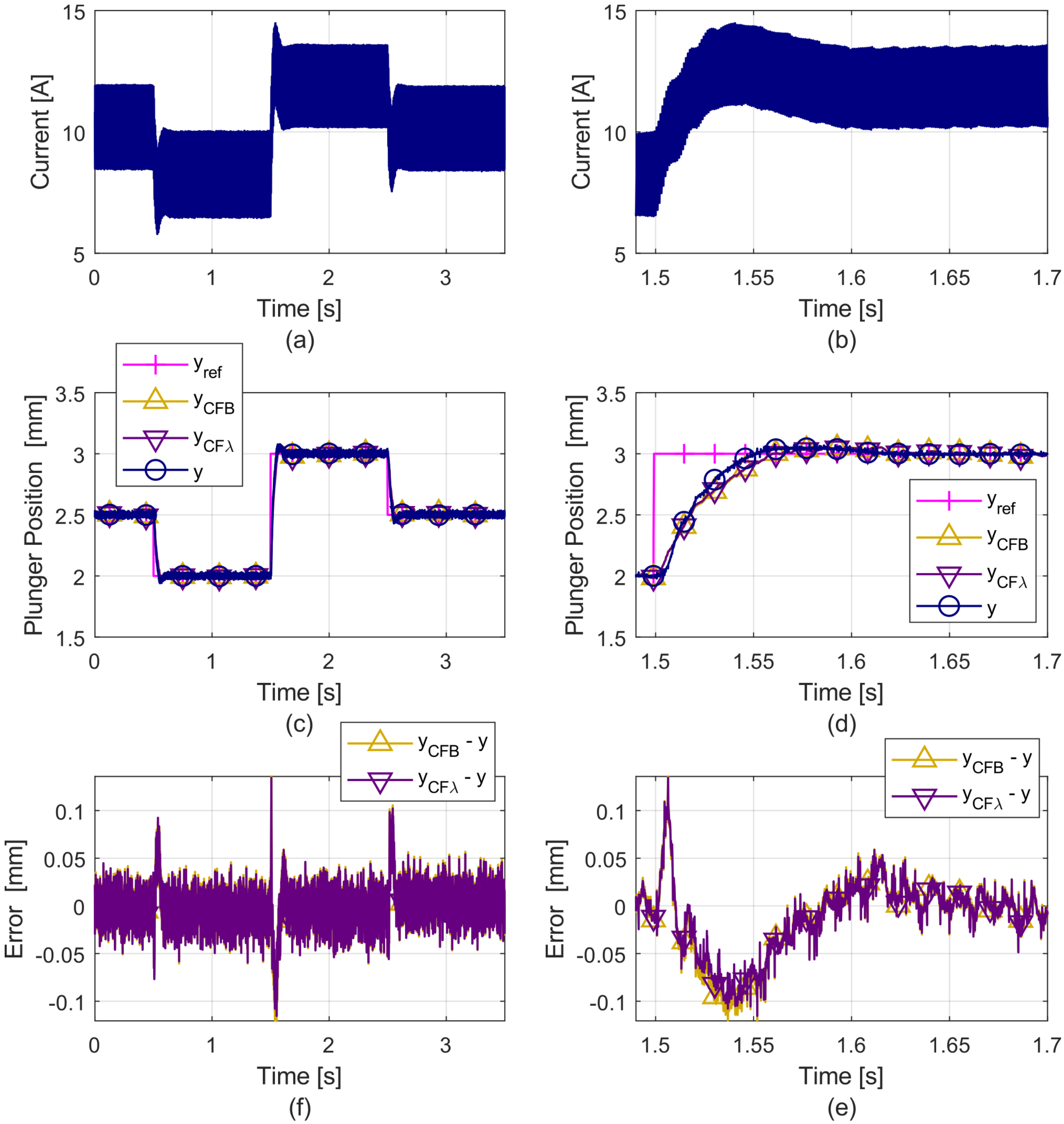

Figure 3.39 Shows how the complementary filter outputs perform relative to the laser vibrometer when being position controlled using the laser vibrometer for feedback. The CAS actuator is driven with the current profiles in (a) and (b) to produce the plunger displacements and measurements in (c) and (d) which results in the errors (e) and (f) that are relative to the measurement produced by the laser vibrometer. The actual plunger position, $\boldsymbol{y}$, is assumed to be the measurement produced by the laser vibrometer.

3.3.3.3 Plunger Position Sensorless Control

In the previous section, the open-loop characteristics of the complementary filter outputs were found to significantly improve upon the individual self-sensing measurements. Furthermore, the complementary filter outputs were found to perform comparably with the laser vibrometer measurements and therefore were feasible candidates for position control over a wide bandwidth. This section investigates the closed-loop sensorless control of the plunger when using the complementary filter outputs as feedback for position control. The sensorless control performance is compared against the closed-loop position control performance when using the laser vibrometer as feedback. Three experiments were run where the feedback for the position controller was switched between the BEMF-based and flux linkage complementary filter outputs and the laser vibrometer. The measurements shown in the plots were recorded with the laser vibrometer.

Figure 3.40 shows a scenario where the CAS actuator attempts to follow a step trajectory. It can be noted that there is a negligible difference between when the BEMF-based and flux linkage complementary filter outputs are used for feedback. Furthermore, it is seen that the sensorless feedback performs similarly with the laser vibrometer feedback, although there is slightly more overshoot. This is expected since the undershoot in Figure 3.39 will lead to overshoot when used as feedback. Overall, Figure 3.40 completes a key objective of this thesis by demonstrating that sensorless control of a physical CAS actuator prototype is possible.

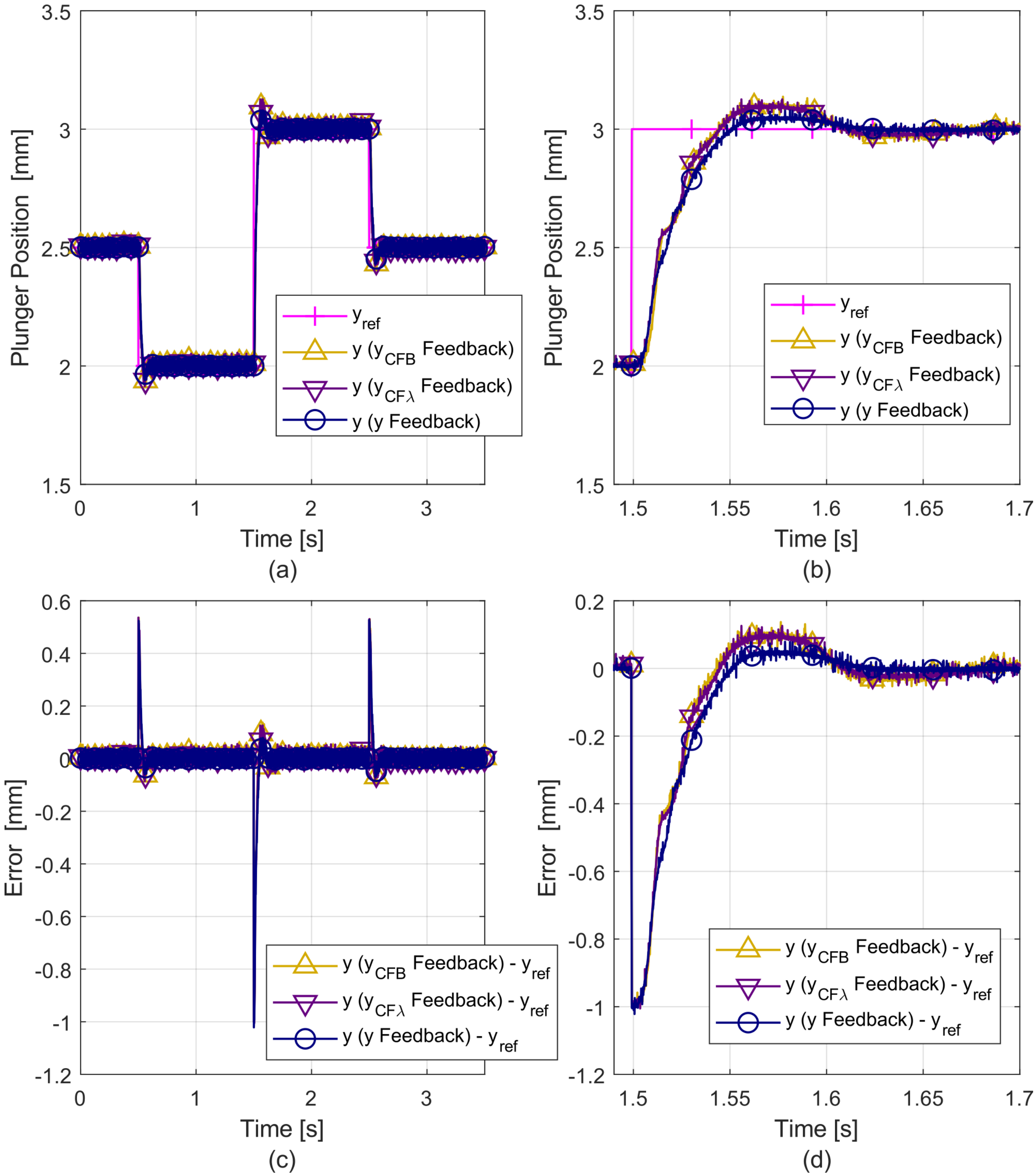

Figure 3.40 Compares the closed-loop plunger position control performance (a) and error relative to the reference trajectory (c) when using the complementary filter outputs as feedback against the measurement produced by the laser vibrometer. The plots (b) and (d) show zoomed-in regions of the step trajectory. The actual plunger position, $\boldsymbol{y}$, is assumed to be the measurement produced by the laser vibrometer.

The prototype CAS actuator can also be demonstrated to follow ramp trajectories using sensorless control as seen in Figure 3.41 and Figure 3.42. Figure 3.41 shows a scenario where the CAS actuator follows a slow 1mm/s ramp trajectory. In this situation, the sensorless feedback methods perform well and there is a negligible difference between them and the case where the laser vibrometer is used as feedback. Figure 3.42 shows a scenario where the CAS actuator follows a fast 10mm/s ramp. During the transient-portion of the ramp trajectory, it is seen that the sensorless feedback also performs nearly as well as the laser vibrometer feedback. However, there is once again more overshoot as was seen in Figure 3.40. Overall, the step and ramp trajectory results demonstrate that the sensorless position control abilities of the CAS actuator are suitable for slow and high-speed plunger movements.

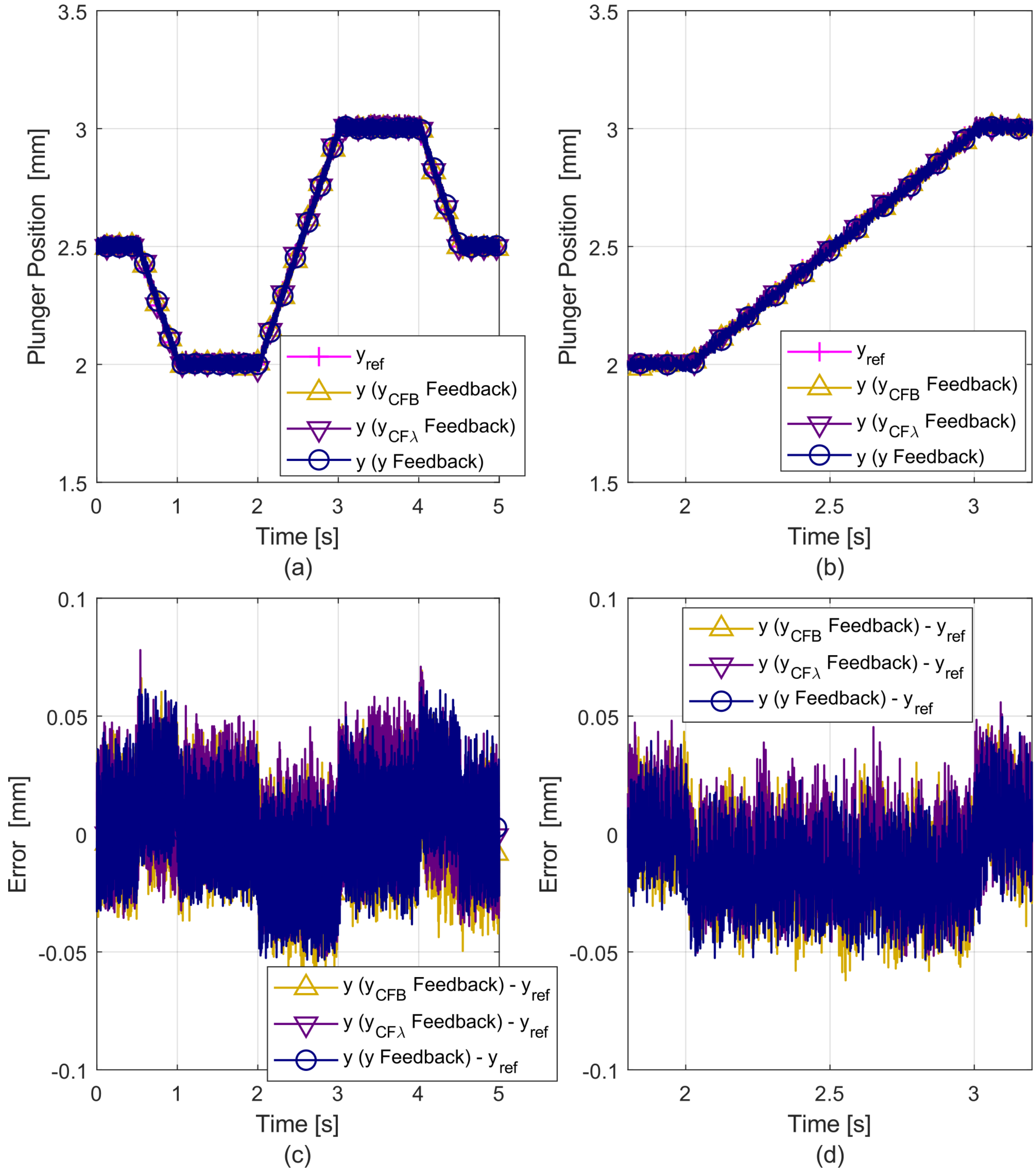

Figure 3.41 Compares the closed-loop plunger position control performance (a) and error relative to the reference trajectory (c) when using the complementary filter outputs as feedback against the measurement produced by the laser vibrometer. The plots (b) and (d) show zoomed-in regions of the slow-ramp trajectory. The actual plunger position, $\boldsymbol{y}$, is assumed to be the measurement produced by the laser vibrometer.

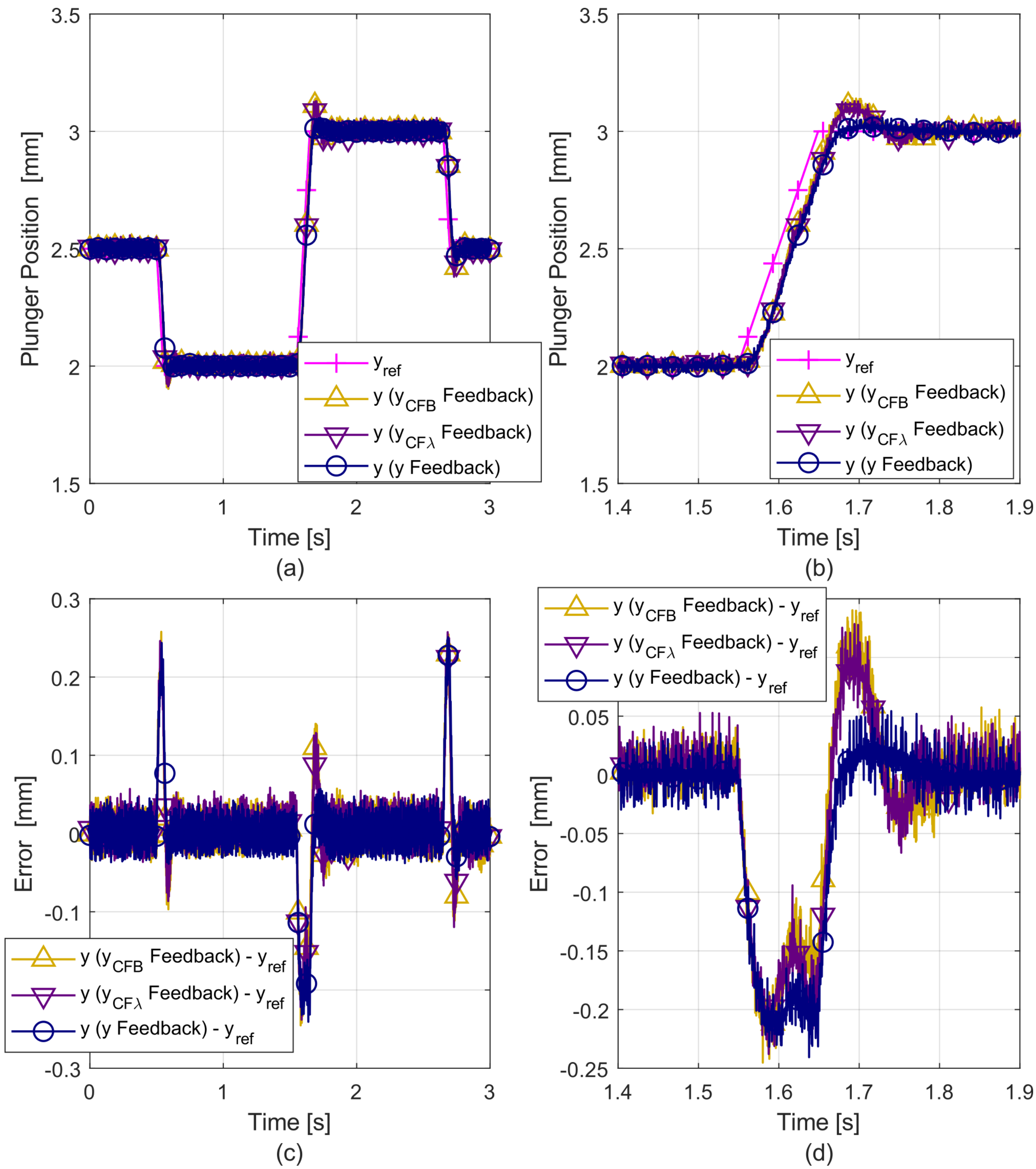

Figure 3.42 Compares the closed-loop plunger position control performance (a) and error relative to the reference trajectory (c) when using the complementary filter outputs as feedback against the measurement produced by the laser vibrometer. The plots (b) and (d) show zoomed-in regions of the fast-ramp trajectory. The actual plunger position, $\boldsymbol{y}$, is assumed to be the measurement produced by the laser vibrometer.

3.4 Summary

In Chapter 3 a proof-of-concept CAS actuator was developed. A bolt-together stacked CAS design was chosen to allow a prototype to be easily fabricated and to enable the design to be converted into a CAS sensor with minor modifications. After selecting a geometry, an FEA simulation was developed that allowed the inductance and force characteristics to be predicted. The results of the FEA simulation showed the CAS actuator had approximately constant force and linear inductance characteristics over its prescribed stroke as was expected from the analytical models developed in Chapter 2. The results of the FEA simulation were then used as lookup table inputs for a Simulink simulation that was built with the CAS actuator models described in Chapter 2. A basic cascaded PID position controller and PI current controller were derived and added to the Simulink simulation. The results of the Simulink simulation revealed that the individual self-sensing methods were quite sensitive to noise and parameter mischaracterization, and therefore would be challenging to use as position feedback for sensorless control. However, it was also shown that the complementary filters robustly removed erroneous aspects of the individual self-sensing methods and produced accurate wide-bandwidth plunger position measurements. The results from the simulation predicted that sensorless control of the CAS actuator plunger should be possible with the complementary filter outputs. The latter part of Chapter 3 attempted to validate the simulated results. Initial characterization experiments revealed inductance-current and friction-current nonlinearities, but were simply avoided by restricting the maximum current. After avoiding the nonlinearities, open-loop experiments were performed that demonstrated the individual self-sensing methods performed poorly relative to the complementary filter outputs, as was predicted in the Simulink simulation. It was then demonstrated that the complementary filter outputs could be used to closed-loop position control the CAS actuator plunger to follow various trajectories.

Overall, the feedback provided by the complementary filter outputs performed nearly as well as the laser vibrometer and only resulted in slightly more position overshoot when tracking high-speed trajectories. In the next Chapter, it is shown that the prototype CAS actuator can be reconfigured into a robust dedicated differential position sensor that possesses the robust wide-bandwidth features of the CAS actuator with additional noise cancelling attributes.

Chapter 4: Design and Validation of a Constant Air Gap Solenoid Sensor

In Chapter 3, a CAS actuator design was investigated that utilized a stacked-CAS design to double the force that would be produced by a single CAS. It is possible to slightly alter the spacing between the stacked stators and plunger cores to produce a pull-pull CAS actuator that is able to pull the plunger bidirectionally as shown in Figure 4.1b. If the coils in the upper and lower CAS in Figure 4.1b are wired in series, then a robust differential sensor is produced that is able to reject common-mode disturbances unlike a CAS actuator. The sections below introduce the premise of a CAS sensor and subsequently design and investigate a proof-of-concept CAS sensor prototype. Initially, the premise of the differential measurement is discussed and analytical equations are derived. Next, the CAS actuator design discussed in Chapter 3 is modified to become a CAS sensor. The CAS sensor characteristics and performance are simulated with FEA and Simulink. In the latter part of the chapter, the investigated CAS sensor design is built and experimentally validated.

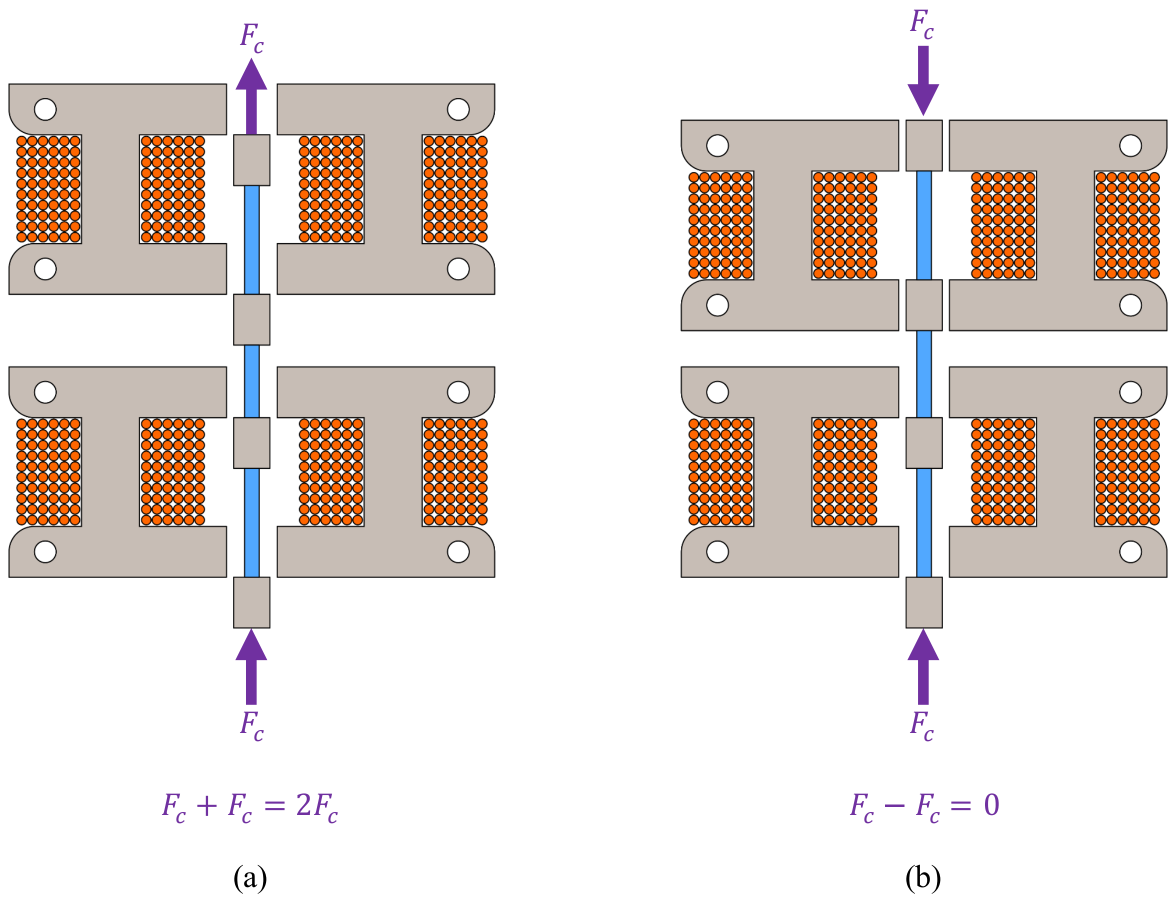

Figure 4.1 Compares the CAS actuator geometry investigated in Chapter 3 (a) with a CAS sensor (b). The purple arrows show the direction of the force exerted on the plunger by each CAS.

4.1 CAS Sensor Premise and Analytical Modeling

In Figure 4.1b, it is seen that the stator-plunger overlap of the top and bottom CAS vary inversely. Therefore, the upper stator-plunger overlap, w_{g1}, and lower stator-plunger overlap, w_{g2}, can be equated after assuming that $w_s = w_p$.

$$w_{g2} = w_s - w_{g1} \tag{4.1}$$

Applying (2.15), (3.3) and (4.1) allows the terminal inductance to be modified.

$$L_t = \frac{N^2 n_p \mu D_g (w_{g1} + w_o)}{2n_s l_g} + \frac{N^2 n_p \mu D_g (w_{g2} + w_o)}{2n_s l_g} \tag{4.2}$$

$$L_t = \frac{N^2 n_p \mu D_g (w_{g1} + w_o)}{2n_s l_g} + \frac{N^2 n_p \mu D_g (w_s - w_{g1} + w_o)}{2n_s l_g} \tag{4.3}$$

$$L_t = \frac{N^2 n_p \mu D_g (w_s + 2w_o)}{2n_s l_g} \tag{4.4}$$

It is evident that the terminal inductance of a CAS actuator is constant since the w_{g1} terms cancel out and all other parameters are constant. The derivative of inductance with respect to position will result in $C_L = 0$ as described in (2.16) since the terminal inductance has no plunger position dependency. When studying (2.43), it is evident that no BEMF will be produced since the inductance slope is zero. At first, this may seem troubling since terminal measurements will not produce an inductive change or BEMF for self-sensing. However, a center tap can be added to the series connection between the upper and lower CAS as seen in Figure 4.2. Voltage measurements relative to the center tap allow the inductance and BEMF information from each CAS to be separately obtained. It is important to note that constant terminal inductance implies that the plunger will not feel a net force since there is no coenergy change with respect to plunger position and therefore $F_c = 0$ as seen in (2.20). This is an important characteristic for a sensor since sensitive mechanical systems could be adversely affected by an external force created by a sensor.

Therefore, the BEMF-based and flux linkage-based measurements can be safely used without producing a force.

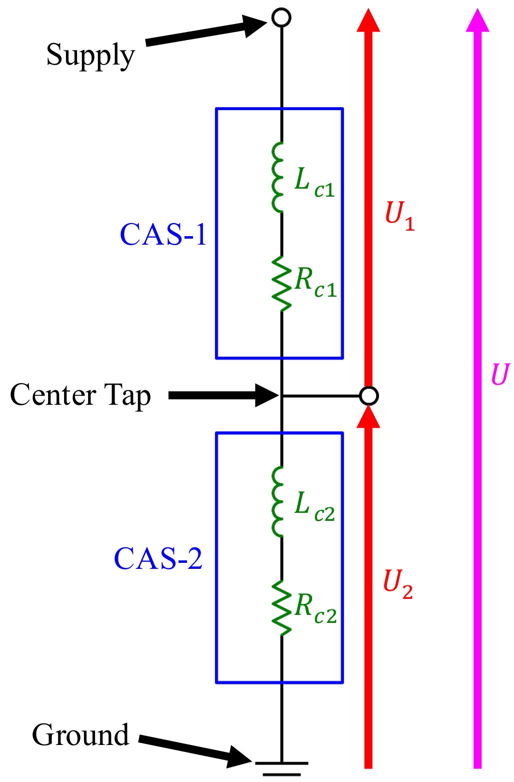

Figure 4.2 Shows how the CAS sensor utilizes a center tap.

Separate self-sensed stator-plunger overlap (position) measurements for CAS-1 and CAS-2 can be produced within a CAS sensor using the methods discussed in Section 2.3. However, averaging the independent measurements produced by CAS-1 and CAS-2 results in a differential plunger position measurement since the w_{g1} and w_{g2} terms subtract.

$$y_d = \frac{w_{g1} + \left(w_s - w_{g2}\right)}{2} \tag{4.5}$$

The differential measurement enables common-mode rejection for all of the self-sensing methods presented in Section 2.3.

To show the common-mode rejection of a differential inductance-based plunger position estimate, we can begin by applying (2.36) to (4.5) assuming that CAS-1 and CAS-2 have the same resistance and inductance characteristics.

$$y_{dL} = \frac{\dfrac{\sqrt{\left(\dfrac{U_{ACRMS1}}{I_{ACRMS}}\right)^2 - R_c^2}}{2\pi f_{AC} C_L} - w_o + \left(w_s - \dfrac{\sqrt{\left(\dfrac{U_{ACRMS2}}{I_{ACRMS}}\right)^2 - R_c^2}}{2\pi f_{AC} C_L} + w_o\right)}{2} \tag{4.6}$$

If resistance is then neglected using Method 1 in Table 2.1, as was proven reasonable in Chapter 3, then (4.6) can be greatly simplified.

$$y_{dL} = \frac{\dfrac{\left(\dfrac{U_{ACRMS1} - U_{ACRMS2}}{I_{ACRMS}}\right)}{2\pi f_{AC} C_L} + w_s}{2} \tag{4.7}$$

It can be appreciated that any common disturbance that affects U_{ACRMS1} and U_{ACRMS2} will subtract and cancel.

The common-mode rejection abilities of a differential BEMF-based plunger position estimate can be shown by combining (2.42) with (4.5), where w_{gp1} and w_{gp2} are the prior stator-plunger overlaps of the CAS-1 and CAS-2 plunger position estimates respectively.

$$y_{dB} = \frac{\int \frac{U_1 - R_c I - C_L(w_{gp1} - w_o)\dot{I}}{IC_L} dt + \left(w_s - \int \frac{U_2 - R_c I - C_L(w_{gp2} - w_o)\dot{I}}{IC_L} dt \right)}{2} \tag{4.8}$$

$$y_{dB} = \frac{\int \frac{U_1 - U_2 + C_L(w_{gp2} - w_{gp1})\dot{I}}{IC_L} dt + w_s}{2} \tag{4.9}$$

From (4.9) it is seen that the CAS-1 and CAS-2 directly subtract and therefore cancel common-mode disturbances. More importantly, it is seen that the resistance terms cancel out. This is a major improvement over the standalone plunger position estimate in (2.42) since drift is greatly influenced by a mischaracterization of the resistance of a CAS. Naturally, this also implies that a differential BEMF-based plunger position estimate will not have a resistance-temperature dependency.

The common-mode rejection abilities of the differential flux linkage-based plunger position estimate can be observed by combining (2.47) and (4.5).

$$y_{d\lambda} = \frac{\frac{\int (U_1 - R_c I)\, dt}{C_L I} - w_o + \left(w_s - \frac{\int (U_2 - R_c I)\, dt}{C_L I} - w_o\right)}{2} \quad \textbf{(4.10)}$$

$$y_{d\lambda} = \frac{\frac{\int (U_1 - U_2)\, dt}{C_L I} + w_s}{2} \quad \textbf{(4.11)}$$

Like the BEMF-based plunger position estimate, the flux linkage-based plunger position estimate subtracts common-mode disturbances through the voltage subtraction. Furthermore, resistance also cancels thereby eliminating the resistance-temperature dependency.

The only parameter that remains in (4.7), (4.9) and (4.11) with the potential for being temperature or age dependent is the inductance slope. However, in Section 2.2 it was noted that the reluctance of a CAS is dictated by its air gap due to the several orders of magnitude separating the permeability of air and electrical steel [123]. Therefore, a change in stator or plunger reluctance due to temperature or aging will produce negligible effects as the reluctance of the air gap predominately defines the inductance slope.

Interestingly, it is seen that characterizing virtual overlap within a CAS sensor is trivial since it gets cancelled by the differential measurements in (4.7), (4.9) and (4.11). This implies that only the inductance slope and maximum stator or plunger tooth overlap need to be characterized, which greatly simplifies the characterization requirements compared to a CAS actuator. However, if resistance continues to be characterized, the CAS can survive a single voltage or current sensor failure. As aforementioned, the terminal inductance of the CAS is constant with respect to position and no BEMF is produced at the terminals. Therefore, if terminal resistance and terminal inductance are known, then the series current or a missing voltage can be calculated based on (2.40).

$$I = \frac{U_1 + U_2}{L_t s + R_t} \tag{4.12}$$

$$U_1 = L_t I s + R_t I - U_2 \tag{4.13}$$

$$U_2 = L_t I s + R_t I - U_1 \tag{4.14}$$

Naturally, (4.12), (4.13) and (4.14) imply that a CAS sensor only needs a combination of a voltage sensor and a current sensor or another voltage sensor. While reducing the sensor requirement by one is attractive from a cost perspective, it is important to note that terminal resistance is required to calculate the missing voltage or current. Therefore, this would reintroduce additional sources of error, such as a resistance-temperature dependency. However, it should be noted that employing Method 3 in Table 2.1 would be beneficial in a two-sensor implementation, unlike a three-sensor implementation, since the resistance could be characterized to account for temperature variation on a continuous basis.

4.2 Simulation Study

A simulation study is presented in the following subsections. The CAS sensor investigated in this study adapts the stacked CAS actuator design in Chapter 3 into a differential sensor by performing the slight alterations shown in Figure 4.1. Furthermore, the same plunger and stator lamination designs shown in Figure 3.2 are reused for the CAS sensor. The CAS sensor design is first imported into an ANSYS Maxwell FEA simulation to determine its force, inductance and field characteristics. Next, these parameters are transferred to a lumped-parameter Simulink simulation to predict its performance as a position sensor.

4.2.1 Magnetic Simulation

An ANSYS Maxwell FEA simulation was configured using many of the same settings discussed in Section 3.2.1. These include using the 2D magnetostatic solver, a balloon boundary condition, and assigning the same built-in materials. Furthermore, the same solver and mesh parametric study was performed. The key difference between the CAS actuator and CAS sensor FEA simulations is the excitation configuration. To enable a faster transient response, the inductance of the CAS actuator in Chapter 3 was small. However, rapid force generation is not a concern for the CAS sensor. Instead, a larger inductance is preferable to enable the CAS to generate a more detectable inductance change and BEMF. However, for a given excitation frequency and excitation voltage, the reactance needs to be kept small enough for the current to be detectable relative to the noise-floor. 250 windings were allocated per stator side, totalling 1000 windings for the entire CAS sensor. An equivalent excitation of 0.5A was configured to be supplied to the series connected windings as this can be produced with the driver discussed in Section 4.3.1. The air gap length was reduced to 0.75mm to reduce fringing and because generating large peak forces is not a concern with the CAS sensor, unlike the CAS actuator.

Field plots of the CAS sensor being operated at various points of its stroke are shown in Figure 4.3. From the figure, it is seen that the maximum flux density generally does not exceed 0.3T and therefore is several multiples away from the saturation limit of silicon steel. Clearly, the amp-turns could be greatly increased at the expense of increased energy losses or the stator size could be reduced to save material. However, spatially optimizing the usage of the magnetic material was not a priority of the investigated design as this is not required to prove the concept and features of a CAS sensor.

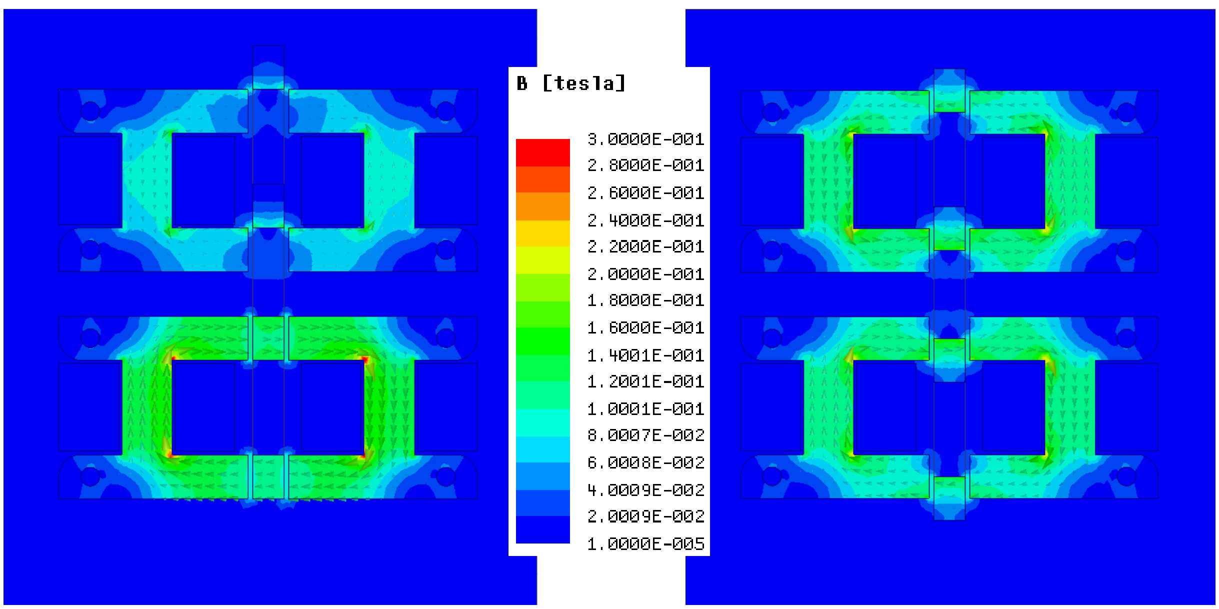

(a) (b)

Figure 4.3 Magnetic flux density plots of the CAS sensor when the plunger is at its topmost position (a) and its middle position (b).

The forces produced by the CAS sensor when energized with 0.5A of current are shown in Figure 4.4. As expected, it is seen that forces produced by CAS-1 and CAS-2 approximately cancel near the middle of its stroke. The net plunger force is negligible over the 2mm to 5mm region, but begins to increase quickly on either side of this region as nonlinear effects, such as fringing, become appreciable. Therefore, the stroke of the CAS should be constrained to operate over the 2mm to 5mm region in order to avoid having its measurement degraded by the nonlinear effects.

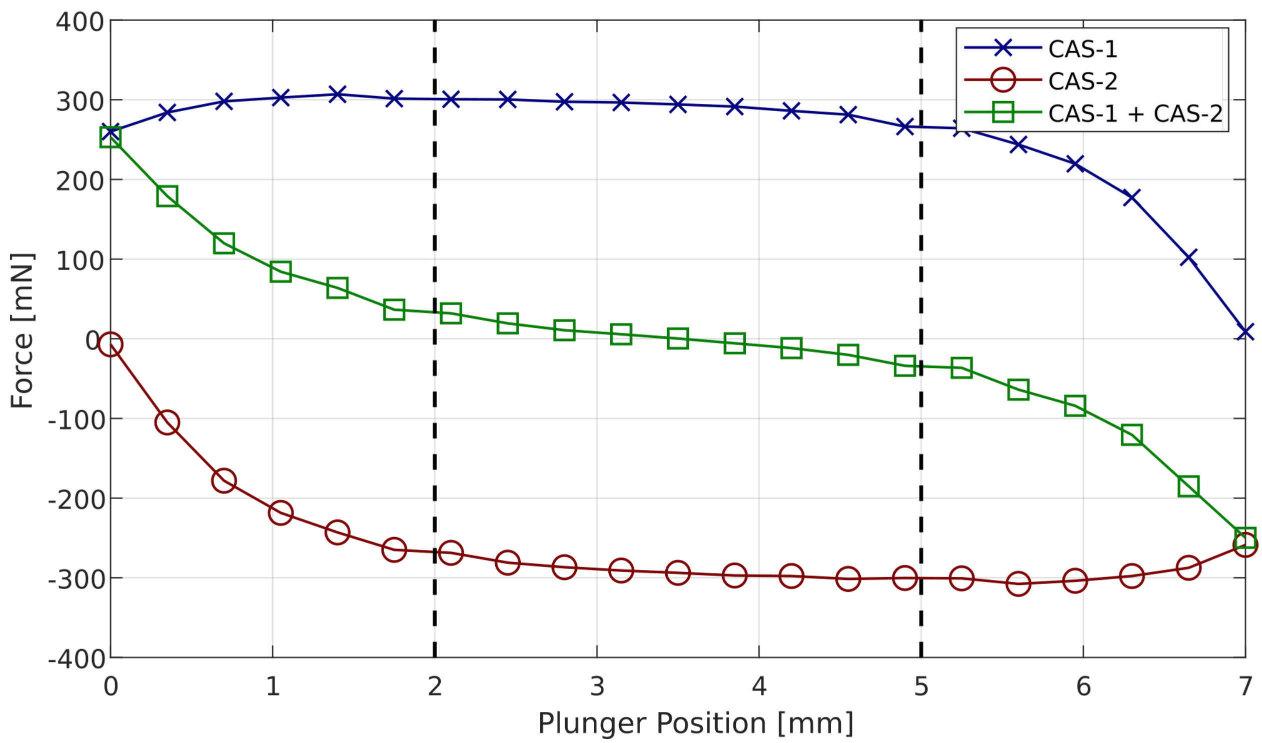

Figure 4.4 Simulated force produced by the CAS sensor over its maximum possible stroke when supplied with 0.5A of current. The vertical dashed lines indicate the prescribed region the CAS should be constrained to operate over to avoid nonlinear performance.

The simulated inductance characteristics from the FEA simulation are shown in Figure 4.5. The CAS-1 and CAS-2 have equal but opposite inductance slopes as expected. When summed, the terminal inductance is approximately constant as was predicted by (4.4). The linearity of the inductance slope begins to degrade near the limits of the stroke, similar to the forces shown in Figure 4.4. This observation further supports limiting the stroke to only operate over the 2mm to

5mm region to maintain a high degree of linearity. Furthermore, constraining the stroke will allow a simple linear regression to be used to map inductance to plunger position. Based on the results shown in Figure 4.5, the slope for CAS-1 can be calculated to be 2.23H/m with a virtual overlap of 10.40mm using a linear regression with a correlation coefficient of 0.9998.

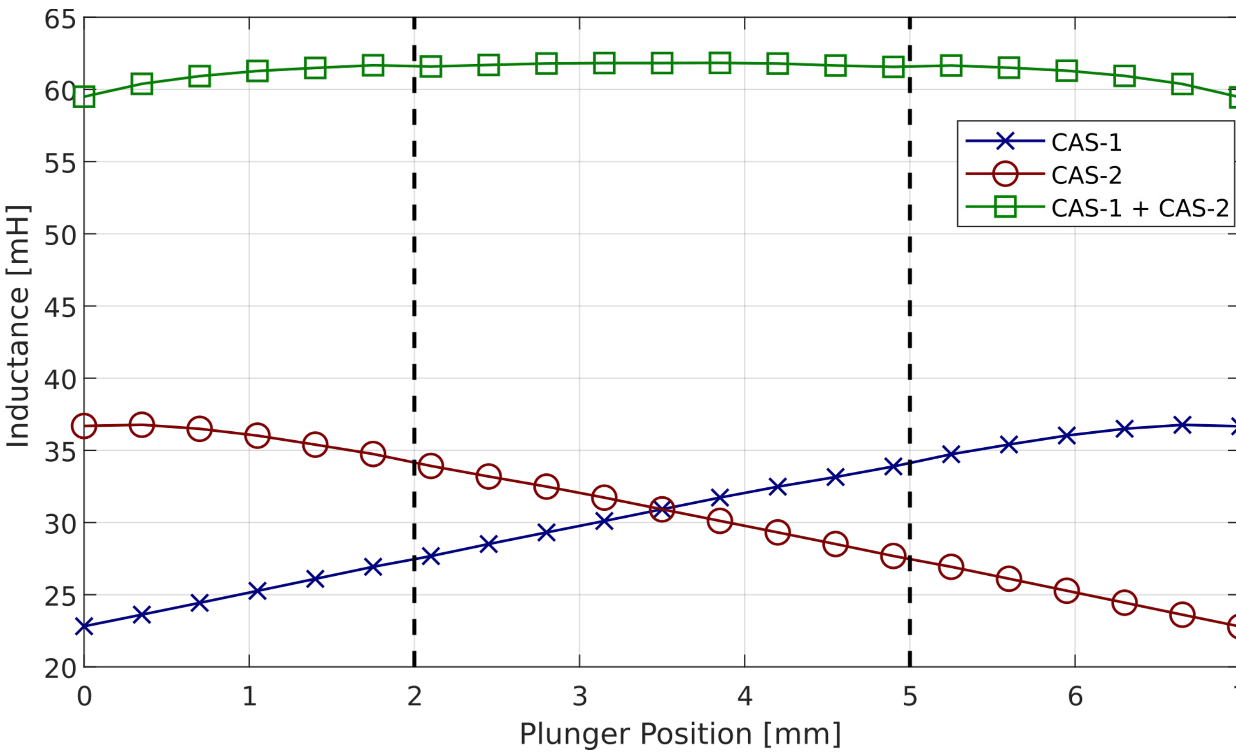

Figure 4.5 The simulated inductance characteristics of the CAS sensor. The vertical dashed lines indicate the prescribed region the CAS should be constrained to operate over to avoid nonlinear performance.

4.2.2 Lumped-Parameter Simulation

The analytical equations derived in Chapter 2 and Section 4.1 can be implemented in a Simulink simulation to predict the position measurement performance of the investigated CAS sensor design. A high-level implementation of the Simulink simulation is depicted in Figure 4.6. The parameters required for the simulation are summarized in Table 4.1. In addition to Table 4.1, the CAS-1 and CAS-2 inductance profiles in Figure 4.5 were imported into the CAS sensor electrical model as lookup tables to capture the nonlinear attributes.

The parameters in Table 4.1 were simulated, calculated or iteratively resolved. The inductance-position slope and virtual plunger-stator overlap were found in Section 4.2.1 by applying a linear regression to Figure 4.5. The terminal inductance was measured at the 3.5mm location of Figure 4.5. The resistances of the CAS-1 and CAS-2 were calculated using (2.24) where N=500, $\rho_r = 16.8$ nΩ·m, D_g=30mm, l_{ht}=15mm, A_w=266mm^2 and C_{ff}=30%. A fourth-order bandpass filter was selected to ensure strong isolation of the superimposed voltage and current signals. The AC and DC input voltages were selected based on the available hardware to experimentally validate the simulated findings. The complementary filter center frequency and damping ratio were iteratively tuned until sufficient performance was obtained. The maximum stroke was established by the stator tooth width of the laminations. The simulation uses the built-in ode5 (Dormand-Prince) solver with a fixed-timestep duration of 10μs.

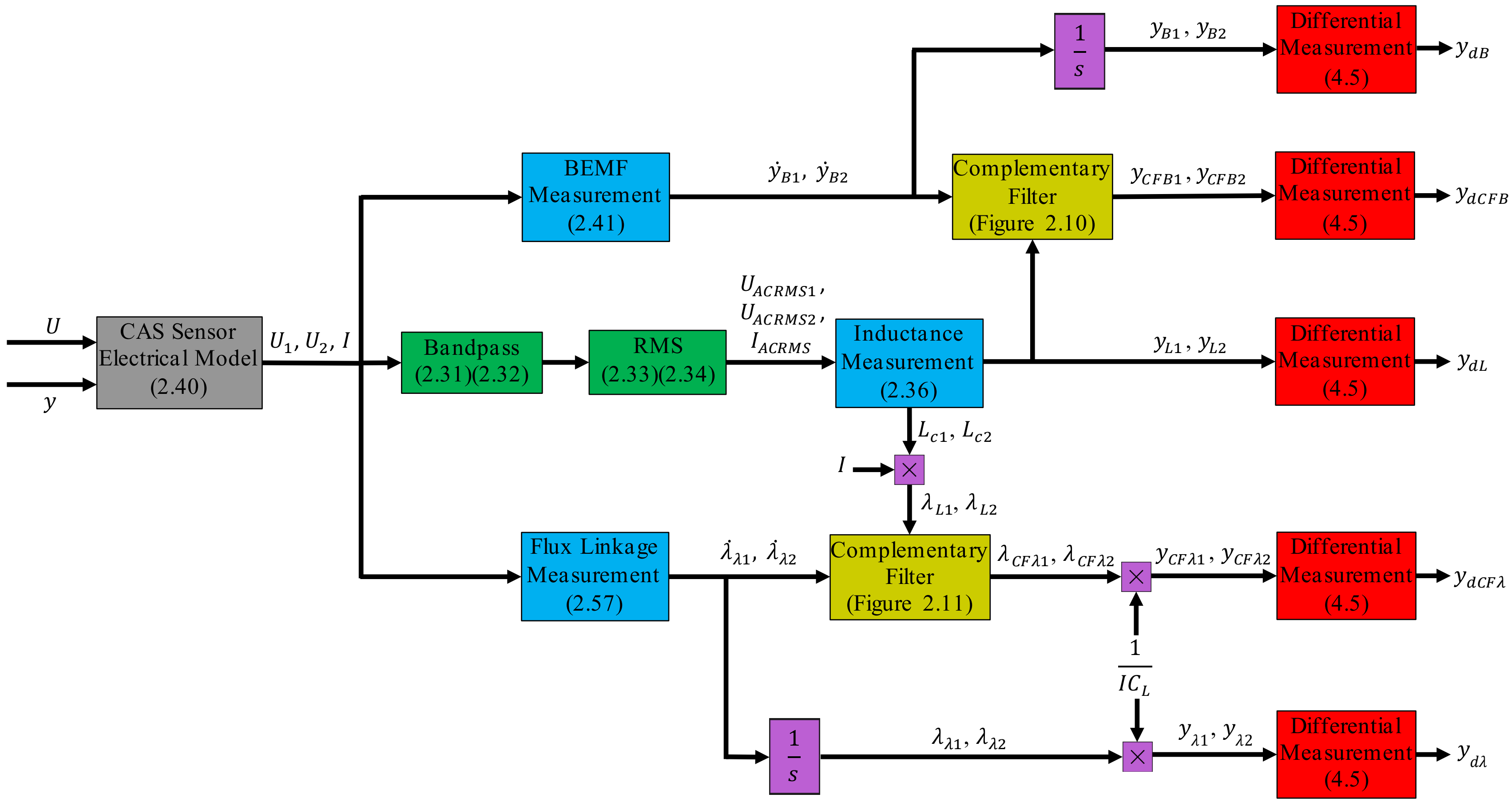

Figure 4.6 High-level block diagram of the CAS sensor lumped-parameter simulation.

Table 4.1 CAS Sensor Lumped-Parameter Simulation Input Parameters

Symbol(s)	Parameter	Value
C_L	Inductance-position slope [mH/mm]	2.23
w_o	Virtual plunger-stator overlap [mm]	10.38
L_t	Terminal inductance [mH]	61.83
$R_{c1} = R_{c2}$	CAS resistance [Ω]	4.74
n_{BPF}	Bandpass filter order	4
Q_{BPF}	Bandpass filter qualify factor	1
U	Input voltage [V]	4 (DC) + 8 (AC)
f_{AC}	Superimposed AC voltage frequency [Hz]	1000
f_{CF}	Complementary filter center frequency [Hz]	3
ζ_{CF}	Complementary filter damping ratio	0.5
w_s	Maximum stroke [mm]	7

The input voltage and resulting current produced by the CAS sensor simulation are shown in Figure 4.7. From the figure, it is seen that the current is always above zero, and therefore ensures the BEMF-based and flux linkage-based plunger position estimates do not encounter a divide-by-zero scenario. Furthermore, it is seen that the resulting current has a superimposed ripple of approximately 44mA peak-to-peak and is a reasonable magnitude to be measured by a current sensor.

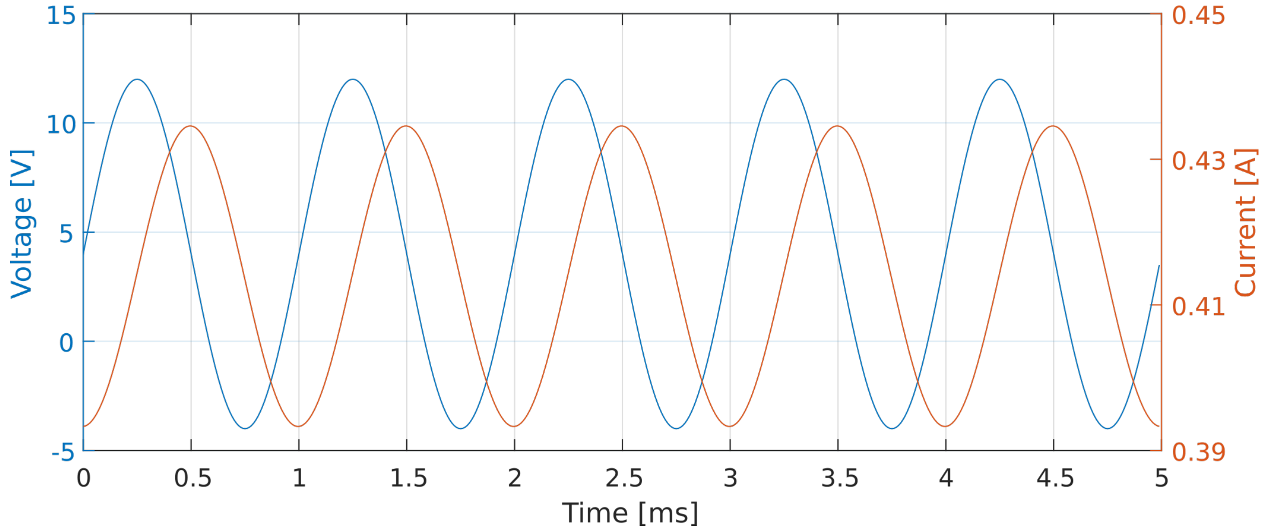

Figure 4.7 Shows the simulated characteristics of the superimposed voltage and current ripple used to calculate the plunger position of the CAS sensor based on inductance.

In Figure 3.16a, it was seen that the BEMF and flux linkage-based plunger position measurements performed well even at low speeds when in ideal conditions without noise or mischaracterized parameters. However, it was also shown that a 5°C increase in temperature (2% resistance change) created significant drift in these measurements. For Figure 4.8, Figure 4.9 and Figure 4.10, R_{c1} and R_{c2} of the CAS sensor electrical model (Figure 4.6) were increased by 2% to show the effects of mischaracterization.

Figure 4.8 shows the simulated performance of the inductance-based measurements of the CAS sensor when measuring the plunger moving at 1Hz and 100Hz. It is seen that the inductance-based method is effective at capturing 1Hz plunger movement. The slight amount of error seen in the CAS-1 and CAS-2 measurements (y_{L1} and y_{L2}) is due to slight discrepancies between the inductance regression and the FEA inductance shown in Figure 4.5. Furthermore, it is seen that this discrepancy, is common to both CAS-1 and CAS-2 and therefore cancels by using a differential measurement (y_{dL}). However, when the plunger is moving at 100Hz, it is seen that a large amount of error results due to there being a substantial amount of phase lag between the actual plunger position and the inductive-based measurements. This phase-lag error is a result of delay introduced by the bandpass and RMS filters as explained in Section 2.3.1. It is important to note that the sizeable error before 4ms is due to the filters being uninitialized at the start, but it is seen that the error quickly decays.

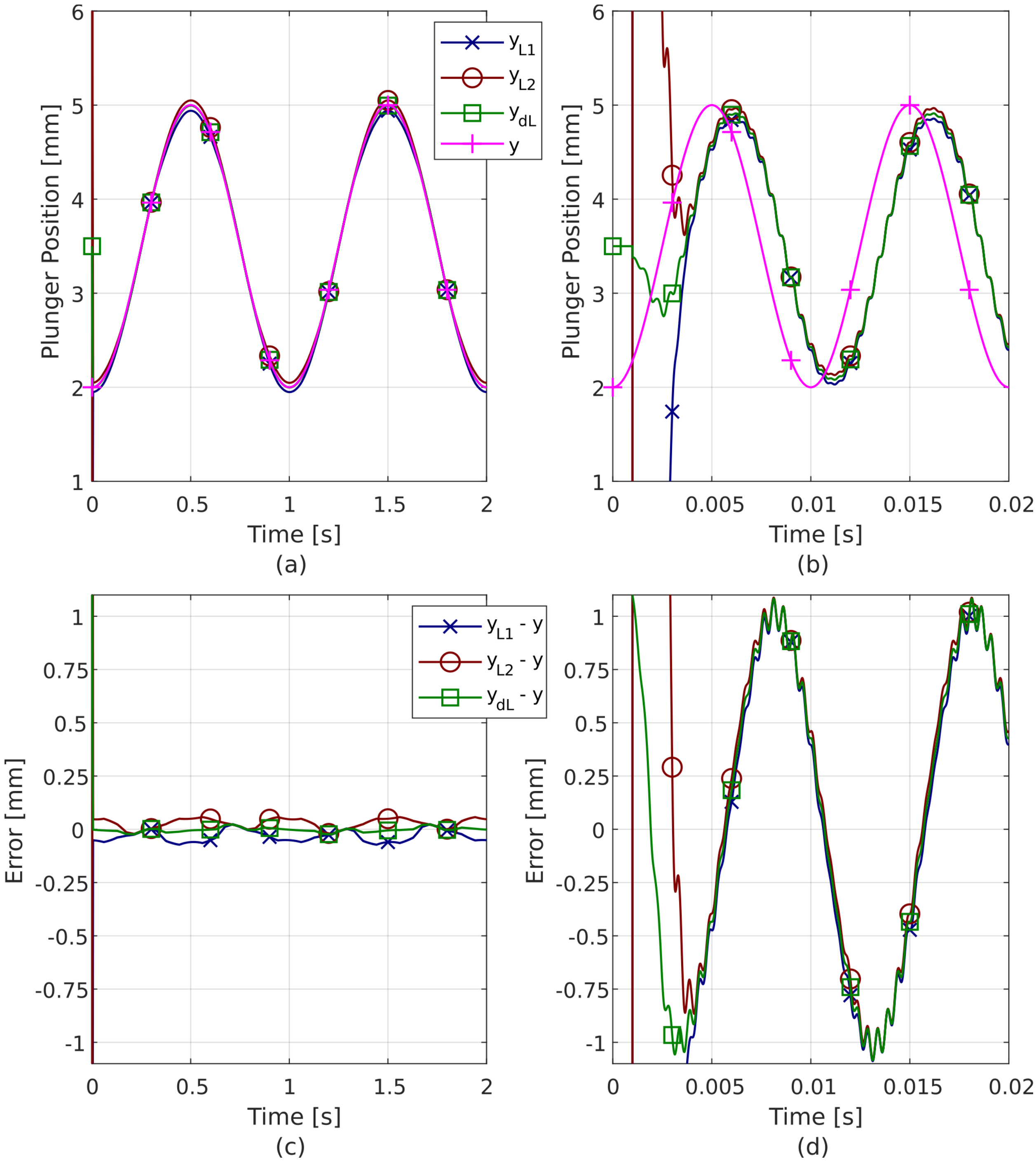

Figure 4.8 Shows the simulated performance of the inductance-based plunger position estimation method when tracking the plunger moving at 1Hz (a) and a 100Hz (b) for a case where the CAS-1 and CAS-2 resistances are mischaracterized by the same amount ($\boldsymbol{R_{c1}}$+2% and $\boldsymbol{R_{c2}}$+2%). The error relative to the actual plunger position is shown in (c) and (d) for the 1Hz and 100Hz cases respectively.

Figure 4.9 shows the simulated performance of the BEMF-based measurements of the CAS sensor when measuring the plunger moving at 1Hz and 100Hz. The mischaracterized resistance creates sizable drift that accumulates quickly and causes the individual BEMF-based measurements (y_{B1} and y_{B2}) to exit the windows of the plots within a fraction of a second. As was seen with the CAS actuator, the individual BEMF-based methods are still very sensitive to the mischaracterization of the resistance. However, it can be seen in Figure 4.9 that the rate of drift for the CAS-1 and CAS-2 measurements are equal and opposite and therefore the differential measurement (y_{dB}) is able to completely remove the drift. The differential measurement is shown to perform well at both 1Hz and 100Hz. However, it is important to note that the drift cancellation is only applicable when common-mode disturbances are present.

Figure 4.10 shows the simulated performance of the flux linkage-based measurements of the CAS sensor when measuring the plunger moving at 1Hz and 100Hz. When comparing Figure 4.9 and Figure 4.10, it is seen that they are nearly identical since the simulation timestep is small. This is expected since the flux linkage-based and BEMF-based methods are algebraically equivalent and only differ by their discrete implementations. Clearly, the individual flux linkage-based measurements, $y_{\lambda 1}$ and $y_{\lambda 2}$, are prone to drift due to mischaracterization of the resistances of CAS-1 and CAS-2. Like the BEMF-based differential measurement, the flux linkage-based differential measurement is able to produce a measurement free from drift when only common-mode disturbances are present.

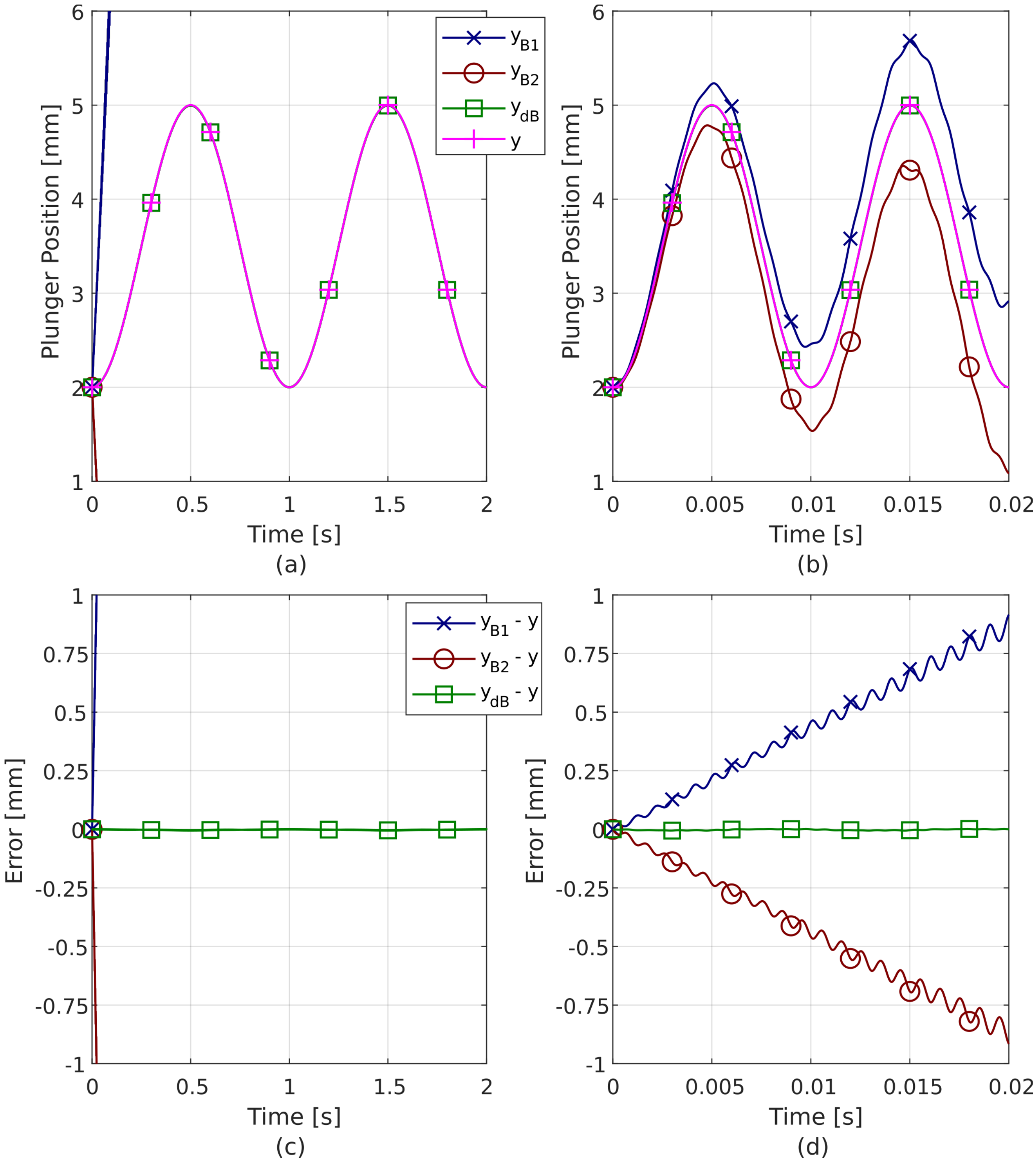

Figure 4.9 Shows the simulated performance of the BEMF-based plunger position estimation method when the plunger is moving at 1Hz (a) and a 100Hz (b) for a case where the CAS-1 and CAS-2 resistances are mischaracterized by the same amount ($\boldsymbol{R_{c1}}$+2% and $\boldsymbol{R_{c2}}$+2%). The error relative to the actual plunger position is shown in (c) and (d) for the 1Hz and 100Hz cases respectively.

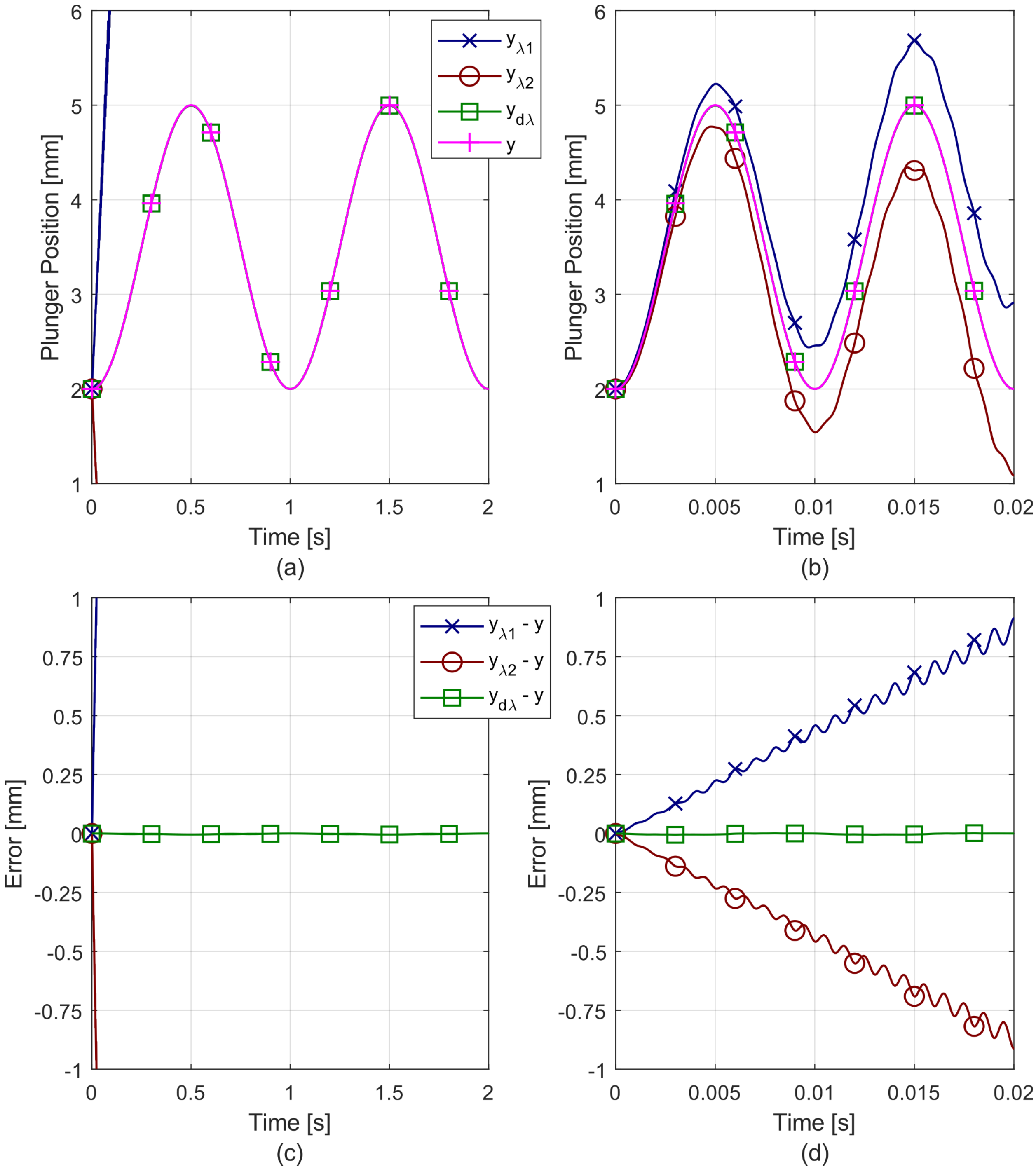

Figure 4.10 Shows the simulated performance of the flux linkage-based plunger position estimation method when the plunger is moving at 1Hz (a) and a 100Hz (b) for a case where the CAS-1 and CAS-2 resistances are mischaracterized by the same amount ($\boldsymbol{R_{c1}}$+2% and $\boldsymbol{R_{c2}}$+2%). The error relative to the actual plunger position is shown in (c) and (d) for the 1Hz and 100Hz cases respectively.

In Figure 4.8, Figure 4.9 and Figure 4.10 it was seen that the differential measurement was able to reject common-mode disturbances. However, in a physical prototype, it is likely that the CAS sensor will be exposed to non-common-mode disturbances. For example, winding imperfections or temperature gradients may cause the CAS-1 and CAS-2 resistances to differ. Figure 4.11 shows the effect increasing R_{c1} by 2% and decreasing R_{c2} by 2% (a 4% difference) has on the differential measurements. It is seen that the differential inductance-based measurement for both the 1Hz and 100Hz cases appears to be negligibly affected by the non-common-mode resistance difference when compared with Figure 4.8. This is expected since the resistance is negligible relative to the reactance and therefore resistive changes have negligible impact on the inductance-based position measurement. Overall, the inductance-based differential measurement performs well at low speed, but is still heavily degraded by phase-lag error at high speed. The BEMF-base and flux linkage-based differential measurements no longer perform well at 1Hz and they quickly drift due to the non-common-mode resistance difference. At 100Hz, the drift is still appreciable, but it is seen that the amplitude of the movement is accurately captured without phase lag. It is unlikely the plunger speed could be operated much higher for a laminated structure due to eddy currents. Therefore, it is unlikely the BEMF-based and flux linkage-based differential measurements would be suitable to use as standalone measurements without a complementary filter.

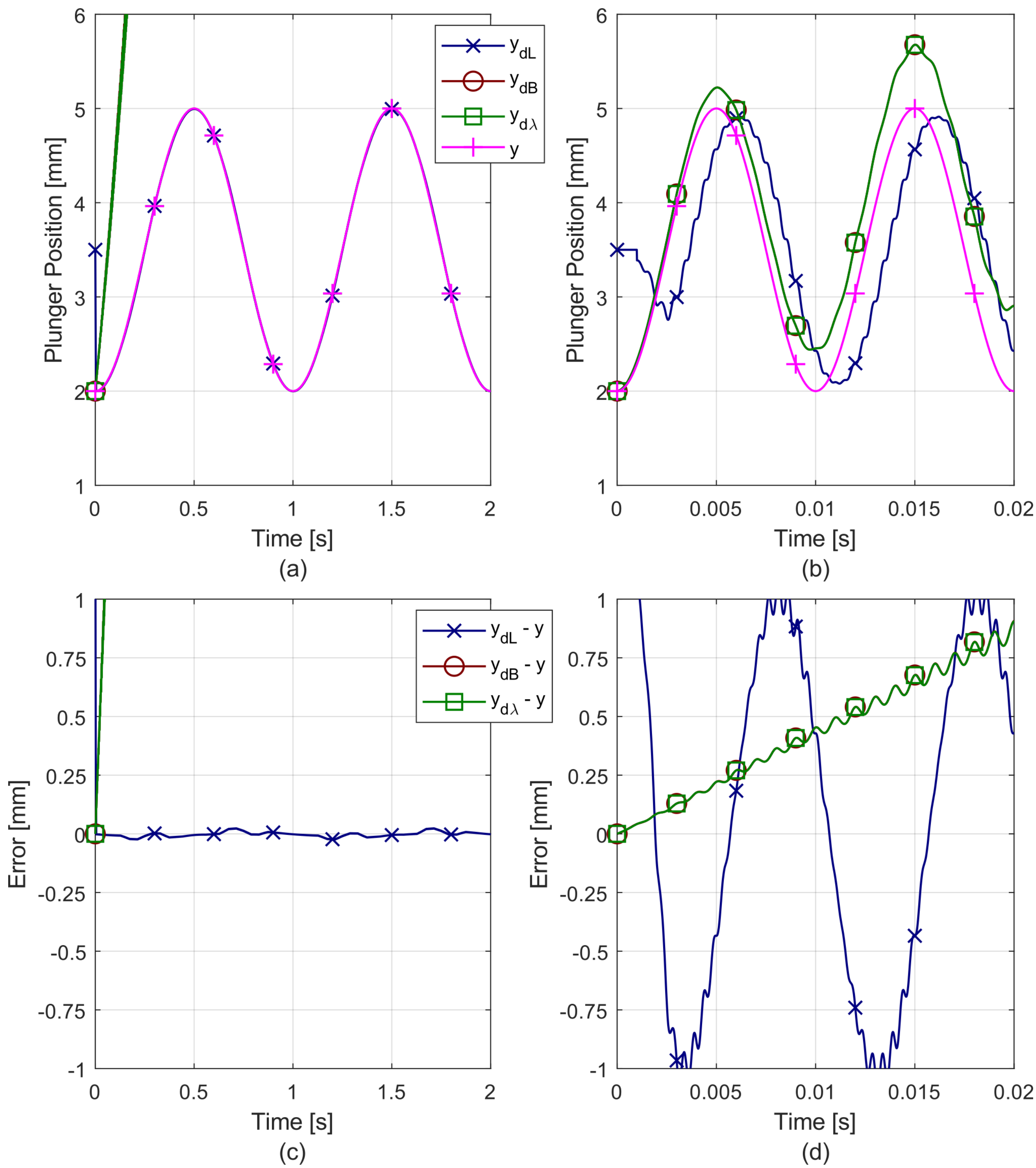

Figure 4.11 Compares the simulated performance of the differential measurements when the plunger is moving at 1Hz (a) and a 100Hz (b) for a case where the CAS-1 and CAS-2 resistances are mischaracterized by different amounts ($\boldsymbol{R_{c1}}$+2% and $\boldsymbol{R_{c2}}$-2%). The error relative to the actual plunger position is shown in (c) and (d) for the 1Hz and 100Hz cases respectively.

In Chapter 3, it was shown that a CAS actuator complementary filter overcomes the phase-lag error produced by the inductance-based measurement and the drift produced by the BEMF-based and flux linkage-based measurements. Figure 4.12 demonstrates that the drift and phase lag seen in Figure 4.11 can also be resolved with a complementary filter when the plunger is moving at 100Hz. For the 1Hz case, it is seen that the BEMF-based and flux linkage-based complementary filter outputs are able to track the actual plunger position accurately. It is important to note that the integrals within Figure 2.10 and Figure 2.11 were not initialized and therefore leads to error at 0s. However, the PI-action of the complementary filters are able to suppress the error over time as expected. Overall, Figure 4.12 demonstrates that the complementary filters are effective at producing plunger position measurements that greatly improve upon the accuracy and bandwidth of the standalone inductance-based, BEMF-based and flux linkage-based measurements.

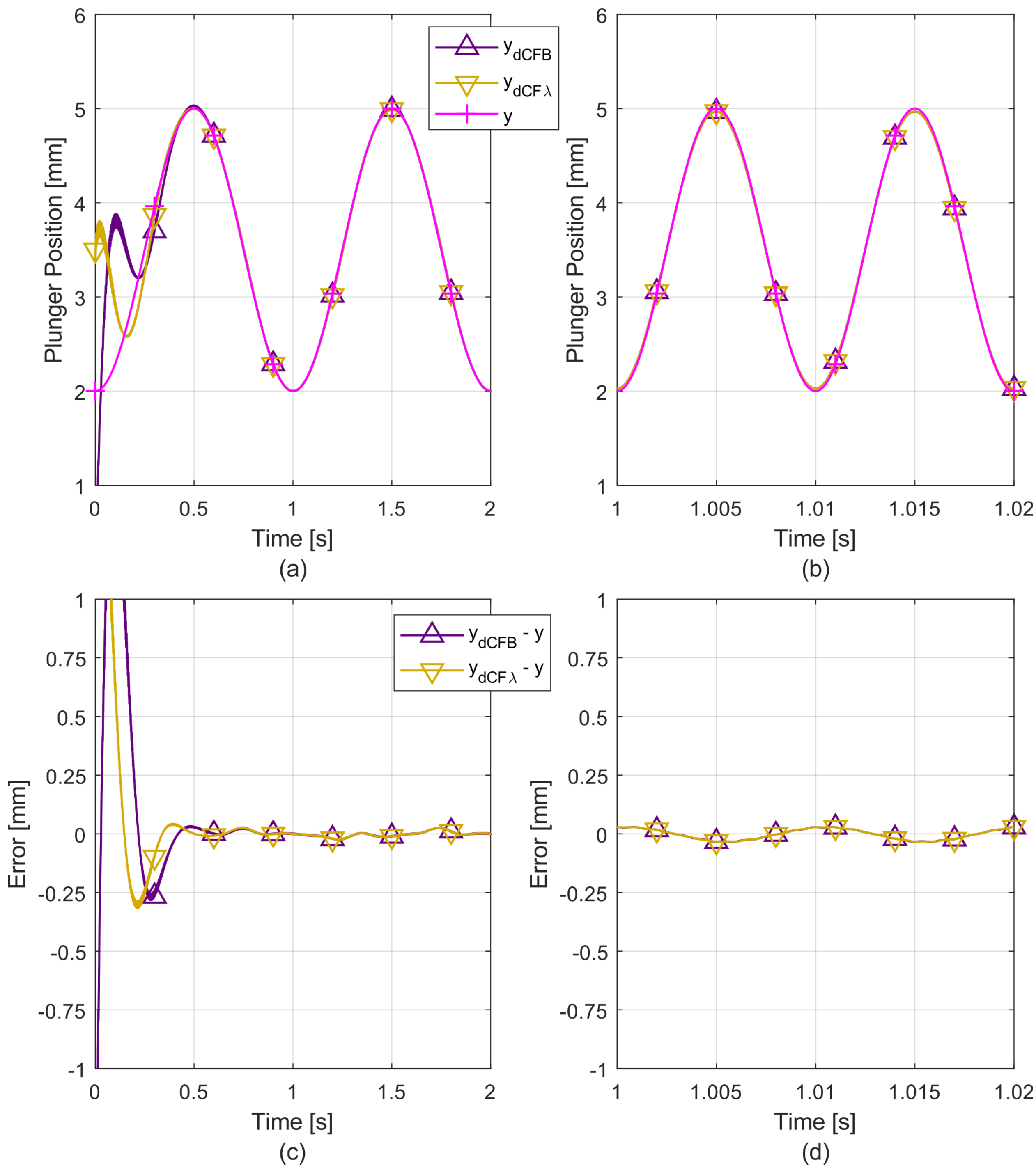

Figure 4.12 Shows the simulated performance of the BEMF-based and flux linkage-based complementary filter outputs when the plunger is moving at 1Hz (a) and a 100Hz (b) for a case where the CAS-1 and CAS-2 resistances are mischaracterized by different amounts ($\boldsymbol{R_{c1}}$+2% and $\boldsymbol{R_{c2}}$-2%). The error relative to the actual plunger position is shown in (c) and (d) for the 1Hz and 100Hz cases respectively.

At the end of Section 4.1, it was explained that the CAS sensor could continue operating if one of its two voltage sensors, or its current sensor was removed for cost reasons or in the event one of the sensors failed. It was also explained that removing a sensor would reintroduce a temperature dependency to the position measurements produced by the CAS sensor since the current becomes a function of terminal resistance and terminal inductance. Figure 4.13 shows a scenario where the current sensor measurement has been removed and replaced with (4.12). Three cases are shown that demonstrate the effect a relative change in resistance has when only using two sensors. When the plunger is moving at 1Hz, only a small amount of error is observed since the amplitude and phase of the bandpass-filtered AC signals of the underlying inductance-based position estimate are negligibly affected by resistive changes. However, at 100Hz, the flux linkage-based complementary filter measurement shows noticeable degradation as the terminal resistance increases from its characterized value. Clearly, the underlying flux linkage-based measurement is sensitive to errors in the current estimate produced by (4.12). It is important to note that a 10% change in resistance for copper windings corresponds to about a 25°C rise in temperature and results in about 5% error for a 3mm stroke while the plunger is moving at 100Hz [131]. However, this could be mitigated by opting to employ Method 3 in Table 2.1 which would allow the resistance to be characterized on a continuous basis.

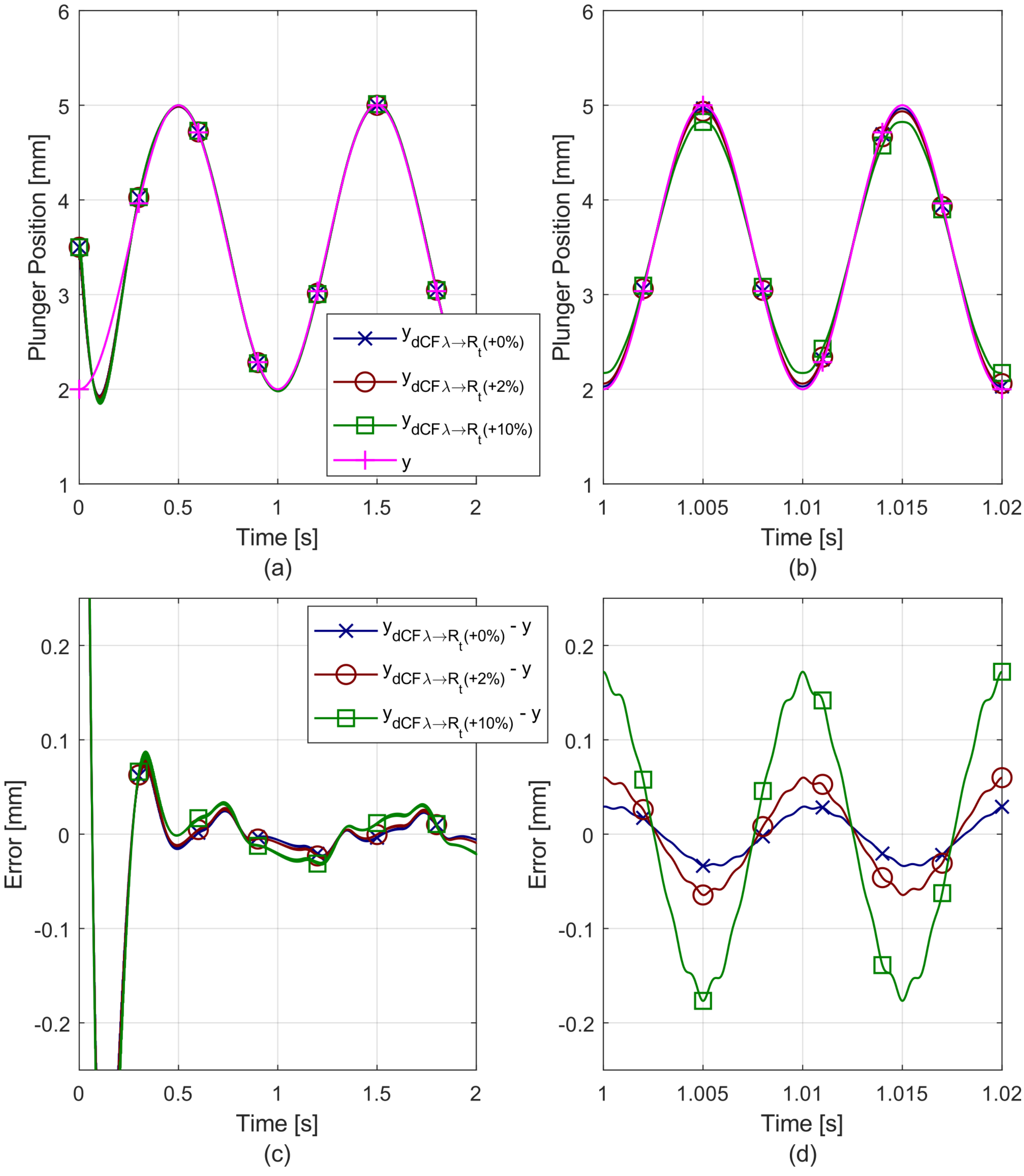

Figure 4.13 Shows the simulated performance of the flux linkage-based complementary filter output when the plunger is moving at 1Hz (a) and a 100Hz (b) for a case where the CAS sensor is operated without a current sensor and its terminal resistance is mischaracterized by different percentages. The error relative to the actual plunger position is shown in (c) and (d) for the 1Hz and 100Hz cases respectively.

4.3 Experimental Validation

This section investigates the real-world performance of a prototype CAS sensor. First, the construction of a prototype CAS sensor and the configuration of the surrounding hardware are discussed. Afterwards, the prototype CAS sensor is used to validate the performance characteristics predicted by the analytical models and prior simulated findings.

4.3.1 CAS Sensor Prototype

In Figure 4.1, it was seen that the CAS actuator, which was investigated in Chapter 3, can be easily converted into a CAS sensor by changing the location of the plunger cores relative to the stator. Naturally, only the plunger core spacers and the stator side braces shown in Figure 3.23 need to be reprinted. However, instead of disassembling the CAS actuator and converting it into a CAS sensor, additional laminations were purchased so that both the CAS sensor and actuator could be built concurrently. The CAS sensor uses the same materials and bolt-together design that the CAS actuator used. Furthermore, the plunger of the CAS sensor is also held in tension with two WW-53 springs from Century Spring Corp. which have a spring constant of 2.4N/mm [134]. The key differences between the CAS sensor and the CAS actuator in Chapter 3 are:

- Plunger core spacer and stator side brace dimensions
- Thinner aluminum end plates and reduced 3D printed material for some components since the CAS sensor does not produce large transverse stator forces like the CAS actuator
- CAS sensor uses 500 windings per CAS
- Air gap of the CAS sensor is 0.75mm.

The finished CAS sensor is shown in Figure 4.14. The final outer dimensions are 162mm x 92mm x 82mm with an effective moving plunger mass of 43.5g.

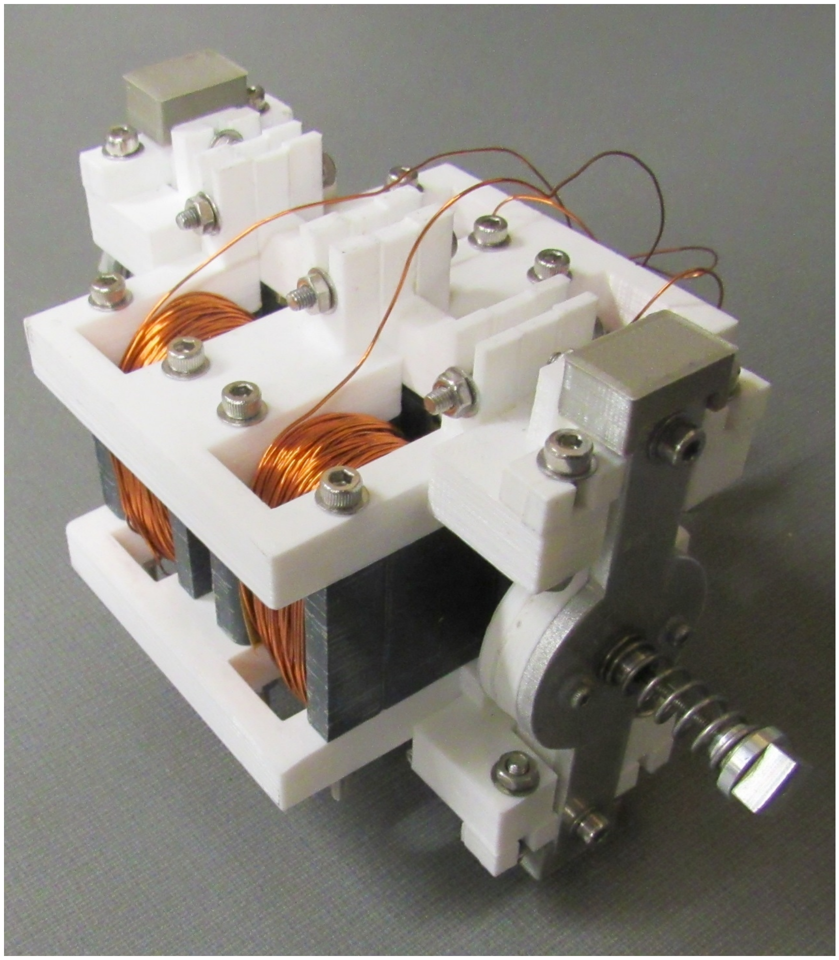

Figure 4.14 Finished CAS sensor prototype.

4.3.2 Hardware Implementation

A diagram of the required hardware to operate the CAS sensor prototype is shown in Figure 4.15. It should be noted that the hardware required to operate a CAS sensor is much simpler than the CAS actuator due to the significantly lower power requirement. For example, a CAS sensor can use a linear amplifier instead of an H-bridge. This is preferable since linear amplifiers can directly produce an AC ripple and bias without needing to attenuate a high-frequency PWM signal with sharp filters afterwards.

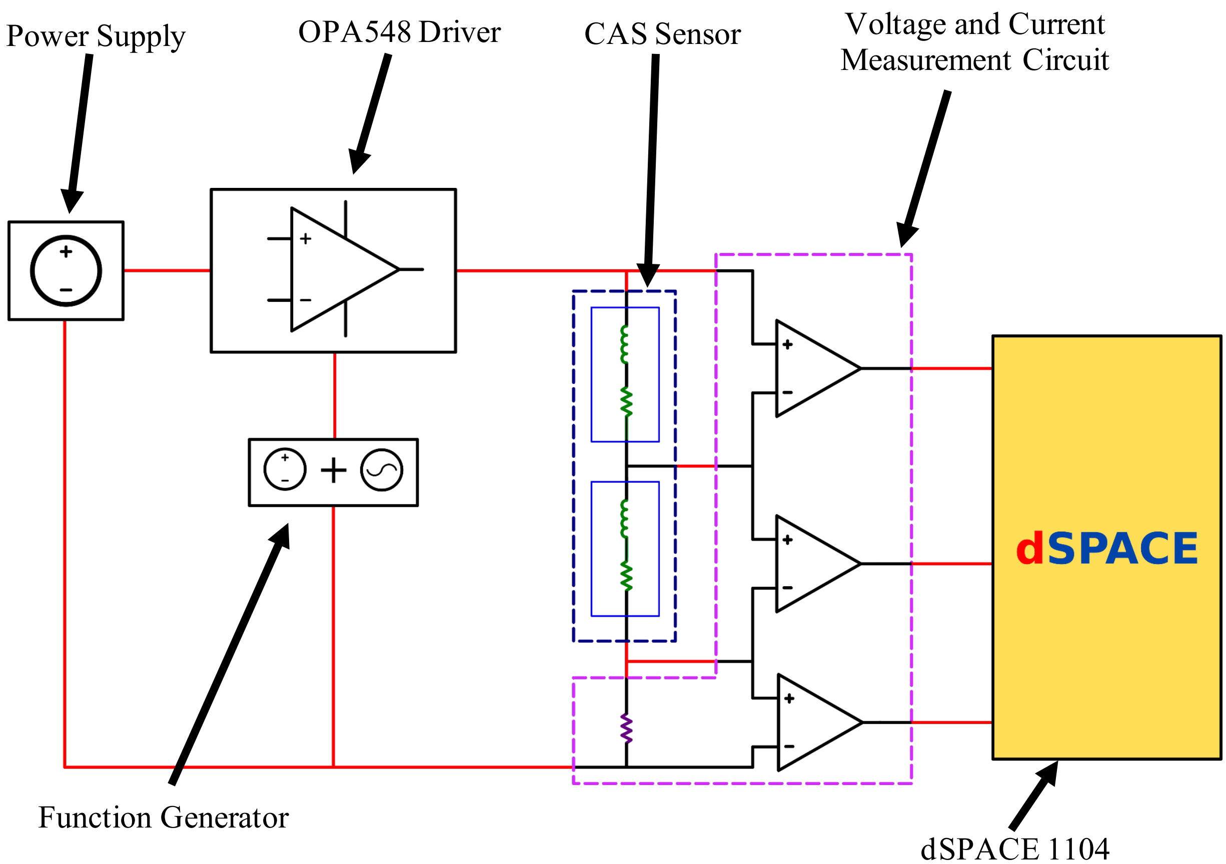

Figure 4.15 A diagram of the CAS Sensor experimental setup.

A low-cost OPA548 operational amplifier was selected to drive the CAS sensor as it meets the power, voltage and bandwidth requirements of the prototype CAS sensor. The OPA548 was configured as a non-inverting amplifier with a gain of 10. The details and fabricated circuit are shown and discussed in Appendix B.1. A Techtronic's AG2021 function generator was used to produce the desired AC and DC waveform characteristics that would be subsequently amplified by the custom CAS sensor driver. Naturally, the use of a linear amplifier and function generator allows the AC and DC waveform characteristics to be altered independently.

The CAS-1 and CAS-2 voltages and the series current are measured using a custom-built circuit discussed in Appendix B.2. The series current is converted into a measurable voltage using a shunt resistor. This circuit measures differential voltages using AD8421 instrumentation amplifiers. The outputs of the instrumentation amplifiers are then relayed to a dSPACE 1104. The dSPACE was programmed with the block diagram shown in Figure 4.6 after noting that U_1, U_2 and I are measured instead of simulated.

4.3.3 Experimental Results

The following subsections display and discuss experimental results produced by the CAS sensor prototype. First the CAS sensor is characterized to determine its characteristic parameters. Afterwards, the established characterized parameters are used to self-sense plunger position against a laser vibrometer. In the results shown in the following subsections, the measurement from the laser vibrometer represents the actual plunger position, y.

4.3.3.1 CAS Sensor Prototype Characterization

Important parameters, such as the inductance slope, are required to be characterized in order to self-sense plunger position. In Section 3.3.2.1 it was explained that an intermediate step within the inductance-based self-sensing method requires inductance to be calculated before position. The calculated inductance can be used to identify the CAS sensor inductance characteristics. To begin characterizing the inductance, a 1000Hz 8V AC sinusoid was superimposed on top of a 4V DC bias and supplied to the prototype CAS sensor as seen in Figure 4.16. The plunger was then slowly pushed by hand over its entire stroke while the CAS-1 and CAS-2 voltages and series current were recorded. The calculated inductances of this experiment were then plotted against the plunger position, which was measured using a laser vibrometer, and is seen in Figure 4.17. A linear regression was then performed on the measured CAS-1 inductance between 2mm and 5mm to determine the slope and the virtual overlap, which are noted in Table 4.2. The correlation coefficient of the CAS-1 regression is 0.9966 and is -0.9962 when the same fit is applied to CAS-2, but with a negative slope. This indicates the inductance characteristics of CAS-1 and CAS-2 are very similar, which is essential to obtain robust common-mode rejection within the differential measurement. Overall, the inductance-position profile of the experimental CAS-1 and CAS-2 measurements are very similar to the FEA results shown in Figure 4.5, including the nonlinearity seen outside of the 2mm-to-5mm range. The discrepancies between the simulated and experimental inductance parameters seen in Table 4.2 can be attributed to the relatively large tolerances of the physical prototype. For example, a slightly smaller air gap could explain the larger inductance slope and virtual overlap.

Characterizing the resistance of a CAS sensor is not required if the CAS sensor is to be operated with two voltage sensors and one current sensor. However, resistance was characterized in order to experimentally validate that the CAS sensor can be run in a limited capacity with only two sensors. To characterize the resistance, a DC voltage of 4V was applied to the terminals of the CAS sensor and the resulting current was measured. The resistance was then calculated using (3.15) and is shown in Table 4.2. The resistance was found to be smaller than the value used in the simulation due to overestimating the length of the winding half-turns.

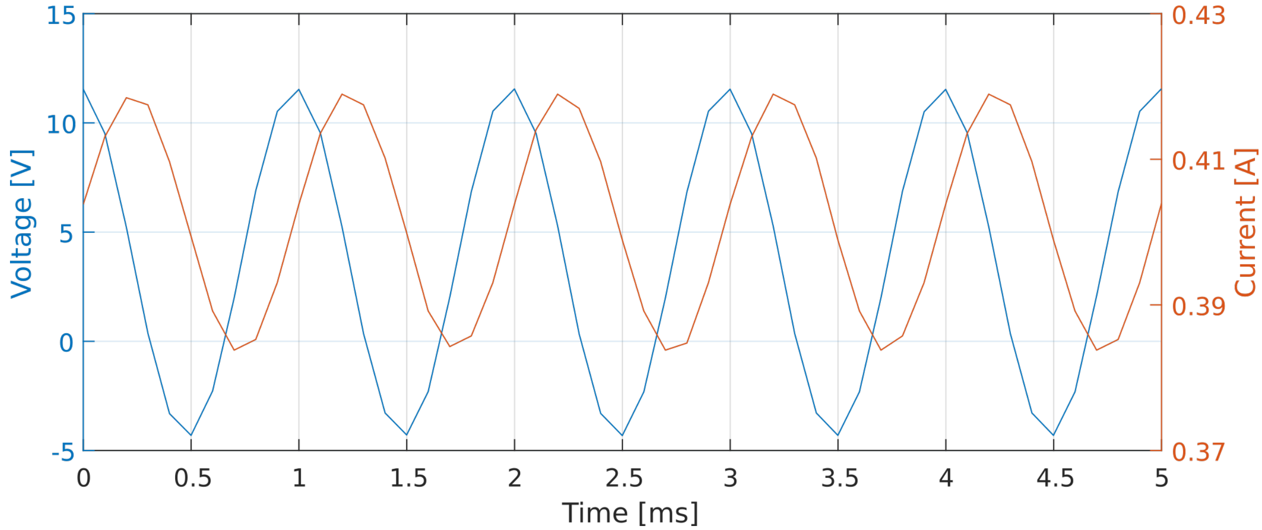

Figure 4.16 Shows the experimentally obtained characteristics of the superimposed voltage and current ripple used to calculate the plunger position of the CAS sensor based on inductance.

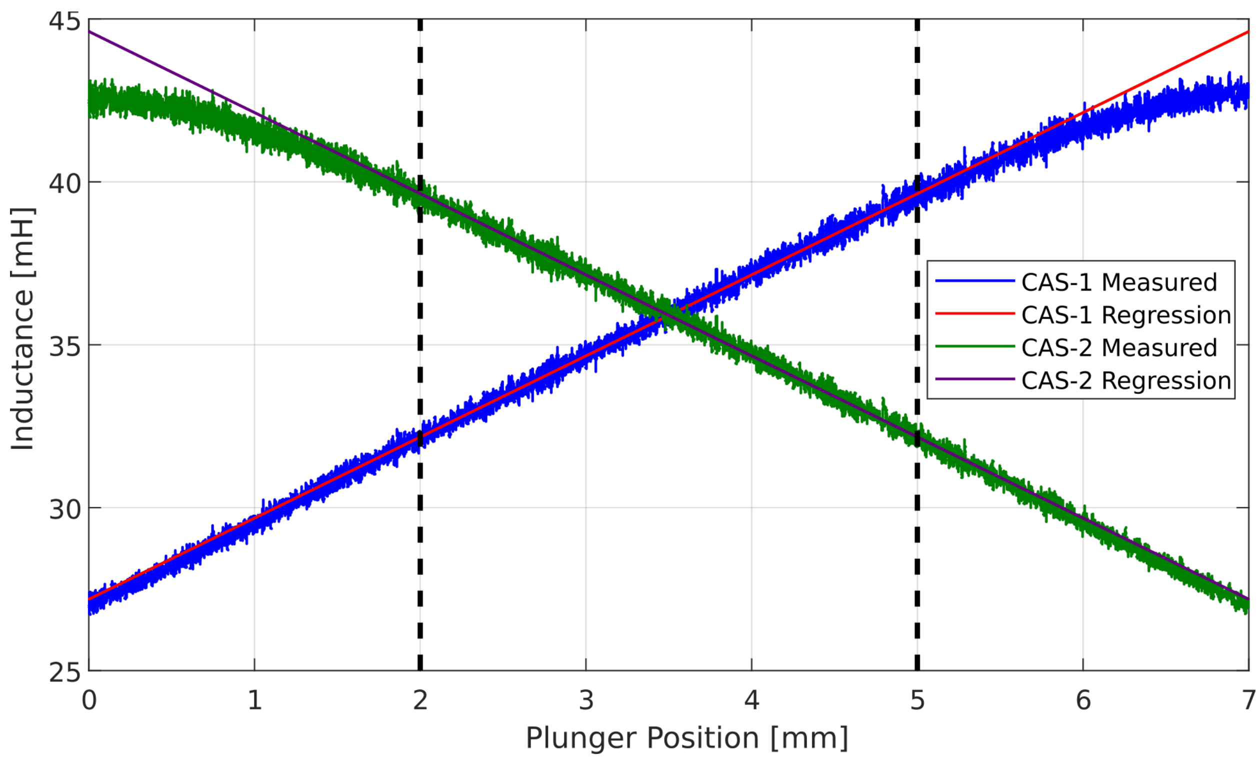

Figure 4.17 Shows the inductance-position mapping for CAS-1 and CAS-2. The linear regression was applied between the vertical dashed lines.

Table 4.2 Comparison of Simulated and Characterized Experimental CAS Actuator Parameters

Symbol(s)	Parameter	Simulated	Experimental
C_L	Inductance-position slope [mH/mm]	2.23	2.29
w_o	Virtual plunger-stator overlap [mm]	10.38	10.90
L_t	Terminal inductance [mH]	61.83	71.80
$R_{c1} = R_{c2}$	CAS resistance [Ω]	4.74	4.45

4.3.3.2 Plunger Position Self-Sensing Performance

The inductance and resistance parameters listed in Table 4.2, along with the filter parameters listed in Table 4.1, were supplied to the CAS sensor Simulink program and subsequently uploaded to the dSPACE 1104. The dSPACE 1104 was configured to sample at 10kHz. The plunger of the prototype CAS sensor was pushed and pulled by hand to generate low-speed results and was struck with a hammer to generate high-speed results. The error of the self-sensed plunger position estimates is calculated based on the difference between their output and the laser vibrometer.

Figure 4.18 shows the low-speed and high-speed results of the prototype CAS sensor differential measurements. For the low-speed case, it is seen that the differential inductance-based estimate closely follows the trajectory while the differential BEMF-based and flux linkage-based estimates quickly drift out of the plotted window. The drift clearly indicates the CAS sensor is experiencing non-common-mode disturbances and is very similar in nature to the simulated results shown in Figure 4.11. The high-speed results also closely align with the simulated results in Figure 4.11 since the differential inductance-based estimate shows large amplitude error due to a phase lag while the differential BEMF-based and flux linkage-based estimates show little amplitude error but a substantial amount of drift. It is important to note that when the CAS sensor is operated outside of its linear 2mm-to-5mm range, position error accrues for both the low-speed and high-speed cases. The flux linkage-based estimate is very noisy as predicted due to inaccurate initial conditions. It is important to recall in Section 2.3.3 that the flux linkage-based estimate is challenging to initialize since highly-accurate knowledge of the current and plunger position is required; slight initialization error results in an offset, that when divided by sinusoidal current in (2.58) produces the large sinusoidal error seen in Figure 4.18. Clearly, the differential BEMF-based estimate is preferable to use as a standalone measurement due to its simpler initialization requirements, which results in substantially lower error. However, the relatively fast drift rate of the differential BEMF-based estimate still makes it challenging to implement as a standalone estimate as was predicted in Section 4.2.2.

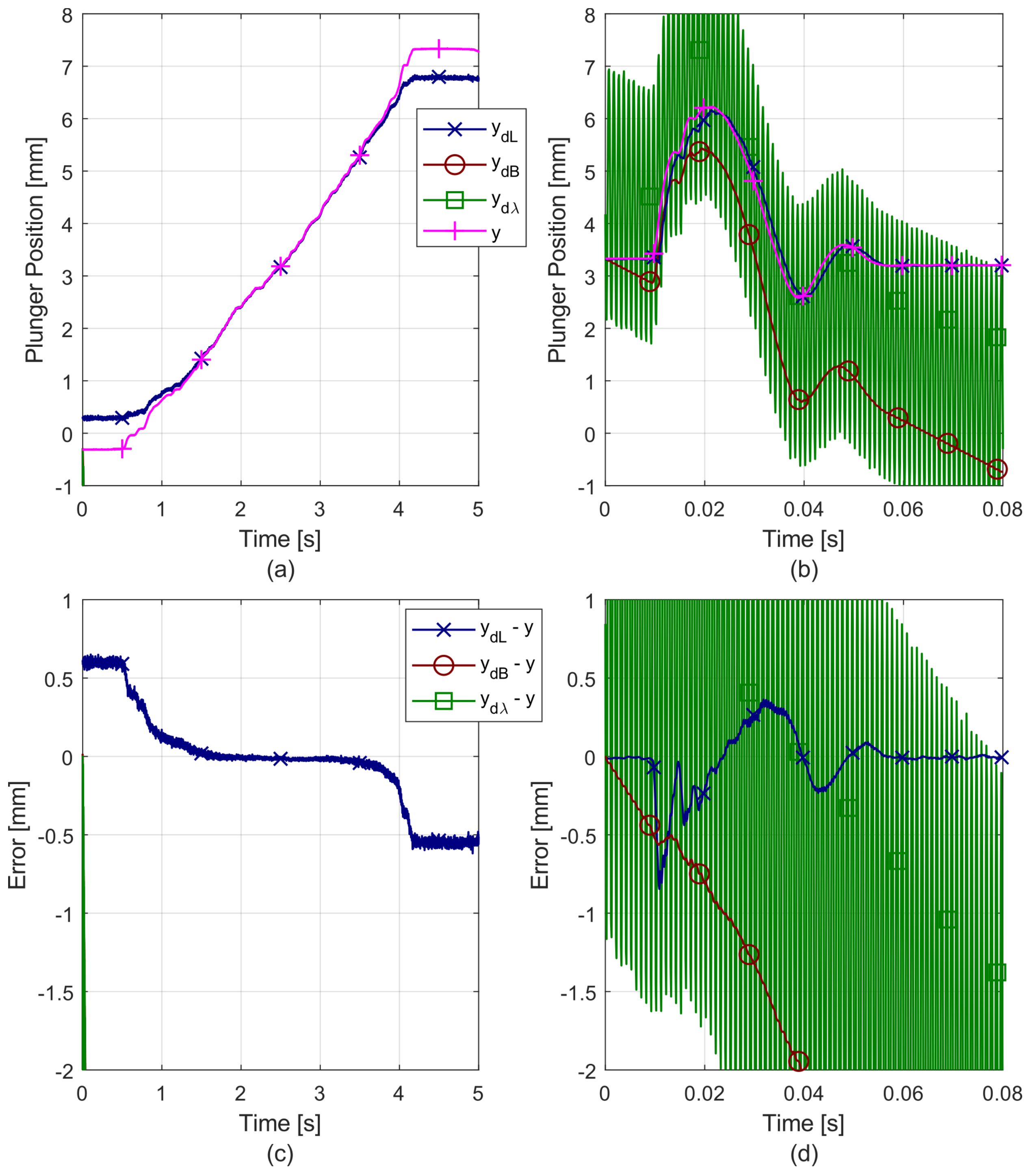

Figure 4.18 Shows standalone differential measurements produced by the prototype CAS sensor for a low-speed case (a) and a high-speed case (b). The error relative to the laser vibrometer measurement is shown in (c) and (d) for the low-speed and high-speed cases respectively. The actual plunger position, $\boldsymbol{y}$, is assumed to be the measurement produced by the laser vibrometer.

The BEMF-based and flux linkage-based complementary filter performance is shown in Figure 4.19 for a low-speed and high-speed case. In the low-speed case, it is seen that the complementary filter measurements are very similar to the differential inductance-based estimate in Figure 4.18 as expected since the complementary filter rejects the high-speed estimates at slow speeds. The complementary filter estimates also show the same nonlinear characteristics as the inductance measurement at the maximum and minimum stroke positions. For the high-speed case, the complementary filter accurately tracks the plunger position without drift unlike the standalone differential BEMF-based and flux linkage-based estimates in Figure 4.18. The high-speed estimates of the complementary filters also do not show the phase lag which degraded the standalone differential inductance-based estimate in Figure 4.18. It is important to note that these findings impeccably align with the simulated performance predicted in Figure 4.12. Clearly, the complementary filter estimates are much more robust than the standalone differential estimates, especially if a wide-bandwidth position measurement is required.

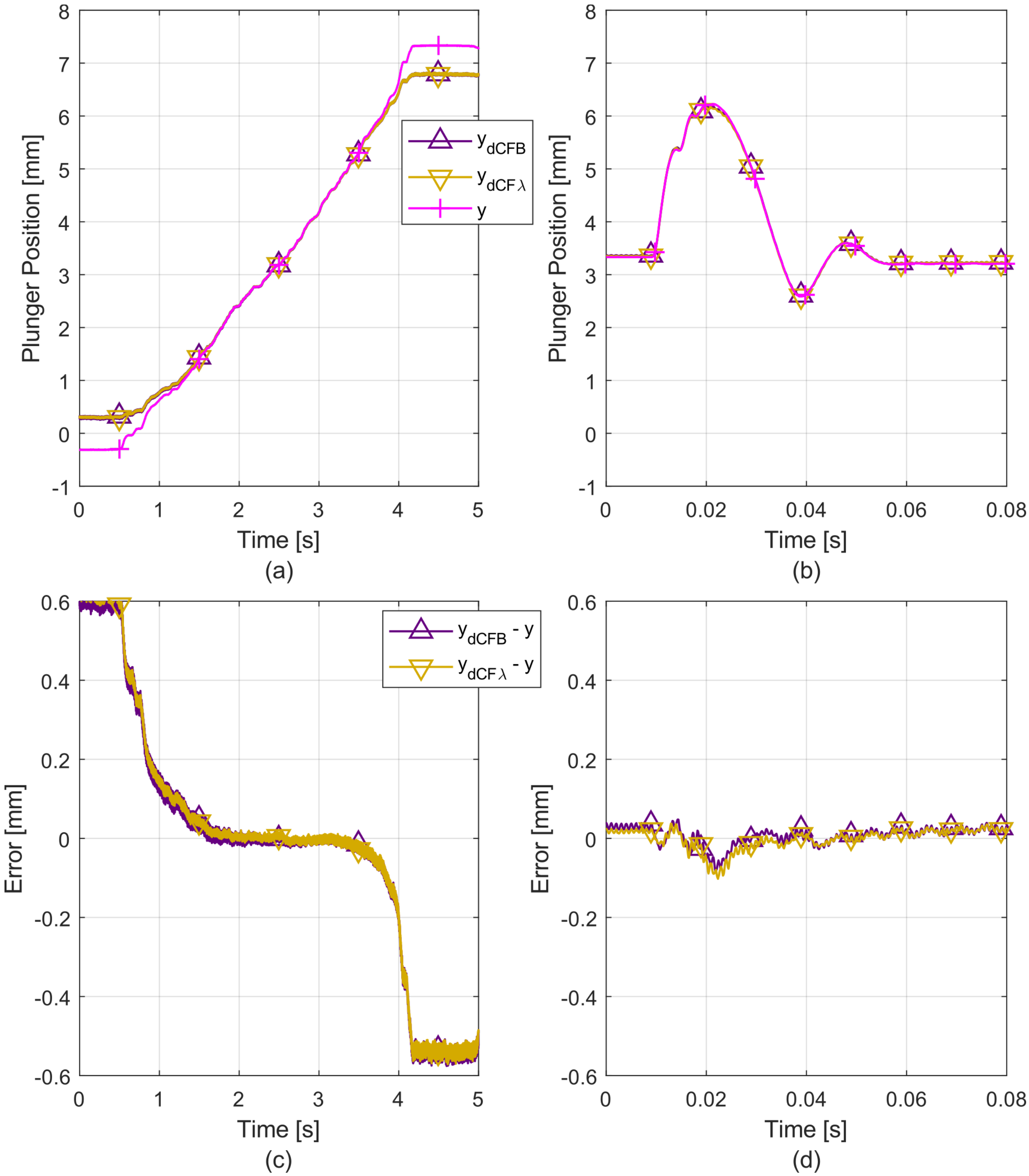

Figure 4.19 Shows complementary filtered differential measurements produced by the prototype CAS sensor for a low-speed case (a) and a high-speed case (b). The error relative to the laser vibrometer measurement is shown in (c) and (d) for the low-speed and high-speed cases respectively. The actual plunger position, $\boldsymbol{y}$, is assumed to be the measurement produced by the laser vibrometer.

The linear regression applied to the inductance-position mapping in Figure 4.17 was only applied to the middle 2mm-to-5mm range of the stroke as this is the region where the CAS sensor is most linear. The prescribed linear region of Figure 4.19 is shown in Figure 4.20. It can be seen that the prototype CAS sensor maintains less than 1% nonlinearity over the prescribed 3mm stroke for both the low-speed and high-speed cases. Furthermore, it can also be seen that the nonlinearity and noise of the BEMF-based and flux linkage complementary filter outputs are very similar.

To demonstrate the robust ability of the CAS sensor to operate without one of its voltage or current sensors, the current sensor measurement was removed from the dSPACE. The missing current measurement was calculated instead with (4.12). The low-speed and high-speed results of two-sensor operation are shown in Figure 4.21. It is seen that the complementary filter estimates are still able to perform accurately at slow speeds. This is expected since the reintroduced resistance-dependency has very little effect on the AC current since the AC characteristics are dominated by reactance rather than resistance. However, as was predicted in Figure 4.13, the absence of the current sensor has a more notable effect on the linearity of the CAS sensor when the plunger is moving at high speed. When comparing Figure 4.20 and Figure 4.21, it is seen that the nonlinearity more than doubles after removing the current sensor for the high-speed case.

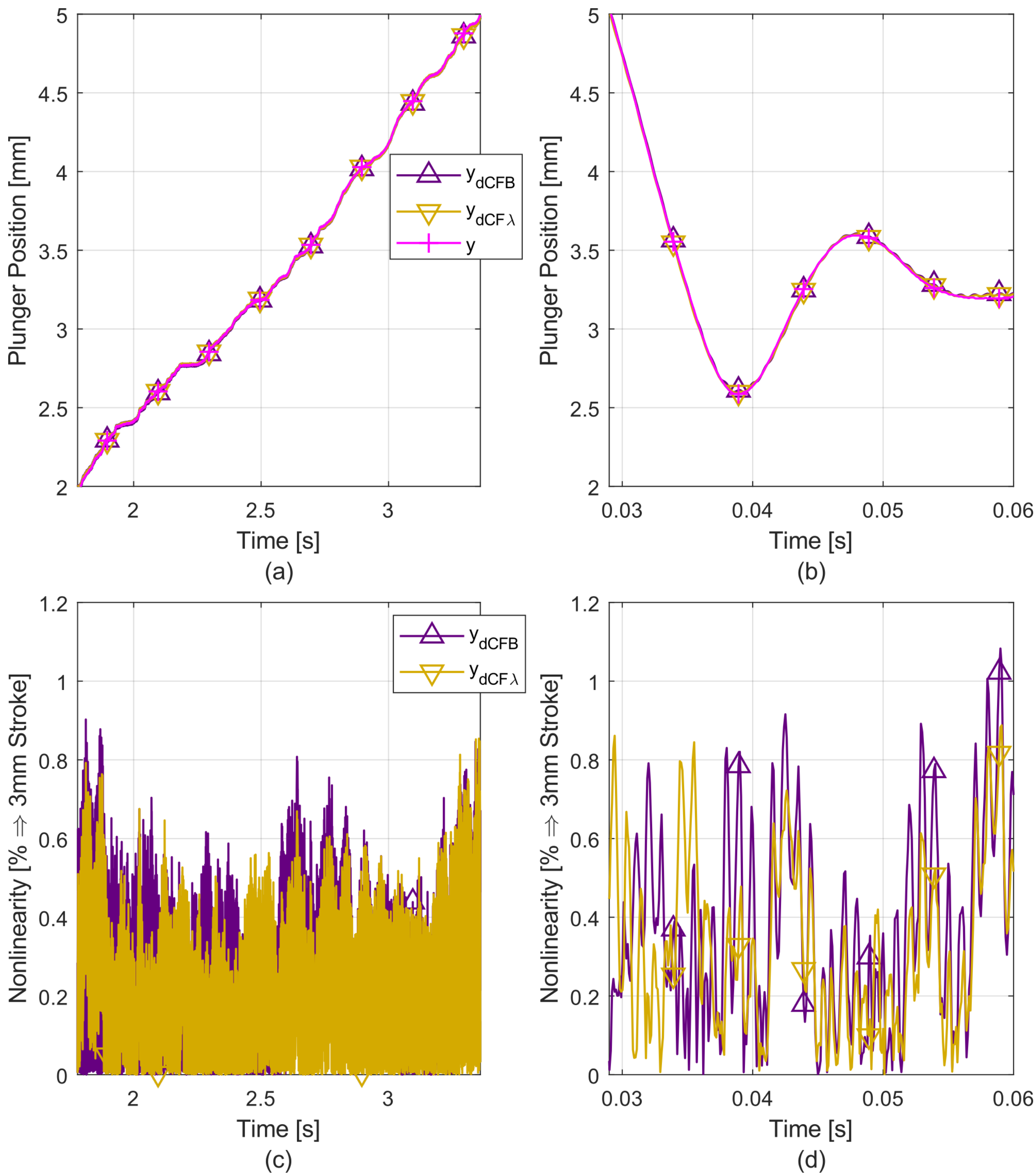

Figure 4.20 Shows the performance of the prototype CAS sensor when only operating within the prescribed 2mm-5mm stroke range for a low-speed case (a) and a high-speed case (b). The nonlinearity of the measurements in (a) and (b) are relative to the laser vibrometer measurement and are shown in (c) and (d) respectively. The actual plunger position, $\boldsymbol{y}$, is assumed to be the measurement produced by the laser vibrometer.

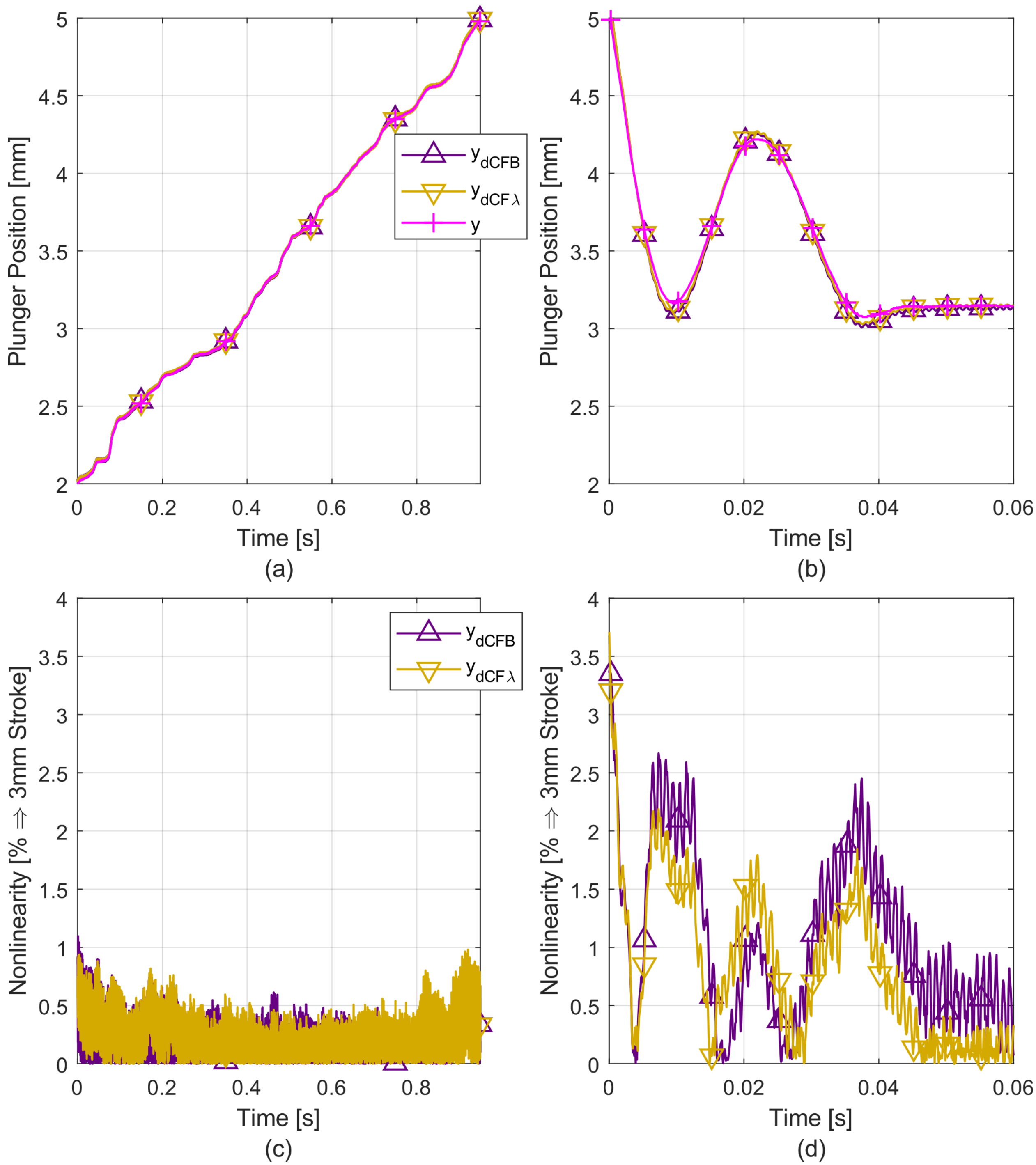

Figure 4.21 Shows the performance of the prototype CAS sensor operating without a current sensor and only within the prescribed 2mm-5mm stroke range for a low-speed case (a) and a high-speed case (b). The nonlinearity of the measurements in (a) and (b) are relative to the laser vibrometer measurement and are shown in (c) and (d) respectively. The actual plunger position, $\boldsymbol{y}$, is assumed to be the measurement produced by the laser vibrometer.

4.4 Summary

In Chapter 4 the premise of a CAS sensor was introduced and developed. First it was explained how the stacked CAS actuator design in Chapter 3 could be adapted into a CAS sensor by changing the plunger and stator spacing so that the upper and lower CASs pulled against each other. Next, analytical models were derived that revealed the CAS sensor has the robust ability to perform differential measurements that reject common-mode disturbances. The differential measurements do not require resistance to be characterized unlike the CAS actuator, and therefore the CAS sensor is immune to resistive temperature changes. The analytical models also revealed that the CAS sensor has inherent redundancy as it can continue to operate with reduced accuracy if a single voltage or current sensor fails. An FEA simulation was then developed and its results showed constant terminal inductance and cancelling plunger force characteristics as was predicted by the analytical models. The FEA results were then imported into a lumped-parameter Simulink simulation. The results of the Simulink simulation showed that the differential measurements were immune to resistance changes assuming the upper and lower CASs had identical windings. However, even if the windings are slightly mismatched, the Simulink simulation predicted that the fused output of a complementary filter would be able to accurately measure plunger position. In order to validate the analytical models and simulated findings, a prototype CAS sensor was fabricated. It was noted that the experimental setup of the CAS sensor is much simpler than the CAS actuator due to the significantly lower power requirement. Furthermore, since the CAS sensor is driven with a constant DC current, it was not affected by the inductance-current nonlinearity unlike the CAS actuator, and therefore no mitigations were required. The experimental results showed that the inductance-based method had phase-lag error while the BEMF-based and flux linkage-based methods suffered from drift as was predicted by the simulations. Furthermore, the experimental results showed that the complementary filter outputs were robust at rejecting the erroneous aspects of the individual self-sensing methods, allowing for accurate wide-bandwidth position measurements. Overall, it was found that the CAS sensor was capable of measuring a 3mm plunger stroke with only 1% error. It was also validated that the CAS could continue to operate when a current sensor failure was emulated; in this scenario the error increased to approximately 3% for a 3mm stroke.

Chapter 5: Discussion

In this chapter, the results and findings produced by the proof-of-concept CAS actuator and CAS sensor are utilized to provide guidance for applying the CAS technology to real-world applications. First, practical design considerations and limitations for applying the CAS technology are discussed. Next, the CAS technology is compared to similar actuator and sensor technologies to determine the applications it would be best suited for.

5.1 CAS Practical Design Considerations and Limitations

The following sections provide guidance for designing a CAS for a specific application. First, guidance is provided for selecting various design parameters. Next, potential sources of error and nonlinearity are discussed that may limit or degrade performance.

5.1.1 Practical Guidance for Selecting CAS Parameters and Geometry

The subsections below provide guidance and summarize compromises to be considered when designing a CAS actuator or CAS sensor for a practical application.

5.1.1.1 CAS Shape

In this thesis a cuboid-shaped CAS was developed and studied. The cuboid shape allowed it to effectively utilize ferromagnetic laminations to suppress eddy currents in both the plunger and stator since the flux was constrained to two dimensions. In a basic cylindrical-shaped CAS, flux would be required to travel in three dimensions. Since laminations can only suppress flux in two dimensions, a large portion of the magnetic circuit within a cylindrical-shaped CAS would be prone to significant eddy currents. Furthermore, in a cylindrical-shaped CAS, the magnetic flux must be channeled axially through the plunger; this would require a large amount of ferromagnetic material and would lead to a heavy plunger relative to a cuboid-shaped CAS. Overall, a cuboid-shaped CAS should have a better force-size density and a lighter plunger than a cylindrical-shaped CAS. Therefore, for applications requiring high-speed actuation, it is expected that a cuboid-shaped CAS will outperform a cylindrical-shaped CAS. The key advantages of a cylindrical-shaped CAS are practical in nature since a round shape may be more conducive for a particular application, and it does not require plunger guides to resist plunger rotation unlike a cuboid-shaped CAS.

5.1.1.2 Desired Stroke Length

Without considering external factors, such as end stops or a spring, the maximum theoretical stroke length of a CAS is dictated by the smaller of the plunger tooth width or stator tooth width as discussed in Section 2.1. However, based on the experimental results shown in Figure 3.31 and Figure 4.17, it is seen that nonlinearity begins to accrue before the plunger and stator teeth are fully overlapped. Therefore, one must decide how much nonlinearity they are willing to tolerate. For example, the prototype CAS sensor presented in this thesis has 7mm plunger and stator tooth widths, but its stroke was further reduced to 3mm which allowed it to achieve 1% nonlinearity. Naturally, this suggests that one may have to design the stator and plunger tooth widths to be more than a factor of two larger than the intended stroke to achieve satisfactory nonlinearity.

5.1.1.3 Desired Plunger Force

The force required to be produced by an actuator will be dictated by the application for which it is to be applied to. The peak force produced by a CAS actuator is defined by (2.28). The peak force is limited by the magnetic flux density at saturation. For a CAS actuator with a particular geometry and stroke, the only way to increase the force is to increase the magnetic saturation limit of the material. However, it is challenging to find materials with significantly higher saturation limits than steel, and materials with high saturation limits often become exotic and expensive. Lowering the permeability of the magnetic circuit would also increase the peak force, but for most CAS actuator designs where the air gap dominates the reluctance of the magnetic circuit, the effective permeability would be equivalent to the permeability of air and infeasible to change. Therefore, it is more reasonable to obtain the required force by carefully selecting the geometric features. For example, to double the force of a CAS, one could double the length of the plunger and stator teeth. One could also stack an additional CAS that shares a common plunger to produce double the force as shown in Figure 3.1. In general, producing a basic cuboid CAS actuator design with a larger force output will require the CAS actuator to be approximately proportionally larger in terms of its volume. One could also attempt to pursue a more advanced CAS design that uses several series air gaps or attempt to increase the length of the air gap, although this would increase the risk of flux leakage and fringing.

5.1.1.4 Maximum Plunger Movement Transient Characteristics

The speed and acceleration the plunger of a CAS is capable of being self-driven at at is inherently limited by its electromechanical design. Naturally, the acceleration of the mechanical system is governed by Newton's Second Law as was applied in (3.6). In a frictionless system with no springs, the mass of the plunger will determine the acceleration of the plunger for a given force. Therefore, CAS designs with a low plunger mass and a high force would be ideal for applications requiring high-speed actuation. However, it is worth noting that generating a larger force to achieve a faster acceleration may not be accomplished easily. For example, a larger acceleration cannot be obtained by stacking CASs or increasing the tooth depth in order to increase the plunger force as this would result in an approximately proportional increase in plunger mass. If the CAS has friction and a spring return system, then the resonant frequency, ω_r, of the mechanical system will limit how quickly the plunger can oscillate where b is the damping.

$$\omega_r = \sqrt{\frac{k_s}{m} - \frac{b^2}{4m^2}} \tag{5.1}$$

Once again, lowering the plunger mass is critical for high-speed applications. Additionally, it is seen that choosing a stiffer spring or reducing damping would allow the plunger to oscillate more quickly.

The transient force characteristics of a CAS are determined by its electromagnetic characteristics. More specifically, it was seen in (2.22) that the force can be related to the current supplied to the CAS. Therefore, the transient current characteristics determine the transient force characteristics. As seen in (3.5) the current flowing in a CAS is dependent on the voltage applied, the resistance, the inductance and the BEMF if the plunger is in motion. Under static plunger conditions, the peak current for a given voltage is determined by the resistance, and therefore one needs to design the resistance to be low enough so that the required current can be applied to generate the desired force. The rate of change of the current for a given supply voltage is determined by the inductance. To achieve a fast current response, which subsequently leads to a fast force response, one needs to design a CAS actuator to have a low inductance or use external driver hardware with a sufficient output voltage to drive the current quickly.

5.1.1.5 Magnetic Flux Path Design

Designing the flux pathways of a CAS requires compromises to be made to provide suitable performance and practicality. In order for the assumption that only the air gap dictates the inductance of a CAS to be valid, it is important that the ferromagnetic sections of the flux paths have negligible impact on the reluctance of the magnetic circuit; as seen in (2.1), this implies one should design the ferromagnetic portions of the magnetic circuit to have as large of a cross-sectional area as possible while being as short as possible. In typical actuators where steel is used as the ferromagnetic material, the permeability will be approximately three orders of magnitude larger than air, and therefore it is likely that the reluctance of the ferromagnetic material will be inherently negligible [123]. However, if exotic materials are opted for, such as powder cores to suppress eddy currents, the ratio between the ferromagnetic permeability and air gap permeability may be significantly smaller and extra care would need to be taken to design the magnetic circuit to ensure the reluctance of the ferromagnetic segments remain negligible. When choosing the cross-sectional area of the ferromagnetic paths, one needs to ensure that enough magnetic flux can be supplied to the air gaps without saturating the ferromagnetic material. However, increasing the cross-sectional area implies that more ferromagnetic material is required which will increase the cost and weight of the CAS.

The air gap length of a CAS has a significant effect on the inductance and force produced by a CAS. Increasing the length of an air gap has several advantages as listed below:

- Increases the peak force that can be produced by a CAS, as seen in (2.28)
- Reduces the inductance, as seen in (2.10)
- Increases the reluctance of the air gap and improves the likelihood that the reluctance of the ferromagnetic portions of the circuit can be neglected
- Requires a smaller AC ripple voltage to generate an appreciable ripple current that can be measured with a sufficient SNR
- Easier to fabricate

However, increasing the length of the air gap also has several disadvantages as listed below:

- The likelihood of flux leakage and significant flux fringing increases
- More current is required to generate the same force and therefore a larger driver is required and more ohmic losses will be produced
- The inductance will get smaller relative to the resistance making the inductance-based self-sensing method more sensitive to resistance changes
- BEMF and flux linkage will be harder to detect making the high-speed self-sensing methods less robust to disturbances

In general, a CAS actuator needs to compromise between force characteristics, avoidance of nonlinearities and the robustness of the self-sensing methods when choosing a suitable air gap length. Since the CAS sensor should not produce a force, a smaller air gap length is more preferable, but is limited by practical fabrication tolerances and the SNR of the current ripple measurement.

5.1.1.6 Winding Design

When designing a CAS, one should always attempt to minimize the resistance since this lowers power loss and improves the accuracy of the self-sensing methods. Ideally, the available area for windings should be as large as possible so that larger-gauge conductors or several parallel strands of wire can be utilized to lower the coil resistance. However, increasing the available area for windings will increase the size of the CAS.

When choosing the number of windings, one needs to consider the amp-turns required to generate the peak force and the peak current that can be supplied by the available driver. For example, if a CAS required 1000 amp-turns and the driver could only supply 20A, then 50 or more windings would be required. Choosing a design with more windings will increase the inductance of the CAS and will help improve self-sensing but reduce the current response. For a CAS actuator, one needs to choose the number of windings to obtain an inductance that compromises between the force response and the self-sensing. For a CAS sensor, one would like to increase the number of windings to increase the inductance and improve the self-sensing measurements while ensuring an adequate SNR can be maintained when measuring the current ripple. In Section 2.2 it was noted that $P_c \propto I^2$ and $P_c \propto N^2$. Therefore, for a given amp-turn excitation, the number of windings has no impact on ohmic power loss. It should also be noted that $L_c \propto N^2$ and $R_c \propto N^2$ as seen in (2.15) and (2.24). Therefore, the electrical time constant is not impacted by the number of windings. Overall, the number of windings should be selected to obtain a desired inductance and to accommodate the available current limit of the driver hardware.

5.1.2 Sources of Self-Sensing Model Error

In the self-sensing models derived in Chapter 2, it can be noted that only resistance and inductance need to be characterized to determine plunger position. Naturally, if these parameters deviate from their characterized setpoint, the accuracy of the self-sensing methods will degrade. The sections below discuss potential sources of error that can affect the resistance and inductance, and mitigating strategies and factors.

5.1.2.1 Sources of Error that Affect Resistance

Accurately characterizing the resistance is important for a CAS actuator and a CAS sensor that is only operating with only two voltage sensors or a voltage sensor and a current sensor. It was seen in Figure 3.18 that a 2% deviation from the characterized resistance produced negligible error in the inductance-based measurement, but produced significant error in the BEMF-based and flux linkage-based measurements. In a practical application, a CAS may experience temperature changes that will create resistance changes that are much larger than 2%. These temperature changes could come as a result of changes to the ambient temperature or self-heating due to friction or ohmic loss. Fortunately, the inductance-based method inherently has a high degree of temperature immunity since often the reactance of a CAS will be significantly larger than the resistance. Therefore, as shown in Figure 3.18, the output of the fused complementary filter measurement will retain the high degree of temperature immunity that the inductance-based measurement had. It was also seen in Section 3.2.2 that an online measurement can be continuously employed to measure the resistance on a continuous bases to further improve the accuracy of the self-sensing measurement. However, it was seen that if the temperature changes too rapidly, it may not be possible to compensate for. If other factors such as the copper aging, causes the resistance to slowly change, the online resistance measurement would also be able to correct the self-sensing models. Overall, the CAS self-sensing methods are quite robust to resistance changes with several mitigations available, such as an online resistance measurement and sensor fusion.

If the plunger of a CAS is moved quick enough to generate appreciable eddy currents, or if the AC ripple frequency is set too high for the ferromagnetic material, then the resistance could acquire a frequency dependence. In particular, if eddy currents form, the terminal resistance will appear to increase. As long as this increased resistance is still negligible relative to the reactance, the inductance-based measurement will remain accurate. If the ripple voltage and ripple current are small relative to the driving signals, the BEMF-based and flux linkage-based methods may still be accurate, although eddy currents could create noticeable sinusoidal error at the ripple frequency. However, additional lowpass filters could be added to mitigate the error produced by the AC ripple eddy currents although this would impose an additional restriction on the maximum plunger movement frequency. Therefore, if resistance changes occur due to eddy currents generated by the AC ripple frequency, it is possible that the self-sensing of the CAS could remain accurate. However, if the eddy currents are generated by fast plunger movements, the eddy currents will cause the BEMF-based and flux linkage-based methods to become inaccurate. For high-speed CAS designs, it is important to design the CAS to avoid eddy currents as discussed in Section 1.1.6.

5.1.2.2 Sources of Error that Affect Inductance

The inductance model in (2.15) is based on the assumption that air gap reluctance dominates the reluctance of the magnetic circuit, making the ferromagnetic contributions negligible. If this assumption holds true, then a CAS is resistant to inductance changes that result from high-order effects in the ferromagnetic material. For example, effects that cause the permeability of the ferromagnetic material to change, such as temperature variation or aging, would only affect the reluctance of the ferromagnetic material and would still be negligible relative to the reluctance of the air gap. Even inductance changes due to eddy currents would be mitigated by the dominating air gap reluctance. However, if nonlinear effects such as eddy currents or magnetic saturation are large, the mitigating effect of the dominating air gap reluctance may not be enough to avoid changing the effective inductance of the CAS as was seen in Figure 3.33. Therefore, not only does designing a CAS with large air gaps help with peak force generation, but it also helps ensure the reluctance of the air gap dominates the inductance characteristics, leading to linear models that are resistant to nonideal effects.

Maintaining a constant air gap length is critical for the self-sensing methods of the CAS. Anything that causes the air gap length to change would alter the inductance of the CAS and would cause the inductance-position regression constants to fall out of calibration. There are several factors that could affect the air gap length:

- Thermal expansion of the stator and plunger material
- The inherent transverse stator force seen in Figure 3.8
- The plunger of a cuboid-shaped CAS rotating about its axis of motion
- External forces, such as a clamp to hold the CAS in place

All of these factors can be mitigated by designing a CAS with larger air gaps since the relative change in air gap length is less for larger air gaps. For example, an air gap length that is deformed by 0.1mm would have a more significant effect on a 0.5mm air gap than a 1mm air gap since the relative change is larger. To avoid changes in shape due to internal or external forces, one should ensure the CAS is designed to be very rigid so that it negligibly deforms under the stresses it is subjected to.

5.2 Comparison of CAS Technology with Similar Actuator and Sensor Technologies

The merit of the CAS technology can be appreciated by comparing its attributes with other traditional actuators. Table 5.1 ranks the CAS actuator against the other comparable translational actuator technologies discussed in Chapter 1. From the table, it is seen that the CAS actuator has the best self-sensing performance out of all of the listed actuators due to its accurate wide-bandwidth characteristics that are not encumbered by challenging nonlinear effects. Furthermore, like other solenoids, the CAS actuator has a simplistic design made of cheap and rugged materials, giving it a significant advantage over permanent magnet or piezoelectric actuators. However, the CAS actuator does struggle with certain attributes such as force-size density since its force output is small relative to its size. The CAS actuator is also relatively inefficient since holding a load would likely require more current than a variable air gap solenoid due to its low force-size density. The CAS actuator has better controllability than the other solenoids due to its highly-linear characteristics. However, it is important to recall that the CAS actuator is only able to generate a unidirectional force, and therefore is less versatile than a voice coil or piezoelectric actuator. Overall, it can be appreciated that the CAS actuator has notable strengths and weaknesses like the other listed actuators. Therefore, like other listed actuators, the CAS actuator has its own niche of applications that it would be well suited for. In particular the CAS actuator would excel at applications requiring low force and self-sensing while remaining inexpensive and robust in harsh environments. For example, the CAS actuator is expected to be well suited for regulators which require precision adjustments to control the delivery of a fluid. It is conceivable that the CAS actuator would be well-suited for the harsh environment of various automotive applications, such as exhaust gas recirculation valves or turbocharger wastegate regulators. However, validating the suitability of the CAS actuator for various applications remains a topic for future research.

Table 5.1 Ranked Comparison of Translational Actuator Technologies

Attribute	Variable Air Gap Solenoid	Proportional Face Solenoid	LSRM	Voice Coil	Piezoelectric Stack Actuator	CAS Actuator
Controllability[1]	6	4	5	1	1	3
Self-Sensing[2]	6	3	3	3	2	1
Force-Size Density[3]	2	6	4	2	1	5
Ruggedness[4]	1	1	1	5	6	1
Cost[5]	1	3	4	5	6	1
Stroke-Length Ratio[6]	5	2	1	2	6	2
Energy Efficiency[7]	2	5	3	6	1	4
Mechanical Speed[8]	3	3	3	2	1	3

---

[1] The CAS actuator has linear inductance characteristics and constant-force characteristics allowing it to maintain similar controllability characteristics throughout its stroke unlike a variable air gap solenoid or an LSRM. It also is not at risk of being pulled into an end stop unlike a proportional face solenoid. However, the CAS actuator can only apply a unidirectional force on the plunger unlike a voice coil or piezoelectric actuator.

[2] The CAS actuator is the only electromagnetic actuator proven to have two self-sensing methods that can be used simultaneously and fused to increase mechanical bandwidth. A piezoelectric actuator also has this ability, but suffers from nonlinear effects that are more difficult to robustly resolve. A variable air gap solenoid has nonlinear force and inductance characteristics throughout its entire stroke, making it the worst candidate for self-sensing out of the listed actuators.

[3] CAS actuators have similar force characteristics as proportional face solenoids and therefore have a notably lower force than the other categories of actuators listed. The force-size density of a CAS actuator is likely higher than a proportional face solenoid since CAS geometry can be more easily adapted to include extra teeth and air gaps to increase the output force.

[4] Permanent magnets and piezoelectric ceramics are more fragile and have relatively low temperature limits compared to common ferromagnetic materials.

[5] Permanent magnets and piezoelectric ceramics are expensive relative to common ferromagnetic materials. Therefore, voice coils and piezoelectric actuators are generally more expensive than solenoids or LSRMs. An LSRM uses more phases than a solenoid and therefore is assumed to be slightly more expensive.

[6] As discussed in Chapter 1, piezoelectric stack actuators can only displace a small amount relative to their length. Basic voice coil, CAS actuator and proportional face solenoid designs could all be built to achieve similar displacements. Variable air gap solenoids usually have high-force designs which require a small air gap and stroke. LSRMs use multiple phases to travel long distances that can easily exceed the stroke of the other listed actuators.

[7] Piezoelectric actuators are electrostatic actuators which require a very small current to account for leakage while holding a load. Electromagnetic actuators require an appreciable current while holding a load and therefore produce significantly larger ohmic losses. The energy efficiency of the LSRM and solenoids will generally be proportional to their force-size density. As noted in Chapter 1, voice coil actuators are very inefficient actuators.

[8] Piezoelectric actuators are noted as being very high-speed actuators while voice coil actuators are generally faster than LSRMs and solenoids since they have a large effective air gap length which leads to a very low reluctance and fast electrical response.

The CAS sensor, like the CAS actuator, also has significant commercial potential. Table 5.2 ranks and compares the CAS sensor with the inductive differential position sensors discussed in Chapter 1. From the table, it is seen that the CAS sensor has advantages over the conventional differential inductive position sensors. The most notable advantage is the improved bandwidth as the CAS sensor can utilize the BEMF-based or flux linkage-based method to increase the high-speed sensing abilities. Furthermore, the ferromagnetic stator of the CAS sensor creates well-defined flux paths that protect it from external magnetic fields unlike an LVDT or DVRT, which normally require external magnetic shielding. The well-defined flux paths also should reduce fringing effects and improve linearity. It is also important to recall that the CAS sensor has internal redundancy if operated with two voltage sensors and a current sensor; it was validated that if one of the voltage or current sensors fail, the CAS sensor can continue to operate with reduced accuracy. Furthermore, each CAS within a CAS sensor can produce its own inductance and resistance measurements, meaning that it can monitor its own health by ensuring the characteristics of each CAS remain matched. For example, a broken wire or a shorted wire could be detected by comparing the resistance measurements of the upper and lower CASs within a CAS sensor. This makes the CAS sensor ideal for critical-function sensors, such as the throttle position sensor of a vehicle. However, the CAS sensor does have notable disadvantages, with the most significant one being that it would need to be larger than an LVDT or DVRT to measure the same displacement. The CAS sensor also requires an AC and DC current, which are significantly larger than the AC current in an LVDT or DVRT. Therefore, the power consumption of the CAS sensor will be larger. The CAS sensor is also expected to cost more since it requires more ferromagnetic material than an LVDT or DVRT. Overall, for applications where larger, higher-power position sensors can be tolerated, the CAS sensor is expected to offer significant improvements over LVDTs and DVRTs, particularly when measuring high-speed movements or when robust redundancy and health monitoring attributes are required. Naturally, the CAS sensor will also allow the robust and noise-cancelling attributes of inductive differential position sensors to be extended to higher-speed applications than would be possible with a conventional LVDT or DVRT.

Table 5.2 Ranked Comparison of Inductive Differential Position Sensors

Attribute	LVDT	DVRT	CAS Sensor
Stroke-Length Ratio[1]	2	1	3
Linearity[2]	2	3	1
External Magnetic Field Resistance[3]	2	2	1
Bandwidth[4]	2	2	1
Cost[5]	1	1	3
Temperature Immunity[6]	3	1	1
Power Consumption[7]	1	1	3
Failure Redundancy[8]	2	2	1
Sensor Health Monitoring[9]	2	2	1

---

[1] DVRTs are smaller than LVDTs since they do not require primary and secondary coils. Figure 4.1b shows the stroke of a CAS sensor must be more than four times smaller than the length of the actuator since it must be divided by four plunger cores. Furthermore, the top and bottom plunger cores of a CAS sensor exit the stator. These factors lead to the CAS sensor having the least favorable stroke-length ratio.

[2] As discussed in Chapter 1, LVDTs are noted as being more linear than DVRTs. The CAS sensor is expected to be more linear than DVRTs since it does not introduce potential nonideal effects created by the mutual coupling between the top and bottom coils. The well-defined flux path through the stator may minimize fringing effects and allow the CAS sensor to be more linear than an LVDT.

[3] The CAS sensor is self-shielding since it has a ferromagnetic stator unlike an LVDT or DVRT.

[4] The CAS sensor is the only sensor listed that has been shown to simultaneously produce a low-speed and high-speed plunger measurement which can be fused to produce a wide-bandwidth measurement.

[5] The CAS sensor is expected to cost the most since it has a ferromagnetic stator that channels appreciable magnetic flux.

[6] As noted in Chapter 1, LVDTs without a center tap do not have inherent temperature cancellation.

[7] The CAS sensor will consume the most power as it requires a significant DC bias current unlike an LVDT or DVRT.

[8] Only the CAS actuator can continue operating if one of its voltage or current sensors fail.

[9] The CAS sensor can compare the resistance and inductance characteristics of the upper and lower CAS independently to infer the health of the sensor.

Chapter 6: Conclusion

In this dissertation, a novel CAS technology was proposed, developed and experimentally validated. The sections below summarize the contributions of the CAS technology to the field of actuators and sensors and proposes future research directions.

6.1 Summary CAS Technology and Research Contributions

The CAS technology proposed in this thesis contains components and implementations which are novel. The core components of the CAS technology can be visualized in Figure 6.1. As depicted, the CAS technology can be divided into an actuator and sensor subset. A CAS actuator can be described as the first electromagnetic actuator with the ability to simultaneously produce two unique plunger self-measurements. Similarly, a CAS sensor can be described as the first inductive-based differential sensor capable of simultaneously producing two unique plunger self-measurements. The novel geometry of the CAS sensor and actuator allow it to have linear-inductance and constant-force characteristics which are required for robust plunger position self-sensing.

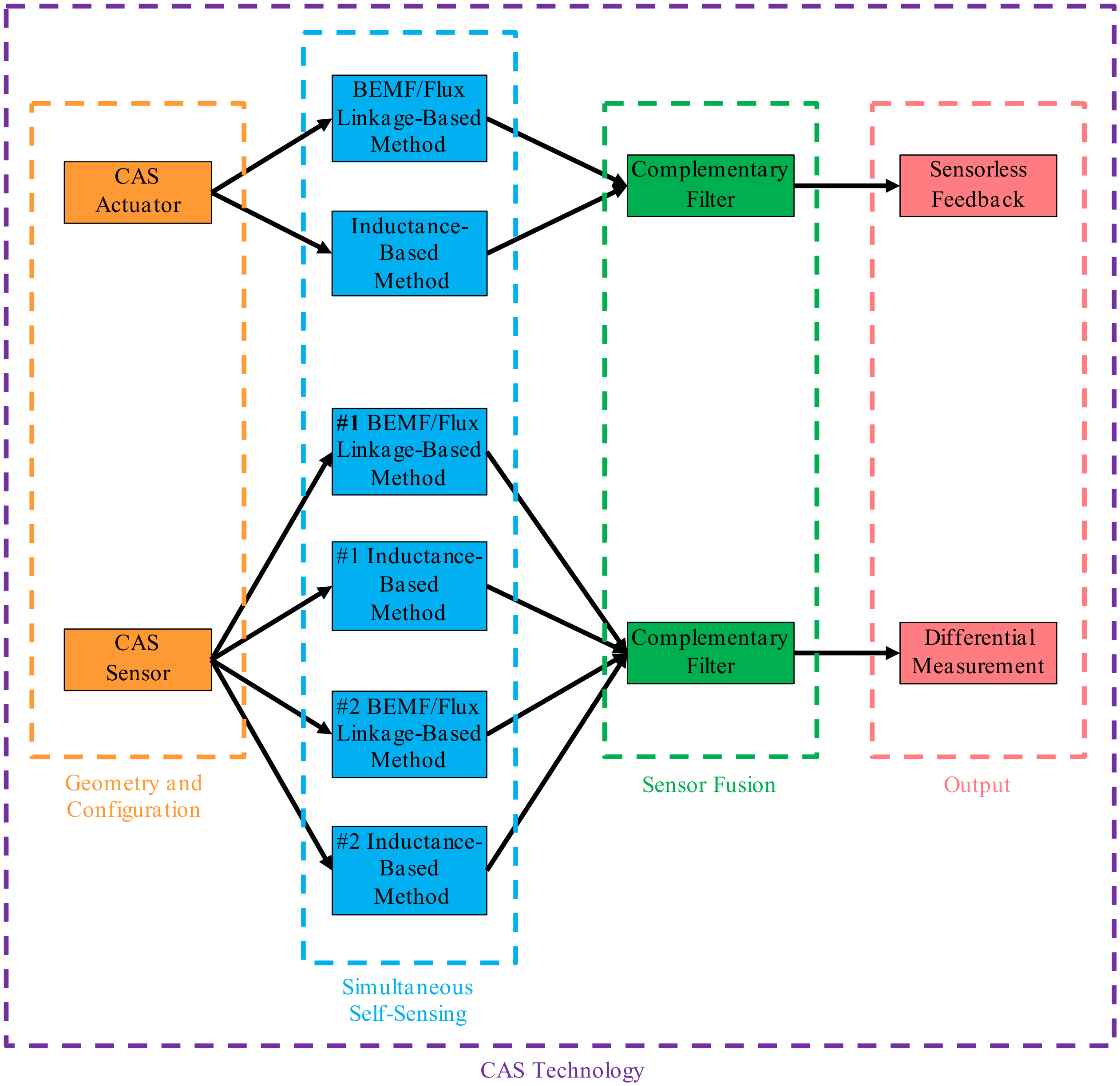

Figure 6.1 A diagram of the key components of the CAS Technology.

To validate the proposed qualitative features of the CAS technology, a proof-of-concept CAS actuator and CAS sensor were developed. The CAS actuator and CAS sensor were both designed to use a similar bolt-together design with identical silicon steel laminations. The CAS actuator was experimentally validated to be capable of performing robust 40Hz sensorless position control when tracking a 1mm/s ramp, a 10mm/s ramp and a step trajectory. The sensorless control results showed very similar performance to the laser vibrometer it was benchmarked against, with only slightly more overshoot being present for the 10mm/s ramp and step trajectories. The robust differential self-sensing attributes of the CAS sensor were experimentally validated to perform as hypothesized. In particular, the CAS sensor was demonstrated to self-sense its plunger position with less than 1% nonlinearity at both low and high plunger speeds. Furthermore, the inherent redundancy capabilities of the CAS sensor were validated by showing the CAS sensor could continue to operate with approximately less than 3% nonlinearity, even if the current sensor failed.

Using inductance, BEMF and flux linkage to self-sense plunger position is not an inherently new concept. However, the prototype CAS actuator experimentally validated that these self-sensing methods can be utilized simultaneously, which had never been demonstrated before. Furthermore, the self-sensing models in Chapter 2 and Chapter 4 are novel since they are derived for the unique CAS geometry. It is important to recall that these self-sensing methods are only well suited for either high-speed or low-speed plunger movements. Having access to multiple self-sensing methods with differing bandwidth characteristics allows sensor fusion techniques to be utilized to generate a single wide-bandwidth plunger position measurement. While theoretically, a CAS sensor or actuator could operate without a sensor fusion technique, it was demonstrated in practice that the BEMF-based or flux linkage-based methods would be challenging to use as standalone measurements. Therefore, sensor fusion could be considered an integral part of the CAS technology since it allows the accurate high-speed aspects of the BEMF-based or flux linkage-based methods to be salvaged. Sensor fusion allows the CAS actuator to produce wide-bandwidth feedback for sensorless plunger position control. It also allows the CAS sensor to produce a wide-bandwidth differential measurement. This allows the CAS actuator and sensor to be applicable for both low-speed and high-speed applications, which is a rare and valuable attribute.

6.2 Future Research

CAS technology is a novel and broad topic with a large potential for future research. The primary goal of this thesis work was to develop and experimentally prove the novel aspects of the CAS technology. To accomplish this goal, performance optimizations were not required. Therefore, the optimal design and implementation of a CAS actuator or sensor would have significant research potential. For example, a complementary filter may not lead to optimal performance, and therefore one could investigate whether other sensor fusion techniques, such as a Kalman filter, would be advantageous to use instead. One could also investigate how a CAS actuator performs with various controller implementations in an effort to achieve better sensorless plunger control.

Methods to overcome the limitations of the CAS technology is another topic of interest. In Figure 3.33 it was noted that the CAS actuator experiences an inductance-current nonlinearity. While this nonlinearity was overcome with additional current and displacement restrictions, modeling this nonlinearity with a regression or lookup table would improve accuracy and allow these restrictions to be removed. One could also look into overcoming the upper speed limits of self-sensing imposed by hardware and nonlinear factors, such as eddy currents. For example, eddy currents could be avoided by investigating alternative magnetic materials, such as ferromagnetic powder cores.

Furthermore, CAS technology research is already underway. One ongoing project at UBC Okanagan is investigating a derivative of the CAS sensor geometry presented in this thesis that uses a design without a ferromagnetic stator. The success of this research will allow the size and cost of the CAS sensor to be significantly reduced and will also greatly mitigate the effects of eddy currents at the expense of linearity and a lack of self-shielding. Westport Fuel Systems Canada Inc. has helped develop and patent the CAS technology and are exploring potential applications within their product lines to apply the CAS technology [137]. Overall, the practical, rugged and robust features of the CAS technology make it applicable for many commercial applications which could be explored through future research. Lastly, it is important to note the CAS technology possesses several of the attributes demanded by future Industry 4.0 cyber-physical systems. CAS technology exhibits characteristics of smart actuators that can self-sense position without a dedicated position sensor, and smart sensors which can self-monitor their health with inherent built-in redundancy. Therefore, the CAS technology will be of interest to the ongoing research and progress towards the fourth industrial revolution.

Bibliography

[1] K. Zhou, T. Liu and L. Zhou, "Industry 4.0: Towards future industrial opportunities and challenges," in *2015 12th International Conference on Fuzzy Systems and Knowledge Discovery*, Zhangjiajie, 2015.

[2] Y. Lu, "Industry 4.0: A survey on technologies, applications and open research issues," *Journal of Industrial Information Integration,* vol. 6, pp. 1-10, 2017.

[3] N. König, Y. Carbon, M. Nienhaus and E. Grasso, "A Self-Sensing Method for Electromagnetic Actuators with Hysteresis Compensation," *Energies,* vol. 14, no. 20, pp. 1-19, 2021.

[4] M. N. Sadiku, Y. Wang, S. Cui and S. M. Musa, "Cyber-physical systems: a literature review," *European Scientific Journal,* vol. 12, no. 36, pp. 52-58, 2017.

[5] J. Lee, B. Bagheri and H.-A. Kao, "A Cyber-Physical Systems architecture for Industry 4.0-based manufacturing systems," *Manufacturing Letters,* vol. 3, pp. 18-23, 2015.

[6] I. Yang, D. Kim and D. Lee, "Fault-tolerant control strategy based on control allocation using smart actuators," Nice, 2010.

[7] N. Jazdi, "Cyber physical systems in the context of Industry 4.0," in *IEEE International Conference on Automation, Quality and Testing*, Cluj-Napoca, 2014.

[8] M. D. Noh and E. H. Maslen, "Self-sensing magnetic bearings using parameter estimation," *IEEE Transactions on Instrumentation and Measurement,* vol. 46, no. 1, pp. 45-50, 1997.

[9] B. Hanson and M. Levesley, "Self-sensing applications for electromagnetic actuators," *Sensors and Actuators A: Physical,* vol. 116, no. 2, pp. 345-351, 2004.

[10] B. A. Reinholz and R. J. Seethaler, "Design and Validation of a Variable Reluctance Differential Solenoid Transducer," *IEEE Sensors,* vol. 19, no. 23, pp. 11063-11071, 2019.

[11] A. G. Cockbain and P. J. Harrop, "The temperature coefficient of capacitance," *Journal of Physics D: Applied Physics,* vol. 1, no. 2, pp. 1109-1115, 1968.

[12] R. Groves, D. L. Harame and D. Jadus, "Temperature dependence of Q and inductance in spiral inductors fabricated in a silicon-germanium/BiCMOS technology," *IEEE Journal of Solid-State Circuits,* vol. 32, no. 9, pp. 1455-1459, 1997.

[13] S. Takagi, "A hot-wire anemometer compensated for ambient temperature variations," *Journal of Physics E: Scientific Instruments,* vol. 19, no. 9, pp. 739-743, 1986.

[14] A. J. Fleming and K. K. Leang, Design, modeling and control of nanopositioning systems, Cham: Springer International Publishing, 2014.

[15] S. Ruoho, J. Kolehmainen, J. Ikaheimo and A. Arkkio, "Interdependence of Demagnetization, Loading, and Temperature Rise in a Permanent-Magnet Synchronous Motor," *IEEE Transactions on Magnetics,* vol. 46, no. 3, pp. 949-953, 2010.

[16] S.-B. Lee and T. G. Habetler, "An online stator winding resistance estimation technique for temperature monitoring of line-connected induction machines," *IEEE Transactions on Industry Applications,* vol. 39, no. 3, pp. 685-694, 2003.

[17] Bunting Magnetics Europe Ltd., "Temperature Effects on Neodymium Iron Boron, NdFeB, magnets," [Online]. Available: https://e-magnetsuk.com/neodymium_magnets/temperature_ratings.aspx. [Accessed 04 17 2020].

[18] T. Sebastian, "Temperature effects on torque production and efficiency of PM motors using NdFeB magnets," *IEEE Transactions on Industry Applications,* vol. 31, no. 2, pp. 353-357, 1995.

[19] J. Fialka, P. Benes, L. Michlovska, S. Klusacek, S. Pikula, P. Dohnal and Z. Havranek, "Measurement of thermal depolarization effects in piezoelectric coefficients of soft PZT ceramics via the frequency and direct methods," *Journal of the European Ceramic Society,* vol. 36, no. 11, pp. 2727-2738, 2016.

[20] R. Bayindir, C. Ocak and İ. Topaloğlu, "Investigation of the effect of magnet thickness on output power and torque of PM BLDC machines using parametric approach method," in *2011 International Conference on Power Engineering, Energy and Electrical Drives, Malaga*, Malaga, 2011.

[21] E. A. Boulter and G. C. Stone, "Historical development of rotor and stator winding insulation materials and systems," *IEEE Electrical Insulation Magazine,* vol. 20, no. 3, pp. 25-39, 2004.

[22] H. Yang, C. Zhou, X. Liu, Q. Zhou, G. Chen, W. Li and H. Wang, "Piezoelectric properties and temperature stabilities of Mn-and Cu-modified BiFeO3–BaTiO3 high temperature ceramics," *Journal of the European Ceramic Society,* vol. 33, no. 6, pp. 1177-1183, 2013.

[23] C.-Y. Chen, G. T.-C. Chiu, C.-C. Cheng and H. Peng, "Passive voice coil feedback control of closed-box subwoofer systems," *Proceedings of the Institution of Mechanical Engineers, Part C: Journal of Mechanical Engineering Science,* vol. 214, no. 7, pp. 995-1005, 2000.

[24] J. M. D. Coey, "Permanent magnets: Plugging the gap," *Scripta Materialia,* vol. 67, no. 6, pp. 524-529, 2012.

[25] T. Stevenson, D. G. Martin, P. I. Cowin, A. Blumfield and A. J. Bell, "Piezoelectric materials for high temperature transducers and actuators," *Journal of Materials Science: Materials in Electronics,* vol. 26, no. 12, pp. 9256-9267, 2015.

[26] K. M. Talluru, V. Kulandaivelu, N. Hutchins and I. Marusic, "A calibration technique to correct sensor drift issues in hot-wire anemometry," *Measurement Science and Technology,* vol. 25, pp. 1-6, 2014.

[27] A. Zambrano and H. G. Kerkhoff, "Determination of the drift of the maximum angle error in AMR sensors due to aging," in *2016 IEEE 21st International Mixed-Signal Testing Workshop*, Sant Feliu de Guixols, 2016.

[28] K. Shcheglov, C. Evans, R. Gutierrez and T. K. Tang, "Temperature dependent characteristics of the JPL silicon MEMS gyroscope," in *2000 IEEE Aerospace Conference. Proceedings*, Big Sky, 2000.

[29] Y. Cao and X. B. Chen, "A Survey of Modeling and Control Issues for Piezo-electric Actuators," *Journal of Dynamic Systems, Measurement, and Control,* vol. 137, no. 1, pp. 1-13, 2015.

[30] D. Hughes and J. T. Wen, "Preisach modeling of piezoceramic and shape memory alloy hysteresis," *Smart Materials and Structures,* vol. 6, no. 3, pp. 287-300, 1997.

[31] P. R. Dahl, "Solid friction damping of mechanical vibrations," *AIAA journal,* vol. 14, no. 12, pp. 1675-1682, 1976.

[32] D. C. Jiles and D. L. Atherton, "Theory of ferromagnetic hysteresis," *Journal of magnetism and magnetic materials ,* vol. 31, pp. 48-60, 1986.

[33] Spang & Company, "Learn More about Powder Cores," Magnetics, 2018. [Online]. Available: https://www.mag-inc.com/products/Powder-Cores/Learn-More-about-Powder-Cores. [Accessed 18 April 2020].

[34] J. O. Aibangbee and O. Onohaebi, "Ferromagnetic materials characteristics: Their Application in Magnetic Core Design Using Hysteresis Loop Measurements," *American Journal of Engineering Research,* vol. 7, no. 7, pp. 113-119, 2018.

[35] R. Szewczyk, "Technical BH saturation magnetization curve models for SPICE, FEM and MoM simulations," *Journal of Automation Mobile Robotics and Intelligent Systems,* vol. 10, no. 2, pp. 3-7, 2016.

[36] K. Yamazaki, "Torque and efficiency calculation of an interior permanent magnet motor considering harmonic iron losses of both the stator and rotor," *IEEE Transactions on Magnetics,* vol. 39, no. 3, pp. 1460-1463, 2003.

[37] F. M. Khater, R. D. Lorenz, D. W. Novotny and K. Tang, "Selection of flux level in field-oriented induction machine controllers with consideration of magnetic saturation effects," *IEEE Transactions on Industry Applications,* Vols. IA-23, no. 2, pp. 276-282, 1987.

[38] B. A. Reinholz and R. J. Seethaler, "Experimental validation of a cogging-torque-assisted valve actuation system for internal combustion engines," *IEEE/ASME transactions on mechatronics,* vol. 21, no. 1, pp. 453-459, 2015.

[39] H. Polinder, J. G. Slootweg, M. J. Hoeijmakers and J. C. Compter, "Modelling of a linear PM machine including magnetic saturation and end effects: Maximum force to current ratio," *IEEE International Electric Machines and Drives Conference,* vol. 2, pp. 805-811, 2003.

[40] J. M. Bostock-Smith, "The jumping ring and Lenz's law—an analysis," *Physics Education,* vol. 43, no. 3, pp. 265-269, 2008.

[41] E. J. Tarasiewicz, A. S. Morched, A. Narang and E. P. Dick, "Frequency dependent eddy current models for nonlinear iron cores," *IEEE Transactions on Power Systems,* vol. 8, no. 2, pp. 588-597, 1993.

[42] S. Han, T. M. Jahns and Z. Q. Zhu, "Analysis of Rotor Core Eddy-Current Losses in Interior Permanent-Magnet Synchronous Machines," *IEEE Transactions on Industry Applications,* vol. 46, no. 1, pp. 196-205, 2010.

[43] Y. Kawase, T. Yamaguchi, S. Sano, M. Igata, K. Ida and A. Yamagiwa, "3-D eddy current analysis in a silicon steel sheet of an interior permanent magnet motor," *IEEE transactions on magnetics,* vol. 39, no. 3, pp. 1448-1451, 2003.

[44] S. Xue, J. Feng, S. Guo, J. Peng, W. Q. Chu and Z. Q. Zhu, "A new iron loss model for temperature dependencies of hysteresis and eddy current losses in electrical machines," *IEEE Transactions on Magnetics,* vol. 54, no. 1, pp. 1-10, 2017.

[45] K. Hwang, T. W. Seo, B. Song and J. H. Kim, "Shorted Turn in the Flat Coil Actuator for Fast Initial Response," *Journal of Magnetics,* vol. 17, no. 1, pp. 56-60, 2012.

[46] B. A. Paden, S. T. Snyder, B. E. Paden and M. R. Ricci, "Modeling and Control of an Electromagnetic Variable Valve Actuation System," *IEEE/ASME Transactions on mechatronics,* vol. 20, no. 6, pp. 2654-2665, 2015.

[47] J. Millinger, O. Wallmark and J. Soulard, "High-Frequency Characterization of Losses in Fully Assembled Stators of Slotless PM Motors," *IEEE Transactions on Industry Applications,* vol. 54, no. 3, pp. 2265-2275, 2018.

[48] A. Boglietti, P. Ferraris, M. Lazzari and M. Pastorelli, "Change of the iron losses with the switching supply frequency in soft magnetic materials supplied by PWM inverter," *IEEE Transactions on Magnetics,* vol. 31, no. 6, pp. 4250-4252, 1995.

[49] K. G. N. B. Abeywickrama, T. Daszczynski, Y. V. Serdyuk and S. M. Gubanski, "Determination of Complex Permeability of Silicon Steel for Use in High-Frequency Modeling of Power Transformers," *IEEE Transactions on Magnetics,* vol. 44, no. 4, pp. 438-444, 2008.

[50] R. Rashedin and T. Meydan, "Solenoid actuator for loudspeaker application," *Sensors and Actuators A: Physical,* vol. 129, pp. 220-223, 2006.

[51] Arnold Magnetic Technologies, "Soft Magnetic Applications Guide," 2015. [Online]. Available: https://www.arnoldmagnetics.com/wp-content/uploads/2017/10/FINAL_Tech-Library_Guides_Soft-Magnetics-Application-Guide.pdf. [Accessed 21 04 2020].

[52] K. J. Sunday and M. L. Taheri, "NiZnCu-ferrite coated iron powder for soft magnetic composite applications," *Journal of Magnetism and Magnetic Materials,* vol. 463, pp. 1-6, 2018.

[53] C. W. T. McLyman and A. P. Wagner, "Designing high frequency AC inductors using ferrite and molypermalloy powder cores (MPP)," in *1985 IEEE Power Electronics Specialists Conference (ESA SP-230)*, Toulouse, 1985.

[54] Z. Yang, H. Suryanarayana and F. Wang, "An Improved Design Method for Gapped Inductors Considering Fringing Effect," in *2019 IEEE Applied Power Electronics Conference and Exposition (APEC)*, Anaheim, 2019.

[55] H. Chang-Chou and Y. H. Cho, "Effects of leakage flux on magnetic fields of interior permanent magnet synchronous motors," *IEEE transactions on magnetics,* vol. 37, no. 4, pp. 3021-3024, 2001.

[56] H. C. Karmaker, "Stray losses in large synchronous machines," *IEEE Transactions on Energy Conversion,* vol. 7, no. 1, pp. 148-153, 1992.

[57] P. K. Sekhar and V. Uwizeye, "Review of sensor and actuator mechanisms for bioMEMS," in *MEMS for Biomedical Applications*, Woodhead Publishing, 2012, pp. 57-76.

[58] H. J. M. T. S. Adriaens, W. L. De Koning and R. Banning, "Modeling piezoelectric actuators," *IEEE/ASME Transactions on Mechatronics,* vol. 5, no. 4, pp. 331-341, 2000.

[59] P. Zhang, "Sensors and actuators," in *Advanced Industrial Control Technology*, William Andrew Publishing, 2010, pp. 73-116.

[60] H. Nouraei, R. Ben-Mrad and A. N. Sinclair, "Development of a piezoelectric fuel injector," *IEEE Transactions on Vehicular Technology,* vol. 65, no. 3, pp. 1162-1170, 2015.

[61] Q. Xu, "Adaptive discrete-time sliding mode impedance control of a piezoelectric microgripper," *IEEE Transactions on Robotics,* vol. 29, no. 3, pp. 663-673, 2013.

[62] H. Jung and D. G. Gweon, "Creep characteristics of piezoelectric actuators," *Review of scientific Instruments,* vol. 71, no. 4, pp. 1896-1900, 2000.

[63] M. N. Islam and R. J. Seethaler, "Sensorless Position Control For Piezoelectric Actuators Using A Hybrid Position Observer," *IEEE/ASME TRANSACTIONS ON MECHATRONICS,* vol. 19, no. 2, pp. 667-675, 2014.

[64] J. J. Dosch, D. J. Inman and E. Garcia, "A Self-Sensing Piezoelectric Actuator for Collocated Control," *Journal of Intelligent Material Systems and Structures,* vol. 3, no. 1, pp. 166-185, 1992.

[65] P. C. Sen, Principles of Electronic Machines and Power Electronics, John Wiley & Sons, 2014.

[66] Z. K. Kocabiçak, E. E. Topçu and İ. Yüksel, "The development of electromechanical valve actuator and the comparison with the camshaft driven system," in *2013 9th Asian Control Conference (ASCC)*, Istanbul, 2013.

[67] K. W. Lim, N. C. Cheung and M. F. Rahman, "Proportional control of a solenoid actuator," in *Proceedings of IECON'94 - 20th Annual Conference of IEEE Industrial Electronics*, Bologna, 1994.

[68] E. Ramirez-Laboreo and C. Sagues, "Reluctance actuator characterization via FEM simulations and experimental tests," *Mechatronics,* vol. 56, pp. 58-66, 2018.

[69] E. Ramirez-Laboreo, E. Moya-Lasheras and C. Sagues, "Real-Time Electromagnetic Estimation for Reluctance Actuators," *IEEE Transactions on Industrial Electronics,* vol. 66, no. 3, pp. 1952-1961, 2019.

[70] Y. Liu, Y. T. Zhang, H. Tian and J. Qin, "Research and applications for control strategy of high-pressure common rail injection system in diesel engine," in *2008 IEEE Vehicle Power and Propulsion Conference*, Harbin, 2008.

[71] H.-W. Joo, Y.-H. Eum, H.-T. Park and S. Park, "Dynamic analysis of linear electromagnetic solenoid for Electric Vehicle Relay," in *The XIX International Conference on Electrical Machines-ICEM 2010*, Rome, 2010.

[72] E. Moya-Lasheras, C. Sagues and S. Llorente, "An efficient dynamical model of reluctance actuators with flux fringing and magnetic hysteresis," *Mechatronics,* vol. 74, p. 102500, 2021.

[73] M. F. Rahman, N. C. Cheung and K. W. Lim, "Position estimation in solenoid actuators," *IEEE Transactions on Industry Applications,* vol. 32, no. 3, pp. 552-559, 1996.

[74] C. Shengnian, Y. Man and L. Yu, "Sensorless position detection in solenoid valve based on inductance model," in *Proceedings 2013 International Conference on Mechatronic Sciences, Electric Engineering and Computer (MEC)*, Shenyang, 2013.

[75] T. Hao and Y. Zhao, "Coil inductance model based solenoid on–off valve spool displacement sensing via laser calibration," *Sensors,* vol. 18, no. 12, pp. 1-14, 2018.

[76] J. Maridor, N. Katic, Y. Perriard and D. Ladas, "Sensorless position detection of a linear actuator using the resonance frequency," in *2009 International Conference on Electrical Machines and Systems*, Tokyo, 2009.

[77] S. T. Wu and W. N. Chen, "Self-sensing of a solenoid valve via phase detection," in *2009 IEEE/ASME International Conference on Advanced Intelligent Mechatronics*, Singapore, 2009.

[78] J. C. Renn and Y. S. Chou, "Sensorless plunger position control for a switching solenoid," *JSME International Journal Series C Mechanical Systems, Machine Elements and Manufacturing,* vol. 47, no. 2, pp. 637-645, 2004.

[79] B. P. Lequesne, "Finite-element analysis of a constant-force solenoid for fluid flow control," *IEEE transactions on industry applications,* vol. 24, no. 4, pp. 574-581, 1988.

[80] S. N. Yun, Y. B. Ham and J. H. Park, "New approach to design control cone for electro-magnetic proportional solenoid actuator," in *2012 IEEE/ASME International Conference on Advanced Intelligent Mechatronics (AIM)*, Kachsiung, 2012.

[81] S.-N. Yun, Y.-B. Ham and H.-B. Shin, "Proportional Fuel Flow Control Valve for Diesel Vehicle," in *International Conference on Control, Automation and Systems*, Seoul, 2008.

[82] I. Dülk and T. Kovácsházy, "Modelling of a linear proportional electromagnetic actuator and possibilities of sensorless plunger position estimation," in *2011 12th International Carpathian Control Conference (ICCC)*, Velke Karlovice, 2011.

[83] N. D. Vaughan and J. B. Gamble, "The modeling and simulation of a proportional solenoid valve," *Journal of Dynamic Systems, Measurement, and Control,* vol. 118, no. 1, pp. 120-125, 1996.

[84] P. J. Lawrenson, J. M. Stephenson, P. T. Blenkinsop, J. Corda and N. N. Fulton, "Variable-speed switched reluctance motors," *IEE Proceedings B (Electric Power Applications),* vol. 127, no. 4, pp. 253-265, 1980.

[85] S. Darabi, Y. A. Beromi and H. R. Izadfar, "Comparison of two common configurations of LSRM: Transverse flux and longitudinal flux," in *2012 International Conference and Exposition on Electrical and Power Engineering*, Lasi, 2012.

[86] W.-C. Gan and N. C. Cheung, "Design of a linear switched reluctance motor for high precision applications," in *IEMDC 2001. IEEE International Electric Machines and Drives Conference*, Cambridge, 2001.

[87] I. Husain and M. Ehsani, "Torque ripple minimization in switched reluctance motor drives by PWM current control," *IEEE transactions on power electronics,* vol. 11, no. 1, pp. 83-88, 1996.

[88] B. S. Lee, H. K. Bae, P. Vijayraghavan and R. Krishnan, "Design of a linear switched reluctance machine," in *Conference Record of the 1999 IEEE Industry Applications Conference. Thirty-Forth IAS Annual Meeting*, Phoenix, 1999.

[89] C. T. Liu and J. L. Kuo, "Experimental investigation and 3-D modelling of linear variable-reluctance machine with magnetic-flux decoupled windings," *IEEE Transactions on Magnetics,* vol. 30, no. 6, pp. 4737-4739, 1994.

[90] J. G. Amoros and P. Andrada, "Sensitivity analysis of geometrical parameters on a double-sided linear switched reluctance motor," *IEEE Transactions on Industrial Electronics,* vol. 57, no. 1, pp. 311-319, 2009.

[91] H. S. Lim, R. Krishnan and N. S. Lobo, "Design and Control of a Linear Propulsion System for an Elevator Using Linear Switched Reluctance Motor Drives," *IEEE Transactions on Industrial Electronics,* vol. 55, no. 2, pp. 534-542, 2008.

[92] U. S. Deshpande, J. J. Cathey and E. Richter, "High-force density linear switched reluctance machine," *IEEE Transactions on Industry Applications,* vol. 31, no. 2, pp. 345-352, 1995.

[93] S. W. Zhao, N. C. Cheung, W.-C. Gan and J. M. Yang, "Position estimation and error analysis in linear switched reluctance motors," *IEEE transactions on instrumentation and measurement,* vol. 58, no. 8, pp. 2815-2823, 2009.

[94] M. Ehsani, I. Husain and A. B. Kulkarni, "Elimination of discrete position sensor and current sensor in switched reluctance motor drives," *IEEE Transactions on Industry Applications,* vol. 28, no. 1, pp. 128-135, 1992.

[95] M. Ehsani, I. Husain, S. Mahajan and K. R. Ramani, "New modulation encoding techniques for indirect rotor position sensing in switched reluctance motors," *IEEE Transactions on Industry Applications,* vol. 30, no. 1, pp. 85-91, 1994.

[96] I. Husain and M. Ehsani, "Rotor position sensing in switched reluctance motor drives by measuring mutually induced voltages," *IEEE Transactions on Industry Applications,* vol. 30, no. 3, pp. 665-672, 1994.

[97] K. B. Saad and A. Mbarek, "Half step position sensorless control of a Linear Switched Reluctance Motor based on back EMF," *Automatika: časopis za automatiku, mjerenje, elektroniku, računarstvo i komunikacije,* vol. 57, no. 3, pp. 660-671, 2016.

[98] J. P. Lyons, S. R. MacMinn and M. A. Preston, "Flux-current methods for SRM rotor position estimation," in *Conference Record of the 1991 IEEE Industry Applications Society Annual Meeting*, Dearborn, 1991.

[99] W. F. Ray and I. H. Al-Bahadly, "A sensorless method for determining rotor position for switched reluctance motors," in *1994 Fifth International Conference on Power Electronics and Variable-Speed Drives*, London, 1994.

[100] Q. Wang, H. Chen, T. Xu, J. Yuan, J. Wang and S. Abbas, "Inductance estimation method for linear switched reluctance machines considering iron losses," *IET Electric Power Applications,* vol. 10, no. 3, pp. 181-188, 2016.

[101] Y. Li and G. C. Chiu, "Control of loudspeakers using disturbance-observer-type velocity estimation," *IEEE/ASME Transactions on Mechatronics,* vol. 10, no. 1, pp. 111-117, 2005.

[102] K. A. Poornima and T. S. Hsu, "Moving magnet loudspeaker system with electronic compensation," *IEE Proceedings-Circuits, Devices and Systems,* vol. 148, no. 4, pp. 211-216, 2001.

[103] Y. Konishi, H. Okuizumi and T. Ohno, "PIV measurement of a flying table tennis ball," *Procedia engineering,* vol. 147, no. 1, pp. 104-109, 2016.

[104] S. W. Youn, J. J. Lee, H. S. Yoon and C. S. Koh, "A new cogging-free permanent-magnet linear motor," *IEEE Transactions on Magnetics,* vol. 44, no. 7, pp. 1785-1790, 2008.

[105] J. Kordík, Z. Broučková, T. Vít, M. Pavelka and Z. Trávníček, "Novel methods for evaluation of the Reynolds number of synthetic jets," *Experiments in fluids ,* vol. 55, no. 6, p. 1757, 2014.

[106] V. Lemarquand, R. Ravaud and G. Lemarquand, "A new linear voice-coil motor for ironless loudspeakers: Analytical study," in *The XIX International Conference on Electrical Machines-ICEM 2010*, Rome, 2010.

[107] R. C. Becerra and M. Ehsani, "High-speed torque control of brushless permanent magnet motors," *IEEE Transactions on Industrial Electronics,* vol. 35, no. 3, pp. 402-406, 1988.

[108] R. L. Bailey, "Lesser known applications of ferrofluids," *Journal of magnetism and magnetic materials,* vol. 39, no. 1-2, pp. 178-182, 1983.

[109] M. R. Bai and H. Wu, "Robust control of a sensorless bass-enhanced moving-coil loudspeaker system," *The Journal of the Acoustical Society of America,* vol. 105, no. 6, pp. 3283-3289, 1999.

[110] M. Martino, A. Danisi, R. Losito, A. Masi and G. Spiezia , "Design of a linear variable differential transformer with high rejection to external interfering magnetic field," *IEEE Transactions on magnetics,* vol. 46, no. 2, pp. 674-677, 2010.

[111] K. Ara, "A differential transformer with temperature-and excitation-independent output," *IEEE Transactions on Instrumentation and Measurement,* vol. 21, no. 3, pp. 249-255, 1972.

[112] M. Mirzaei, P. Ripka and V. Grim, "A Position Sensor With Novel Configuration of Linear Variable Differential Transformer," *IEEE Sensors Journal,* vol. 21, no. 20, pp. 22899-22907, 2021.

[113] W. Petchmaneelumka, P. Mano and V. Riewruja, "Linear Variable Differential Transformer Temperature Compensation Technique," *Sensors and Materials,* vol. 30, no. 10, pp. 2171-2181, 2018.

[114] F. F. Yassa and S. L. Garverick, "A multichannel digital demodulator for LVDT/RVDT position sensors," *IEEE Journal of Solid-State Circuits,* vol. 25, no. 2, pp. 441-450, 1990.

[115] C. W. De Silva, Mechatronics : An Integrated Approach, CRC Press, 2005.

[116] H. Mandal, S. K. Bera, S. Saha, P. K. Sadhu and S. C. Bera, "Study of a Modified LVDT Type Displacement Transducer With Unlimited Range," *IEEE Sensors Journal,* vol. 18, no. 23, pp. 9501-9514, 2018.

[117] R. M. Ford, R. S. Weissbach and D. R. Loker, "A novel DSP-based LVDT signal conditioner," *IEEE Transactions on Instrumentation and Measurement,* vol. 50, no. 3, pp. 768-773, 2001.

[118] G. W. Midgley, D. Howe and P. H. Mellor, "Improved Linearity Linear Variable Differential Transformers (LVDTs) Through the Use of Alternative Magnetic Materials," in *Electric and Magnetic Fields*, Boston, Springer, 1995, pp. 311-314.

[119] C. J. Allred, M. R. Jolly and G. D. Buckner, "Real-time estimation of helicopter blade kinematics using integrated linear displacement sensors," *Aerospace Science and Technology,* vol. 42, pp. 274-286, 2015.

[120] S. Hao, "Analysis of the self-calibration process in a displacement sensor in applications of hip or knee implants," *Sensors & Transducers,* vol. 141, no. 6, pp. 106-118, 2012.

[121] M. De Volder, J. Coosemans, R. Puers and D. Reynaerts, "Characterization and control of a pneumatic microactuator with an integrated inductive position sensor," *Sensors and Actuators A: Physical,* vol. 141, no. 1, pp. 192-200, 2008.

[122] A. Flammini, D. Marioli, E. Sisinni and A. Taroni, "A multichannel DSP-based instrument for displacement measurement using differential variable reluctance transducer," *IEEE transactions on instrumentation and measurement,* vol. 54, no. 1, pp. 178-183, 2005.

[123] T. Aho, V. Sihvo, J. Nerg and J. Pyrhonen, "Rotor materials for medium-speed solid-rotor induction motors," in *2007 IEEE International Electric Machines & Drives Conference*, Antalya, 2007.

[124] N. Storey, Electronics: a systems approach, Harlow: Pearson Education Limited, 2009.

[125] A. D. Cheok and Z. Wang, "DSP-based automated error-reducing flux-linkage-measurement method for switched reluctance motors," *IEEE Transactions on Instrumentation and Measurement,* vol. 56, no. 6, pp. 2245-2253, 2007.

[126] B. A. Reinholz and R. J. Seethaler, "Flux Linkage Sensor Fusion of a Variable Reluctance Differential Solenoid Transducer," in *International Conference on Manipulation, Automation and Robotics at Small Scales (MARSS)*, 2020.

[127] W. T. Higgins, "A comparison of complementary and Kalman filtering," *IEEE Transactions on Aerospace and Electronic Systems,* vol. 11, no. 3, pp. 321-325, 1975.

[128] I. Tariqul, M. S. Islam, M. Shajid-Ul-Mahmud and M. Hossam-E-Haider, "Comparison of complementary and Kalman filter based data fusion for attitude heading reference system," in *AIP Conference Proceedings*, 2017.

[129] M. Nowicki, J. Wietrzykowski and P. Skrzypczyński, "Simplicity or flexibility? Complementary Filter vs. EKF for orientation estimation on mobile devices," in *2015 IEEE 2nd International Conference on Cybernetics (CYBCONF)*, Gdynia, 2015.

[130] H. Q. T. Ngo, T. P. Nguyen, V. N. S. Huynh, T. S. Le and C. T. Nguyen, "Experimental comparison of complementary filter and kalman filter design for low-cost sensor in quadcopter," in *2017 International Conference on System Science and Engineering (ICSSE)*, Ho Chi Minh City, 2017.

[131] J. H. Dellinger, The temperature coefficient of resistance of copper, vol. 147, US Government Printing Office, 1911.

[132] O. Umezawa and K. Ishikawa, "Electrical and thermal conductivities and magnetization of some austenitic steels, titanium and titanium alloys at cryogenic temperatures," *Cryogenics,* vol. 32, no. 10, pp. 873-880, 1992.

[133] D. Yaping, T. C. Cheng and A. S. Farag, "Principles of power-frequency magnetic field shielding with flat sheets in a source of long conductors," *IEEE Transactions on Electromagnetic Compatibility,* vol. 38, no. 3, pp. 450-459, 1996.

[134] Century Spring Corp, "Catalog," 2015. [Online]. Available: https://www.centuryspring.com/wp-content/uploads/2015/12/csc_catalog_web.pdf. [Accessed 15 June 2021].

[135] S. K. Chung, "Flatness-Based End-Control of a Gas Exchange Solenoid Actuator for IC Engines," University of Alberta, 2005.

[136] International Rectifier, "IRG4BC40WSPbF," 2010. [Online]. Available: https://www.infineon.com/dgdl/irg4bc40wspbf.pdf?fileId=5546d462533600a4015356434e5622a2. [Accessed 19 June 2021].

[137] B. Reinholz, R. Seethaler, G. McTaggart-Cowan, A. Singh and D. Reinholz, "Solenoid Apparatus and Methods". International Patent WO2020186358, 20 3 2020.

[138] Texas Instruments Inc., "OPA548 High-Voltage, High-Current Operation Amplifier," 2019. [Online]. Available: https://www.ti.com/lit/ds/symlink/opa548.pdf?ts=1594210979826&ref_url=https%253A%252F%252Fwww.ti.com%252Fproduct%252FOPA548. [Accessed 8 July 2020].

[139] Analog Devices, "AD8421," 2012. [Online]. Available: https://www.analog.com/media/en/technical-documentation/data-sheets/AD8421.pdf. [Accessed 9 September 2020].

[140] H. A. Wheeler, "Formulas for the Skin Effect," *Proceedings of the IRE,* vol. 30, no. 9, pp. 412-424, 1942.

[141] G. Grandi, M. K. Kazimierczuk, A. Massarini, U. Reggiani and G. Sancineto, "Model of laminated iron-core inductors for high frequencies," *IEEE Transactions on Magnetics,* vol. 40, no. 4, pp. 1839-1845, 2004.

[142] C. R. Sullivan, "Optimal choice for number of strands in a litz-wire transformer winding.," *IEEE Transactions on power electronics,* vol. 14, no. 2, pp. 283-291, 1999.

Appendices

Appendix A: Parameter Tuning for the Self-Sensing Methods

In Chapter 3 and Chapter 4, various parameters, such as the superimposed AC voltage and the complementary filter center frequency, required tuning to achieve suitable performance. For the purpose of this thesis, optimal tuning was not required as the goal was to prove and validate the expected characteristics of the CAS actuator and CAS sensor. Furthermore, optimal parameters are likely dependent on the intended application for the CAS actuator or CAS sensor. However, obtaining suitable performance to demonstrate the prototype CAS actuator and CAS sensor often required iterative tuning.

Some parameters, such as the superimposed AC voltage magnitude, have an obvious optimum value to use since increasing the AC voltage magnitude improves the SNR as was postulated in Section 2.3.1. This was validated experimentally using the CAS actuator and is shown in Figure A.1. For both the CAS actuator and CAS sensor, the largest possible AC voltage was chosen while ensuring the supply voltage would not be exceeded after adding it to the driving or bias voltage.

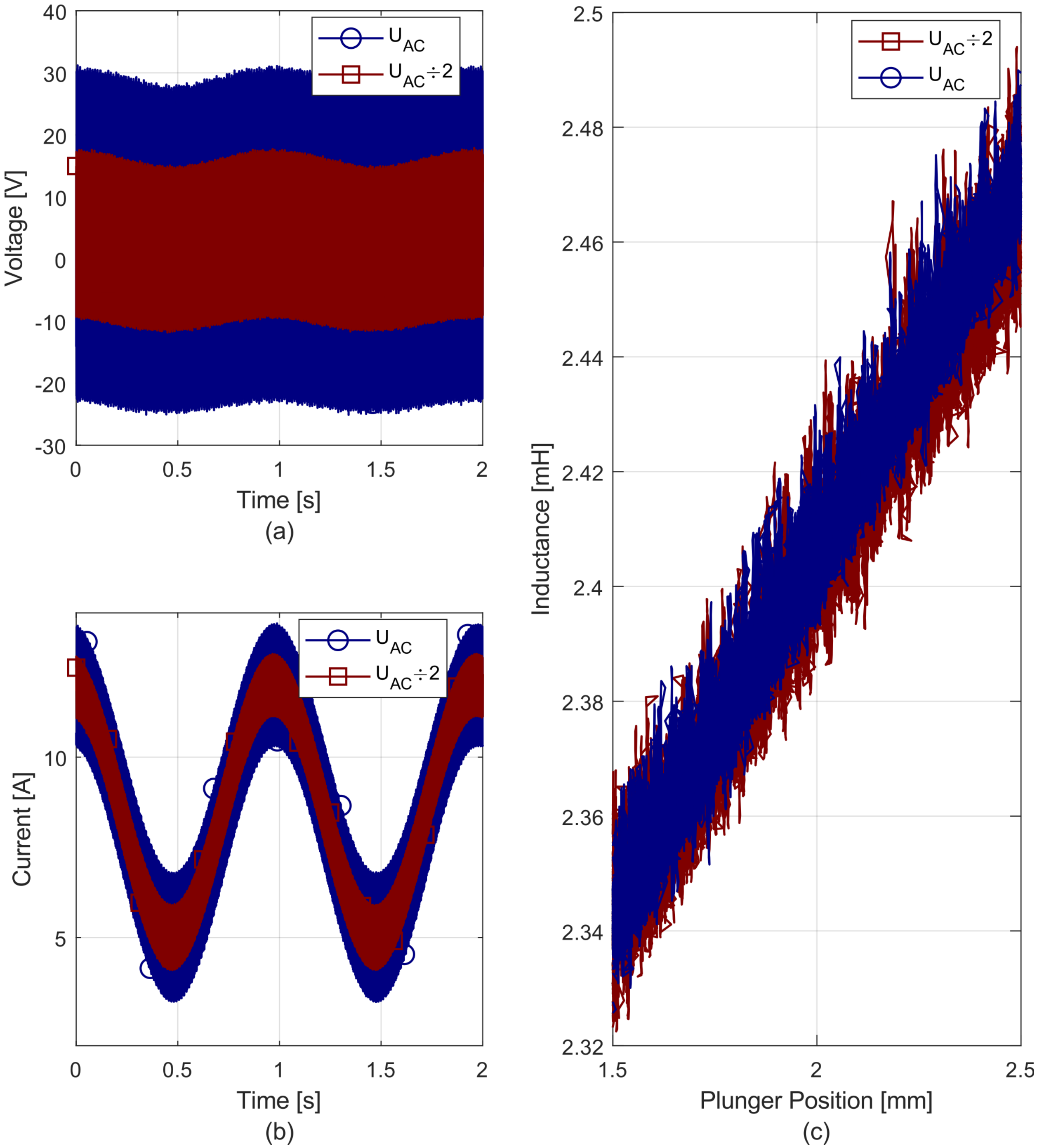

Figure A.1 Shows the effect when the superimposed AC voltage supplied to the CAS actuator is reduced.

Some parameters, such as the complementary filter center frequency, likely require iterative tuning as it is challenging to estimate a suitable frequency since noise is difficult to predict and significantly affects the bandwidth of the self-sensing measurements. Figure A.2 shows a visualization of the bandwidth of the self-sensing methods. It is ideal when the inductance-based and BEMF-based or flux linkage-based methods significantly overlap as this provides bandwidth for the complementary filter to transition between favoring one of the methods. If there is no overlap, as is seen in Figure A.2b, then the complementary filter output will have deadband where the measurement will become less accurate. The upper bound of the inductance-based measurement depends on several factors, such as the magnitude and frequency of the AC voltage and current. The lower bound of the BEMF-based and flux linkage-based methods are determined by factors such as the magnitude of the driving or bias current relative to the amount of noise in the current measurement. Naturally, since the CAS sensor can differentially cancel noise, its self-sensing measurements are much more likely to avoid deadband issues unlike a CAS actuator. Ultimately, hardware limitations or a noisy environment could lead to deadband. When there is deadband, the accuracy of the complementary filter outputs will become very sensitive to the placement of the center frequency and may require compromises to be made regarding low-speed and high-speed self-sensing performance.

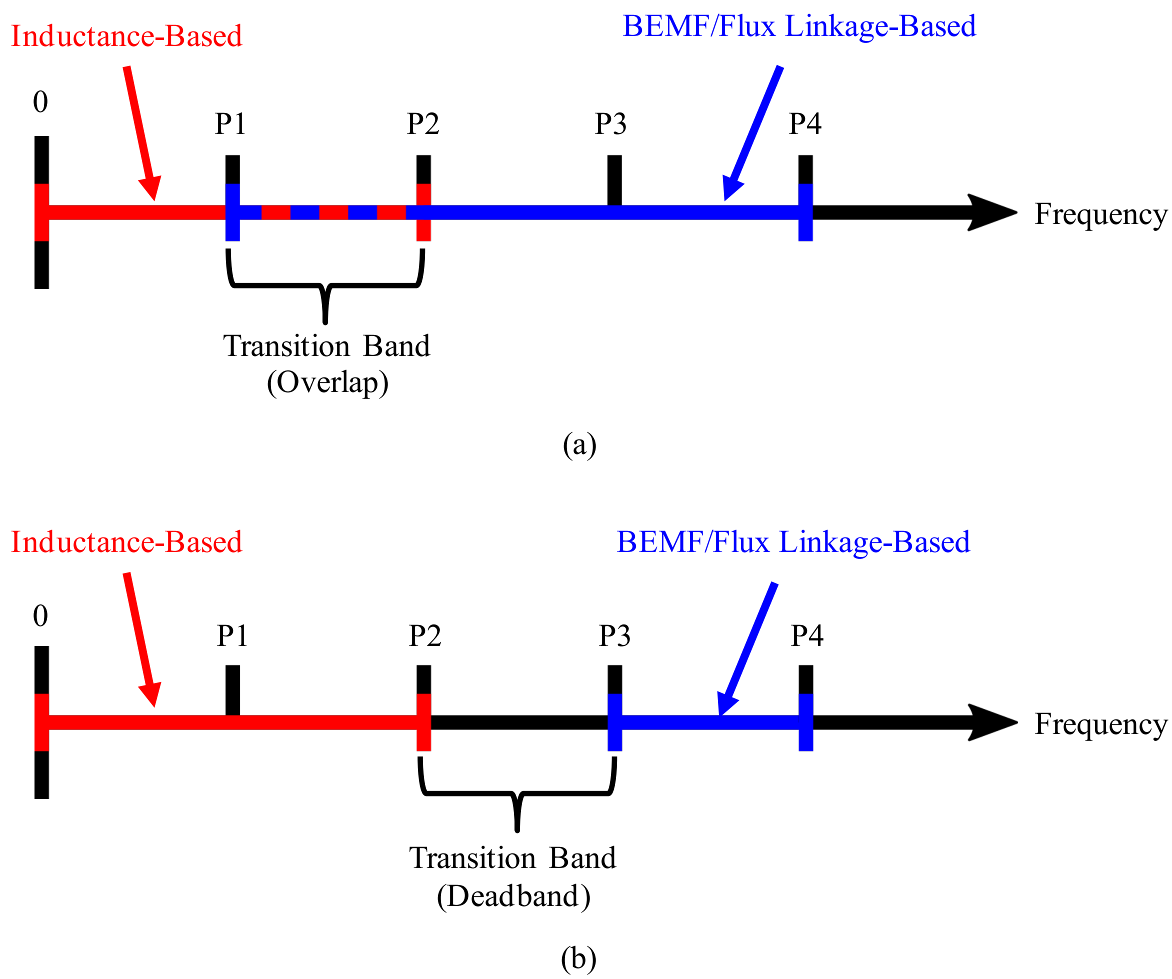

Figure A.2 A visualization of the bandwidth of the individual self-sensing methods. An ideal transition band is shown in (a) since there is overlap between the measurements and a nonideal transition band is shown in (b) since there is deadband between the measurements.

It was noted the self-sensing performance of the CAS actuator significantly changed when adjusting the complementary filter center frequency. In particular, the center frequency used in the CAS actuator simulation did not perform well when applied to the prototype, unlike the CAS sensor. A parametric study was conducted by driving the plunger with the current controller at various mechanical frequencies as was done in Figure 3.38. Afterwards, the results were post-processed and the flux linkage-based complementary filter output was compared to the laser sensor. The error between these measurements is shown in Figure A.3. It was noted that a center frequency of 20Hz performed significantly better at high-frequencies than the 10Hz center frequency used in the simulation; increasing the center frequency to 30Hz increased the error. The other interesting observation to note is that the error for the 20Hz center frequency increases between the plunger moving at 1Hz and 40Hz. This indicates the prototype CAS actuator has some deadband between its self-sensing methods. However, this deadband was small enough to allow sensorless control to still be demonstrated in Chapter 3. The effect complementary filter center frequency has on trajectory-tracking performance can be visualized in Figure A.4. A 20Hz center frequency outperformed the other frequencies shown and agrees with the results from Figure A.3. Therefore, 20Hz was selected and was used when producing the results in Chapter 3.

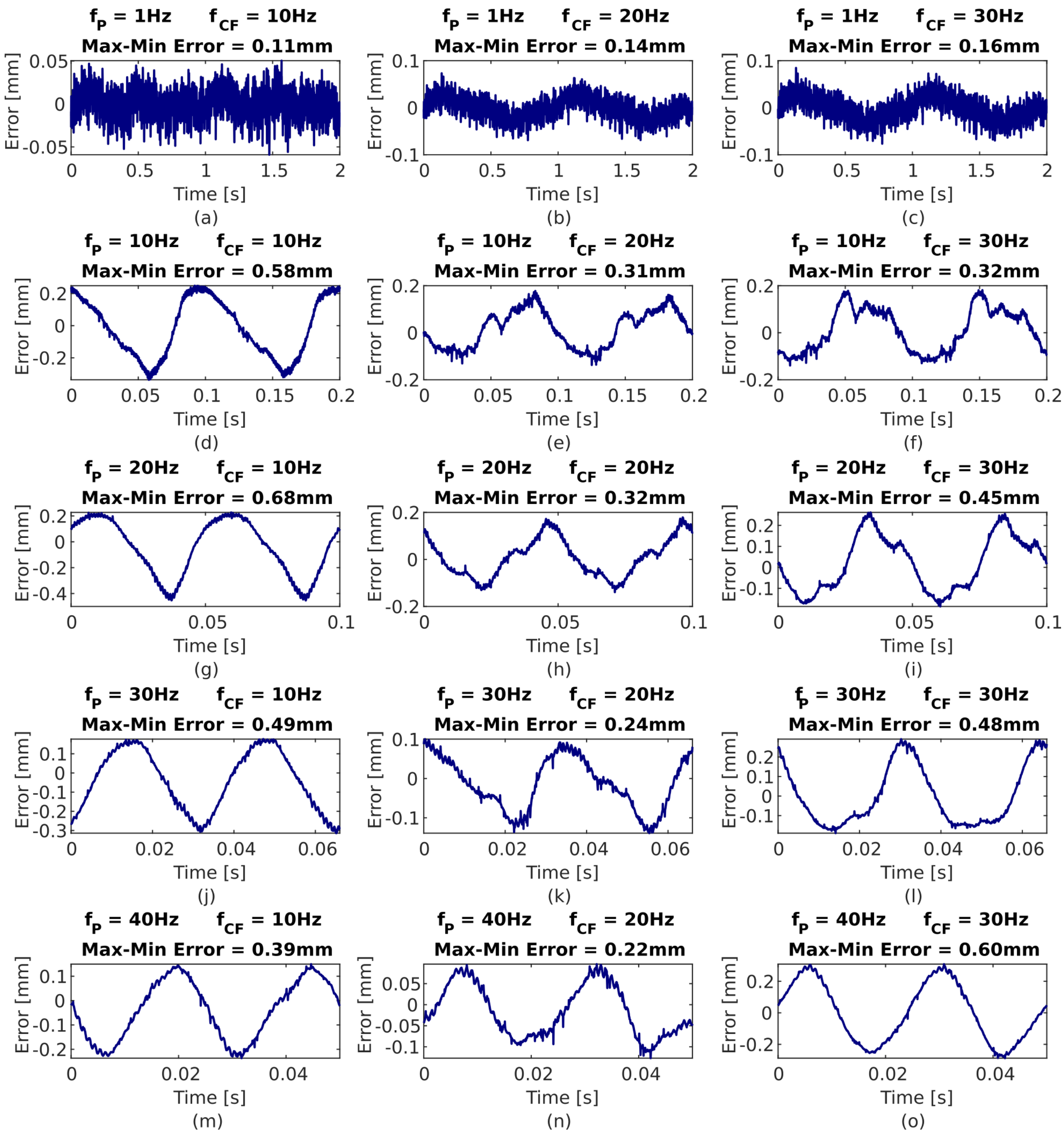

Figure A.3 A parametric study at specific mechanical frequencies for determining a suitable complementary center frequency. The error is calculated as the subtraction between the flux linkage-based complementary filter output and the laser vibrometer.

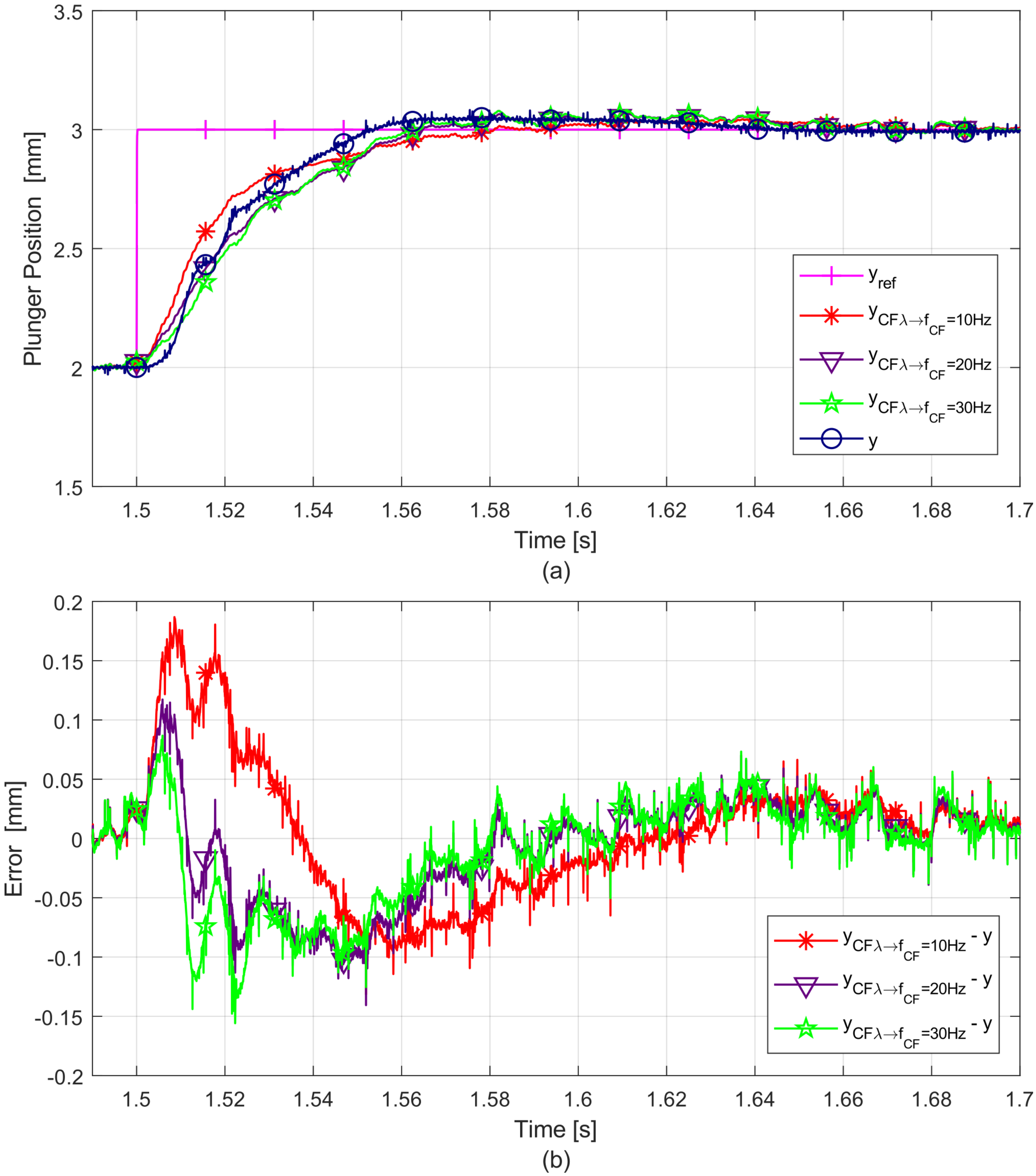

Figure A.4 A parametric study using a step trajectory for determining a suitable complementary filter center frequency. (a) shows the plunger position and (b) shows the error relative to the measurement produced by the laser vibrometer. The actual plunger position, $\boldsymbol{y}$, is assumed to be the measurement produced by the laser vibrometer.

Appendix B: CAS Sensor Custom Circuits

This appendix contains schematics and additional details regarding the custom circuitry used to operate the CAS sensor.

B.1 **CAS Sensor Driver**

The CAS sensor driver is a non-inverting operational amplifier circuit and a schematic is provided in Figure B.1. The circuit was adapted from the example OPA548 non-inverting amplifier circuit shown in [138]. The passive components in Figure B.1 are able to withstand the maximum ratings of the OPA548. The gain of the circuit can be adjusted by varying the R1 and R2 potentiometers. For the CAS sensor experiments in Chapter 4, R1 and R2 were adjusted to attain a gain of 10. The R3 potentiometer is used to limit the maximum output current of the OPA548. The enable/status pin was left floating as its functionality was not required. The fabricated circuit is seen in Figure B.2.

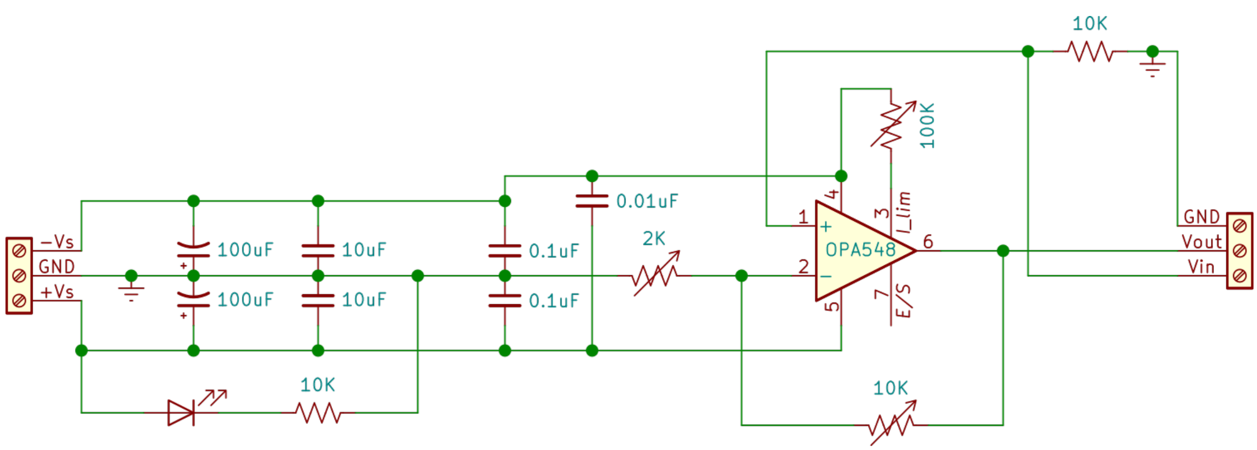

Figure B.1 Schematics of the circuit used to drive the CAS sensor.

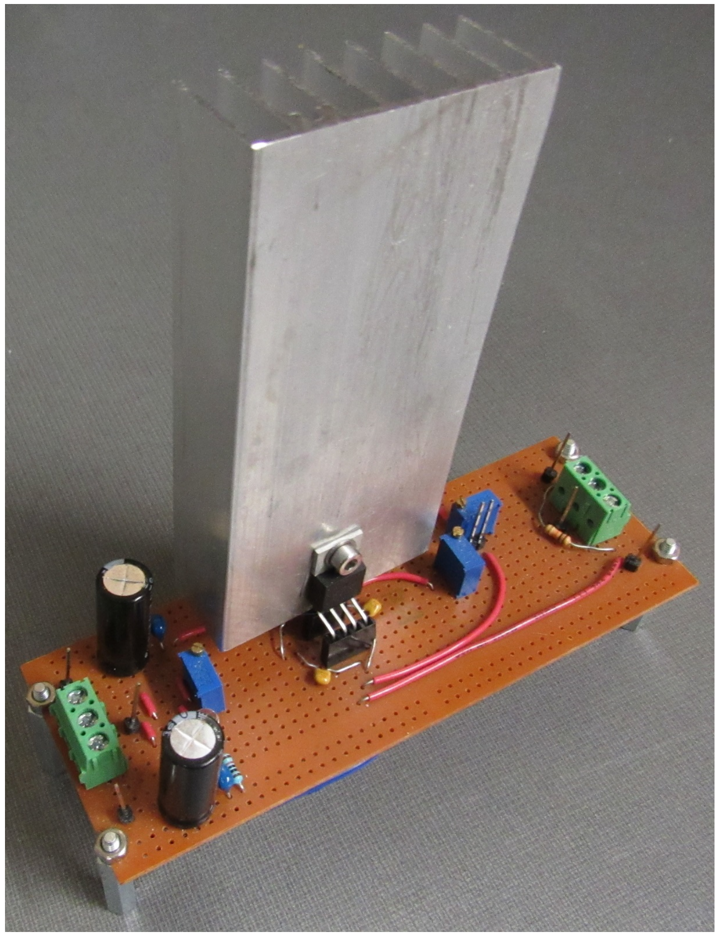

Figure B.2 Fabricated custom CAS sensor driver.

B.2 **CAS Sensor Voltage and Current Measurement Circuit**

The CAS sensor voltages, U_1 and U_2, and the series current, I, are measured using the circuit shown in Figure B.3. All of the measurements use AD8421 instrumentation amplifiers which are designed for measuring differential signals and rejecting common-mode disturbances. A VPR221 1Ω shunt resistor is used to convert the current through the CAS sensor into a measurable voltage. The Rg ports are used to adjust the output gain of the AD8421. Potentiometers were added to allow the AD8421 gain to be adjusted and fine-tuned. In the datasheet, it was noted that a gain of around 10 provided a preferable compromise for various parameters such as noise rejection, settling time and dynamic response [139]. Therefore, for the final CAS sensor experiments, the AD8421 current gain was set to 10 and the voltage gains were set to 8 using the potentiometers. It is important to note that the net voltage gains are only 1/2 since a resistor network pre-gain of 1/16 is applied prior to the instrumentation amplifiers to ensure the voltages are within the range of the dSPACE analog-to-digital converters. The outputs of the AD8421 were lowpass filtered using an analog resistor-capacitor network. The corner frequencies of the filters were set to approximately 16kHz to attenuate high-frequency noise while being distant from the superimposed AC voltage and current in order to avoid influencing the self-sensed position estimates. The fabricated circuit is shown in Figure B.4.

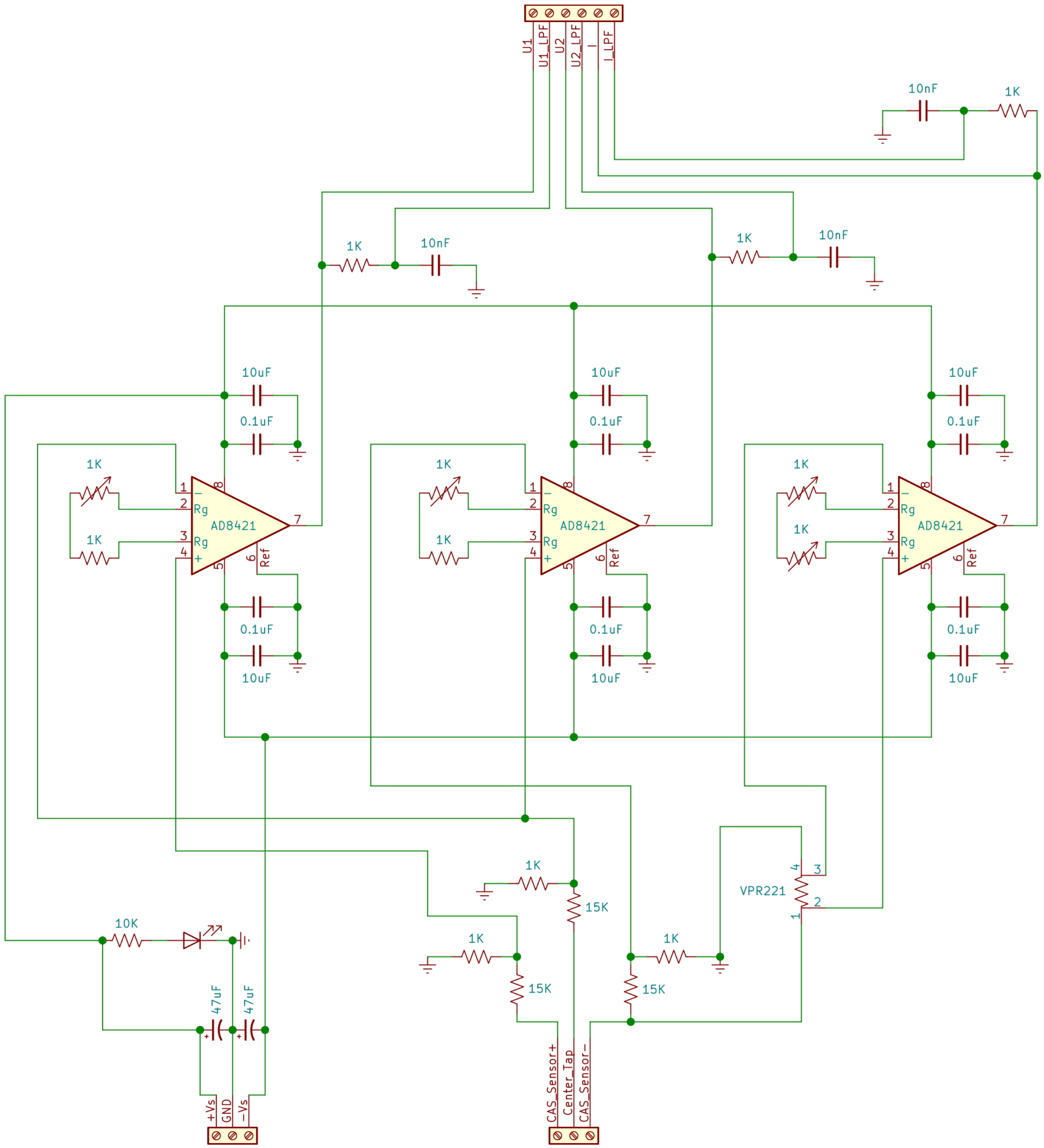

Figure B.3 A custom circuit used to measure the voltage and current across the CAS sensor.

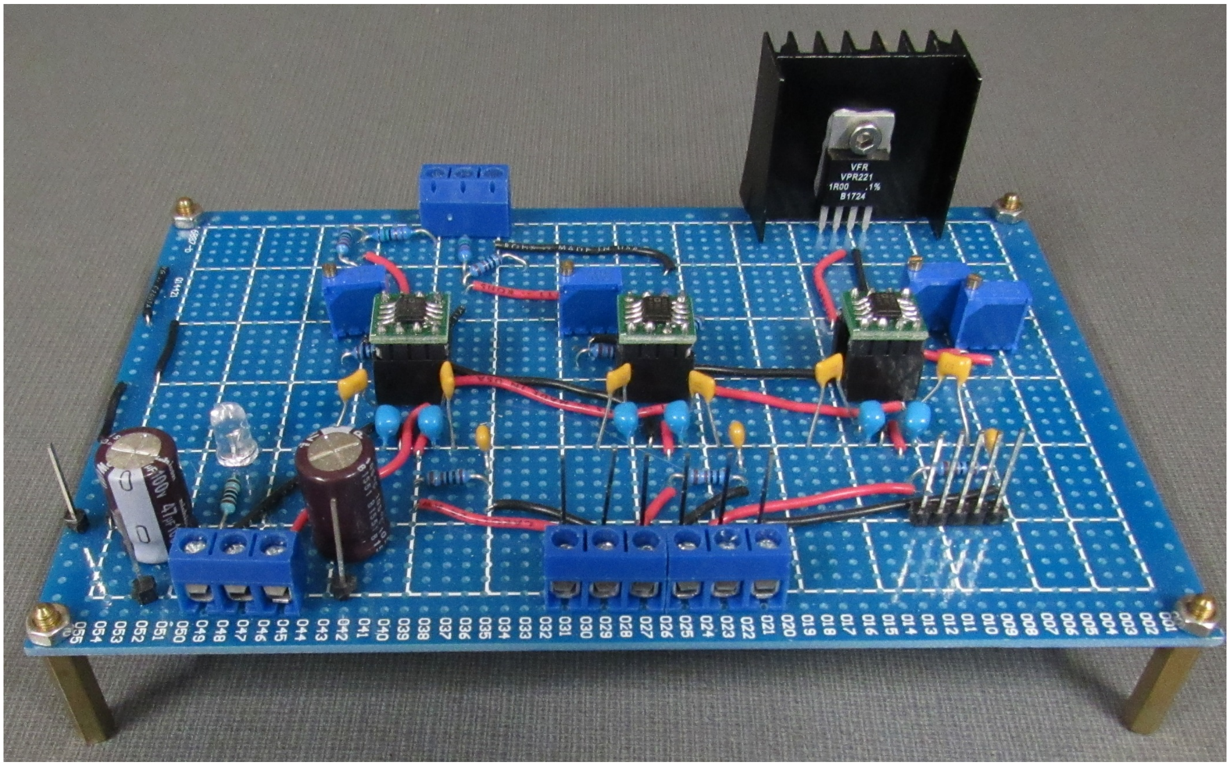

Figure B.4 Fabricated custom circuit used to measure the voltage and current across the CAS sensor.